Stability of Beams, Plates and Membranes due to Subsonic Aerodynamic Flows and Solar Radiation Pressure

by

Samuel Chad Gibbs IV

Department of Mechanical Engineering and Materials Science
Duke University

Date: _____

Approved:

_____
Earl H. Dowell, Supervisor

_____
Donald B. Bliss

_____
Kenneth C. Hall

_____
Thomas P. Witelski

Dissertation submitted in partial fulfillment of the requirements for the degree of Doctor of Philosophy in the Department of Mechanical Engineering and Materials Science
in the Graduate School of Duke University
2014

Abstract

Stability of Beams, Plates and Membranes due to Subsonic Aerodynamic Flows and Solar Radiation Pressure

by

Samuel Chad Gibbs IV

Department of Mechanical Engineering and Materials Science
Duke University

Date: _____

Approved:

_____
Earl H. Dowell, Supervisor

_____
Donald B. Bliss

_____
Kenneth C. Hall

_____
Thomas P. Witelski

An abstract of a dissertation submitted in partial fulfillment of the requirements for the degree of Doctor of Philosophy in the Department of Mechanical Engineering and Materials Science
in the Graduate School of Duke University
2014

Abstract

This dissertation explores the stability of beams, plates and membranes due to subsonic aerodynamic flows or solar radiation forces. Beams, plates and membranes are simple structures that may act as building blocks for more complex systems. In this dissertation we explore the stability of these simple structures so that one can predict instabilities in more complex structures. The theoretical models include both linear and nonlinear energy based models for the structural dynamics of the featureless rectangular structures. The structural models are coupled to a vortex lattice model for subsonic fluid flows or an optical reflection model for solar radiation forces. Combinations of these theoretical models are used to analyze the dynamics and stability of aeroelastic and solarelastic systems. The dissertation contains aeroelastic analysis of a cantilevered beam and a plate / membrane system with multiple boundary conditions. The dissertation includes analysis of the transition from flag-like to wing-like flutter for a cantilevered beam and experiments to quantify the post flutter fluid and structure response of the flapping flag. For the plate / membrane analysis, we show that the boundary conditions in the flow direction determine the type of instability for the system while the complete set of boundary conditions is required to accurately predict the flutter velocity and frequency. The dissertation also contains analysis of solarelastic stability of membranes for solar sail applications. For a fully restrained membrane we show that a flutter instability is possible, however the post flutter response amplitude is small. The dissertation also includes analysis of a membrane

hanging in gravity. This systems is an analog to a spinning solar sail and is used to validate the structural dynamics of thin membranes on earth. A linear beam structural model is able to accurately capture the natural frequencies and mode shapes. Finally, the dissertation explores the stability of a spinning membrane. The analysis shows that a nonlinear model is needed to produce a conservative estimate of the stability boundary.

Contents

List of Tables

List of Figures

List of Abbreviations and Symbols

Symbols

D	Plate stiffness ($D = Eh^3/(12(1-\nu^2))$)
E	Young's modulus
E'	$E/(12(1-\nu^2))$
g	Gravitation acceleration
GJ	Beam torsional stiffness
h	Thickness
I	Beam moment of inertia
k_m	Beam radius of gyration
$\bar{K}$	Stiffness matrix
L_x, L, a	x-direction length
L_y, S, b	y-direction length
m	Mass per unit length ($\rho_s h L_y$)
M	Mach number
$\bar{M}$	Mass matrix
$P_i^{n+1/2}$	Aerodynamic force on the i'th panel at a time step between n and $n+1$
P_o	Solar radiation pressure strength
$q_n(t)$	n'th generalized coordinate
Q_n	n'th generalized force

S_c	Number of structure elements in x-direction of VLM mesh
S_s	Number of structure elements in y-direction of VLM mesh
T, V	Kinetic and potential energy
T_x, T_y	Tension in the x-direction and y-direction
U_∞	Free stream flow velocity
$v_n(x)$	Beam in plane bending mode shape
$w(x, y, t)$	Out of plane displacement
α	VLM relaxation factor, angle between solar radiation and unit normal to a structure
β	Yaw angle between the flow and the beam
γ	Sun inclination angle
Γ_i^n	i'th circulation strength at time step n
ν	Poisson ratio
ω	Natural frequency
Ω	Heliogyro spin rate
$\phi_n(x), w_n(x), h_n(\eta)$	Beam bending mode shape
ψ	Solar sail yaw angle
$\Psi_n(x, y)$	n'th plate mode shape
ρ	Air density
ρ_s	Structure density
σ	Applied tensile stress
$\Theta_n(x), g_n(x)$	Beam torsion mode shape

Superscripts

$\tilde{}$	Non-dimensional
$\dot{}$	Time derivative
$'$	Spatial derivative

bold	Vector quantity
$\bar{}$	Matrix quantity

Abbreviations

VLM	Vortex Lattice Method

Acknowledgements

The author would like to acknowledge Dr. Earl H. Dowell for his support as a research mentor throughout his graduate school career. Further, the author acknowledges his committee, Dr. Donald Bliss, Dr. Kenneth Hall, and Dr. Thomas Witelski for their technical guidance. The author would also like to acknowledge the members of the Duke Aeroelasticity Research Group for their guidance and support. In particular the author would like to acknowledge the contributions of Dr. Deman Tang and Dr. Ivan Wang. Outside of Duke, the author would like to acknowledge the research support from Dr. Keats Wilkie, Dr. Karen Lyle, and Dr. Jay Warren, members of the Structural Dynamics Branch at NASA's Langley Research Center. The author would also like to acknowledge Dr. Sergio Ricci, Sebastiano Fichera, and Dr. Alex Zanotti from the Politecnico di Milano, in Milan Italy, for hosting him and supporting his research. Finally, the author would like to acknowledge the support of his family and friends. In particular, his father Sam, his mother Cynthia, his sisters Maria and Laura, and his best friend Sarah.

The author is also grateful for the funding support from the following organizations. First, the NASA Office of the Chief Technologist Space Technology Research Fellowship, which funded the author's research from 2012 through 2014. In addition, NASA's Langley Research Center supported on-site experiments through the Student Career Experience Program in the summer of 2012. Second, the Duke Chapter of Sigma Xi's Sally Hughes-Schrader travel grant for supporting the authors research

in Milan Italy. Finally, the author would also like to acknowledge the funding support from the Duke Mechanical Engineering and Material Science Department for conference travel and first year research funding.

1

Introduction and Literature Review

Understanding the stability of relatively simple structures is the foundation for predicting and avoiding instabilities in more complex systems. In this dissertation, we will explore the stability of such structures in the presence of aerodynamic or solar radiation forces, providing a rational basis for designing aerospace systems with a wide range of applications. Specifically, we will analyze the stability of rectangular uniform structures by coupling linear and nonlinear beam, plate and membrane structural models with varying fidelity aerodynamic or solar radiation forcing models. Additionally, we will validate theoretical models with experiments. The models in this dissertation are developed to be preliminary design tools for application that range from energy harvesting and noise reduction on subsonic transport aircraft, to next generation solar sail space propulsion technology. The introduction will provide a brief overview of the relevant literature and motivation for both the aeroelastic and solarelastic research found throughout this document.

1.1 Aeroelastic Research Motivation and Selected Literature

The aeroelastic research focuses on the theoretical and experimental analysis of rectangular plates and membranes in different subsonic flow conditions. The research is centered around two topics. The first topic is a detailed study of the aeroelastic stability of cantilever beam-rods and the second topic is an exploration of a plate with various boundary conditions.

For the cantilever beam, two aspects are explored. First, we explore the transition from flapping flag to wing-like flutter of a cantilever beam-rod as we vary the angle between the clamped edge and free stream flow. Second, we conduct experimental observations on the flapping flag configuration. The interaction between a cantilevered elastic plate and a uniform axial flow is a canonical fluid-structure interaction problem. If the flow is oriented *parallel* to the clamped leading edge the system is described as a wing-like configuration. If the flow is oriented *normal* to the clamped edge then the system is referred to as flapping flag-like. There is extensive research on the aeroelastic stability of the wing-like configuration due to the similarities between the simple cantilevered beam and aircraft wings. Researchers have been interested in the stability of aircraft wings since a 1916 flutter incident on a Handley Page O/400 twin engine biplane bomber (Garrick and Reed III (1981), Kehoe (1995)). Wing-like aeroelastic systems typically lose stability due to a coalescence between a bending and torsion mode. The simplest aeroelastic models for a wing are typical section models that include just a single degree of freedom each in plunge and twist (Dowell et al. (2004)). Goland (1945) is the classic paper describing the coupled bending torsion flutter of a simple cantilever beam-rod in the wing configuration. Of particular interest to the current research are aeroelastic studies of swept wings. Bisplinghoff et al. (1996) contains a review of the classic literature relating to the aeroelastic stability of swept wings. These authors note that modeling a swept

wing is particularly challenging due to the misalignment between the normal to the pitching axis and the incoming flow.

The research in this dissertation differs from the classic explorations of the swept wing due to the application of the clamped boundary condition. For a traditional swept wing configuration the clamp is applied parallel to the flow, changing the shape of the structure for every angle. For the current research the clamped edge is rotated with the structure. This is similar to the rotated wing experiments conducted by Barmby et al. (1951). In their study, the authors look at the flutter characteristics of a wing that is rotated up to 60 degrees. The current work extends this research to explore the rotated wing all the way to the second classic fluid structure interaction configuration for a cantilever.

It is well known that this second classic aeroelastic configuration exhibits a bending only flutter instability in low subsonic flow as the free stream velocity is increased above a critical velocity. Typically the instability is caused by the coalescence of the two lowest frequency bending modes for the mass ratios explored in this dissertation (Doaré et al. (2011), Eloy et al. (2007, 2008), Gibbs et al. (2012b), Tang et al. (2003)). Since the experimental observations of the flapping flag by Taneda (1968) and Kornecki et al. (1976), many scholars have explored the stability of this system experimentally and theoretically. In addition to the problem's inherent physical significance, Doaré and Michelin (2011), Dunnmon et al. (2011) and Giacomello and Porfiri (2011) have recently proposed using the phenomena for energy harvesting applications and Eloy and Schouveiler (2011) and Hellum et al. (2011) have explored the potential of using flutter for propulsion. Furthermore, Balint and Lucey (2005), Huang (1995) and Howell et al. (2009) have shown that cantilevered plate flutter in the human soft palate can explain snoring and Watanabe et al. (2002a) has explored this type of flutter in the printing industry.

Many of the applications presented in the previous paragraph also rely on un-

derstanding the post-flutter response of the flapping flag system. Understanding the response of this system at velocities above the flutter velocity includes predicting the amplitude of the LCO and capturing a hysteresis loop that is observed in experimental studies (Dunnmon et al. (2011), Eloy et al. (2012), Gibbs et al. (2012b), Tang et al. (2003)). A hysteresis loop is a non-linear phenomenon that describes a system whose response depends on its past states. For the flapping flag, the hysteresis loop manifests itself in a range of flow velocities where it is possible to have either a stable and unstable responses depending on whether one is increasing or decreasing the flow velocity.

It is difficult to model the post critical behavior of the system because nonlinear effects cause both the LCO and hysteresis. Many authors including Dunnmon et al. (2011), Eloy et al. (2012), Michelin et al. (2008) and Tang and Païdoussis (2007), Tang and Païdoussis (2008) have created non-linear models. Currently, the non-linear theoretical models of the flapping flag largely focus on nonlinearities in the structural dynamics. For example, Tang et al. (2003) developed a theoretical model using a non-linear inextensible beam coupled to a linear three-dimensional vortex lattice aerodynamic model to predict the post critical response. The theoretical predictions accurately predicted the flutter boundary, but underestimated the LCO amplitude and did not capture the hysteresis loop. In general, previous aeroelastic models that include classical structural nonlinearities have not been able to predict accurately the LCO amplitude.

Aeroelastic models are usually based on both linear or nonlinear structural models combined with potential flow aerodynamic models. With advances in computational power, recent studies have also studied viscous effects by using CFD techniques to solve the Navier-Stokes equations (Balint and Lucey (2005), Gordnier and Visbal (2002), Watanabe et al. (2002b)). However, even with the advances in computational power, it is still not efficient to use these computational tools for three dimensional

simulations and parameter variation studies. Furthermore experiments by Zhang et al. (2000) on a flexible filament in a flowing soap films indicated that no flow separation occurs along the flexible body suggesting viscous effects may not be important. Our current research complements the previous experimental work from Zhang et al. (2000) by looking at the flow around the flapping flag in air.

In addition to looking at the stability of the cantilevered plate, this dissertation also explores the stability of a rectangular plate with different boundary conditions. The aeroelastic literature is filled with studies of simple systems, such as the rectangular plate, that have analogs to real aerospace systems because they allow theoretical models to be developed and validated with controlled experiments. For example, results from the previously referenced paper by Goland (1945) are often used as validation cases for aeroelastic explorations ranging from design of folding wing aircraft (Wang et al. (2012b)) to validating new CFD aeroelastic codes (Marques et al. (2013)).

In addition to the wing and flapping-flag configurations described earlier, there is a third rectangular plate boundary condition combination that is studied in the aeroelastic literature. This configuration is a plate with all edges geometrically constrained, or, for the two dimensional case, the leading and trailing edge restrained. This configuration is referred to as panel flutter due to the similarity between this configuration and the panels that make up the skin of an aircraft. Panel flutter studies often only consider flow over a single side of the rectangular structure. For this configuration the critical instability in subsonic flow is a divergence instability (Kornecki (1974)).

The push for novel aerospace designs has introduced the need to understand the stability of aerospace structures with boundary conditions not similar to the classic configurations. One example comes from NASA, which is currently designing the next generation of commercial transport aircraft with several performance require-

FIGURE 1.1: Contrails Created by an Extended Flap on a Transport Aircraft During Landing (Berens (2008))

ments, one of which is noise reduction (NASA (2000)). Experimental and numerical studies demonstrated that a large portion of aircraft noise during landing is generated by the shed vortices at the discontinuity between the wing and the trailing edge flap (Choudhari et al. (2002), Streett et al. (2003)) shown in Figure 1.1. The noise reduction potential of several geometries and mechanisms were studied, but experiments showed that the most effective method for significant noise reduction is to introduce a continuous mold-line link (CML), which is a fairing surface that smoothly connects the edge of the flap to the wing (Streett et al. (2006)). This is shown in Fig. 1.2. The acoustic experiments were performed using a rigid fairing, but to implement a fairing on an aircraft it must be deformable. A flexible plate, or a plate-membrane structure, is an ideal candidate for the fairing structure because it can be stored during flight, but extended and tensioned when the trailing edge flaps are deployed. A plate has stiffness primarily due to bending, while the stiffness of a plate-membrane comes from both bending and applied tension. Both types of structures will herein be referred to as plates for simplicity.

Despite significant progress in reducing noise from other sources, such as airframe

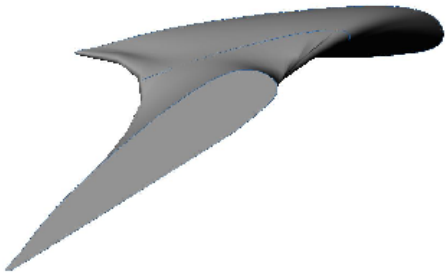

FIGURE 1.2: Schematic of NASA's Proposed Continuous Mold-Line Link

and propulsive devices, an assessment by Berton et al. (2009) of the overall progress toward the next generation of aircraft showed that additional research in CML's may be necessary for meeting the noise reduction goal. Because these structures are flexible and would be designed to be light-weight, it is important to analyze their aeroelastic behavior to prevent structural failure due to divergence or flutter. The behavior of panels with three sides clamped, the correct analog to the current CML design, is not one of the classic aeroelastic configurations and therefore has not been studied in the aeroelastic literature. NASA's CML project is just one of many problems that may require the use of novel plate configurations. Examples range from designing micro air vehicles (Han et al. (2009), Abdulrahim et al. (2004)) to analyzing animals in flight (Templin (2000), Song et al. (2008), Zhao et al. (2010)). As the design and analysis of aerospace structures focuses more on lighter materials and novel configurations, analytical and experimental results for unexplored boundary conditions and different materials will be important in determining viable designs and validating analysis codes.

1.2 Solarelastic Research Motivation and Selected Literature

In 2016, NASA will launch the Sunjammer solar sail towards the sun.[1] The Sunjammer is a 1200 m^2 solar sail named after the Arthur C. Clarke short story of the same name about a solar sail race around the moon (Clarke (1973)). This mission represents NASA's reinvestment in bringing solar sail technology from science fiction to reality. The interest in solar sail technologies both at NASA and at space agencies around the world was sparked by the successful launch of the JAXA IKAROS solar sail on May 21st, 2010, that demonstrated controlled flight using solar sail propulsion (Tsuda et al. (2011)). Solar sails are a form of propellant-less spacecraft propulsion that generate thrust by reflecting incoming solar radiation. The force acts in the direction normal to the local surface in a manner analogous to a Newtonian fluid flow. Although the forces are small, on the order of 10^{-5} N/m^2 at 1 astronomical unit (AU), or 150 million kilometers from Earth's sun, the lack of energy dissipation in space allows solar sails to accelerate continuously. Solar sails are able to outperform chemical propulsion for missions ranging from orbital debris capture and removal, de-orbit of spent satellites, station keeping in unstable locations in space, to deep space propulsion (Gibbs and Dowell (2013), Wilkie et al. (2013),[2]).

While solar sail spacecraft come in many shapes and sizes, the research in this dissertation focuses on two particular architectures. The first is often referred to as a "square-rig" solar sail. For this type of solar sail, the reflective membrane is supported by rigid booms that are deployed in space. For example, the Sunjammer will use four inflatable booms connected by streamers to support the solar sail's reflective membrane. Another solar sail spacecraft architecture that NASA is currently

[1] Leone, D., "Building A Better Space-weather Buoy: Tests Continue on Sunjammer," www.spacenews.com, October 2013.

[2] Steitz, D.,"Communications, Navigation and In-Space Propulsion Technologies Selected For NASA Flight Demonstration," NASA Website, 2011.

exploring is the heliogyro architecture proposed by MacNeal (1971) in the late 1960's. Heliogyro solar sails are comprised of a set of slender reflective membrane blades that rotate around a central hub. The appeal of this class of spinning solar sails includes the ability to replace rigid members used by traditional solar sails to stiffen the large reflective membranes with centrifugal forces, minimizing the spacecraft weight and improving the spacecraft performance. An added benefit of the heliogyro architecture is the ability to use root blade pitch control to provide attitude control in all six axes (Wilkie et al. (2013)). The analysis of heliogyro spacecraft dates back to the 1978 heliogyro design effort when MacNeal and Hedgepath presented their research on the heliogyro dynamics at the 34th National Forum of the American Helicopter Society (MacNeal and Hedgepeth (1978)). The design concept proposed by the authors featured 12 blades in two counter-rotating tiers, as shown in Fig. 1.3. The proposed design was never flown due to the perceived overall high risk associated with unproven solar sail technology (MacNeal and Hedgepeth (1978)).

Today NASA is reevaluating the heliogyro propulsion technology. In particular, NASA's Langley Research Center is spearheading the development of a CubeSat-based flight demonstration mission named the HELIOS (High-Performance, Enabling, Low-Cost, Innovative, Operational Solar Sail) to develop and demonstrate the capability of heliogyro technologies. The nominal design calls for a set of six blades, each with a span of 220 m, chord of 0.75 m and a nominal thickness of 2.54 microns that spin around the hub at a rate of 1 RPM.

One of the potential problems faced by all solar sails is that the reflective sails, which are thin membranes, remain only lightly tensioned and therefore may be susceptible to dynamic instabilities. In a recent note, Dowell (2011) utilized the mathematical similarity between solar radiation forcing and supersonic piston theory aerodynamics to predict that solar sail structures may flutter. Dowell describes how the the feedback between elastic solar sail deflections and the solar radiation forcing is

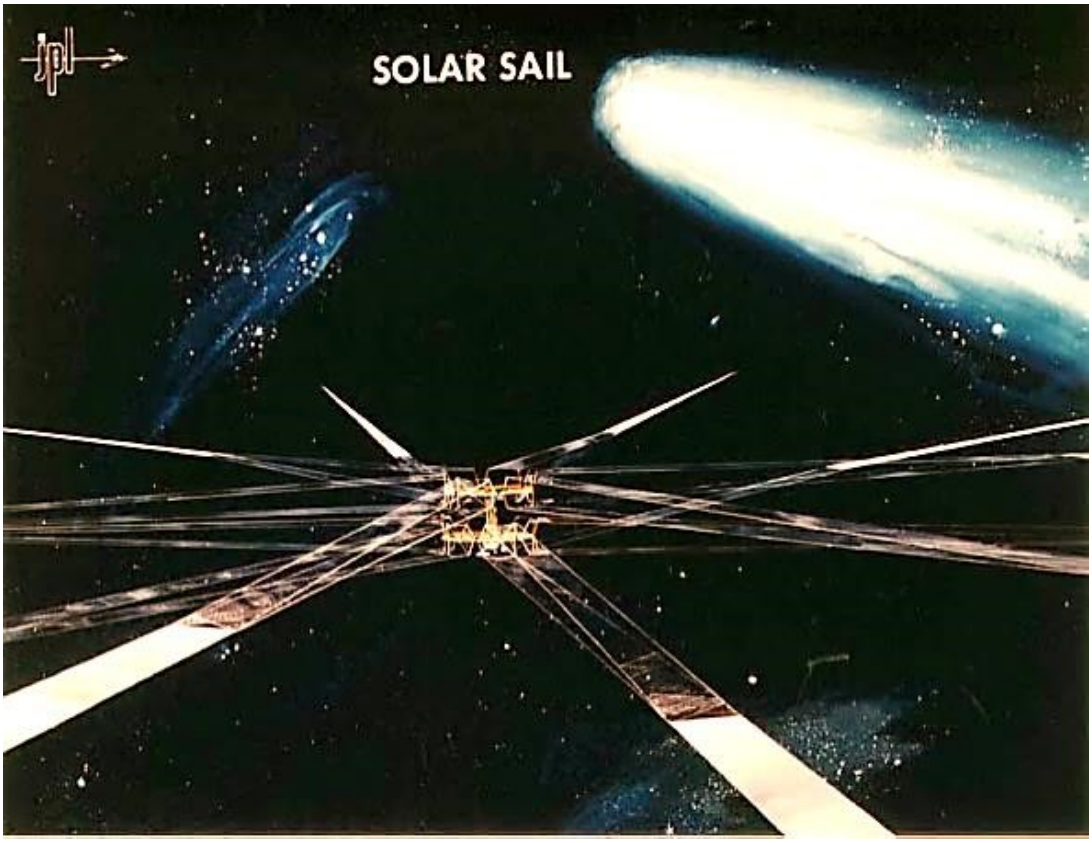

FIGURE 1.3: Artist Rendition of the Comet Halley Heliogyro Design from NASA JPL

capable of causing instabilities for solar sails. While the potential for this type of instability has been referenced in the the literature (MacNeal (1971), Dowell (2011)), detailed modeling of the phenomenon has only been published in a single conference paper by Natori et al. (1989).

For solar sail membranes, much of the stiffness is derived from tension-like terms. When analyzing the stability of this type of structure we may encounter the "membrane paradox" described in the aeroelastic literature (Ellen (1965)). In early modeling of thin membranes forced by supersonic flows, researchers noted that as the thickness of the membrane approached zero, the instability dynamic pressure grew to infinity. Upon further inspection, Spriggs et al. (1969) identified that the membrane limit is a singular perturbation problem and the stability is largely influenced by

small structural boundary layers at the leading and trailing edges of the membrane. In this dissertation we analyze the stability of a rectangular solar sail membrane by adapting the techniques presented in Spriggs et al. (1969) and Dowell and Ventres (1970).

To analyze the structural dynamics and stability of the heliogyro we also borrow heavily from previous aeroelastic research. In our research, we capture the structural dynamics of the blade using the Hodges and Dowell (1974) rotating beam equations. For the thin lightweight membranes used in the heliogyro design, the bending stiffness is dwarfed by the centrifugal forces, a case that is not often explored for traditional rotorcraft.

1.3 Dissertation Outline

This section includes an outline the specific research that is presented in this dissertation. In Chapter 2 we provide theoretical derivations of the structural and forcing models that are used throughout this dissertation. The structural models include linear models for stings, beams, membranes and plates and a nonlinear model for a rotating beam. The forcing models includes a three dimensional vortex lattice model for subsonic aerodynamic flows and an optical reflection model for solar radiation fields.

Chapters 3 and 4 present aerolastic analysis and experiments. In Chapter 3 we explore the stability and post-flutter behavior of a cantilevered beam in subsonic flow. In this chapter we analyze the transition between classic aeroelastic configurations, the flapping flag and the wing as we vary the flow yaw angle. In addition we present two experimental studies conducted to advance the understanding of the post-flutter response for the flapping flag. The experimental studies are conducted to guide and support future work on the flapping flag aeroelastic system by providing guidance on the most important fluid model improvements as well as providing experimental

data to validate theoretical models.

Expanding on the work presented in Chapter 3, in Chapter 4 we replace the beam structural model with a plate structural model. This allows us to predict the stability of rectangular structures with various boundary condition combinations. In this chapter we explore the impact that boundary conditions play on the stability of three dimensional plates.

In Chapters 5 - 7 we replace the vortex lattice aerodynamic model with a solar radiation model to explore the stability of plates and membranes in space. This research supports the ongoing effort to design solar sail spacecraft. In Chapter 5 we analyze the stability of a plate using the structural model from the previous chapter coupled to a solar radiation model. The parameter values required to model the proposed solar sail structures require special treatment of the equations. In this chapter, we adapt a classic aeroelastic analysis technique to determine the stability of our rectangular membrane.

In Chapter 6 we build on the work from Chapter 5 by exploring a solar sail analog that can be studied on earth. Specifically, this chapter presents the structural dynamics and stability of a thin cantilevered membrane hung in gravity. We can build and analyze this system in a vacuum chamber on earth. This chapter presents a suite of ground vibration experiments conducted at NASA's Langley Research Center that validates our structural model for the thin membrane and builds confidence in the ability of our theoretical models to capture the fundamental physics of solar sail structures.

In Chapter 7 we apply our solarelastic analysis to a proposed solar sail design. The heliogyro is a spinning solar sail that has a set of helicopter-like blades that rotate around a central hub. In this chapter a nonlinear structural model borrowed from classic helicopter structural dynamics is used to analyze the stability of a proposed heliogyro design. The chapter includes analysis of the nominal configuration,

deployment and identifies critical areas that require higher fidelity modeling during the final design of a heliogyro spacecraft.

Finally, Chapter 8 contains a summary of the significant research findings and lists the avenues for future research illuminated by the analysis and experiments presented in this dissertation.

2

Derivation of Theoretical Models

The theoretical analysis discussed throughout this dissertation relies on implementing models that describe the dynamics of beams, plates and membranes forced by dynamic external forces. In this section we will present the structural and forcing models that are the foundation for the analysis throughout this dissertation. While individual applications will require us to couple and solve models with varying methods the building blocks are similar.

Models

- **Structural Models**

  Linear Beam / String Model: This structural model is a classic model for the linear dynamics of a rectangular structure when one dimension, such as the length, is much larger than the other two dimensions, such as the width and thickness.

  Linear Plate / Membrane Model: This structural model is an extension of the previous model for a rectangular structure where two dimensions, such as the length and width, are much larger than the third dimension, such as the

thickness.

Nonlinear Spinning Beam / String Model This nonlinear model includes nonlinear stiffness terms that arise when a cantilevered beam / string is rotating around one of its edges and undergoing large deformations.

- **Forcing Models**

  Vortex Lattice Aerodynamic Model: This linear aerodynamic model is capable of modeling three dimensional unsteady potential flows. We will use this model to model subsonic airflows around streamlined structures.

  Optical Solar Radiation Model: This linear or nonlinear solar radiation model allows us to predict the forces on a reflective structure placed in a solar radiation field.

2.1 Structural Models

The first task in determining the dynamic stability of any system due to an external forcing, whether that forcing is from subsonic aerodynamics or solar radiation, is modeling the structural dynamics of the systems. An elegant aspect of the models implemented in this dissertation is the capability to leverage similar structural models regardless of the origin of the forcing. This allows multiple forcing-structure analyses to use the same structural model. This section will outline three energy-based methods for modeling simple rectangular structures. The first structural model is a beam with bending and torsional degrees of freedom. This model allows for out of plane displacements and twist angles that vary with a single coordinate of the system. This model is accurate for slender structures where one length is much greater than the other two characteristic lengths. The second model is a plate model. Unlike the beam model, the plate structural model only assumes that the thickness is much smaller than the other characteristic dimensions. This model allows for displacements that

are a function of both directions in the structure, as well as boundary conditions on all of the edges of the plate. The final structural model is a modified version of the Hodges and Dowell (1974) nonlinear equations of motion for a spinning beam. This model of the rotating blade is particularly important to the heliogyro related research research.

2.1.1 Beam / String Model

The first model that is useful for many applications in both aeroelasticity and solarelasticity is that of a beam in bending and torsion. Although this is a very classical model this section provides a summary of the derivation and outlines the modifications that are necessary to more completely capture the dynamics of the structures explored in this document. Specifically, the section will outline the inclusion of rigid body modes as well as tension into the elastic structural model. With these modifications, the structural model can be used for applications ranging from the stability of an aluminum cantilever to a hanging membrane in a vacuum chamber to a spinning membrane in space. Although there are many ways to derive the beam structural model, this document will outline a method of applying Lagrange's equation to the energies of the beam system. This method provides a concise method of deriving the governing equations of a beam.

As with many structural derivations, the first step in deriving the model is to define the displacements of the system. For this derivation we assume the center of mass lies along the elastic axis of the system. This uncouples the beam bending and torsion modes. We assume the displacements can be described by Eq. 2.1.

$$w(x,y,t) = \sum_{n}^{N} q_n(t)\phi_n(x) + \sum_{m}^{M} q_m(t)\Theta_m(x)(y - y_{ea}) \tag{2.1}$$

In the previous equation, N is the number of bending modes in the expansion and M is the number of torsion modes. $\phi_n(x)$ and $\Theta_m(x)$ are eigenmodes of a beam that

satisfy the correct geometric boundary conditions. Gibbs (2012) discusses the form of these mode shapes. Because the model is linear and the modes are uncoupled, this section will mostly deal with each degree of freedom separately, however the kinetic energy for both degrees of freedom is the same.

$$T = \frac{1}{2}\rho h \int_0^{L_y} \int_0^{L_x} \left(\frac{\partial w}{\partial t}\right)^2 dx\, dy \tag{2.2}$$

Substituting the assumed solution from Eq. 2.1 into Eq. 2.2 and integrating with respect to y yields:

$$\begin{aligned} T =& \frac{1}{2} m \int_0^{L_x} \left(\sum_{n1}^{N} \sum_{n2}^{N} \dot{q}_{n1}(t) \dot{q}_{n2}(t) \phi_{n1}(x) \phi_{n2}(x) \right) dx \\ &+ \frac{1}{2} I_{ea} \int_0^{L_x} \left(\sum_{m1}^{M} \sum_{m2}^{M} \dot{q}_{m1}(t) \dot{q}_{m2}(t) \Theta_{m1}(x) \Theta_{m2}(x) \right) dx \end{aligned} \tag{2.3}$$

The first line in Eq. 2.3 is the kinetic energy of the bending modes and the second is for the torsion modes. In the previous equation m is equal to $\rho h L_y$ and I_{ea} is equal to $\rho h L_y^3/12$. Next, the classical potential energy term for the bending degrees of freedom that comes from the strain energy potential associated with bending the beam is:

$$V = \frac{1}{2} EI \int_0^{L_x} \left(\frac{\partial^2 w}{\partial x^2}\right)^2 dx \tag{2.4}$$

where E is the Young's modulus of the plate and I is the area moment of inertial of the cross section. Substituting the bending portion of the assumed displacements into Eq. 2.4 yields:

$$V = \frac{1}{2} EI \int_0^{L_x} \left(\sum_{n1}^{N} \sum_{n2}^{N} q_{n1}(t) q_{n2}(t) \phi''_{n1}(x) \phi''_{n2}(x) \right) dx \tag{2.5}$$

There is also a potential energy associated with the torsion degrees of freedom. This

potential is in the literature and is Dowell (1975):

$$V = \frac{1}{2} GJ \int_0^{L_x} \left(\frac{\partial w}{\partial x} \right)^2 dx \tag{2.6}$$

where G is the shear modulus, which like the Young's modulus is a material property, and J is the polar moment of inertial. For a beam where the length is much larger than the thickness the polar moment of inertia is approximated by $4L_y h^3/12$. Substituting the twist degrees of freedom from Eq. 2.1 into Eq. 2.6.

$$V = \frac{1}{2} GJ \int_0^{L_x} \left(\sum_{m1}^{M} \sum_{m2}^{M} q_{m1}(t) q_{m2}(t) \Theta'_{m1}(x) \Theta'_{m2}(x) \right) dx \tag{2.7}$$

FIGURE 2.1: Schematic of the Gravitational Stress

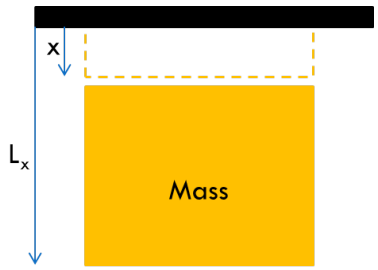

Before substituting the kinetic and potential energies into Lagrange's equation, this document will outline how we can include the influence of tension in the x-direction. This is important because it allows us to model the influence of gravity as well centripetal acceleration on thin membranes. In some cases, when the membrane is thin enough, the bending terms no longer dominate the stiffness of the model. Instead, the main stiffness arises due to the membrane-like stress. Figure 2.1 contains a graphical representation of how the gravitational acceleration influences the structure. Mathematically, the gravity induces a linearly varying stress distribution described by Eq. 2.8.

$$\sigma_g(x) = g\rho h(L_x - x) \tag{2.8}$$

Similarly the stress induced when a membrane is spun around the z-axis at $x = 0$, as is the case for the simplified heliogyro:

$$\sigma_c(x) = \rho h \Omega^2 (L_x^2 - x^2) \tag{2.9}$$

The potential energy captures the stress from either gravity or centripetal accelerations by including a spatially varying tension term with the form given in Eq. 2.10

$$V_t = \frac{1}{2} \int_0^{L_y} \int_0^{L_x} \sigma(x) \left(\frac{\partial w}{\partial x} \right)^2 dx\, dy \tag{2.10}$$

Expanding out the stress term, evaluating the integral with respect to y and substituting in the assumed bending modes into Eq. 2.10 yields:

$$V_t = \frac{1}{2} \int_0^{L_x} \sigma(x) \sum_{n1}^{N} \sum_{n2}^{N} q_{n1}(t) q_{n2}(t) \phi'_{n1}(x) \phi'_{n2}(x)\, dx \tag{2.11}$$

Following similar steps with the torsion assumed modes yields:

$$V_t = \frac{1}{2} \int_0^{L_x} \sigma(x) \sum_{m1}^{M} \sum_{m2}^{M} q_{m1}(t) q_{m2}(t) \Theta'_{m1}(x) \Theta'_{m2}(x)\, dx \tag{2.12}$$

The last addition to the model before deriving the equations of motion is the inclusion of rigid body modes. These modes are necessary to simulate the experimental procedure for adding energy to the system. For the hanging membrane vacuum chamber experiments, the structures are excited using a piezoelectric actuator at the root of the membrane. The boundary condition at this location in the previous theoretical model is a clamp that does not allow displacements. Including the capability to model the actual experiment requires adding a rigid body bending mode and a rigid body rotation mode to the assumed displacements expressed in Eq. 2.1. This is captured numerically by summing the bending modes and torsion modes

to $N+1$ and $M+1$ respectively where ϕ_{N+1} is a rigid body translation described in Eq. 2.13 and Θ_{M+1} is a rigid body rotation described in Eq. 2.14

$$\phi_{N+1} = 1 \tag{2.13}$$

$$\Theta_{N+1} = 1 \tag{2.14}$$

Because of the form of these rigid body modes, they will contribute inertia to the system but will not provide any stiffness to the system.

With the energies of the system described and the rigid body modes included, this derivation uses Lagrange's equation, repeated in Eq. 2.15 for reference, to derive the equations of motion.

$$\frac{d}{dt}\left[\frac{\partial L}{\partial \dot{q}_n}\right] - \frac{\partial L}{\partial q_n} = Q_n \tag{2.15}$$

where L is the Lagrangian which equals the kinetic energy T minus the potential energy V and the generalized force Q_n accounts for the contributions of all non-conservative forces on the system. Applying Lagrange's equation to each of the bending and torsion generalized coordinates yields a system of equations that describe the dynamics of the system. The equations of motion contain two types of equations; first equations that govern the bending degrees of freedom and second equations that govern the torsion degrees of freedom. Eq. 2.16 gives the typical governing equation for the n'th bending coordinate.

$$\begin{aligned} Q_n = \sum_{n1}^{N+1} \Bigg(& m\ddot{q}_{n1}(t) \int_0^{L_x} \phi_n(x)\phi_{n1}(x)\, dx \\ & + q_{n1}(t) \int_0^{L_x} \sigma(x)\phi_n'(x)\phi_{n1}'(x)\, dx \\ & + EIq_{n1}(t) \int_0^{L_x} \phi_n''(x)\phi_{n1}''(x) \Bigg) \end{aligned} \tag{2.16}$$

In the previous equation, orthogonally relationships limit the number of integrals that actually have to be calculated. The typical governing equation for the m'th

torsion coordinate is given in Eq. 2.17

$$Q_m = \sum_{m1}^{M+1} \Bigg(I_{ea} \ddot{q}_{m1}(t) \int_0^{L_x} \Theta_m(x) \Theta_{m1}(x)\, dx + q_{m1}(t) \int_0^{L_x} \big(GJ + \sigma(x) \big) \Theta'_m(x) \Theta'_{m1}(x)\, dx \Bigg) \tag{2.17}$$

We can combine Eqs. 2.16 and 2.17 into a governing matrix equation that is in a familiar form.

$$\bar{M} \ddot{\boldsymbol{q}} + \bar{K} \boldsymbol{q} = \boldsymbol{Q} \tag{2.18}$$

where, $\boldsymbol{q}$ is a vector with the bending and torsion generalized coordinates, $\bar{M}$ is the Mass matrix, $\bar{K}$ is the stiffness matrix that combines the stiffness due to bending and tension, and $\boldsymbol{Q}$ is the vector of generalized forces. Eq. 2.18 is the common form for the structural dynamics equation.

This section provided a brief overview of the derivation of the beam structural model that continues to be a valuable tool for predicting the dynamic response of simple structures. For structures that have boundary conditions that the beam model cannot capture or aspect ratios where the beam model is no longer applicable, the more complex, plate / membrane is used.

2.1.2 Plate / Membrane Model

This section will briefly outline the derivation of a classic plate model, which progresses in a similar manner as the beam derivation. The model is labeled a plate / membrane model because the structure's stiffness includes both terms relating to the structural rigidity, which is common for plate, and the applied tension, which is common for membranes. For the solar sail structures both the tension and structural rigidity terms contribute to the stiffness, with their relative importance varying depending on the specific configuration. By including all of the terms, the model

becomes a good framework for analyzing all of the structures that are of interest for the current research. From this point forward, the model will be referred to as a plate model for simplicity.

As with the beam derivation, the first step is to write out the displacements of the system. Instead of relying on a finite element simulation to determine the response of the plate, we use an analytical approach. A direct solution of the plate partial differential equation with the appropriate boundary conditions is difficult without using special functions. As is common, a separation of variables technique transforms the problem into a set of ordinary differential equations governing the modal coordinates of the system. For this method, the assumed modes are a product of beam modes that satisfy the appropriate boundary conditions in each of the two coordinate directions of the plate.

The Rayleigh-Ritz method begins with the assumed form of the displacement of the plate.

$$w(x,y,t) = \sum_n q_n(t)\Psi_{jk}(x,y) \tag{2.19}$$

In Eq. 2.19, the n'th structural mode is labeled Ψ_{jk} because the mode shape can be separated into two components.

$$\Psi_{jk}(x,y) = \phi_j(x)\theta_k(y) \tag{2.20}$$

where $\phi_j(x)$ is a beam mode shape that satisfies the geometric boundary conditions in the x direction and $\theta_k(y)$ is a beam mode shape that satisfies the geometric boundary conditions in the y direction. Combining Eq. 2.20 and Eq. 2.19 and representing the sum with a vector multiplication, we can represent the displacement in the following compact format.

$$w(x,y,t) = \boldsymbol{q}^T\boldsymbol{\phi\theta} = \boldsymbol{\phi\theta}^T\mathbf{q} \tag{2.21}$$

where $\boldsymbol{q}$ is a column vector with the generalized coordinates and $\boldsymbol{\phi\theta}$ is a column

vector with the mode shapes evaluated at the (x, y) location of interest.

Now that the displacements have been written, the energies of the system need to be derived and then placed into Lagrange's equations. The kinetic and potential energies for a plate in tension can be written in the following manner (Dowell (1975)):

$$T = \frac{1}{2}\rho \cdot h \int_0^{L_y} \int_0^{L_x} \left(\frac{\partial w}{\partial t}\right)^2 dx\, dy \tag{2.22}$$

$$\begin{aligned} V = \frac{1}{2} \int_0^{L_y} \int_0^{L_x} \Bigg[& T_x \left(\frac{\partial w}{\partial y}\right)^2 + T_y \left(\frac{\partial w}{\partial x}\right)^2 \\ & + D_x \left(\frac{\partial^2 w}{\partial x^2}\right)^2 + D_y \left(\frac{\partial^2 w}{\partial y^2}\right)^2 \\ & + 2D_1 \left(\frac{\partial^4 w}{\partial x^2 \partial y^2}\right) + 4D_{xy} \left(\frac{\partial^2 w}{\partial x \partial y}\right)^2 \Bigg] dx\, dy \end{aligned} \tag{2.23}$$

Substituting the assumed displacement from Eq. 2.19 into the energies from Eqs. 2.22 and 2.23 and applying Lagrange's Eq. yields the equation of motion

$$-\left[\bar{M}\frac{\partial^2 \boldsymbol{q}}{\partial t^2} + \left(\bar{K}_{Tx} + \bar{K}_{Ty} + \bar{K}_{Dx} + \bar{K}_{Dy} + \bar{K}_{D1} + \bar{K}_{Dxy}\right)\boldsymbol{q}\right] = \boldsymbol{Q} \tag{2.24}$$

with

$$\bar{M} = \rho h \int_0^{L_y} \int_0^{L_x} \boldsymbol{\phi\theta} \cdot \boldsymbol{\phi\theta}^T\, dx\, dy \tag{2.25}$$

$$\bar{K}_{Tx} = T_x \int_0^{L_y} \int_0^{L_x} \boldsymbol{\phi'\theta} \cdot \boldsymbol{\phi'\theta}^T\, dx\, dy \tag{2.26}$$

$$\bar{K}_{Ty} = T_y \int_0^{L_y} \int_0^{L_x} \boldsymbol{\phi\theta'} \cdot \boldsymbol{\phi\theta'}^T\, dx\, dy \tag{2.27}$$

$$\bar{K}_{Dy} = D \int_0^{L_y} \int_0^{L_x} \boldsymbol{\phi}\boldsymbol{\theta}'' \cdot \boldsymbol{\phi}\boldsymbol{\theta}''^T \, dx \, dy \tag{2.28}$$

$$\bar{K}_{Dx} = D \int_0^{L_y} \int_0^{L_x} \boldsymbol{\phi}''\boldsymbol{\theta} \cdot \boldsymbol{\phi}''\boldsymbol{\theta}^T \, dx \, dy \tag{2.29}$$

$$\bar{K}_{D1} = 2\nu D \int_0^{L_y} \int_0^{L_x} \boldsymbol{\phi}''\boldsymbol{\theta} \cdot \boldsymbol{\phi}\boldsymbol{\theta}''^T \, dx \, dy \tag{2.30}$$

$$\bar{K}_{Dxy} = 4\left(\frac{1-\nu}{2}D\right) \int_0^{L_y} \int_0^{L_x} \boldsymbol{\phi}'\boldsymbol{\theta}' \cdot \boldsymbol{\phi}'\boldsymbol{\theta}'^T \, dx \, dy \tag{2.31}$$

where we assume $D_x = D_y = D$, $D_1 = \nu D$, and $D_{xy} = D(1-\nu)/2$.

We can solve Eq. 2.24 to determine the natural frequencies and mode shapes of the plate system. This model allows a variety of boundary conditions to be studied by changing the assumed mode shapes. Figures 2.2 - 2.4 show the natural modes and frequencies for three of the configurations explored later in the dissertation. For each mode shape the title gives the natural frequency followed by the mode shape composition ($\Psi_{jk} = \phi_j(x)\theta_k(y)$) given in the form ($j$, k).

In this model the assumed modes are not solutions to the plate PDE, therefore the mass and stiffness matrices from the previous equation are not diagonal and therefore all of the generalized coordinates are coupled. Eq. 2.24 can be diagonalized using the method described in the following section. The process recasts the governing equations of the structural model in terms of a set of orthogonal mode shapes.

2.1.3 Solving the Linear Structural Models

The goal of any structural analysis is to solve the ordinary differential equations for the generalized coordinates due to a given initial condition or external forcing. For the linear models presented previously, we can do this by placing the governing

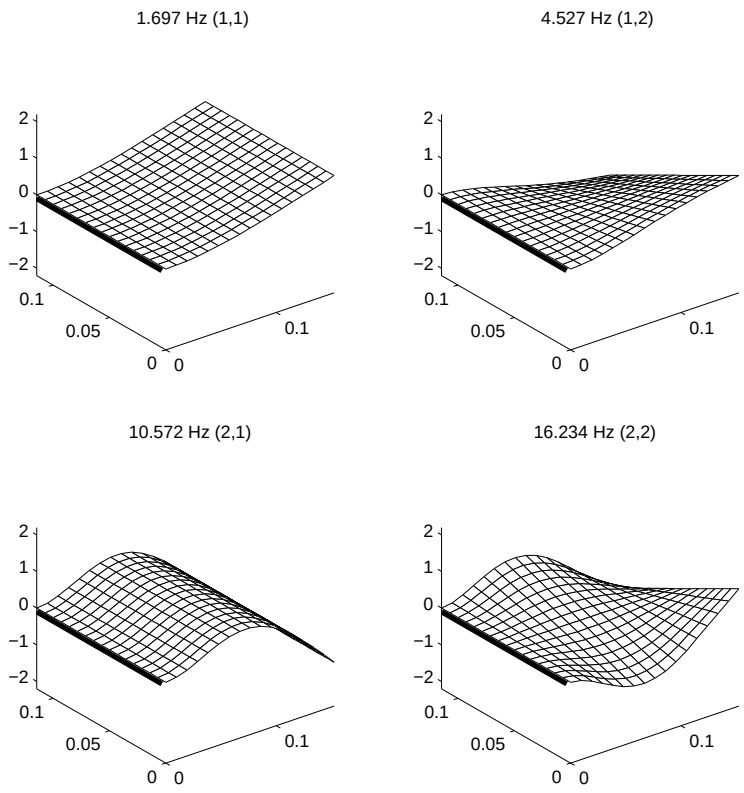

FIGURE 2.2: Clamped Free Free Free Beam Mode Shapes

system of equation into matrix form and taking advantage of the tools from linear algebra. Eq. 2.32 is the matrix form of the governing structural equations for both the beam and plate models.

$$\bar{M}\ddot{\boldsymbol{q}} + \bar{K}\boldsymbol{q} = \boldsymbol{Q} \tag{2.32}$$

where the $\boldsymbol{q}$ is a vector of the generalized coordinates, and the $\bar{M}$ and $\bar{K}$ are the mass and stiffness matrices. In general the mass and stiffness matrices may not be diagonal and therefore the equations may be coupled. Setting the generalized force to zero and assuming a harmonic response, we can use Eq. 2.32 to solve for the natural modes of the specific system we are exploring. These natural modes allow us to describe the structural dynamics with a set of uncoupled equations and may allow us to reduce the order of our structural model when we conduct solarelastic or aeroelastic analysis. The process beings by assuming the response is equal to

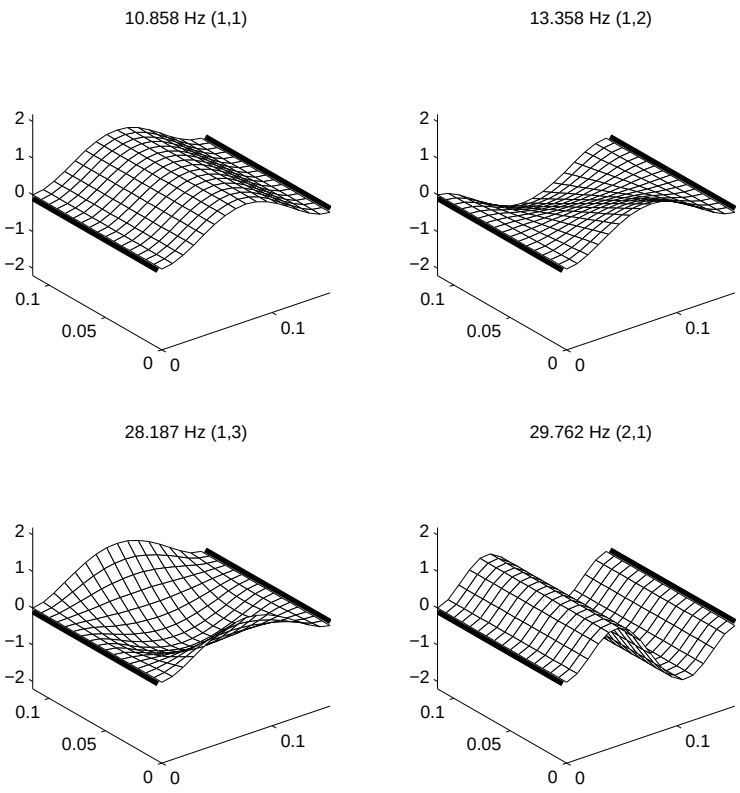

FIGURE 2.3: Clamped Free Clamped Free Beam Mode Shapes

$\bar{\boldsymbol{q}} \exp(i\omega t)$. Using this assumption in Eq. 2.32 yields the generalized eigenvalue problem in Eq. 2.33.

$$\left(\omega^2 \bar{M} + \bar{K}\right) \bar{\boldsymbol{q}} = 0 \tag{2.33}$$

The eigenvectors, defined as $\boldsymbol{V}$, of the previous equation describe the normal modes of the system and, if scaled correctly, diagonalize the mass and stiffness matrix.

$$\tilde{M} = \bar{V}' \bar{M} \bar{V} = \begin{bmatrix} \ddots & & \\ & 1 & \\ & & \ddots \end{bmatrix} \tag{2.34}$$

$$\tilde{K} = \bar{V}' \bar{K} \bar{V} = \begin{bmatrix} \ddots & & \\ & \omega_n^2 & \\ & & \ddots \end{bmatrix} \tag{2.35}$$

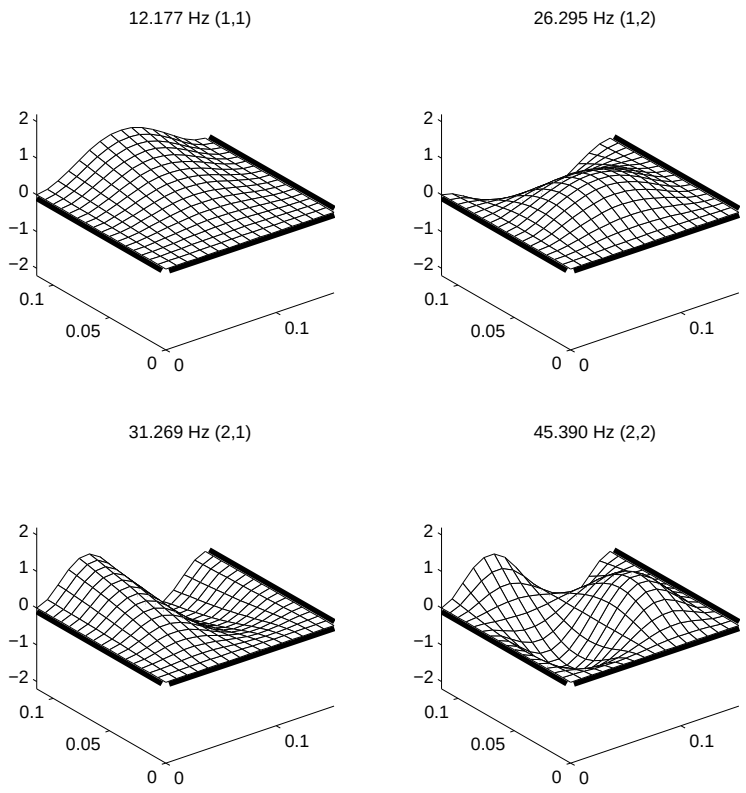

FIGURE 2.4: Clamped Free Clamped Clamped Beam Mode Shapes

where $\bar{V}$ is a matrix made up of the column eigenvectors $\boldsymbol{V}$. Eq. 2.36 is the uncoupled governing equation whose generalized coordinates ($\tilde{\boldsymbol{q}}$) are associated with the normal modes of the structure.

$$\tilde{M}\ddot{\tilde{\boldsymbol{q}}} + \tilde{K}\tilde{\boldsymbol{q}} = \bar{V}'\boldsymbol{Q} \tag{2.36}$$

This document uses Eq. 2.36 throughout when discussing the ground vibration experiments to compare the experimental transfer functions measured in the lab to this theoretical model. The experimental sections of this dissertation contains a more detailed description of the specific application of the model for each of the experiments.

The combination of the plate structural model and the beam structural model presented in the previous sections provide a robust foundation for analyzing the linear dynamics of simple rectangular structures in stationary reference frame. The

experimental section will discuss the performance and limitations of these models, but in general, they have proved to be very accurate at predicting and capturing the linear response of the simple structures that this document explores. These linear structural models allow rapid exploration of the parameter space, without relying on finite element simulations. This is especially valuable when conducting preliminary design work when the fundamental dynamics are of interest and higher fidelity structural modeling is time prohibitive. Finally, the fact that both models can be transformed into a governing equation that has the form given in Eq. 2.36, allows the models to be used in a common framework when conducting an aeroelastic or solarelastic simulation. In fact, by casting the problem in the current form, linear finite element mode shapes and modal mass and stiffness matrices can also be included if the analysis requires a higher fidelity structural model.

2.1.4 Nonlinear Spinning Model

The final structural model that we will describe is a nonlinear structural model for a spinning thin beam. The equations are modified from the equations presented in Hodges and Dowell (1974). The governing equations of motion for the blade are simplified to include no pre-cone angle of the blade, no blade hub offset and no blade root actuation. The equations allow for motion in twist, flap and in-plane bending directions. Figure 2.5 shows a schematic of the structure that we are attempting to model. For this structure the Hamiltonian is:

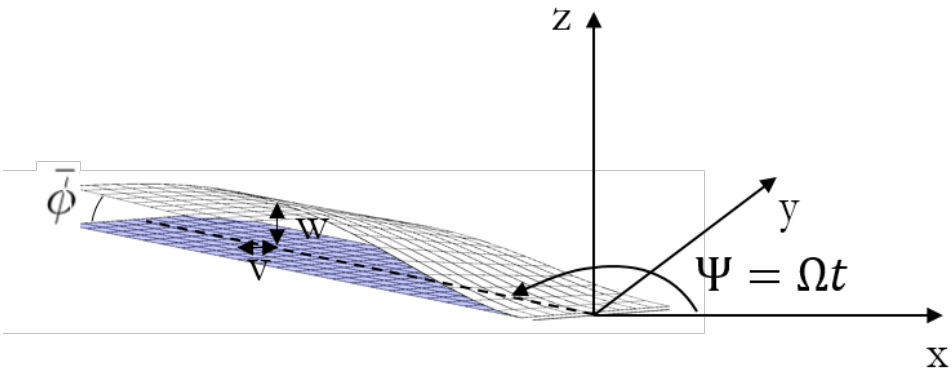

FIGURE 2.5: Schematic of the Heliogyro Coordinate System.

$$
\begin{aligned}
0 = \int_0^1 \Bigg[& \bar{G}J\phi'\delta\phi' + \bar{T}\bar{k}_a^2\phi'\delta\phi' + \Delta\bar{E}I\bar{v}''\bar{w}''\delta\phi \\
& + \bar{m}\Big\{\bar{k}_m^2\ddot{\phi} + (\bar{k}_{m1}^2 - \bar{k}_{m2}^2)\phi\Big\}\delta\phi - \bar{M}_\phi\delta\phi \\
& + \Big\{\bar{E}I_1\bar{w}'' + \Delta\bar{E}I\phi\bar{v}''\Big\}\delta\bar{w}'' + \bar{T}\bar{w}'\delta\bar{w}' + \bar{m}\ddot{\bar{w}}\delta\bar{w} \\
& - \bar{L}_w\delta\bar{w} \\
& + \Big\{\bar{E}I_2v'' + \Delta\bar{E}I\phi\bar{w}''\Big\}\delta\bar{v}'' + \bar{T}\bar{v}'\delta\bar{v}' \\
& + \bar{m}\left[\ddot{\bar{v}} + 2\dot{u} - \bar{v}\right]\delta\bar{v} - \bar{D}_v\delta\bar{v}\Bigg] d\xi
\end{aligned}
\tag{2.37}
$$

$\bar{\phi}$, $\bar{w}$, and $\bar{v}$ are the twist, flap and in-plane deflections normalized by the plate span. $\bar{K}_a$ is the non-dimensional radius of gyration and $\bar{K}_m$,$\bar{K}_{m1}$, and $\bar{K}_{m2}$ are the non-dimensional mass radii of gyration. The tension due to the centrifugal forces on the blade is captured by the $\bar{T}$ term in Eq. 2.37. The non-dimensional time $\tilde{t} = t\Omega$. The tension as a function of the non-dimensional span (ξ) is:

$$
\bar{T}(\xi) = \int_\xi^1 \bar{m}(\nu + 2\dot{\bar{v}})\, d\nu \tag{2.38}
$$

The non-dimensional terms in the previous equation are related to the dimensional quantities using the following relationships.

$$\begin{aligned}
&\bar{T} = \frac{T}{m_r \Omega^2 L^2}, \bar{GJ} = \frac{GJ}{m_r \Omega^2 L^4}, \bar{EI}_1 = \frac{EI_1}{m_r \Omega^2 L^4} \\
&\bar{EI}_2 = \frac{EI_2}{m_r \Omega^2 L^4}, \Delta\bar{EI} = \frac{EI_2 - EI_1}{m_r \Omega^2 L^4} \\
&\bar{K}_\phi = \frac{K_\phi}{m_r \Omega^2 L^3}, \bar{m} = \frac{m}{m_r}
\end{aligned} \tag{2.39}$$

The governing equation includes the influence of the external forcing through a moment ($\bar{M}_\phi$), a lift ($\bar{L}_w$) and a drag ($\bar{D}_v$) terms. To solve the equations a conventional Rayleigh-Ritz procedure is applied using beam modes for twist, flap, and in-plane bending.

$$\begin{aligned}
&\bar{w}(\tilde{t}, \xi) = \sum_i W_i(\tilde{t}) w_i(\xi), \quad \bar{v}(\tilde{t}, \xi) = \sum_i V_i(\tilde{t}) v_i(\xi) \\
&\phi(\tilde{t}, \xi) = \sum_i \Phi_i(\tilde{t}) g_i(\xi)
\end{aligned} \tag{2.40}$$

$w_i(\xi)$ is the i'th out-of-plane bending mode shape that satisfies the typical clamped-free beam in bending equation, $g_i(\xi)$ is the i'th torsion mode shape that satisfies the typical fixed-free beam torsion equation and $v_i(\xi)$ is is the i'th in-plane bending mode shape that satisfies the typical clamped-free beam bending equation. Substituting the modal expansion from Eq. 2.40 into Eq. 2.37 transforms the problem into a nonlinear ODE for the modal coordinates. Eq. 2.41 gives the characteristic equation for the i'th twisting degree of freedom.

$$\begin{aligned}
M_\phi = \sum_j \Big[& A_{ij} \Phi_j + B_{ij} \ddot{\Phi}_j \\
& + \sum_k \Big(C_{ijk} V_j W_k + D_{ijk} \dot{V}_j \Phi_k + T1_{ijk} \Phi_j \dot{V}_k \Big) \Big]
\end{aligned} \tag{2.41}$$

with

$$
\begin{aligned}
A_{ij} &= \int_0^1 \Big[\bar{G}Jg_i'g_j' + \frac{1}{2}\bar{m}(1-\xi^2)\bar{k}_a^2 g_i'g_j' \\
&\quad + \bar{m}(\bar{k}_{m2}^2 - \bar{k}_{m1}^2)g_i g_j\Big]\, d\xi \\
B_{ij} &= \int_0^1 \bar{m}\bar{k}_m^2 g_i g_j\, d\xi \\
C_{ijk} &= \int_0^1 \Delta\bar{E}\bar{I}g_i v_j'' w_k''\, d\xi \\
D_{ijk} &= \int_0^1 2\bar{m}\bar{k}_a^2 g_i' \frac{v_j'''}{\omega_i^4} g_k'\, d\xi \\
T1_{ijk} &= 2\bar{k}_a^2\bar{m}\int_0^1 g_i'g_j'\left[\int_\xi^1 v_k(\eta)\, d\eta\right] d\xi
\end{aligned}
\tag{2.42}
$$

Similarly Eq. 2.43 provides the characteristic equation for the i'th out-of-plane bending degree of freedom.

$$
\begin{aligned}
L_w = \sum_j \Big[&E_{ij}W_j + F_{ij}\ddot{W}_j \\
&+ \sum_k \Big(G_{ijk}\Phi_j V_k + H_{ijk}\dot{V}_j W_k + T2_{ijk}W_j\dot{V}_k\Big)\Big]
\end{aligned}
\tag{2.43}
$$

with

$$
\begin{aligned}
E_{ij} &= \int_0^1 \left[\bar{E}\bar{I}_1 w_i'' w_j'' + \frac{1}{2}\bar{m}(1-\xi^2)w_i'w_j'\right] d\xi \\
F_{ij} &= \int_0^1 \bar{m}w_i w_j\, d\xi \\
G_{ijk} &= \int_0^1 \Delta\bar{E}\bar{I}w_i'' g_j v_k''\, d\xi \\
H_{ijk} &= \int_0^1 2\bar{m}w_i' \frac{v_j'''}{\omega_i^4} w_k'\, d\xi \\
T2_{ijk} &= 2\bar{m}\int_0^1 w_i'w_j'\left[\int_\xi^1 v_k(\eta)\, d\eta\right] d\xi
\end{aligned}
\tag{2.44}
$$

Finally Eq. 2.45 provides the characteristic equation for the i'th in-plane bending degree of freedom.

$$\begin{aligned} L_v = \sum_j \Big[& K_{ij} V_j + L_{ij} \ddot{V}_j \\ & + \sum_k \Big(M_{ijk} \Phi_j W_k + N_{ijk} \dot{V}_j V_k + T3_{ijk} V_j \dot{V}_k \\ & \qquad - U1_{ijk} W_j \dot{W}_k - U2_{ijk} V_j \dot{V}_k \Big) \Big] \end{aligned} \tag{2.45}$$

with

$$\begin{aligned} K_{ij} &= \int_0^1 \left[\bar{E} I_1 v_i'' v_j'' + \frac{1}{2} \bar{m} (1 - \xi^2) v_i' v_j' - \bar{m} v_i v_j \right] d\xi \\ L_{ij} &= \int_0^1 \bar{m} v_i v_j \, d\xi \\ M_{ijk} &= \int_0^1 \Delta \bar{E} I v_i'' g_j w_k'' \, d\xi \\ N_{ijk} &= \int_0^1 2 \bar{m} v_i' \frac{v_j'''}{\omega_i^4} v_k' \, d\xi \\ T3_{ijk} &= 2 \bar{m} \int_0^1 v_i' v_j' \left[\int_\xi^1 v_k(\eta) \, d\eta \right] d\xi \\ U1_{ijk} &= 2 \bar{m} \int_0^1 v_i \int_0^\xi w_j'(\eta) w_k'(\eta) \, d\eta \, d\xi \\ U2_{ijk} &= 2 \bar{m} \int_0^1 v_i \int_0^\xi v_j'(\eta) v_k'(\eta) \, d\eta \, d\xi \end{aligned} \tag{2.46}$$

Combining Eqs. 2.41, 2.43 and 2.45 produces a set of non-linear ODE's governing the generalized coordinates in twist, flap and in-plane bending. In general the external forcing terms may be time varying so the equations are normally solved using a time stepping algorithm. However, for some special cases, as will be described later, the equations can be written in a time invariant form and then we can conduct a linear perturbation eigenanalysis around the static equilibrium.

2.2 Forcing Models

The analysis presented in this dissertation largely relies on coupling the structural models presented in the previous section with external forcing. We couple the forcing with the structural dynamics using the generalized force that appears in all of the structural equations of motion. In particular we will look at forces due to solar radiation as well as forces due to subsonic aerodynamic flows. In this dissertation we will model the aerodynamics using a 3D Vortex Lattice aerodynamic model and the solar radiation using an optical reflection model. This section provides the details of these theoretical models.

2.2.1 Vortex Lattice Aerodynamic Model

For our aerodynamic model we use a vortex lattice model. Full derivations can be found in the literature, for examples see Tang et al. (2003), Hall (1994) and Gibbs et al. (2012b). This method accounts for the discrete vortex filaments as they progress through time and space and allows for the modeling of a three dimensional incompressible, inviscid and irrotational flow and includes the effect of the wake due to the unsteady flow over the plate. The wake of the system is prescribed to be in the plane of the plate system for the present linear analysis. Figure 2.6 show a schematic of a typical vortex lattice mesh.

The set of governing equations for the vortex lattice method can be segmented into four types of equations that govern the circulation on a given element. On the elastic and support structure a set of horseshoe vortex elements with circulation strength Γ are attached to fixed points at the 1/4 chord of each panel. These panels are identified as region (1) in Fig. 2.6. We determine the strength of the circulation elements by applying a no flow through boundary condition at collocation points at the 3/4 chord of each panel. The boundary condition requires that velocity induced

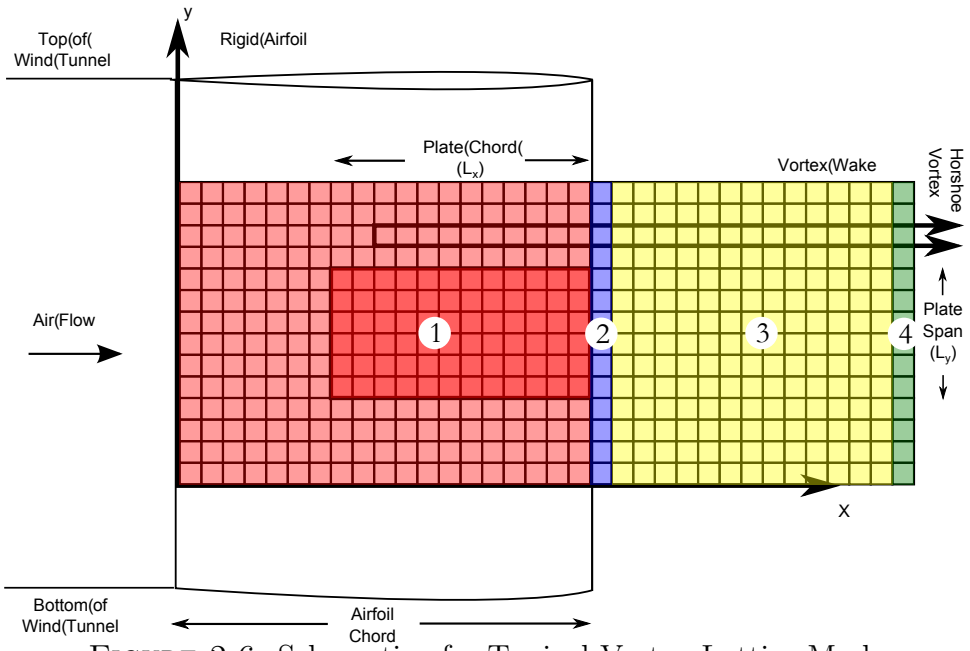

FIGURE 2.6: Schematic of a Typical Vortex Lattice Mesh

by all of the horseshoe vortex elements in the mesh equal the vertical velocity of the plate at the collocation points. The linearized form of this zero normal velocity boundary condition is described by Eq. 2.47

$$V_d = \left.\frac{dw}{dt}\right|_{fluid} = \left.\frac{\partial w}{\partial t}\right|_{plate} + U_\infty \left.\frac{\partial w}{\partial x}\right|_{plate} \tag{2.47}$$

We determine the velocity induced by the circulation elements in the mesh using a kernel function that relates the strength of a circulation element linearly to the induced velocity at a specific point. The kernel function for the horseshoe vortex elements used in this analysis can be found in the literature, for example see Bisplinghoff et al. (1996).

The remaining three sections of the vortex lattice mesh account for the unsteady wake. The change in circulation over the structure over time is shed into the first row in the wake, region (2). These shed horseshoe vortex elements then move at the free stream velocity through region (3) of the wake. The wake convection equations

require a time step dt equal to dx/U_∞ and assume that there is zero tangential velocity on the structure normal to the flow direction. Finally the last row in the mesh, region (4), includes a relaxation factor that accounts for the finite length of the wake. The relationships in each of the four sectors combine to give a set of equations that are equal in number to the number of elements in the aerodynamic mesh. The final form of the aerodynamic equation is:

$$\boldsymbol{V}_d^{n+1} = \bar{A}\boldsymbol{\Gamma}^n + \bar{B}\boldsymbol{\Gamma}^{n+1} \tag{2.48}$$

where $\boldsymbol{V}_d$ is the downwash at the collocation points on the structure and $\bar{A}$ and $\bar{B}$ contain the downwash relationship from Eq. 2.47 and the wake convection relationships described in the previous paragraph.

We use the circulation strength ($\boldsymbol{\Gamma}$) from the vortex lattice model to calculate the aerodynamic force on the structure. Discretizing an application of Bernoulli's equation using a Crank-Nicolson scheme yields:

$$P_i^{n+1/2} = \rho U_\infty \left[\frac{1}{2}(\Gamma_i^n + \Gamma_i^{n+1}) + \sum_k \left(\Gamma_k^{n+1} - \Gamma_k^n \right) \right] \Delta y \tag{2.49}$$

where $P_i^{n+1/2}$ is the aerodynamic force on the i'th panel at time step $n + 1/2$, Γ_i^n indicates the strength of the i'th circulation element at time step n, and the sum over k indicates a sum over all of the elements upstream of, and in the same row as the i'th circulation element. This aerodynamic force can substituted into the generalized force equation for a structural model to couple the aerodynamics with the structural equations. The aerodynamic equations are discrete in time and space, so when combined with any structural model, some manipulations are implemented to ensure that the models are consistent. These modifications will be described in more detail later in the dissertation.

One of the novel theoretical advancements that we completed was modeling flow conditions that are yawed with respect to structural model. This advancement allows

us to explore the transition from wing flutter to flag flutter. We can capture this rotation by modifying the aerodynamic mesh. In order to implement this model with the existing structural model, we use the two coordinate systems shown in Fig. 2.7. For this system, the prime notation dictates quantities measured in the structural coordinate system. By thinking of the system in two separate coordinate systems, the model can treat the strictly aerodynamic and strictly elastic portions of the aeroelastic equations as before. The downwash and generalized force relations capture the rotation by accounting for the different coordinate systems.

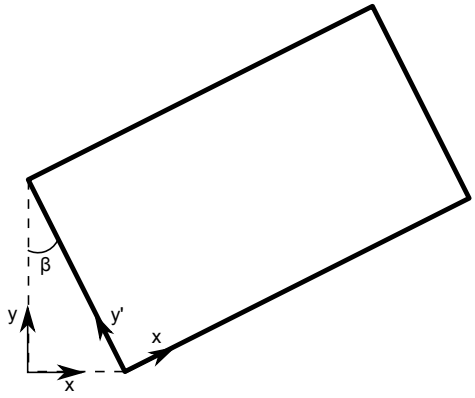

FIGURE 2.7: Aerodynamic and Elastic Coordinate Systems for Yawed Flow Aeroelastic Model

In order to use the typical horseshoe elements and a square mesh, the first step is to define a square box aligned with the flow that completely encompasses the rotated structure. A rectangular grid in the flow coordinate system is then defined that has S_s elements in the normal to flow direction and S_c elements in the flow direction. We loop though all of the collocation points and determine if they lie on the structure. Practically this is done by transforming all of the collocation points to their coordinates in the structure coordinate system and checking that $0 \leq x'_c \leq Lx'$ and $0 \leq y'_c \leq Ly'$. While looping through the points, if the collocation point is on the structure the $[x, y]$ location of the collocation point and the $[x, y]$ location of the

top and bottom of the horseshoe element for that panel are stored, as well as the row in the mesh that the element falls in.

Fig. 2.8 shows the mesh that is generated for a panel at a yaw angle of $\beta = 45\,\text{deg}$. The trailing edge of the wake directly mirrors the trailing edge of the panel to allow the use of simple convection and relaxation relations described previously. Because the structure rotates with respect to the flow, the usual aerodynamic definitions of the span and chord are ambiguous. For the purpose of this paper the chord is the length of the structure in the x' direction and the span is the length of the structure in the y' direction, i.e. the usual convention used when describing the flapping-flag.

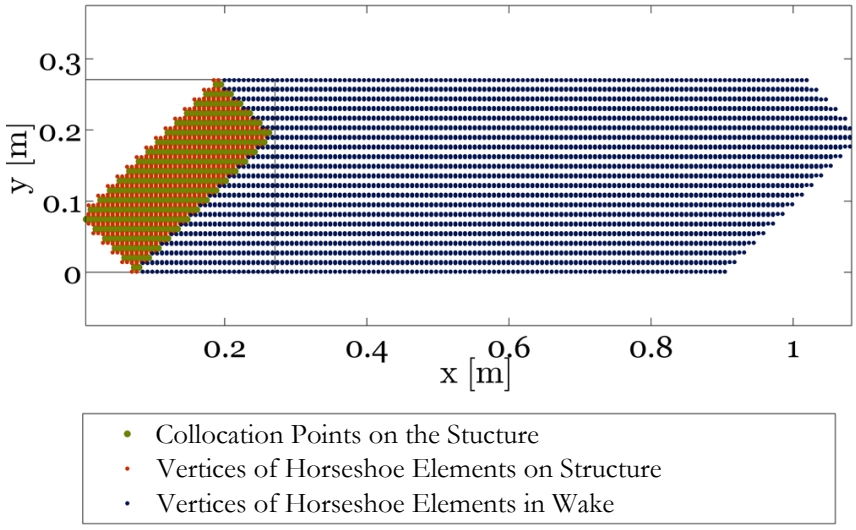

FIGURE 2.8: VLM Mesh Visualization for Yawed Flow Aeroelastic Model

2.2.2 Solar Radiation Pressure Model

For the solarelastic analysis we use an optical solar radiation pressure model. This model of the forces caused by incident radiation on a reflective surface essentially accounts for the momentum transfer as photons are reflected off a surface. For the metalized materials proposed for solar sails the perfect reflector is an appropriate

model. From the literature (Dowell (2011), MacNeal (1971)) the pressure for a perfectly reflective surface is:

$$P_r = P_o \cos^2 \alpha \tag{2.50}$$

where α is defined as the angle between the unit normal and the incident solar radiation as shown in Figure 2.9

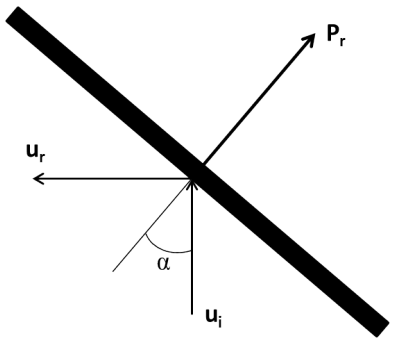

FIGURE 2.9: Schematic of a Perfectly Reflective Surface

In order to accurately model the forces using this model one must be able to define the cosine of the angle α between the normal to the structure and the incident solar radiation. In general, the unit normal to the structure changes with the deformation of the structure. To consider the general case the normal to a structure that has been rotated around the z-axis an angle of Ψ, and then up around the x-axis β and finally twisted around the new rotated y-axis and angle of Θ will be determined using a series of rotation matrices. In the end, the goal is to use the law of cosines to determine the cosine of the angle between the unit normal and the incident solar radiation. A figure displaying the rotations described in words is given in Figure 2.10.

$$\cos \gamma = \frac{\boldsymbol{P} \cdot \boldsymbol{n}}{|\boldsymbol{P}||\boldsymbol{n}|} \tag{2.51}$$

While the transformations are relatively straightforward, the derivation is not explicitly given in the prior literature. In order to take the dot product of the normal

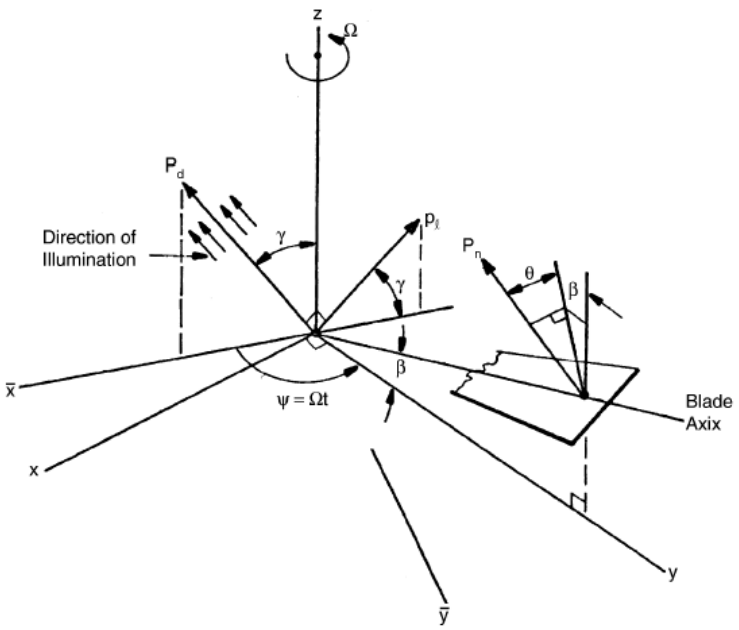

FIGURE 2.10: Schematic showing the coordinate systems and angles for a rotating heliogyro blade. Figure taken from Dowell (2011).

and incident radiation vectors it is necessary to be able to define the unit vectors in each of the directions in the same coordinate system. The first coordinate system is the coordinate system of the vehicle which has incoming solar radiation in the x-z plane at angle of γ between the incident radiation and the z-axis. This can be recreated schematically in Figure 2.11.

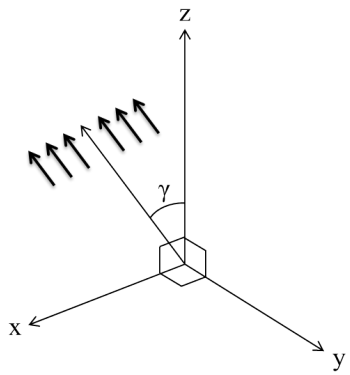

FIGURE 2.11: Schematic showing the heliogyro global coordinate systems

In this coordinate system the unit vector in the γ direction is:

$$\boldsymbol{P} = \begin{bmatrix} \sin\gamma \\ 0 \\ \cos\gamma \end{bmatrix} \tag{2.52}$$

The other coordinate system of interest is the coordinate system in which the z-axis aligned with the normal to the local surface (x_1, y_1, z_1). The goal is to now transition from this coordinate system to the global coordinate system. A series of three rotations accomplishes this. First there is a rotation of $-\Theta$ around the y-axis then a rotation of $-\beta$ around the x-axis and then a rotation of Ψ around the z-axis.

The first rotation is $-\theta$ around the y_1-axis. Figure 2.12 shows a projection of the x_1-z_1 plane.

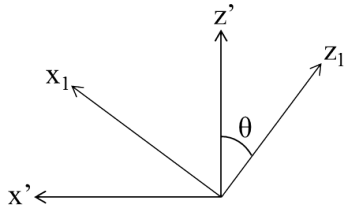

FIGURE 2.12: Schematic showing the first rotation from the normal to the surface coordinate system.

Mathematically the transformation in matrix form is:

$$\begin{bmatrix} x_1 \\ y_1 \\ z_1 \end{bmatrix} = \begin{bmatrix} \cos\theta & 0 & \sin\theta \\ 0 & 1 & 0 \\ -\sin\theta & 0 & \cos\theta \end{bmatrix} \begin{bmatrix} x' \\ y' \\ z' \end{bmatrix} \tag{2.53}$$

where the subscripts in the coordinates denote that it is the first rotation from the normal to the surface.

The next transformation is the rotation around the x'-axis down an angle of β. Similarly, to the previous rotation the transition matrix is:

$$\begin{bmatrix} x_2 \\ y_2 \\ z_2 \end{bmatrix} = \begin{bmatrix} 1 & 0 & 0 \\ 0 & \cos\beta & \sin\beta \\ 0 & -\sin\beta & \cos\beta \end{bmatrix} \begin{bmatrix} x_1 \\ y_1 \\ z_1 \end{bmatrix} \tag{2.54}$$

The final rotation that is used to transform the coordinates completely back to the

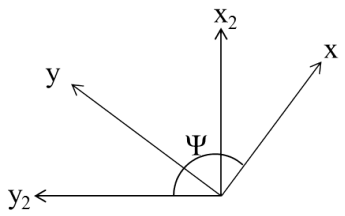

FIGURE 2.13: Schematic showing the third rotation from the normal to the surface coordinate system.

original global coordinate system is a rotation around the z_2 (which is aligned with the z axis) through an angle of $(\Psi - 90)$ as shown in Figure 2.13. The transformation matrix for this rotation is:

$$\begin{bmatrix} x \\ y \\ z \end{bmatrix} = \begin{bmatrix} \sin\Psi & -\cos\Psi & 0 \\ \cos\Psi & \sin\Psi & 0 \\ 0 & 0 & 1 \end{bmatrix} \begin{bmatrix} x_2 \\ y_2 \\ z_2 \end{bmatrix} \tag{2.55}$$

Multiplying the three rotation matrices together in the correct order and then defining a unit vector in the positive z' direction representing the unit normal from the reflective surface allows one to write the normal vector in the global coordinate system.

$$\begin{bmatrix} x \\ y \\ z \end{bmatrix} = \begin{bmatrix} \sin\Psi\sin\theta - \sin\beta\cos\theta\cos\Psi \\ \sin\Psi\sin\beta\cos\theta + \cos\Psi\sin\theta \\ 1\cos\beta\cos\theta \end{bmatrix} \tag{2.56}$$

The final step is to take the dot product of this with the incident pressure vector given in Eq. 2.52 to determine the cosine of the angle between the two vectors.

$$\cos\alpha = \sin\gamma\left[\sin\Psi\sin\theta - \cos\Psi\sin\beta\cos\theta\right] + \cos\gamma\cos\beta\cos\theta \tag{2.57}$$

This result matches the results published by both Dowell (2011) and MacNeal (1971).

If we define the displacements as shown in Figure 2.14, we can rewrite Eq. 2.57 in terms of the structural displacements. Furthermore, we will linearize the equation

assuming that the displacements and slopes are small.

$$\cos\alpha = \sin\gamma\left[\sin\Psi\bar{\phi} - \cos\Psi\bar{w}'\right] + \cos\gamma \tag{2.58}$$

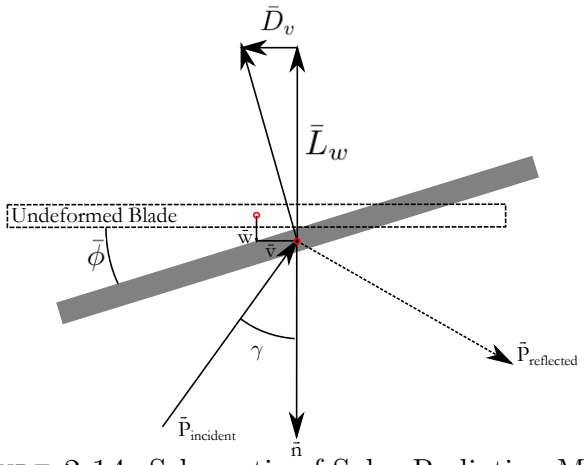

FIGURE 2.14: Schematic of Solar Radiation Model

To calculate the forces we substitute Eq. 2.58 into Eq. 2.50. This normal force can then be substituted into the generalized force equation for a given model. The details of the specific form of the generalized force can be found in the specific sections where the solar radiation force is integrated with a specific structural model.

2.3 Summary of Theoretical Models

This chapter outlines the theoretical models that provide the foundation of the analyses that are conducted throughout this document. The remainder of this dissertation describes the ways to combine our theoretical models to produce insight into coupled systems that vary from energy harvesters to an advanced space propulsion technique. In addition to coupling the models in multiple ways, this document will also explore experiments that are used to validate the theoretical models to confirm that the models described in this chapter are capable of capturing the essential physics of the systems we explore.

3

Stability and Nonlinear Response of Cantilevers in Subsonic Flow

This chapter will explore the stability and post-flutter response of one of the most classical aeroelastic systems, a cantilevered plate. The aeroelastic stability of cantilevered plates with their clamped edge oriented either parallel or normal to a subsonic flow is a classical fluid-structure interaction problem. When the clamped edge is parallel with the flow the system loses stability in a coupled bending and torsion motion known as wing flutter. When the clamped edge is normal to the flow the instability is exclusively bending and is referred to as flapping flag flutter. The work presented in this section has been published in the following forms.

Publications:

1. **Gibbs et al. (2014a)**: This paper explores the stability of plates during the transition between the flapping flag and wing configurations. The aeroelastic model couples a classical beam structural model to a three-dimensional vortex lattice aerodynamic model. The aeroelastic stability is evaluated in the frequency domain and the flutter boundary is presented as the plate is rotated

from the flapping flag to the wing configuration. In this paper we show that the transition between the flag-like and wing-like instability is often abrupt and the yaw angle of the flow for the transition is dependent on the relative spacing of the first torsion and second bending natural frequencies. This paper also includes ground vibration and aeroelastic experiments carried out in the Duke University wind tunnel that confirm the theoretical predictions.

2. **Tang et al. (2014a)**: This paper is a follow on to Gibbs et al. (2014a) where the yawed vortex lattice method developed in the previous article is coupled with a nonlinear structural model to theoretically explore the post flutter regime in yawed flow configurations. A large amplitude Limit Cycle Oscillation (LCO) beyond the linear flutter speed has been observed in both the computations and in a wind tunnel experiment. The computations and experiments for the LCO response of the several yawed plate aeroelastic models show that the inextensible plate theory produces results in good agreement with measurements. This paper also includes a comparison with results obtained using von Karman's nonlinear plate theory.

3. **Gibbs et al. (2014b)**: This technical note provides recent flow field visualizations in a single longitudinal plane for a cantilevered aluminum plate in axial flow during its LCO. Particle Image Velocimetry (PIV) techniques are used to show that the flow over the midspan of the plate is attached even during the violent LCO motion. This observation suggests that potential flow aerodynamic models may be able to capture the essential features in the flow field.

4. **Tang et al. (2014b)**: This paper explores the post flutter response of the flapping flag. The computations and experiments for flutter and LCO response of a flapping flag aeroelastic model show that the inextensible beam theory pro-

duces results in good agreement with the linear flutter speed and rms LCO amplitude. However, there are two significant differences between the computation and experiment: 1. The measured LCO data is a single harmonic oscillation, but the computational LCO is a burst or a chaotic oscillation. 2. A slight hysteresis LCO response was found in the experiment, but was not found in the computations.

This chapter will explore aspects of the yawed flow analysis and post flutter experiments for the flapping flag. Specifically the chapter explores the theoretical and experimental work on the linear stability of the yawed flow plate (Gibbs et al. (2014a)), flow visualization of the post-flutter flapping flag (Gibbs et al. (2014b)) and experiments to capture the tip displacement during the LCO for the flapping flag which appear in Tang et al. (2014b,a).

3.1 Linear Stability of a Cantilevered Plate in Yawed Subsonic Flow

This section focuses on exploring the transition from a flapping flag flutter to wing-like flutter of a cantilever beam as the angle between the clamped edge and free stream velocity changes. In particular this section presents a linear theoretical model for the rotated aeroelastic system. We create the aeroelastic model by coupling a classic linear beam structural model with a rotated vortex lattice model. We validate the theoretical predictions with aeroelastic experiments conducted in the Duke University Wind Tunnel. This section explores three distinct aspect ratios that show markedly different transition behaviors from wing flutter to flapping flag flutter.

3.1.1 Theoretical Model

We build the model of the aeroelastic system by coupling a classic linear structural model of a beam in bending and torsion to a vortex lattice aerodynamic model.

The governing structural dynamics equation for a beam is derived in Section 2.1.1, specifically Eq. 2.18, repeated below for reference.

$$\bar{M}\ddot{\boldsymbol{q}} + \bar{K}\boldsymbol{q} = \boldsymbol{Q} \tag{3.1}$$

The generalized forcing term $\boldsymbol{Q}$ comes from the aerodynamic forces on the structure. If the pressure along the structure is known, the generalized force on the n'th bending degree of freedom is:

$$Q_n = \int_0^L \int_{-\frac{S}{2}}^{\frac{S}{2}} p(x,y) g_i(x)\, dy\, dx \tag{3.2}$$

Similarly the generalized moment on the m'th twist degree of freedom is:

$$Q_m = \int_0^L \int_{-\frac{S}{2}}^{\frac{S}{2}} p(x,y) h_i(x) y\, dy\, dx \tag{3.3}$$

The structural model is coupled to the vortex lattice lattice model described in Section 2.2.1. Specifically, we substitute the pressure from Eq. 2.49 into discretized forms of Eqs. 3.2 and 3.3 to relate the generalized forces to the circulation strengths. We then combine the structural dynamics equation given in Eq. 2.18, the governing aerodynamic equation given in Eq. 2.48 with the generalized forces in the form described in the previous sentence, into a single matrix equation. To achieve this, we place the structural model into a state space form and time discretize the equation in a method consistent with the aerodynamic temporal discretization. This allows us to define the structures state at time n and $n+1$ in terms of the circulation and generalized coordinate strengths at that time. The resulting equation is a time discrete linear system that we solve in the frequency domain to determine the aeroelastic eigenvalues as a function of the flow velocity. The final form of the equation is given in Eq. 3.4.

$$\bar{\alpha}\boldsymbol{y}^{n+1} + \bar{\beta}\boldsymbol{y}^{n} = 0 \tag{3.4}$$

where $\boldsymbol{y}$ is the state variable that contains the discretized circulation and generalized coordinate strengths. $\bar{\alpha}$ and $\bar{\beta}$ contain the elastic, aerodynamic and coupling relationships described in this section. Eq. 3.4 is in the form of a generalized eigenvalue problem that we solve using available eigenvalue computational packages.

We use the aeroelastic model to explore the transition from flag flutter to wing flutter for three configurations. We chose the configurations in this paper to highlight three types of transition behavior. We discovered that the flow angle and abruptness of the transition from coupled bending-torsion flutter typical of wings to coupled bending-bending flutter typical in the flapping flag configuration depends on the relative locations of the first torsion and second bending natural frequencies with respect to the first bending natural frequency. In order to explore the different regimes of this phenomenon the present studies explored the baseline configuration given in Table 3.1. Changing the span, S, for a fixed chord, L, changes the torsion frequencies of the beam without changing the bending frequencies. These parameters correspond to a mass ratio ($\rho_a L/\rho_s h$) of 0.305

Table 3.1: Yawed Flow Plate Configuration Properties

Property	Symbol	Value
Density	ρ_s	2840 kg/m^3
Young's Modulus	E	72 GPa
Poisson's Ratio	ν	0.3
Thickness	h	.381 mm
Chord	L	275 mm
Span	S	Varied mm

3.1.2 Structural Simulations and Experiments

Before exploring the aeroelastic behavior of the cantilever plate, this section first presents the structural dynamics of the three cantilever plates. We determine the theoretical natural frequencies by solving Eq. 3.1 without the aerodynamic forcing terms. The experimental natural frequencies are determined using an impact response ground vibration test. Fig. 3.1 shows a schematic of the ground vibration test setup, including the impact and measurement locations used during the experiment. We impact the structure with a low mass hammer and measure the response using a point laser vibrometer connected to Labview. Fig. 3.2 is an example of two measured experimental frequency responses for the 55 mm span plate. The black line is the frequency response taken when the laser vibrometer is focused at the 1/4 chord and mid span of the plate. The red dashed line is the frequency response for the same beam but this time the laser vibrometer collected data at the 1/4 chord and edge of the beam. The red dashed frequency response contains all of the peaks of the black line, with an additional two peaks that are highlighted in the figure. There are additional peaks for the data collected at the edge of the plate because the torsion modes have small displacements at the mid span but large displacements near the plate edges. For this reason the laser vibrometer does not pick up torsion frequencies when focused on the mid line of the structure. By collecting data both at the midpoint and at the edge, we ensure that we can identify which peaks are associated with symmetric (bending) modes and, by process of elimination, what peaks are associated with anti-symmetric (torsion) modes.

Fig. 3.3 shows the experimental versus theoretical natural frequencies for the three plates explored in this paper. The three configurations have spans of 55, 108 and 151 mm. There is good agreement between the theoretical and experimental model both in magnitude and trend. Comparing the theoretical predictions to the

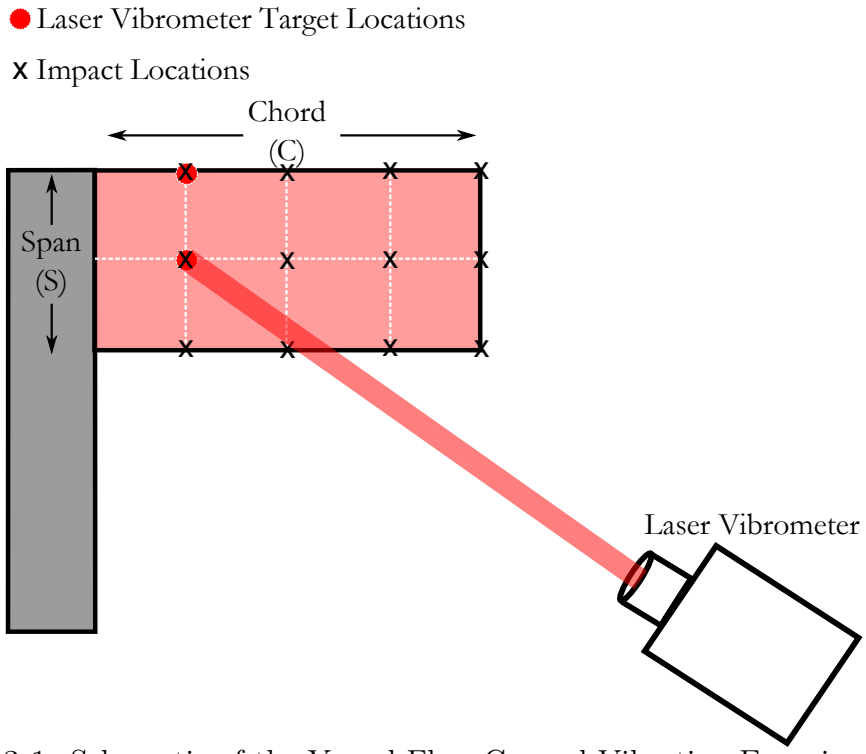

FIGURE 3.1: Schematic of the Yawed Flow Ground Vibration Experiment Setup

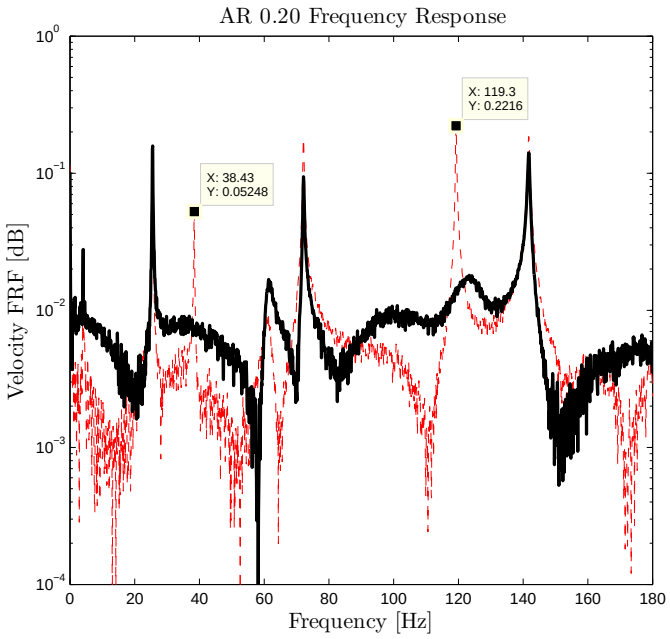

FIGURE 3.2: Yawed Flow Frequency Response Comparison for 55 mm Span Plate

experiment results, the agreement deteriorates as the span increases. This observation is consistent with the assumptions of the beam structural model that the length in the clamped-free direction is much longer than the thickness and width of the structure. As the span, or width increases to the largest value of 151 mm, this assumption is less appropriate. Overall the agreement between the theory and the experiment allows us to use the current structural model in the aeroelastic simulations. Future work could include improving the structural model to a plate structural model.

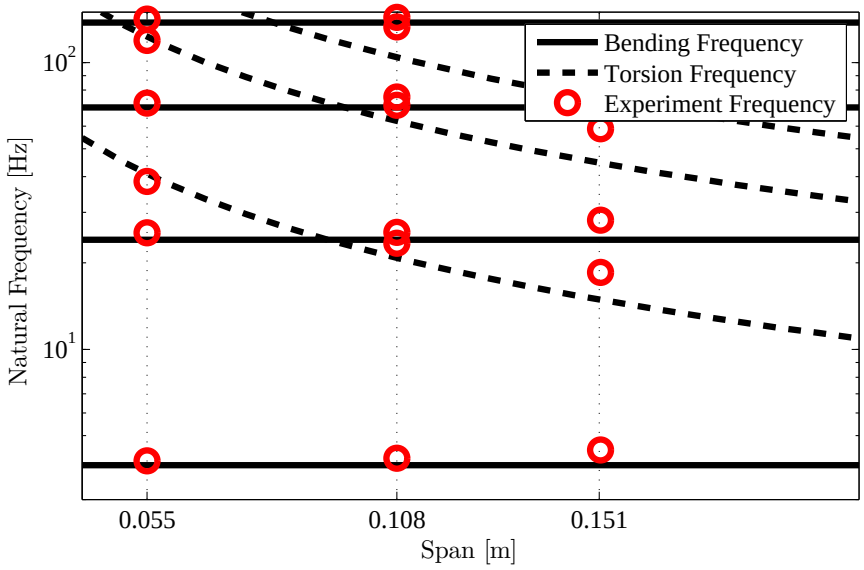

FIGURE 3.3: Yawed Flow Theoretical vs. Experimental Natural Frequencies

Fig. 3.3 also provides some insight into why the specific configurations used for this paper are selected. When looking at initial aeroelastic simulations we observed that the yaw angle at which the system transitioned from the flag-like to the wing-like instabilities depends on the spacing of the natural frequencies of the system. In order to validate and explore this observation we choose the spans of 55, 108 and 151 mm. These configurations include a case where the first torsion mode frequency is larger than, smaller than and nearly the same as the second bending frequency.

3.1.3 Aeroelastic Simulations and Experiments

The author and colleagues conducted the experiments for all of the plates in the Duke University Wind Tunnel. Instrumentation for the experiments included a hotwire to measure the wind tunnel velocity, a potentiometer dial to control to the wind tunnel velocity and an accelerometer to measure the response of the plates during the experiments. Labview recorded the time histories of the velocity and the accelerometer. We mounted the plates in the wind tunnel using a rigid airfoil section. The airfoil section has a pivot point that is out of the wind tunnel. An android application titled "Smart Tools", which projects an angle, measurement on the camera image measures the angle between the plate and the flow. Fig. 3.4 shows the experimental setup for the structure with a span of 108 mm.

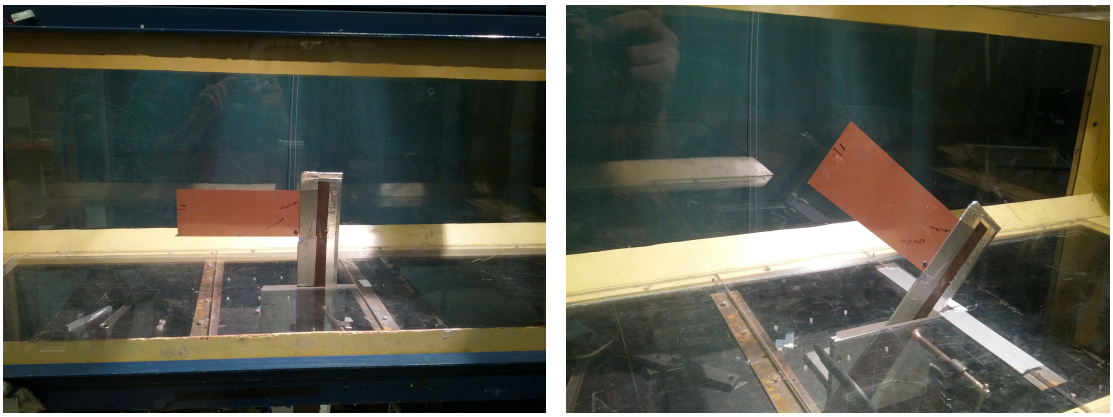

FIGURE 3.4: Yawed Flow Aeroelastic Experiment Setup for the AR 0.393 Plate

For each experiment, the upper flutter velocity is the velocity when the panel enters an unstable limit cycle oscillation after slowly incrementing the velocity of the wind tunnel. For some of the plates and flow angles there is a significant hysteretic response. For these configurations, we cite a "Lower" flutter velocity as well as an "Upper" flutter velocity. The lower flutter velocity is the velocity at which the system goes from an unstable limit cycle oscillations back to a steady, stable position as the flow velocity is decreased.

For the theoretical simulations, the aeroelastic eigenvalues are determined for a given configuration at different flow velocities. The stability boundary is determined by linear interpolating the two eigenvalues that bracket the instability onset boundary. The aeroelastic simulations use $S_c = 50$, $S_s = 40$, an aerodynamic wake three times the chord, a density of air of 1.2 kg/m^3, and a vortex lattice relaxation factor α of 0.992.

55 mm Span Results

The structure with the 55 mm span is the only experimental specimen where the first torsion natural frequency is larger than the second bending natural frequency. The first two theoretical natural frequencies in bending are 3.95 Hz and 24.08 Hz and the first torsion frequency is 41.19 Hz. The experimental frequencies match these results quite well with the first two natural frequencies in bending of 4.08 Hz and 25.50 Hz and the first torsion frequency of 38.42 Hz. Based on the frequency spacing of this configuration, the hypothesis is that the transition from primarily bending and coupled bending and torsion will occur at an angle near the wing configuration.

Fig. 3.5 confirms this hypothesis. In the figure, solid lines denote the theoretical flutter boundary. The analysis predicts that the critical flutter velocity will decrease as we rotate the plate away from the flag flutter. This may be caused by the increased aerodynamic loads on the structure due to a reduction in three dimensional aerodynamic effects as the length of the plate normal to the flow increases with β. The figure also shows that the flutter frequency does not change significantly as a function of the rotation angle until an angle near 90 degrees. This shift in frequency is caused by a shift from fluttering in a coupled first and second bending mode to fluttering in a coupled bending torsion mode.

Fig. 3.6 explores the transition between the flag-like flutter and wing like flutter by looking at the real part of the aeroelastic eigenvalues as a function of flow velocity

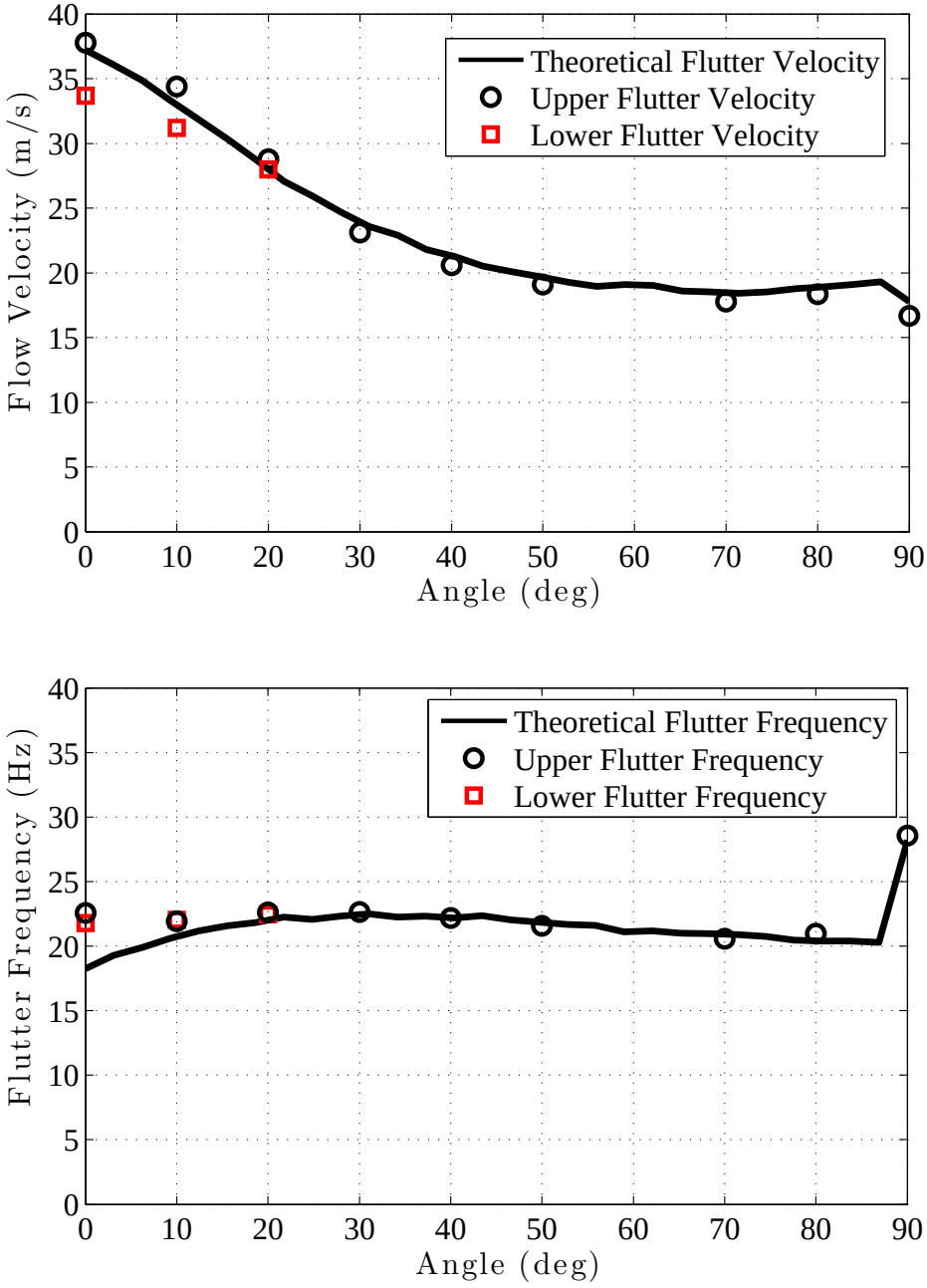

FIGURE 3.5: Span = 55 mm: Comparison of the Yawed Flow Theoretical and Experimental Flutter Velocity and Frequency

for $\beta = 80$ and $\beta = 90$ degrees. The major difference between the two figures is a hump-like mode that remains stable for the 80 degree case, but goes unstable in the 90 degree case. The eigenvalue branch with the hump mode is associated with the first torsion mode. The abrupt transition near the wing configuration corresponds with the hump mode becoming unstable. When the hump mode does not go unstable the instability is driven by the eigenvalue branch associated with the second bending mode. The observation that the instability is driven by the second bending mode for a slender beam at angles so close to the wing configuration was also observed by Barmby et al. (1951) who noted the appearance of a significant second bending mode contributions at small rotation angles from the wing configuration in their experiments.

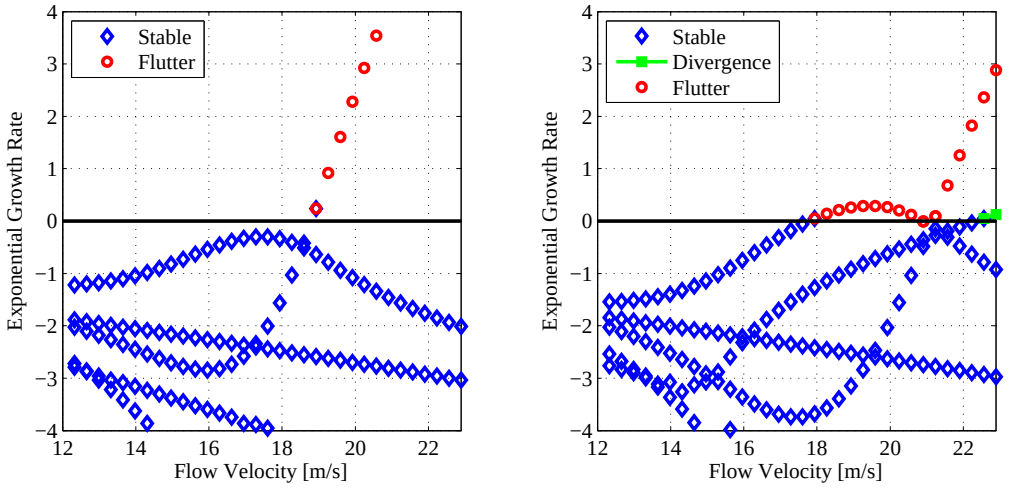

(a) 80 Degrees (b) 90 Degrees

FIGURE 3.6: Span = 55 mm: Comparison of the Real Part of the Eigenvalues for β = 80 and 90 Degrees

Looking at the eigenvector of the instability also gives insight into the difference in the transition behavior. Fig. 3.7 is a plot of the absolute value of the eigenvector associated with the unstable eigenvalue as the flow angle changes. For this case, up until 90 degrees the majority of the contribution to the unstable eigenvector comes

from the values associated with the first and second bending coordinates. This is typical for flag flutter.

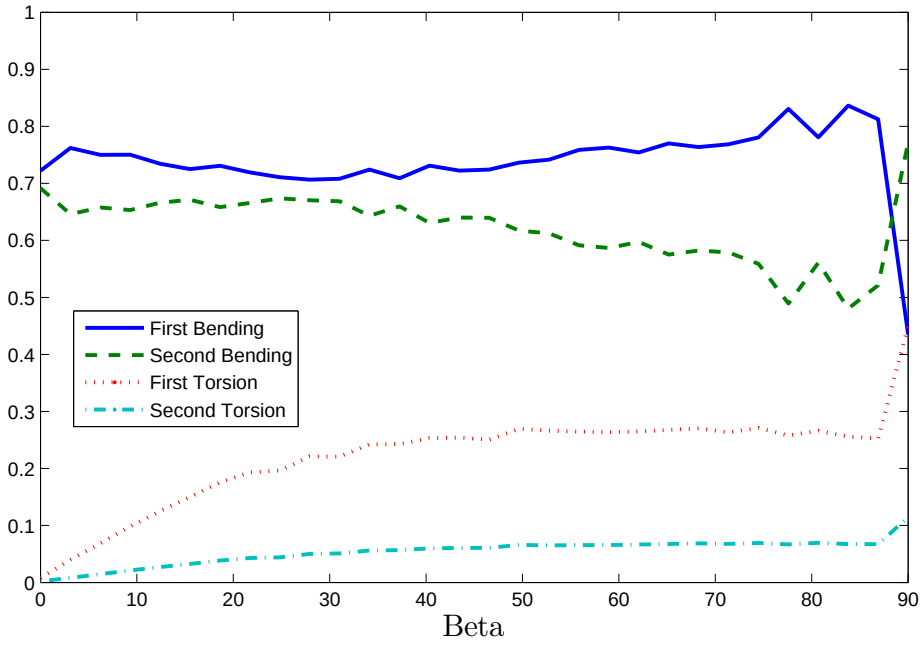

FIGURE 3.7: Plot of the Unstable Eigenvector versus Flow Yaw Angle for the Span = 55 mm plate

Fig. 3.5 also contains the experiment results. There is good agreement between the theoretical predictions and the experimental results. Qualitatively, the instability did appear to contain a large amount of the second bending mode up to the strictly wing alignment, confirming the trend described in the discussion of the theoretical predictions. Furthermore, the experiment does show an abrupt jump in frequency at $\beta = 90$. Additional experiments between $\beta = 80$ and $\beta = 90$ degrees were not conducted to confirm the exact transition angle, but would be a good area for future research. Another important trait that can be deduced by looking at these figures is the size of the initial amplitude of the instability. For the small flow angles there is a hysteresis loop in the experiment captured by the distance between the lower and upper flutter boundaries in Fig. 3.5. In situations where there is the hysteresis loop,

as the velocity of the wind tunnel is increased above the upper flutter boundary, the system enters a large and violent limit cycle oscillation. The amplitude of the oscillations can often be on the order of the chord of the beam (Tang et al. (2014b)). The system remains in this large limit cycle oscillation until the velocity of the wind tunnel is lowered back to below the lower flutter velocity. But for the larger flow angles, e.g. the β=30 case, while the motion is still primarily bending, there is no longer the large experimental hysteresis band. Without a hysteresis loop, as the velocity is increased the system gently transitions into a limit cycle oscillation that is on the order of the thickness of the beam.

108 mm Span Results

Unlike the previous configuration where there was a large gap between the second bending and first torsion natural frequency, the second bending and first torsion frequencies are near each other for the 108 mm span configuration. In the previous configuration, the spacing in the natural frequencies causes an abrupt change in the flutter boundary at the change from flag to wing flutter. For the present configuration, the theoretical predictions from Fig. 3.8 shows a smooth transition with no abrupt changes in flutter velocity or frequency. The theory predicts that both the flutter velocity and the flutter frequency will decreases as the yaw angle increases.

Although the transition is smooth in both frequency and velocity, a study of the flutter mode shapes for the different flow angles suggests that there is a large contribution from the twisting modes at small β angles. Fig. 3.9 shows snapshots of the flutter mode at a β=3.1 degrees. Even at this small angle the figure clearly shows significant torsion contribution. The similarity between the second bending and first torsion frequency, allows the transition to occur without an abrupt change in flutter velocity and frequency.

Fig. 3.8 also shows the experimental results for the 108 mm span plate. The

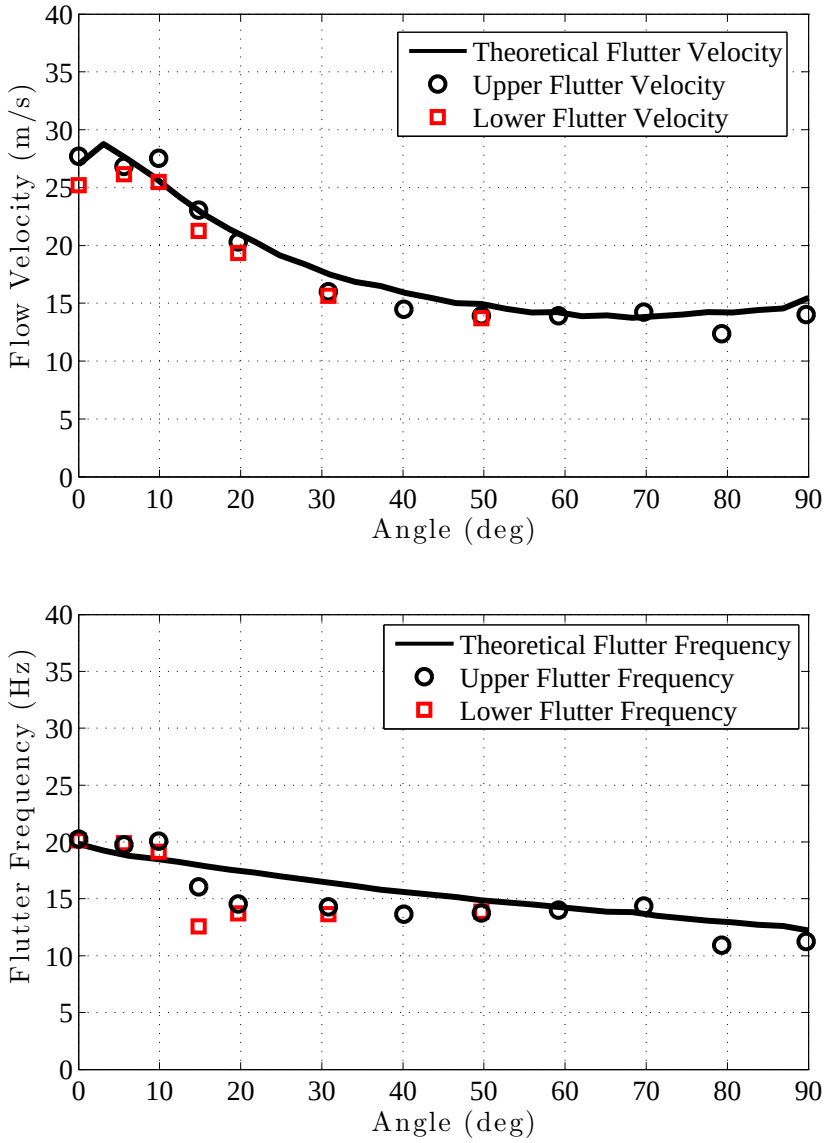

FIGURE 3.8: Span = 108 mm: Comparison of the Yawed Flow Theoretical and Experimental Flutter Velocity and Frequency

experimental results match well with the theoretical predictions. Specifically the flutter velocity for all of the incident flow angles matches very well between theory and experiment. The flutter frequency between 10 and 20 degrees diverges modestly from the theoretical line. In the experimental data there is also noticeable drop in flutter velocity and frequency between 70 and 80 degrees that is not predicted by

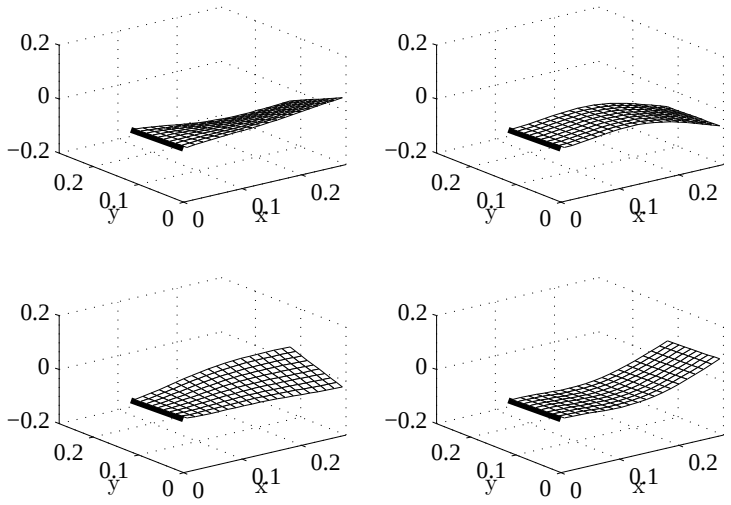

FIGURE 3.9: Span = 108 mm: Theoretical Flutter Mode Shape at β=3.1 degrees

the theory. The discrepancy may be caused by a misalignment in the experiment setup that provides a small angle of attack, thus causing the experimental specimen to deflect statically and thereby changing the dynamics of the system.

Span 151 mm Results

The final configuration has a lower first torsion frequency then the second bending frequency. For this configuration, the first and second bending theoretical natural frequencies are 3.95 Hz and 24.08 Hz and the first torsion natural frequency lies between these two points at 14.92 Hz. For this configuration, Fig. 3.10 shows an abrupt transition from flag flutter to wing flutter at an angle close to the flag (small β) configuration. The theoretical prediction clearly shows an abrupt drop in frequency and a cusp in the velocity at yaw angle of 10 degrees.

Fig. 3.11 shows the theoretical snapshots of the flutter mode shape before and after the sharp transition at 10 degrees. For the snapshots taken at β=6.2 degrees the mode shape is largely symmetric around the elastic axis and appears to be similar to the classic flapping-flag mode shape. For the snapshots taken at β=12.4

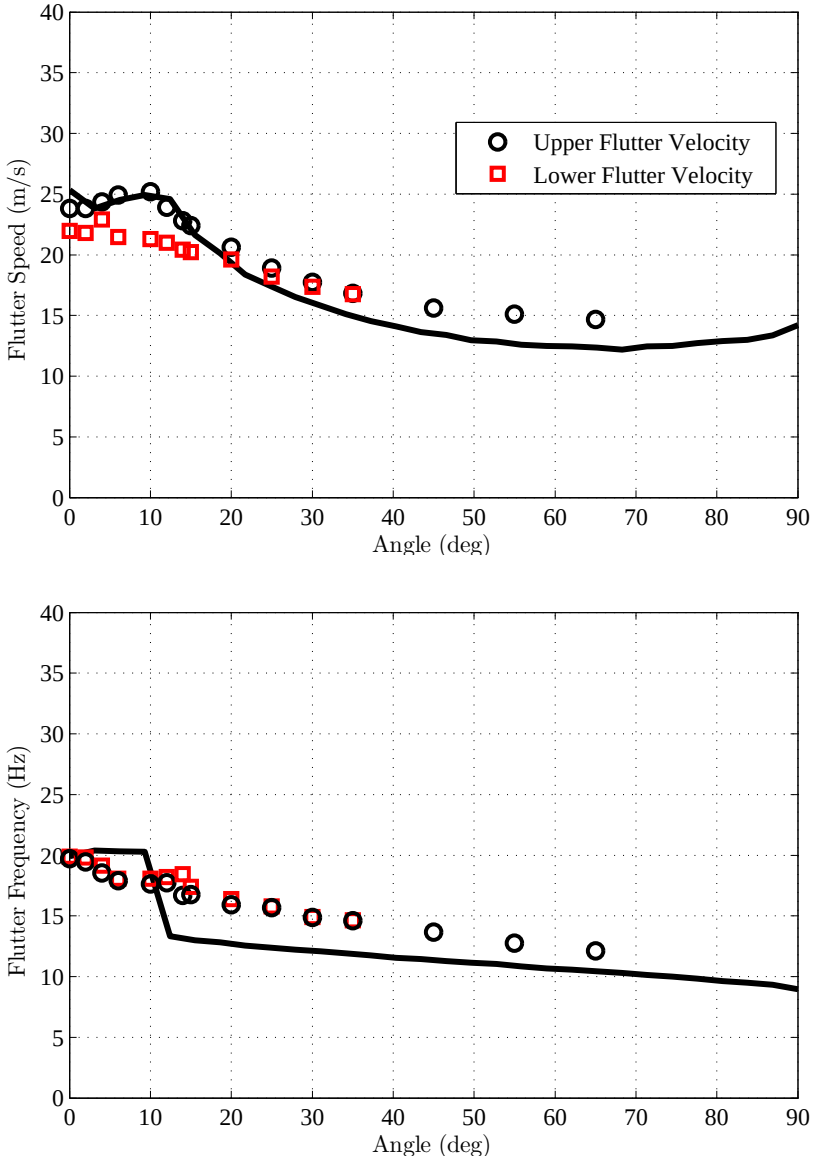

FIGURE 3.10: Span = 151 mm: Comparison of the Yawed Flow Theoretical and Experimental Flutter Velocity and Frequency

degrees the motion is no longer symmetric and there is clearly a large first torsion mode contribution. Comparing Fig. 3.11(a) to Fig. 3.9 shows that 151 mm span configuration remains in a flag-like instability to a higher angle than the 108 mm span plate even though the torsion frequency is lower in the former configuration. However, while the transition for the 108 mm span plate is smooth, the transition

for the 151 mm span plate shows an abrupt drop in flutter frequency.

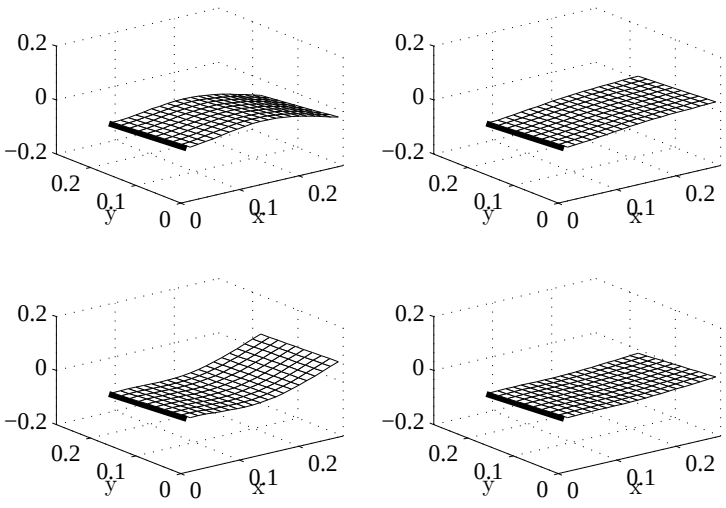

(a) β=6.2 degrees

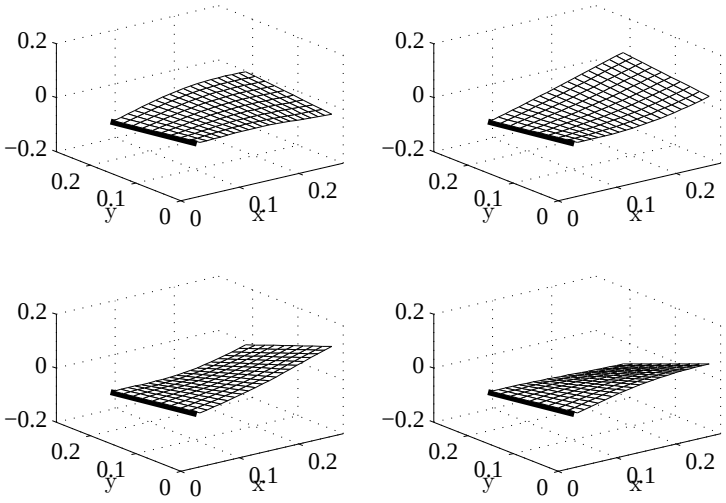

(b) β=12.4 degrees

FIGURE 3.11: Span = 151 mm: Theoretical Flutter Mode Shape at β=6.2 and 12.4 degrees

The experimental results in Fig. 3.10 show a sharp change in flutter velocity near the 10 degree yaw angle, matching the aeroelastic prediction. A qualitative observations of this experiment confirmed the large contribution of the torsion modes

at β angles larger than 10 degrees. As with the previous cases, the hysteris loop disappears as the yaw angle increases. The largest difference between the theory and the experiment is the magnitude of the drop in frequency associated with the transition from wing to flag flutter. While it is quite large in the theoretical model, the drop observed in the experiment is not as precipitous. We do not yet have a physical understanding of what causes this discrepancy.

3.1.4 Conclusions for the Stability of Plates in Yawed Flows

This section presents the aeroelastic stability of plates that rotate from the flag-like configuration to the wing-like configuration. Our model uses a classical beam structural model coupled to a rotated three dimensional vortex lattice model. Our research demonstrates that the transition between the flag-like flutter characterized by a coupled bending instability to the wing-like flutter characterized by a coupled bending-torsion instability depends strongly on the natural frequency spacing of the elastic structure. We show that for a slender plate with a second bending natural frequency lower that the first torsion natural-frequency, the system will flutter in a flag-like manner until the plate is nearly in the wing configuration. Alternatively, when the first torsion frequency is near or lower than the second bending frequency, we observe an abrupt transition to wing-like flutter near the flapping-flag configuration. The difference in the behavior is directly a result of the mechanism that causes the aeroelastic instability. Our theoretical predictions show that both the wing-like and flag-like instabilities arise due to a coalescence between system eigenmodes. Our results demonstrate that the aeroelastic system has a tendency to coalesce between the closest available eigenmodes and therefore by changing the frequencies of our structure we can effectively change its preferred instability behavior. Aeroelastic experiments conducted in the Duke University Wind Tunnel confirm the theoretical predictions for the three configurations.

Future Work

1. **Structural Limitations**: We note that the theoretical beam structural model is limited to exploring simple and slender structures. To expand the current work a structural model for an elastic plate can be implemented to increase the types of structures that can be explored by the existing framework.

2. **Mode Shape Information**: While the experiments provide quantitative data on the flutter velocity and frequency, and qualitative data on the mode shape of the instability, future experiments could include instrumentation to quantify the amount of bending and torsion motion that is present in the instabilities.

3. **Post Flutter Model**: Our current analysis is limited to the stability boundary determination. A nonlinear theoretical model and companion experiment study reported by Tang et al. (2014b) and Tang et al. (2014a) and subsequently improving on their earlier work Tang et al. (2003) can be used to explore the nonlinear post critical response of the plate.

3.2 Post Flutter Flow Visualization for the Flapping Flag

The second research topic related to the aeroelastics of a cantilevered plate is visualizing the flow around the flapping flag. This research complements the previous experimental work from Zhang et al. (2000) by looking at the flow around the flapping flag in air. This section presents flow visualization around the midspan of an elastic plate in air during a LCO using Particle Image Velocimetry (PIV) techniques. This research quantifies the flow field in a single plane during the LCO and suggests how researchers can improve fluid models to capture more accurately the aerodynamic features of the flow field. Improving fluid models is an important task as we work to improve our understanding of the post critical response of the flapping flag.

Whereas the previous section described a research project where we attempt to correlate a theoretical prediction to experimental results, this research focuses on experimental observations. We believe that visualizing the actual flow field around the flapping flag will appropriately motivate the theoretical improvements to the fluid model that need to be made in order to capture the physics of the flapping flag in the post flutter regime.

3.2.1 Flow Visualization Experimental Methodology

The test article is a 275 mm by 151 mm piece of aluminum with the properties listed in Table 3.2. These parameters correspond to a mass ratio ($\rho_a L_x/\rho_s h$) of 0.305 and an aspect ratio (L_y/L_x) of 0.55. For this configuration, the literature (Eloy et al. (2008), Gibbs et al. (2012b)) suggests that the system will lose stability in a flutter mode that is a coalescence of the first and second elastic bending modes. A simulation done with the theoretical model from Gibbs et al. (2012b) predicts a flutter instability at 24 m/s and 20 Hz. We validate the structural model by comparing the ground vibration experiment natural frequencies to theoretical predictions.

We conducted the aeroelastic experiment in the Politecnico di Milano Small Wind Tunnel (PSWT), a closed circuit low-speed wind tunnel, with a rectangular test section of 1.5 x 1 x 3 m and no heat exchangers installed. For the aeroelastic experiment, a rigid airfoil clamps the elastic plate at its leading edge. The rigid airfoil is then mounted horizontally in the wind tunnel. This alignment differs from the vertical mounting in previous experiments, but is necessary to accommodate the PIV setup. Figure 3.12 shows the actual experimental setup and Figure 3.13 shows a schematic representation of the setup.

The PIV setup shown in Figure 3.13 uses a double shutter CCD camera with a 12 bit, 1952x1112 pixel array and a 50 mm lens to acquire the image pairs. The setup uses a Nd:Yag double pulsed laser with 200 mJ output energy and a wavelength of

Table 3.2: PIV Experimental Beam Properties

Property	Symbol	Value
Density	ρ_s	2840 kg/m^3
Young's Modulus	E	72 GPa
Thickness	h	0.381 mm
X Length	L_x	275 mm
Y Length	L_y	151 mm

FIGURE 3.12: PIV Test Specimen Mounted in the Wind Tunnel in Preparation for Experiments

532 nm. The laser sheet passes through an opening in the wind tunnel roof aligned with the flow and positioned in the midspan of the experiment specimen. The laser and the camera are mounted on a external metallic structure made of aluminum profiles that are connected to the heavy basement in order to avoid the transfer of the wind tunnel vibrations to the PIV measurement devices during the tests. A particle generator with Laskin nozzles is used for the flow insemination. The tracer particles, consist of small oil droplets with a diameter within the range of 1-2 μm. The particles are injected in a section just after the fans and fill the wind tunnel volume with homogeneous density. The image pairs post-processing is carried out

using the PIVview 2C software PIVTEC (2013) of PIVTEC. Multigrid technique Raffel et al. (1998) is employed to correlate the image pairs, up to an interrogation window of 64x64 pixels

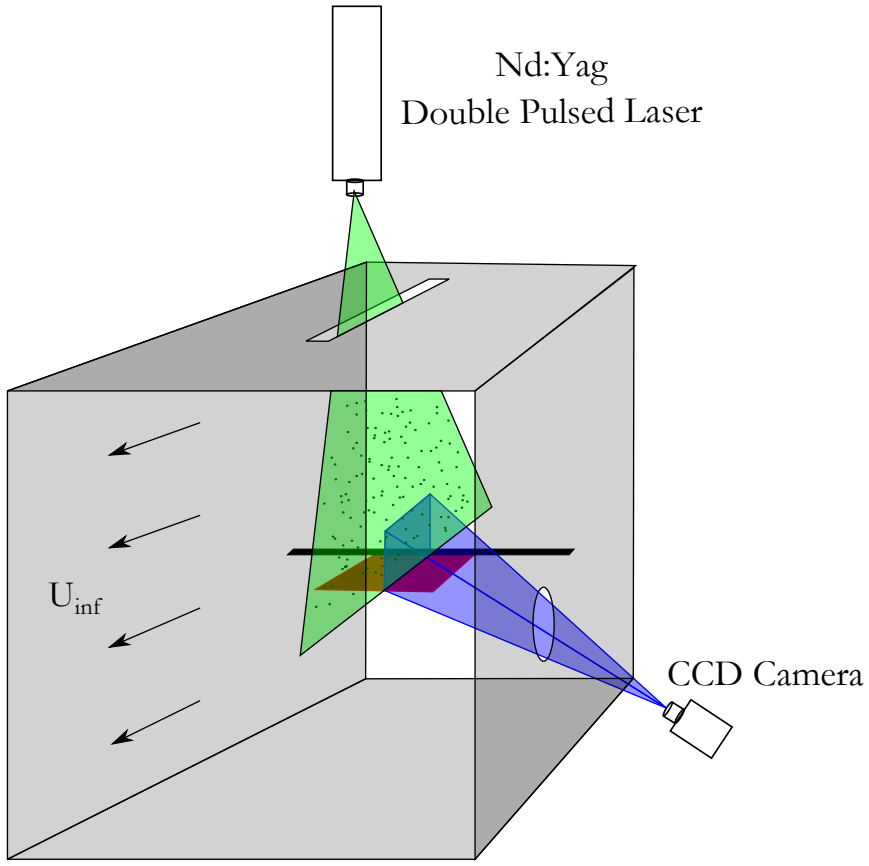

FIGURE 3.13: Schematic of PIV Wind Tunnel Setup

Table 3.3 contains the stability boundary results for the aeroelastic experiments. The precision was limited because we did not instrument the panel during the aeroelastic experiments in order to minimize aerodynamic disturbances in the flow. The experiment was conducted by slowly increasing the flow velocity until the system entered a LCO. We acquired the PIV snapshots at a velocity of 26 m/s, a velocity slightly above the flutter velocity, at a sample period selected to freeze the panel motion between snapshots, effectively identifying the frequency of the LCO. At this

velocity, the LCO amplitude is about 1/2 of the streamwise length of the plate. After collecting data, we reduced the flow velocity until the system returned to a stable state. As noted in the literature (Dunnmon et al. (2011), Eloy et al. (2012), Gibbs et al. (2012b), Tang et al. (2003)), the velocity where the system regains stability is lower than the velocity at which the system becomes unstable. For the experiment the Reynolds Number is 2x10^5 and the LCO Strouhal number, ($\omega L_x/U$) is 0.07.

Table 3.3: PIV Aeroelastic Experiment Results

Upper Flutter Velocity	[m/s]	25.5
Lower Flutter Velocity	[m/s]	24.0
LCO Frequency(@ 26 m/s)	[Hz]	19.73

3.2.2 Flow Field Visualization

For the experiments there are two types of PIV visualizations that are conducted. The first set uses images captured at the same phase of the flag oscillation and the second set includes images taken at different steps in a single period of the oscillation. The first set is used to analyze the phase average of the flow field. This is a common technique in PIV analyses to separate a flow into a mean and a fluctuating part. This is important because it allows researchers to identify turbulent structures in the flow. This type of measurement is important if we are to observe flow separation on the plate. The second type of experiment is useful for creating a visualization of how the flow changes during a single oscillation period. This is useful for producing visualizations of the flow evolution.

We explored the phase averaged flow fields for two different times in the LCO. Figure 3.14 shows the theoretical flutter mode shapes, the PIV viewing window and highlights the two flag shapes that we will analyze. Please note the mode shapes

in Figure 3.14 do not take into account the effect of the gravity that would lead to a slight up/down asymmetry. The first image set analyzed is taken at a moment when the point of the plate on the upstream boundary of the PIV viewing window is moving up and the trailing edge is moving down. The document will refer to this as the upstroke configuration.

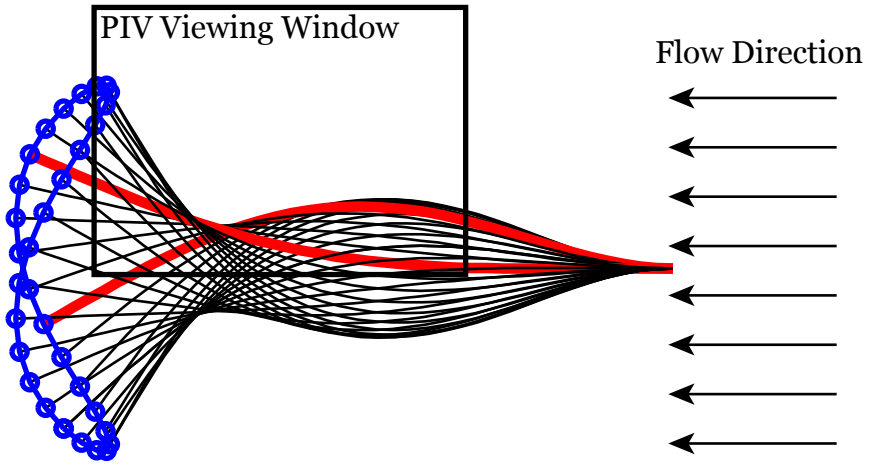

FIGURE 3.14: Theoretical Flutter Mode Shapes with PIV Window Identified

Figure 3.15 shows the phase-averaged flow-field in the upstroke. The fluid moves from right to left in the figure. The figure also contains streamlines seeded at the right hand side of the image. The region with no streamlines is the location of the panel that is masked to avoid displaying confusing and physically irrelevant flow vectors. Figure 3.16 shows the vertical component of the velocity field. Figure 3.16 clearly shows the flow following the upward motion of the front half of the plate and the downward motion of the back portion of the plate. The most striking feature of this analysis is that the flow is attached along the panel. According to the images the flow completely conforms to the structural motion with the streamlines following the local slope of the flapping flag. The streamlines also suggest that there is no inverse flow flux.

Figure 3.15 shows no separation at this specific point in the oscillation, but it is possible that there could be other points in the limit cycle that are more critical. The second analysis explores snapshots taken when the point on the plate on the upstream boundary of the PIV viewing window is beginning to descend and the trailing edge is still moving in the upward direction. This portion of the oscillation is at the beginning of the downstroke. We choose this portion of the motion because the plate curves in the opposite direction to the first pair of images. Figures 3.17 and 3.18 show the phase averaged flow field and phase averaged vertical component of the flow field. As was the case previously, the streamlines in the figures suggest a fully attached flow with no flow separation.

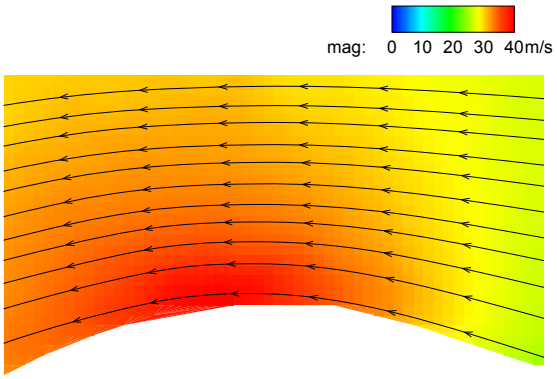

FIGURE 3.15: Upstroke Phase Average Flow-field with Streamlines

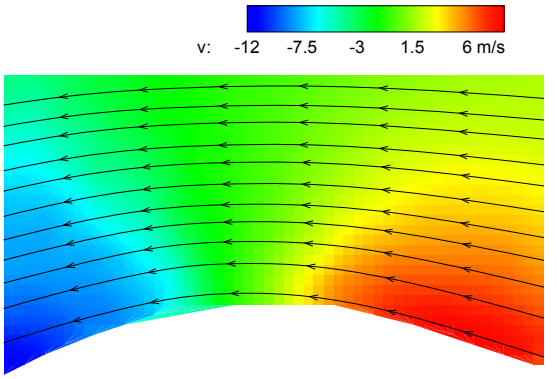

FIGURE 3.16: Upstroke Phase Average Vertical Component of the Flow-field

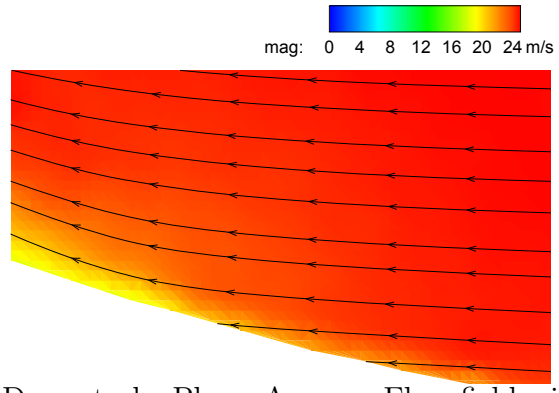

FIGURE 3.17: Downstroke Phase Average Flow-field with Streamlines

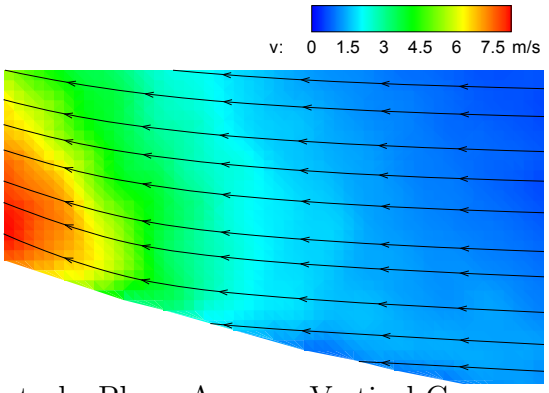

FIGURE 3.18: Downstroke Phase Average Vertical Component of the Flow-field

Because the phase averages suggest that the flow is attached, we can select single snapshots throughout the oscillation period and create a set of images that captures the fluid motion through a full period of the flag motion without needing to phase average every image. Figure 3.19 shows snapshots from eight different times in the flag cycle. The figures progress left to right and top to bottom. The figures contain streamlines and the flow velocity. The figures confirm the benign and attached nature of the flow for this system, where at a given position the flow is conformal to the structural motion.

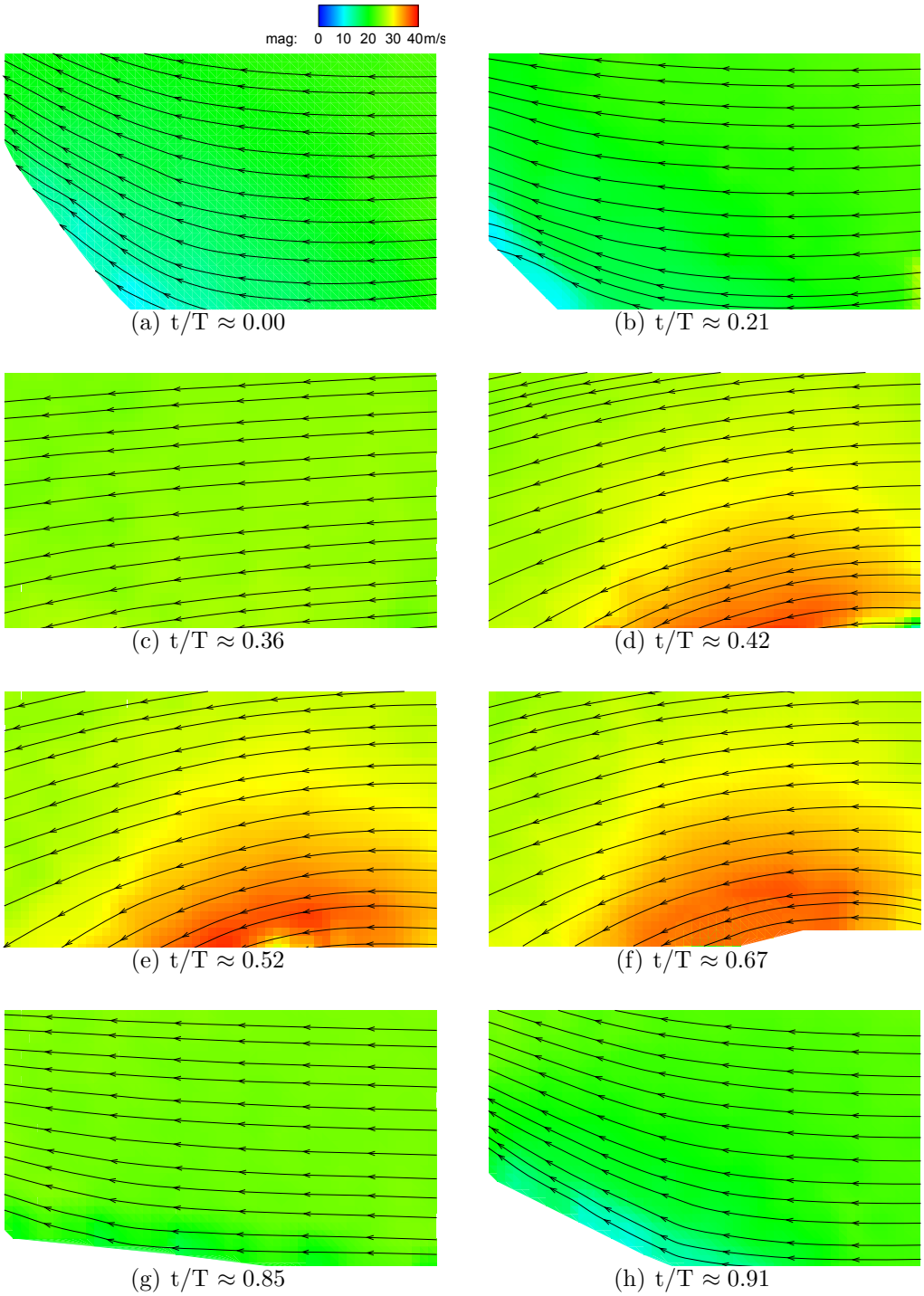

(a) t/T ≈ 0.00 (b) t/T ≈ 0.21

(c) t/T ≈ 0.36 (d) t/T ≈ 0.42

(e) t/T ≈ 0.52 (f) t/T ≈ 0.67

(g) t/T ≈ 0.85 (h) t/T ≈ 0.91

FIGURE 3.19: PIV Snapshots from Different Phases in the LCO with Streamlines

3.2.3 Conclusions for the Flow Field Around the Flapping Flag

This section presents experimental observations of the flow field around the midspan of the flapping flag while in a LCO. The flow fields are captured using typical PIV techniques and show that the flow remains attached to the flapping flag within the observation area, even while the structure is in a violent, large amplitude LCO. This observation has significant implications for the way that we model the aerodynamics in aeroelastic models of the system. Because the flow is attached and well behaved, linear or nonlinear potential flow aerodynamic theories used in many of the flapping flag aeroelastic theories may be capable of accurately capturing the flow field seen in the experiment. Furthermore, for the case of heavy flags in light fluids, which corresponds to small mass ratios, including viscous effects by solving the Navier-Stokes equations may not be the best way to improve the theoretical predictions of the post critical response. Instead, potential flow theories that are capable of capturing the large geometric deflections during the LCO may be adequate. An example of an applicable model would be to extend the linear vortex lattice model used by previous researchers to model nonlinear effects. An example of such a model is found in Attar (2003) where the vortex elements are shed at the trailing edge of the displaced structure into a free wake that is allowed to convect and move freely.

Our observations also suggest that continued improvements to the structural nonlinear models may improve the agreement between theory and experiment for the post-critical response of the flapping flag. A particularly promising development from Tang et al. (2014b) that includes nonlinear inertia effects as well as nonlinear stiffness effects shows promise in matching limit cycle oscillation amplitude theoretical predictions to experimental measurements.

Finally, there are additional flow visualizations that would be an interesting avenue for future research.

1. **Field of View Improvements**: Due to camera's view field limitations, we focused on capturing the flow over the plate so that we could identify regions of flow separation. With additional time and resources, one could investigate the wake behind the plate to explore any large wake structures that are formed during the LCO.

2. **Three Dimensional Flow Effects**: The current study is also limited to exploring the flow in a single plane over the midspan of the flapping flag. Exploring the flow field in a plane transverse to the flow as well as locations near the edges of the plate could identify strong 3D aerodynamic effects and further strengthen the conclusions of the current study

3.3 Post Flutter Response of the Flapping Flag

The final research exploration related to a cantilevered plate is quantifying the amplitude of the structural Limit Cycle Oscillation (LCO) and the hysteresis loop that we observe when we conduct flapping flag aeroelastic experiments. Although the linear Vortex Lattice Method (VLM) based aeroelastic model presented in this dissertation is not capable of predicting the post-flutter behavior quantified by this experiment, the experimental data can be used by other researchers to validate nonlinear aeroelastic models for the system. For example we will present theoretical predictions from Tang et al. (2014b) that validate a new nonlinear aeroelastic model with our experimental data.

3.3.1 Ground Vibration Experiments

For our experiment we used a plate with structural properties the same as presented in the previous section in Table 3.2. Before conducting aeroelastic experiments, we conducted ground vibration testing to validate the properties of the structure. To conduct the ground vibration experiment we placed an accelerometer at the tip/edge

Table 3.4: Post Flutter Ground Vibration Experiment Results

Mode	ANSYS code Freq [Hz]	Experiment Freq [Hz]	Error [percent]
1st Bending	4.16	3.95	5.06
2nd Bending	25.84	24.98	3.3
3rd Bending	72.12	69.91	3.06
4th Bending	144.06	142.37	1.1

of the cantilevered structure. The accelerometer data is stored by Labview and then post processed in Matlab. The structure is then excited at different locations. For this experiment, we record the location of the pulse impact but not the strength of the impact. To determine whether a mode was symmetric (bending) or anti-symmetric (twisting), we compared the frequency response for cases where we impacted the structure near the elastic axis to cases where we impacted far from the elastic axis. We assume that the additional frequency peaks in the frequency response of the signal for the latter case are due to twisting modes.

Table 3.4 shows the results of the ground vibration experiments in bending. The first column has the theoretical predictions using a ANSYS structural model with the parameters listed in Table 3.2. There is very good agreement between the theory (ANSYS code) and the experiment for all of the bending modes.

3.3.2 Quantifying the Limit Cycle Oscillation Amplitudes

The goal of the aeroelastic experiments was to quantify the LCO amplitude of the flapping flag. To capture the LCO amplitude, a Light Emitting Diode, LED, was placed at the tip and mid-span of the structure. Using 30 frame per second (FPS) video, the path of the LED can be traced. Additionally the color coherence of the LED light, made it easier to use automated filtering in Matlab to track the path.

Figure 3.20 shows a frame of the video that has been analyzed by the Matlab script. The figure demonstrates how the script is able to isolate the LED path.

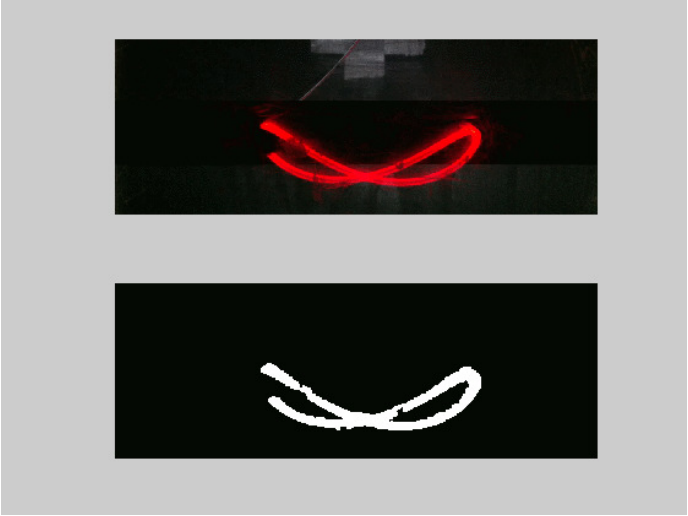

FIGURE 3.20: Image from Post Processing Script

FIGURE 3.21: Flapping Flag During the Transition Between Stable and LCO

An additional method that we used to improve the video captured by our low-speed camera was using a strobe. Figures 3.21 and 3.22 show snapshots of the

videos. Figure 3.21 is taken during the initial flutter before the limit cycle oscillation is reached. Figure 3.22 is a set of snapshots of the limit cycle oscillation that show the shape of the LCO. The figures show that the LCO is largely second bending. Additionally the mode shape is similar to the flutter mode predicted by a linear vortex lattice model.

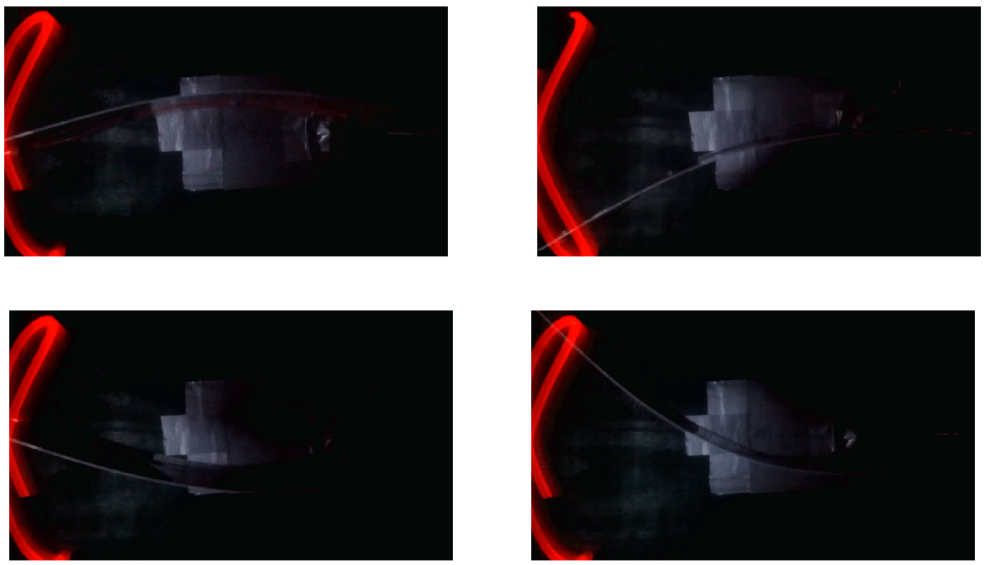

FIGURE 3.22: Flapping Flag Limit Cycle Oscillation Snap Shots

To determine the amplitude of the oscillation, the code averages the snapshots from a full second of the video (30 frames) to get the average path. The script then automatically identifies the pixel of the far left and far right portion of the path and defines this as the LCO amplitude. This amplitude is then synchronized with the wind tunnel velocity data to determine the amplitude as a function of the velocity. The amplitude is converted to a real length using the camera calibration conducted before the experiment that calculates the pixels per centimeter in the plane of the LED. This method is able to provide the LCO amplitude to +/- 1 centimeter. This could be improved by using a camera with a higher resolution.

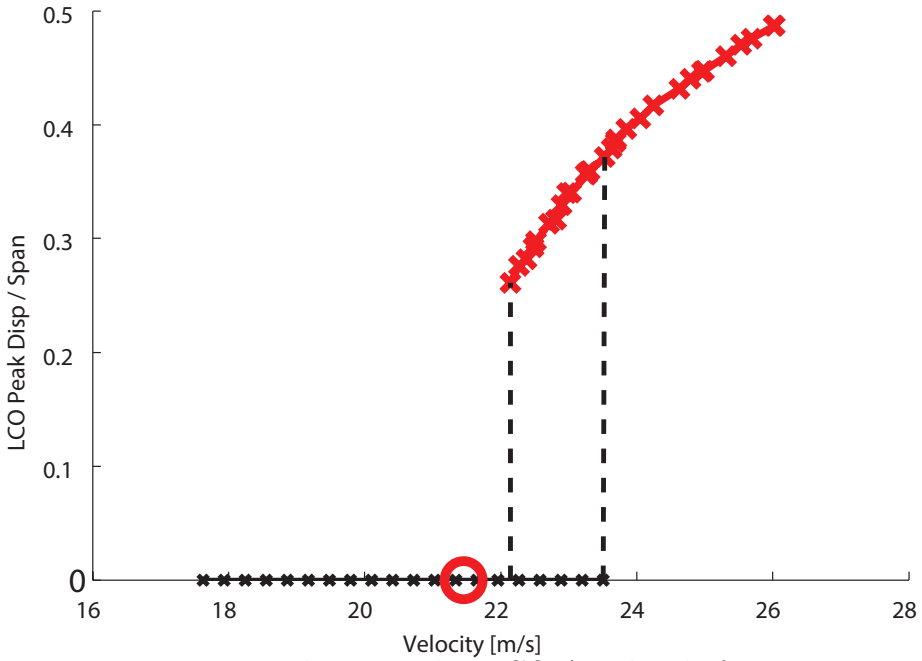

FIGURE 3.23: Flapping Flag LCO Amplitude for Run-1

The most important observation from the experiment is the LCO amplitude as a function of the flow velocity. Figure 3.23 shows this relationship for a single run. The LCO amplitude has been plotted as the non-dimensional quantity LCO Peak Disp / Span. This quantity is calculated using the oscillation amplitude divided by two and normalized by the span of the structure. The circle in the figure is the flutter velocity predicted by the linear VLM aeroelastic model. For the experiment the wind tunnel velocity was increased until the system became unstable at 23.64 m/s. After a rapid growth with time indicated by the dotted line on the far right of the figure, the system entered a LCO. Next the flow velocity was increased and then decreased to populate the LCO amplitude line. The sweep included dropping below the flutter velocity, but still above the stable LCO onset velocity of 22 m/s and then increasing the velocity to ensure that the LCO amplitude was the same whether the velocity was increasing or decreasing. Finally the velocity was slowly lowered until the system exited the LCO and returned to a stable state.

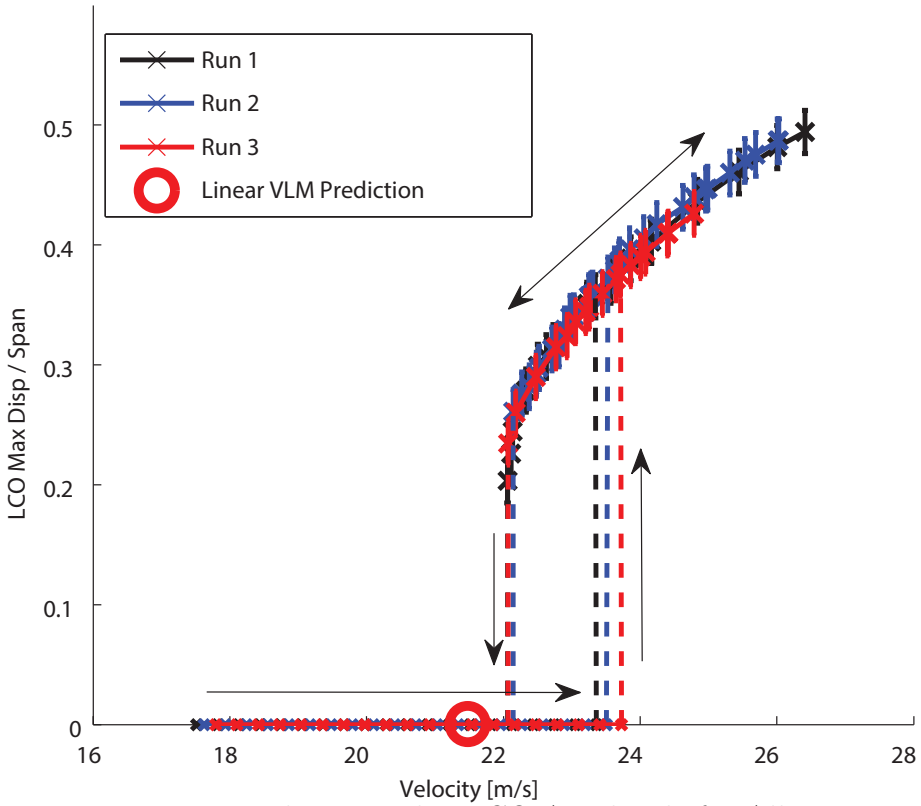

FIGURE 3.24: Flapping Flag LCO Amplitude for All Runs

Figure 3.24 contains the amplitude data for three (3) different runs. This data demonstrates the repeatability of the experiments. This is especially apparent in the overlap of the LCO amplitude for all of the experiments. The largest noticeable difference in the response is the initial flutter velocity which changes by up to 2.5 percent between the experiments. We limited the max velocity for this experiment because the LCO amplitude was growing larger than the field of vision of the camera.

A spectogram for the LCO in Figure 3.25 shows the frequency and velocity as a function of time. In general there is not much variation in the frequency as the flow velocity changes and therefore the LCO amplitude changes. FFT analysis results are shown in Figure 3.26 for the flow velocities U=22.82, 24.77, 25.53 and 26.03 m/s. The LCO response is primarily a single specific harmonic oscillation.

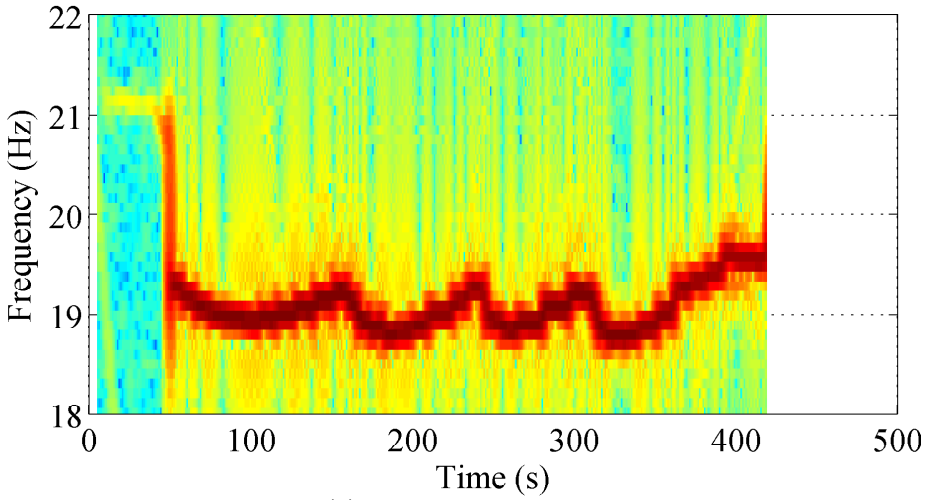

(a) Frequency vs. time

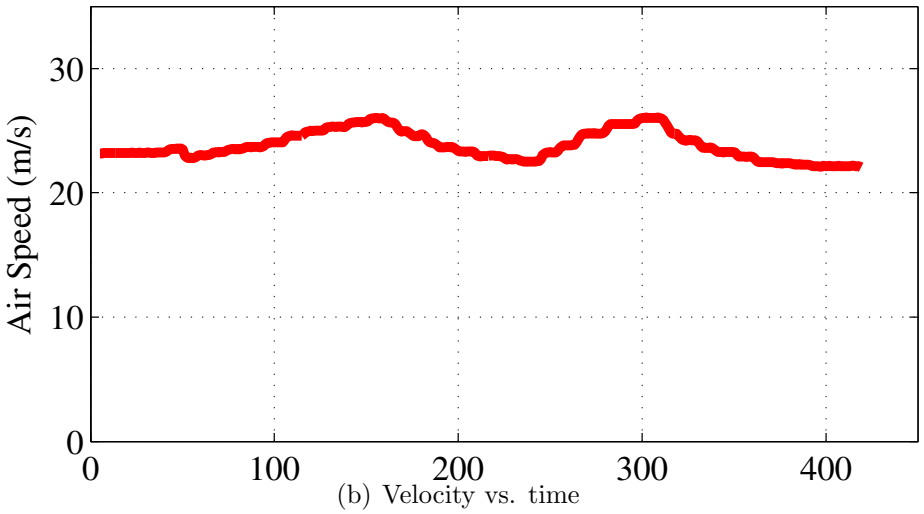

(b) Velocity vs. time

FIGURE 3.25: Flapping Flag Frequency and Velocity vs Time

3.3.3 Comparing Limit Cycle Oscillation Amplitudes to Theoretical Prediction

The goal of this research exploration is to create an experimental data set that researchers can use to validate theoretical models. Since completing the experiment Tang et al. (2014b) have used the experimental results to validate a new nonlinear structural model. Figure 3.27 is taken from Tang et al. (2014b).

Figure 3.27(a) shows the nondimensional rms flap amplitude vs. the flow velocity. The theoretical results include two nonlinear cases: a full stiffness nonlinearity only

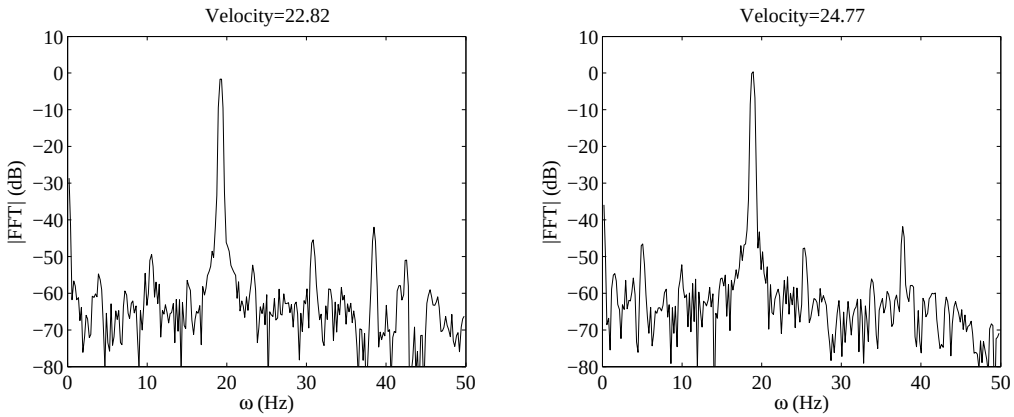

(a) U=22.82 m/s

(b) U=24.77 m/s

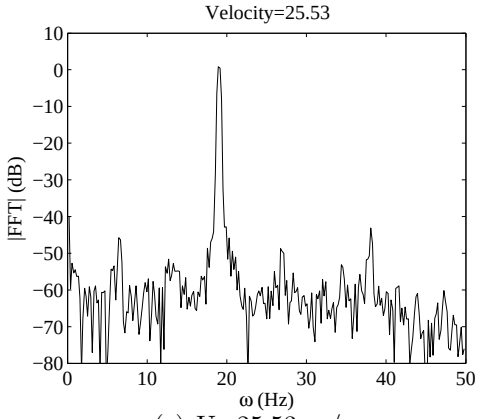

(c) U=25.53 m/s

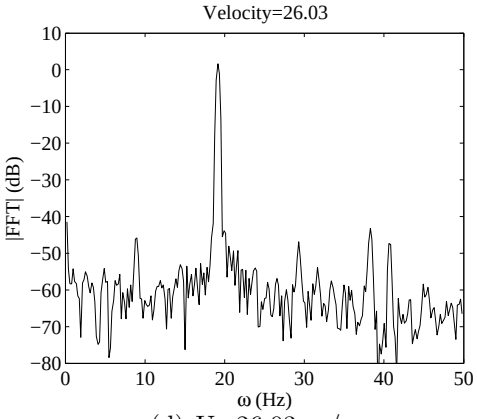

(d) U=26.03 m/s

FIGURE 3.26: Flapping Flag LCO FFT Response for Several Flow Velocities

and a full stiffness nonlinearity plus an inertia nonlinearity. The experimental results contain the LCO amplitude data for all three experimental runs. Corresponding to the LCO amplitude, the LCO frequencies are shown in Figure 3.27(b). Because the theoretical LCO responses are bursts or intermittent motion while the experimental results are primarily a single harmonic oscillation, the theoretical LCO frequency has many frequency components from the FFT analysis. Each frequency from the FFT whose amplitude is larger than 0.1 for a given flow velocity has been shown.

It is interesting that the theoretical results for the full nonlinearities (inertia plus stiffness) agree best with experiment for the LCO amplitude. However when only the stiffness nonlinearity is included the response is a single dominant frequency as

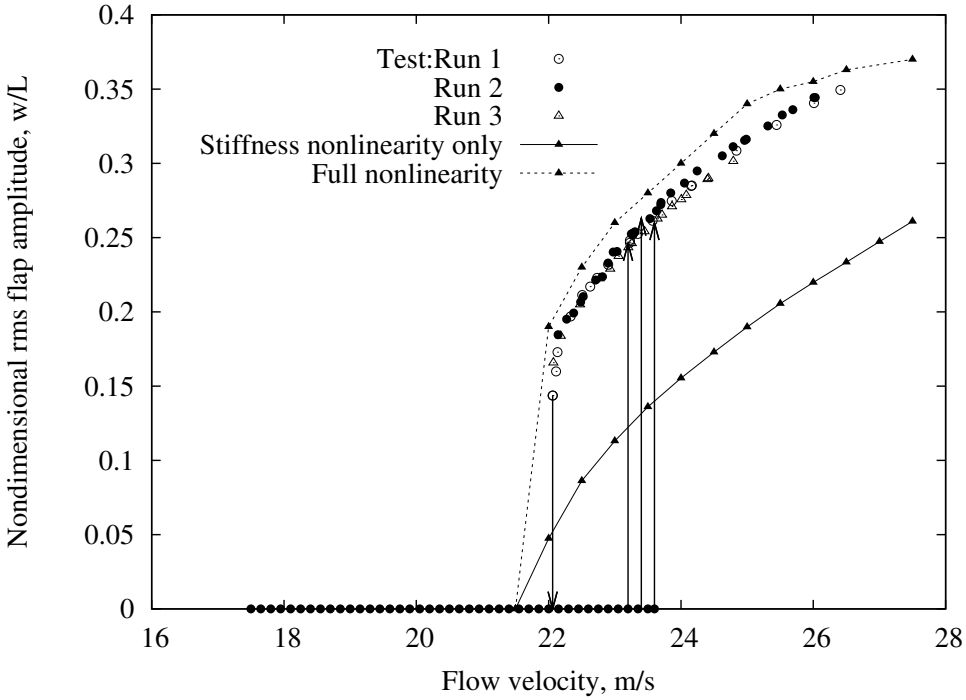

(a) LCO rms amplitude

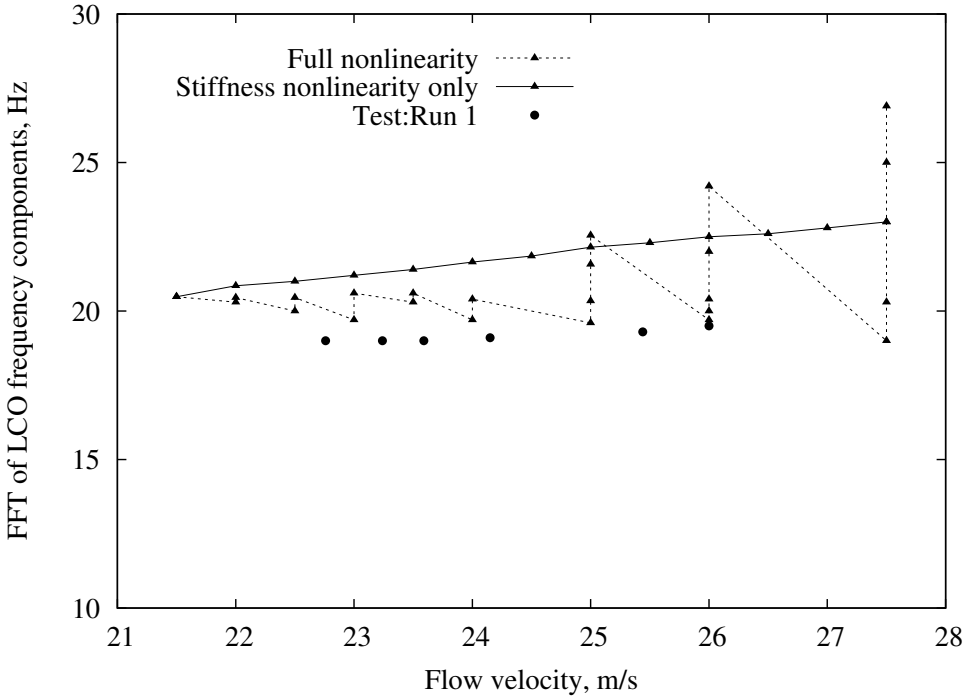

(b) LCO frequency

FIGURE 3.27: Comparison of linear and nonlinear inertia theoretical predictions of RMS LCO tip displacement amplitude to experimental data.

found in the experiment.

3.3.4 Conclusions for the Post Flutter Response of the Flapping Flag

In this section we presented experimental work conducted to quantify the tip LCO amplitude as a function of velocity for the flapping flag. This is a valuable dataset for evaluating the validity of the new nonlinear models that are being developed to model the system. The methodology developed for this research allowed us to efficiently identify the limit cycle oscillation amplitude. Our work has already been used to validate an advanced nonlinear aeroelastic model.

Future work related to this research might include conducting experiments on additional configurations and improving the sensitivity of our experiment. We could improve the sensitivity by upgrading our camera to a high speed camera where we could capture multiple frames throughout the LCO. This would allow us to capture the motion of all of the points on the structure as opposed to just the tip.

4

Stability of Plates with Various Boundary Conditions in Subsonic Flow

An ongoing push for lighter aerospace structures and novel designs requires advancing the understanding of the aeroelastic stability of plates with non-conventional boundary condition combinations. This chapter summarizes the aeroelastic theory and experimental results on the flutter and/or divergence mechanisms of a rectangular plate with different sets of structural boundary conditions. The theory combines a linear plate structural model with a three-dimensional vortex lattice aerodynamic model to create a high-fidelity frequency domain aeroelastic model. The chapter also discusses the development of a modular experimental test bed to test the different boundary conditions. A pair of well-understood boundary condition configurations act as validation points, and then results of additional configurations that have not been extensively explored are presented. The results presented in this chapter can be used to support the design efforts of projects involving plates or plate-membranes. In addition, the work done for this chapter adds to the fundamental understanding of plate aeroelasticity and provides experimental data for comparison and future validation. The work in this chapter has appeared in multiple publications.

Publications:

1. **Gibbs et al. (2014c)**: This journal publication combines the insight developed from three conference papers (Gibbs et al. (2012a), Wang et al. (2012a,c). The paper explores the stability of a rectangular structure with multiple boundary conditions. The paper contains the development of a theoretical framework for determining the stability of a plate with various boundary conditions by coupling a linear rectangular plate to a three dimensional vortex lattice aerodynamic model. For four configurations where a flutter instability is predicted, aeroealstic experiments validate the theoretical model.

2. **Gibbs et al. (2012a), Wang et al. (2012a)**: A companion set of papers presented at the 53rd AIAA/ASME/ASCE/AHS/ASC SDM Conference explore the stability of a three sides restrained plate. The research was motivated by a proposed membrane by NASA to reduce the noise on subsonic transport aircraft. In the papers we construct a model for a single rectangular configuration by coupling the plate model with the three dimensional vortex lattice model. The flutter boundary prediction is validated with an aeroelastic experiment.

3. **Wang et al. (2012c)** This paper summarizes the aeroelastic theory, numerical results, and experimental results of a study on the flutter and/or divergence mechanisms of a rectangular plate with four different sets of structural boundary conditions. The theory combines a three-dimensional vortex lattice aerodynamic model with a plate structural model to create a high-fidelity frequency domain aeroelastic model. Combined with the work from Gibbs et al. (2012a) and Wang et al. (2012a) and incorporating suggestions made during the conference presentations we created a journal publication (Gibbs et al. (2014c)).

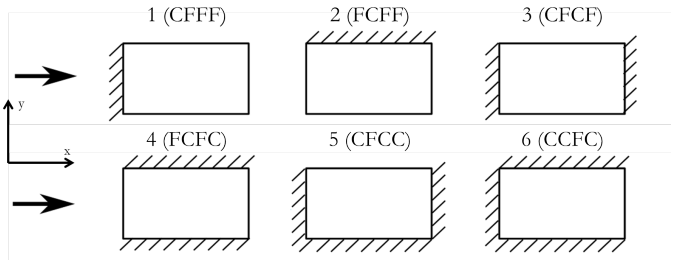

FIGURE 4.1: Combinations of boundary conditions and flow directions explored in this chapter. The diagonal marks indicate a clamped boundary and other boundaries are free with no restraint. The arrows indicate different fluid flow directions that are considered. Each configuration considers a single fluid flow direction.

4.1 Theoretical Model

This theoretical model couples a classic linear plate model described in Section 2.1.2 to the vortex lattice aerodynamic model described in Section 2.2.1. The structural model is coupled to the aerodynamics through the aerodynamic force defined in Eq. 2.49. This force appears on the right hand side of Eq. 2.24 as generalized force terms Q_n which in discrete form can be expressed as:

$$Q_n = \sum_i P_i \Psi_{jk}(x_i, y_i) \tag{4.1}$$

where $\Psi_{jk}(x_i, y_i)$ is the value of the n'th mode shape evaluated at the i'th colocation point. We then combine the plate equation of motion from Eq. 2.24, with the aerodynamic equation given in Eq. 2.48 and the force relationship from Eq. 2.49 into a single matrix equation. To achieve this, we place the structural model into a state space form and time discretize the equation in a method consistent with the aerodynamic temporal discretization. This allows us to define the state at time n and $n+1$ in terms of the circulation and generalized coordinate strengths at that time. The resulting equation is a time discrete linear system that we solve in the frequency domain to determine the aeroelastic eigenvalues as a function of the flow velocity.

4.2 Numerical Simulations

Linear aeroelastic stability analysis was conducted on all of the configurations shown in Fig. 4.1 with the material properties listed in Table 4.1. The model includes the baffle sections as well along any clamped edge. The top and bottom baffle sections have heights approximately equal to 25% of the span of the specimen, and the leading and trailing edge baffle sections have widths about 50% of the chord of the specimen. The theory does not predict significant differences in aeroelastic results when the sizes of the baffle sections are changed. The vortex lattice mesh contains 100 elements in the streamwise direction, 10 elements in the normal to the flow direction on the elastic structure. The wake extends 3 times L_x beyond the trailing edge of the structure. The density of air is assumed to be 1.2 kg/m^3, and a vortex lattice relaxation factor of 0.992 is used. The structural model contains 6 modes in the streamwise direction and 3 modes in the normal to the flow direction, giving the system 18 structural degrees of freedom. A nominal structural damping ratio of 0.02 is used unless otherwise noted.

Table 4.1: Various Boundary Condition Membrane Structure Properties

Property	Symbol	Value
Density	ρ_s	1230 kg/m^3
Young's Modulus	E	18.4 MPa
Poisson's Ratio	ν	0.5
Thickness	h	1.727 mm
L_x		152.4 mm
L_y		114.3 mm

Before looking at the summary of the aereoelastic results for the different configurations, this section will explore the aeroelastic simulation results for the CFFF (Configuration 1) plate. Figure 4.2 shows the eigenvalues for the configuration. The eigenvalues are plotted in three different ways. Figure 4.2(a) shows the aeroelastic

damping ratio vs the flow velocity. In order to generate this plot eigenvalues are determined at discrete flow velocities and connected based on their distance in the complex plane to eigenvalues for a previous flow velocity. The aeroelastic damping ratio, ζ_{aero} is the negative of the imaginary part of the eigenvalue divided by the real part of the eigenvalue. This allows us to write the time varying portion of the displacement as $\exp[\omega_n(i + \zeta_{aero})t]$. The figure shows the evolution of the aeroelastic eigenvalue as the flow velocity is increased. This figure indicates that the system loses stability at a velocity near 10 m/s as the aeroelastic damping ratio moves from negative to positive. Figure 4.2(b) gives additional insight into the nature of the instability. This figure contains the real or frequency component of the eigenvalue plotted versus the flow velocity. The plot indicates that the instability likely arises due to the interaction between the lowest frequency mode, which changes significantly with the flow velocity, and the third mode. These modes correspond with the first and third mode shapes. Figure 4.2(c) is a Root Locus plot. This figure also shows that the instability arises in an oscillatory manner near 8 Hz.

Using a similar analysis we can predict the stability information for each of the six configurations. Table 4.2 lists the instability type for each configuration, the air speed at which the instability occurs, and the frequency of the instability. We computed these results using a structural damping ratio of 0.02 for all modes, and no applied tension. The structural dynamics experiments described in the next section, suggest that the structural damping ratio for our specimen may be as high as 0.05, which is higher than what is seen in typical materials. Table 4.3 shows the aeroelastic results with a higher damping ratio of 0.03, again with no applied tension. By comparing the two tables it is clear that the larger damping value does not significantly change the instability boundary for the divergence configurations. Theoretically there should be no change in divergence speed with increases in structural damping. The small discrepancy in the predictions is likely caused by the way that

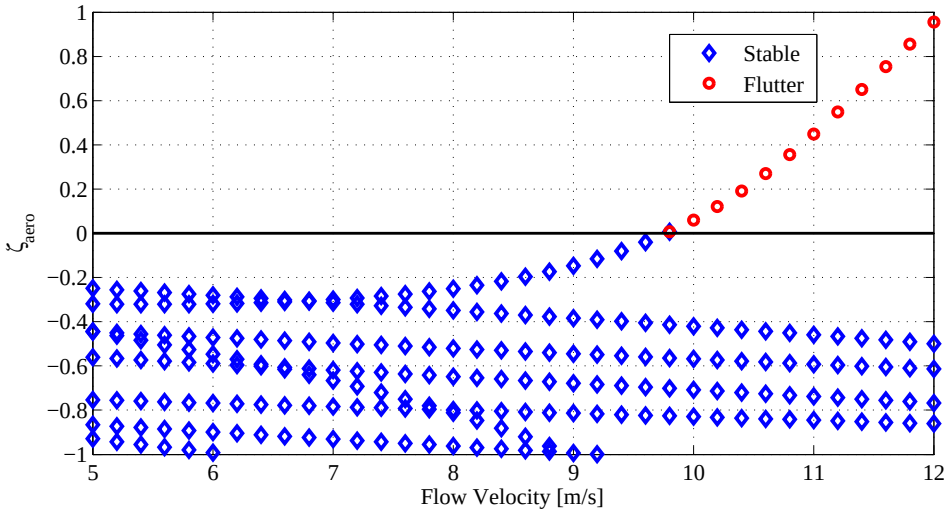

(a) Aerodynamic Damping Ratio vs. Flow Velocity

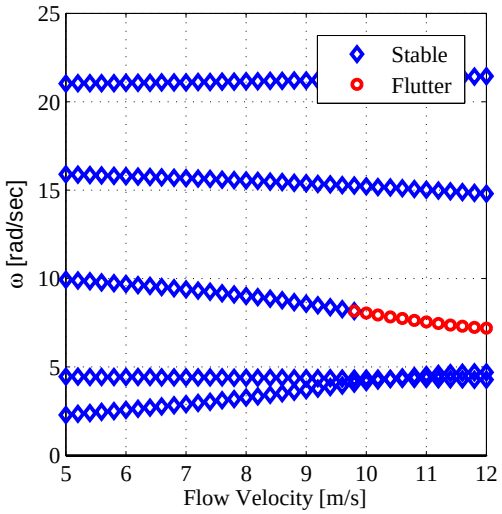

(b) Frequency vs. Flow Velocity

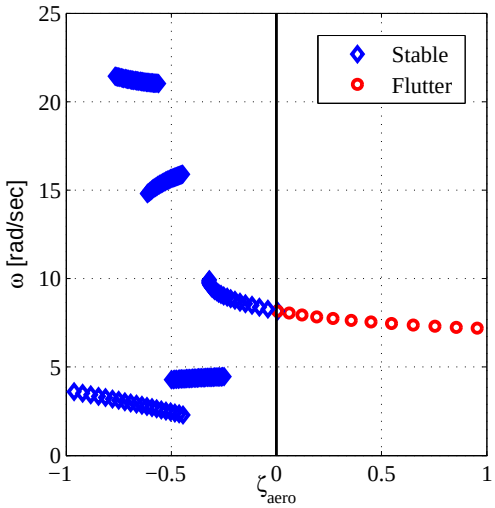

(c) Root Locus

FIGURE 4.2: Aeroelastic Eigenvalues for CFFF (Configuration 1) Plate

the code interpolates to determine the stability boundary. The largest change in response was for Configuration 6 which has the trailing edge free and all other sides clamped. For this configuration the aeroelastic damping ratio crosses the stability boundary with a shallow slope so increasing the structural damping by 0.01 increased the flutter boundary by 10%.

Additional numerical simulations are computed for Configurations 4 and 6 with

Table 4.2: Various Boundary Condition Membrane Aeroelastic Results ($\zeta_s = 0.02$)

Configuration	Type	Velocity [m/s]	Frequency [hz]
1 (CFFF)	Flutter	9.78	8.27
2 (FCFF)	Flutter	7.71	3.92
3 (CFCF)	Divergence	18.01	–
4 (FCFC)	Flutter	18.35	23.29
5 (CFCC)	Divergence	20.85	–
6 (CCFC)	Flutter	23.33	23.86

Table 4.3: Various Boundary Condition Membrane Aeroelastic Results ($\zeta_s = 0.03$)

Configuration	Type	Velocity [m/s]	Frequency [hz]
1 (CFFF)	Flutter	10.15	8.03
2 (FCFF)	Flutter	7.90	3.83
3 (CFCF)	Divergence	18.06	–
4 (FCFC)	Flutter	19.36	22.96
5 (CFCC)	Divergence	20.88	–
6 (CCFC)	Flutter	25.73	24.16

different values of applied tension. These are discussed along with the structural dynamics and aeroelastic experimental results.

4.3 Experiment Setup and Results

4.3.1 Design of Experimental Setup

The primary experimental apparatus is a modular baffle structure that can apply a clamped boundary condition on one or more sides of a rectangular plate. The baffle also provides a means to streamline the flow that goes over the plate. A CAD rendering of the baffle design is shown in Fig. 4.3(a). The figure shows (1) the top baffle, (2) the bottom baffle, (3) the leading edge baffle, (4) the trailing edge baffle, and (5) the connector pieces that link the individual baffle sections. Each baffle section consists of a front and back structure, as well as a clamp that can be screwed on to constrain the test specimen. The manufactured and assembled baffle structure is shown in Fig. 4.3(b).

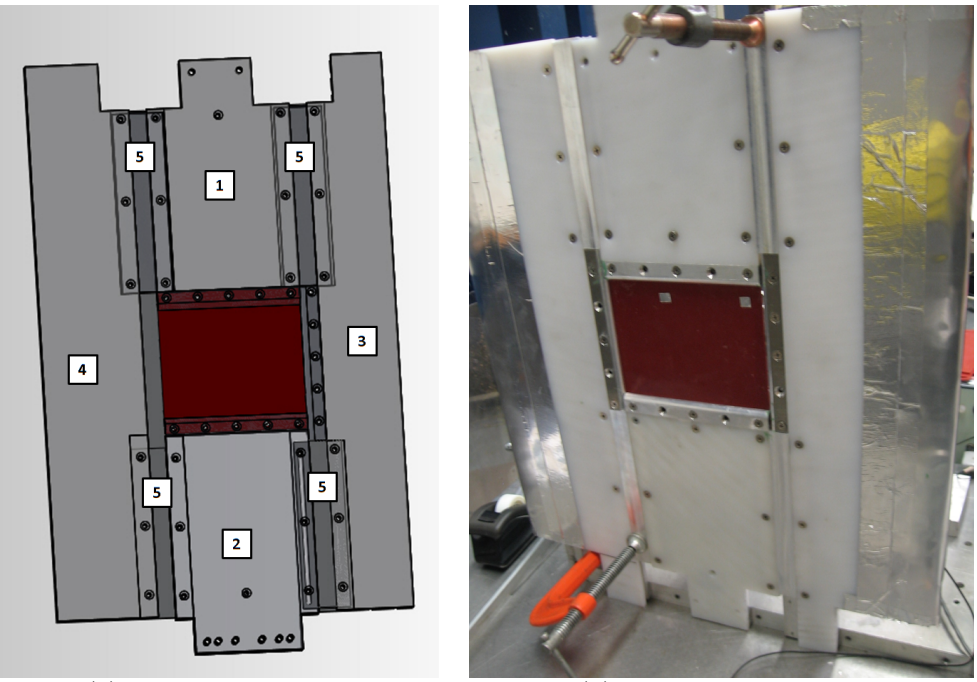

(a) Rendering of Baffle (b) Photograph of Baffle

FIGURE 4.3: CAD Rendering and Photograph of Assembled Baffle

Each baffle section also has a flange that can be secured to a fixed structure outside the wind tunnel. Therefore, each baffle section can be mounted in the wind tunnel individually, allowing all combinations of boundary conditions to be tested. The baffle also allows the plate to be tensioned by setting the strain. This is possible because the top and bottom baffles are designed to be able to slide with respect to the leading and trailing edge segments. From a practical point of view, some tensioning is necessary in order to avoid free play nonlinearities, but typically designs that use flexible plate membranes are deployed with some tension, so tensioning is a necessary feature for these types of studies.

4.3.2 Preliminary Tensile Tests on Membrane

The nominal properties (Bloomhardt and Dowell (2011)) of the red plate-membrane used in the studies are listed in Table 4.1. It should be noted that in the Reference (Bloomhardt and Dowell (2011)), the elastic modulus may have been reported in-

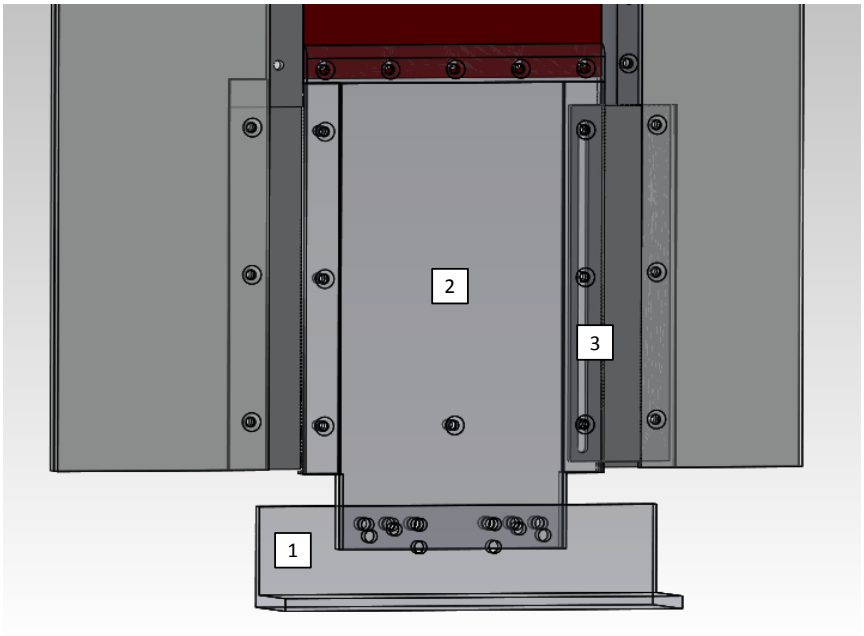

FIGURE 4.4: Closeup Of Tension Mechanism in the Baffle

correctly by an order of magnitude. The reference states a value of 1.84 MPa, but recent structural dynamics tests have shown that an elastic modulus of 18.4 MPa results in better agreement between theory and experiment. Before conducting the aeroelastic experiment, some simple tension tests are done to obtain estimates of the elastic modulus and Poisson's ratio in order to validate the given material properties. A material sample is secured in an axial load cell, and the load cell is used to pull on the sample to apply a measurable amount of tension. The sample has a length of 11.35 cm, and a width of 1.27 cm. The axial strain (change in length) and transverse strain (change in cross sectional width) are then measured to calculate a stress-strain curve as well as to estimate Poisson's ratio. Figure 4.5 shows the stress-strain plot for one of the trials of the tensile test. The results are shown up to a strain of 5%. Some nonlinearity can be observed in the curve.

The variation in the elastic modulus with respect to strain is calculated from taking the derivative of the stress-strain curve obtained from the axial load cell data. The results are summarized in Fig. 4.6. The stiffness is about 17 MPa for very low

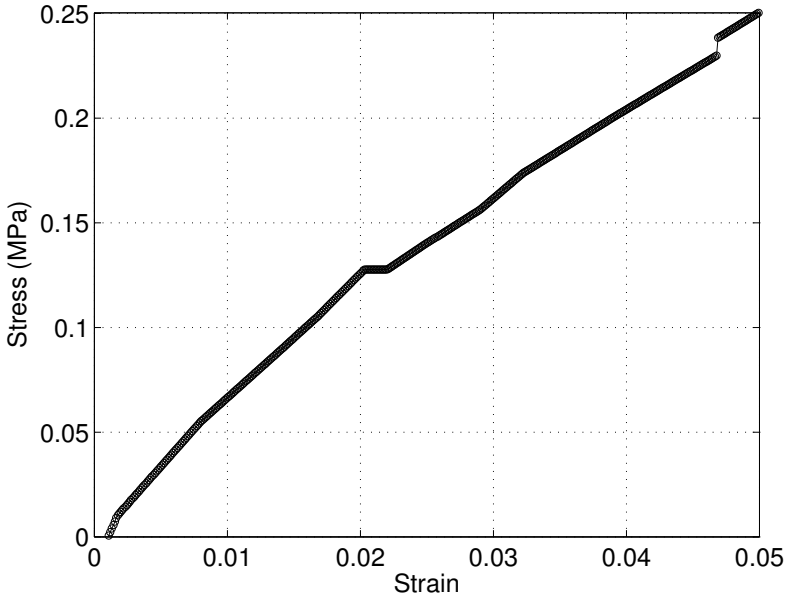

FIGURE 4.5: Example of Measured Stress Strain Curve for NASA Plate

strain, and then averages around 5 MPa for higher strains. Note that tensile tests may not give the same results for the elastic modulus as structural dynamics testing. In fact, for the ground vibration testing stiffness value of 18.4 MPa is used. Typically for the purposes of aeroelastic analysis, the elastic modulus obtained from structural dynamics testing would be more appropriate. Nevertheless, a general trend observed from tensile testing is that the stiffness decreases with increasing strain.

Poisson's ratio is estimated by measuring the transverse dimension (width) of the sample cross section under tension, and calculating the ratio of transverse strain to axial strain. Three separate trials were conducted. This is a rough estimate because it does not account for the curvature of the sides of the test sample as it is stretched, and the error in the transverse strain measurement may be large. These reasons likely cause unrealistic values of Poisson's ratio that are greater than a half. The results for Poisson's ratio, shown in Fig. 4.7, suggest that the Poisson's ratio is near 0.5 on average, which is expected of elastic polymers.

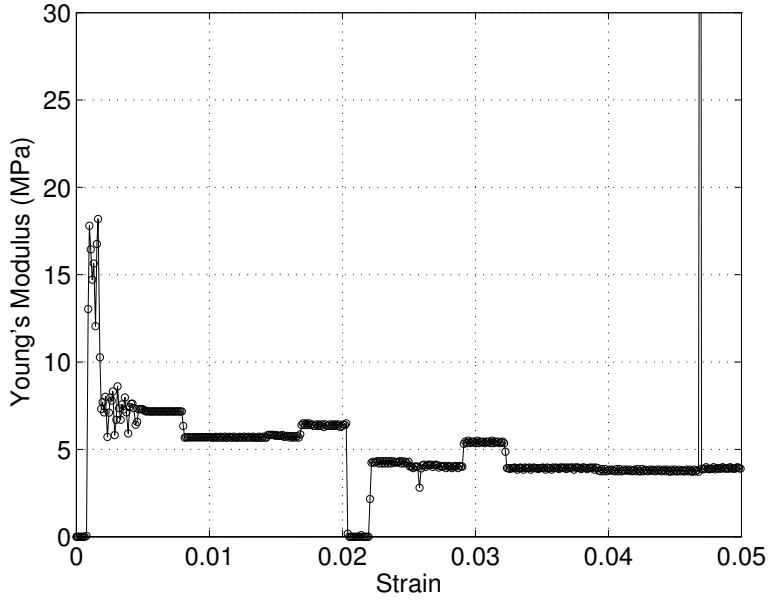

FIGURE 4.6: Estimated Elastic Modulus vs Axial Strain for NASA Plate

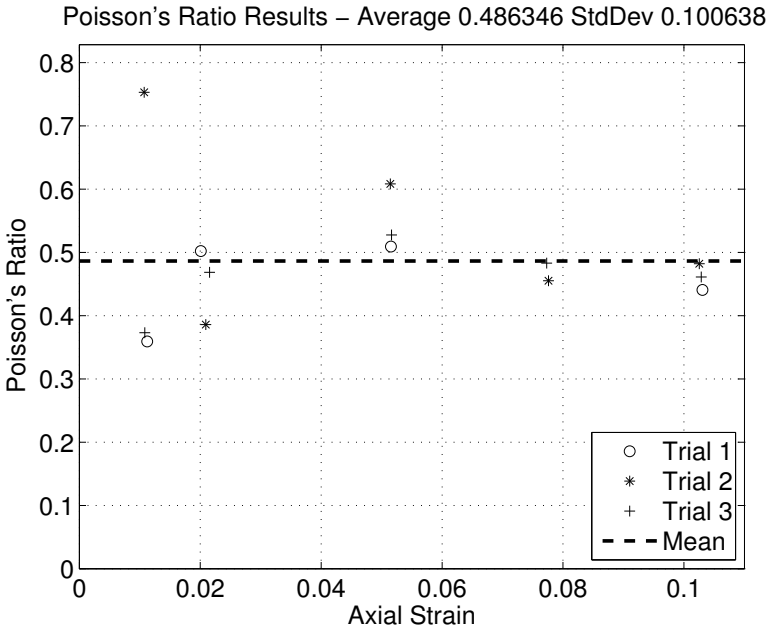

FIGURE 4.7: Estimated Poisson's Ratio NASA Plate

4.3.3 Structural Dynamics Results

Structural dynamic experiments are done to measure the natural frequencies and mode shapes of the plate under different boundary conditions. A photograph of the experimental set up is shown in Fig. 4.8. The set up consists of (1) the plate secured inside the baffle, (2) clamps that secure the baffle to a stationary structure, (3) an electromagnetic shaker that is clamped to a stationary structure and attached to the plate using wax, and (4) a laser vibrometer that points at a location on the plate and gives the velocity of that point. Impact testing is done first without the shaker to obtain the natural frequencies. Additional experiments are then conducted in which the plate is excited by the shaker with a sine sweep. Then the transfer function is calculated using a spectrum analyzer from the data, and the peaks in the transfer function are also identified as the natural frequencies. The primary purpose of the shaker tests is to excite the plate at natural frequencies such that the mode shapes can be observed. The experimental results of impact tests and shaker tests agree well on average and are also in good agreement with the theoretical predictions.

Figure 4.9 shows the predicted frequencies with a black line and the measured natural frequencies with a red circle, organized by the mode shape, for Configuration 1 with leading edge clamped and all other edges free. The theoretical frequencies are only defined at integer mode numbers, however they are connected in Fig. 4.9 to distinguish them from the experimental values. The mode shape designation contains the mode numbers in the stream-wise direction and the cross-flow (also noted as normal-to-flow) direction, respectively. For example, the (2,1) mode is a combination of the second mode in the stream-wise direction and the first mode in the cross-flow direction. The far left figure shows the first three natural frequencies that exhibit the first mode in the cross-flow direction - the (1,1), (2,1), and (3,1) modes - the middle figure shows the first three natural frequencies that exhibit the

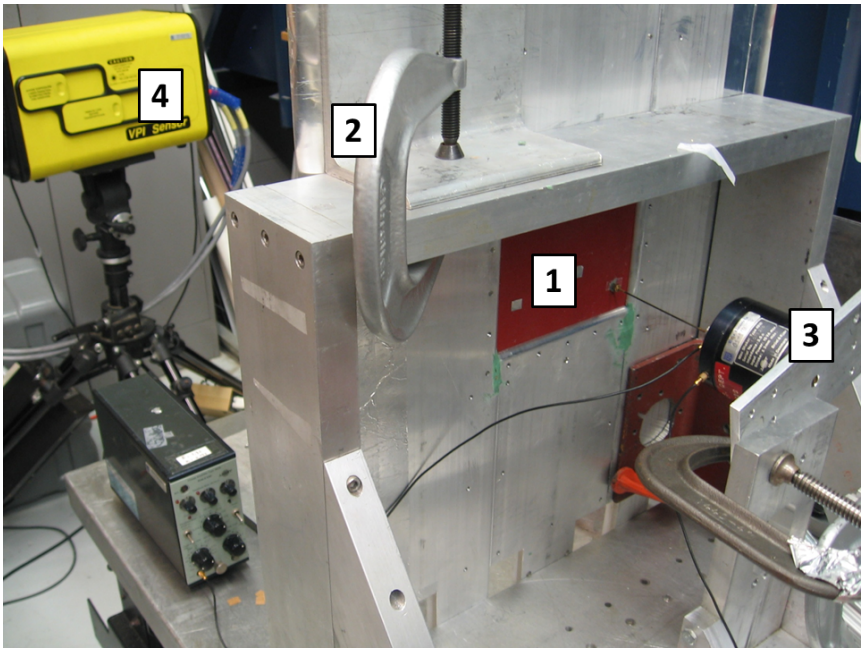

FIGURE 4.8: Natural Frequency Test for a Plate Clamped in the Baffle

second mode in the cross-flow direction - the (1,2), (2,2), and (3,2) modes - and the far right figure shows the first three natural frequencies that exhibit the third mode in the cross-flow direction - the (1,3), (2,3), and (3,3) modes.

Figures 4.10, 4.11 and 4.12 show the comparison of the theoretical and experimental natural frequencies for Configurations 2, 3 and 4 respectively. As with the CFFF (Configuration 1) results there is good agreement between the predictions and observations in magnitude and trend. The figures show that the more clamped edges the structure has, the higher the natural frequencies become. Also, as more edges become clamped and the frequencies increase, the amplitudes in the experiment become smaller making it difficult to identify the higher modes in the cross flow direction, hence, Fig. 4.12 only has comparisons for the first two modes in the cross flow direction. In general the difference between the theory and the mean of the experimental results is less than 10 %.

The final configuration with ground vibration results is Configuration 6 which

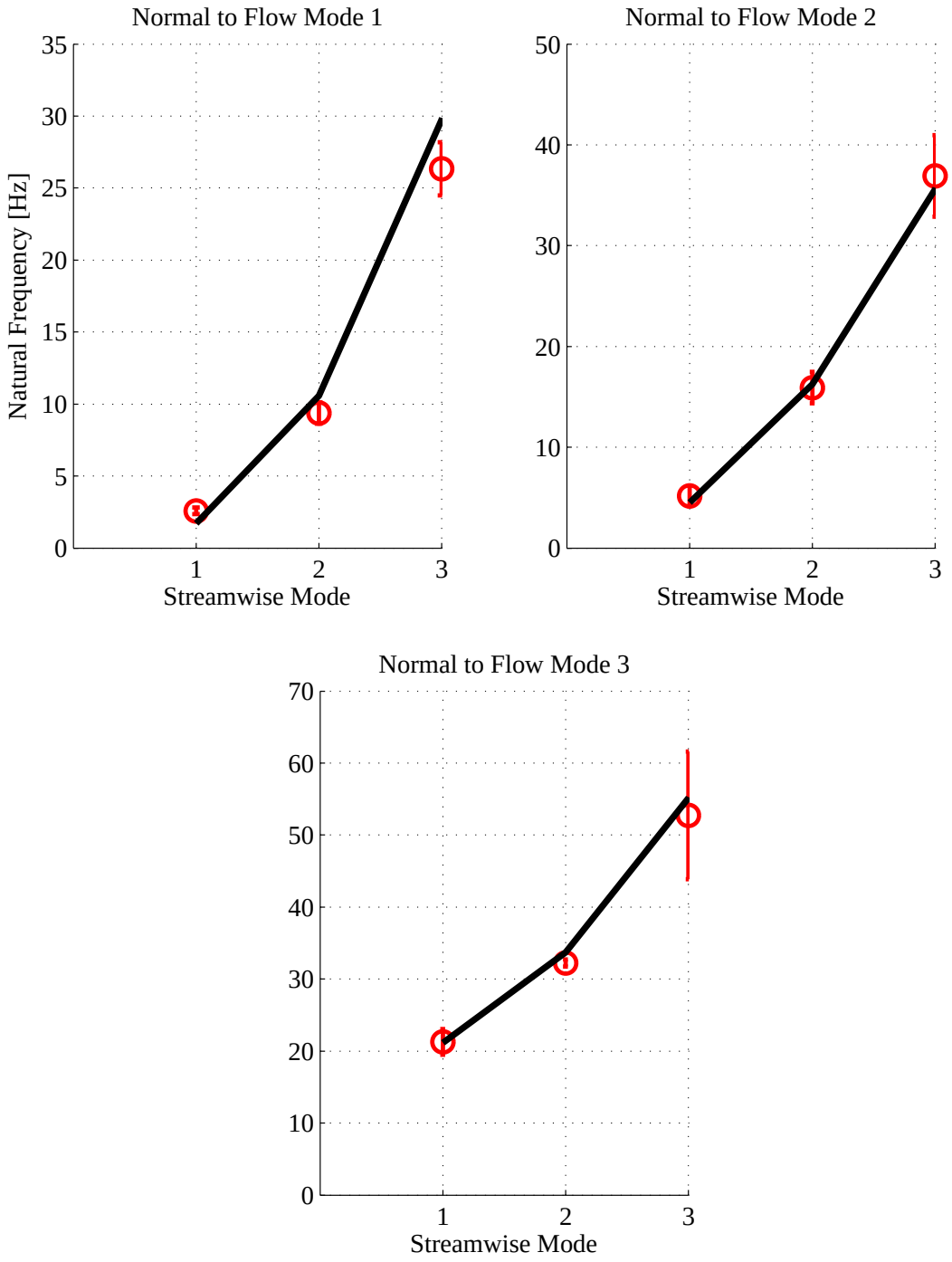

FIGURE 4.9: Natural Frequencies of the CFFF (Configuration 1) Plate: Theory and Experiment

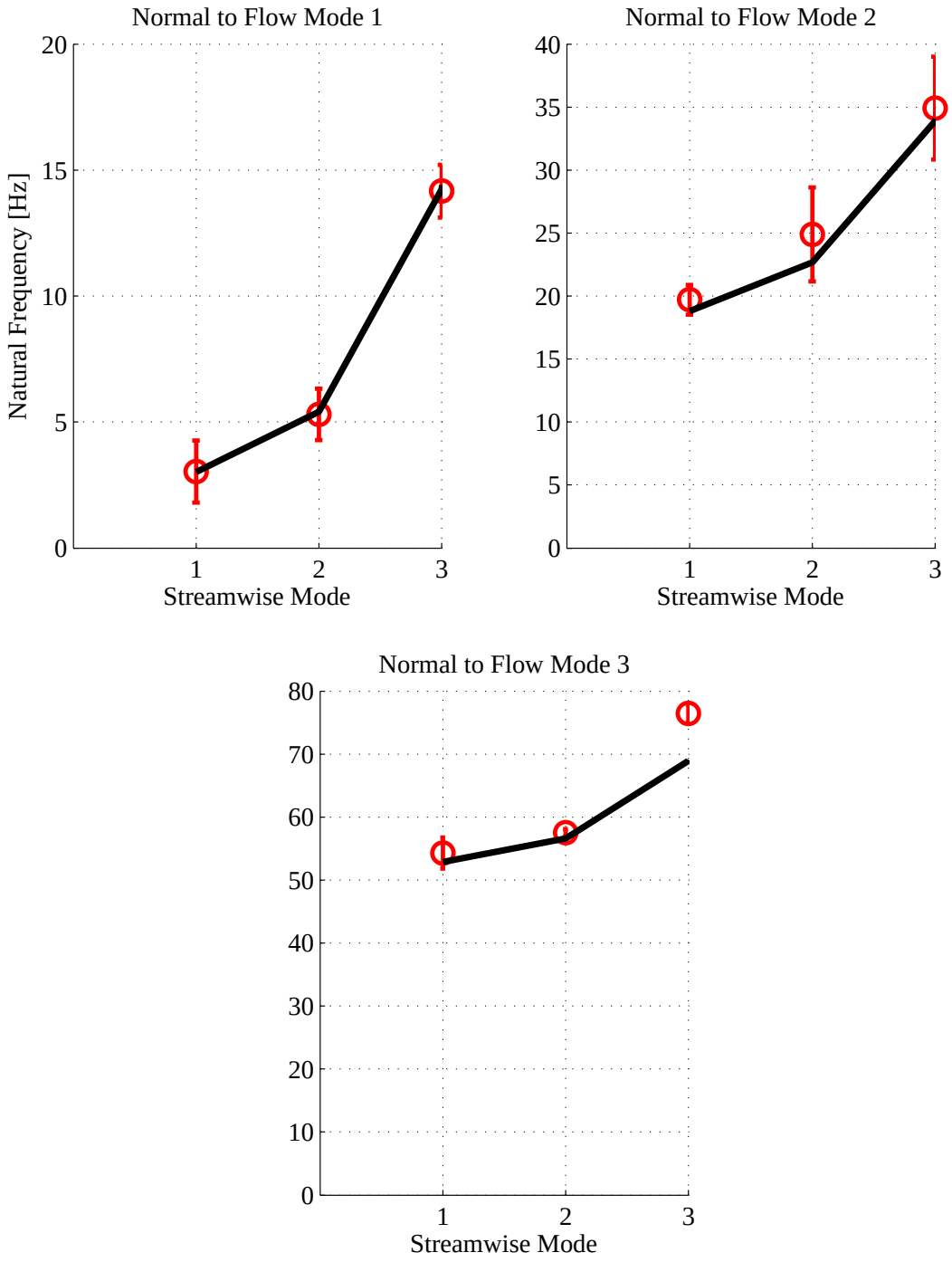

FIGURE 4.10: Natural Frequencies of the FCFF (Configuration 2) Plate: Theory and Experiment

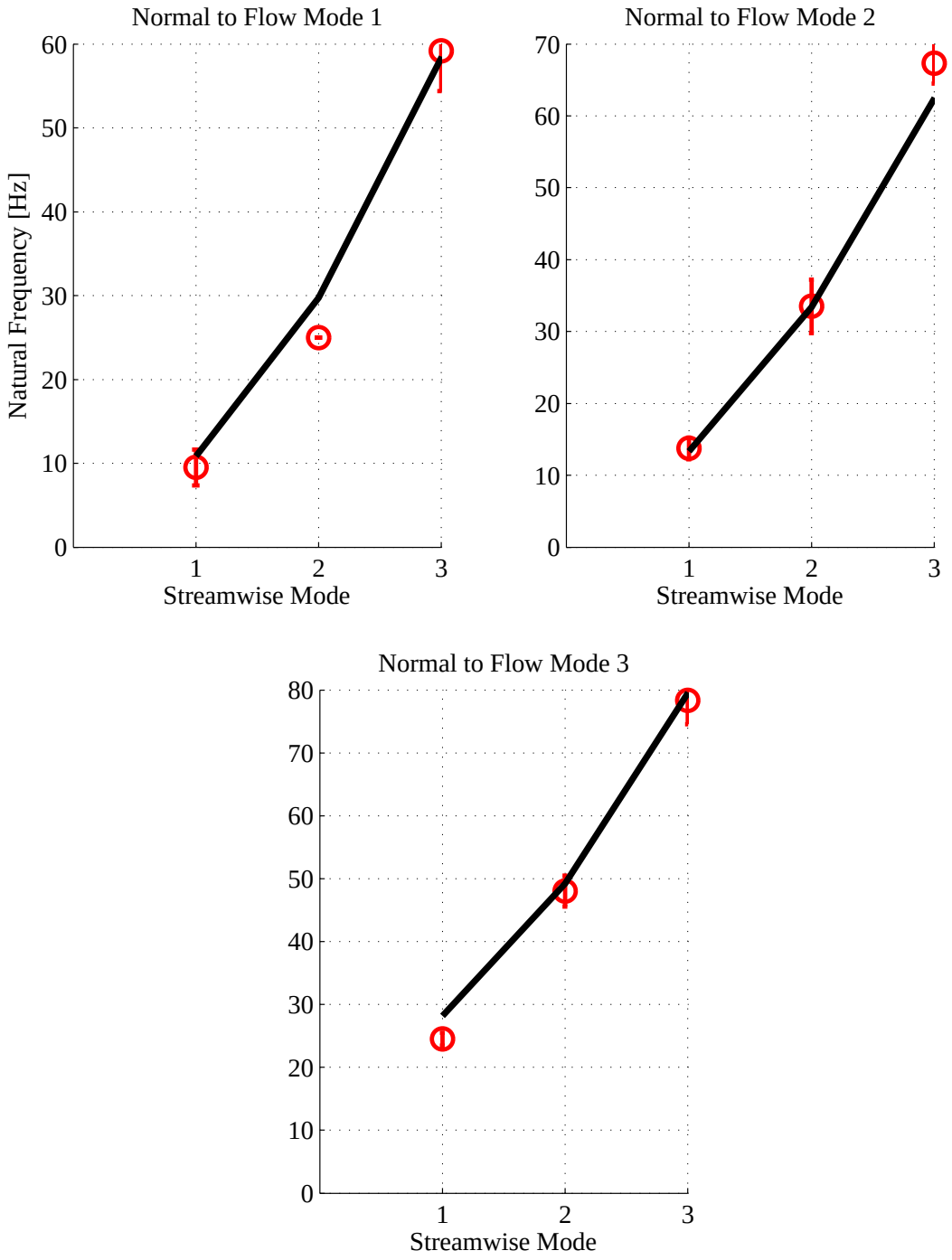

FIGURE 4.11: Natural Frequencies of the CFCF (Configuration 3) Plate: Theory and Experiment

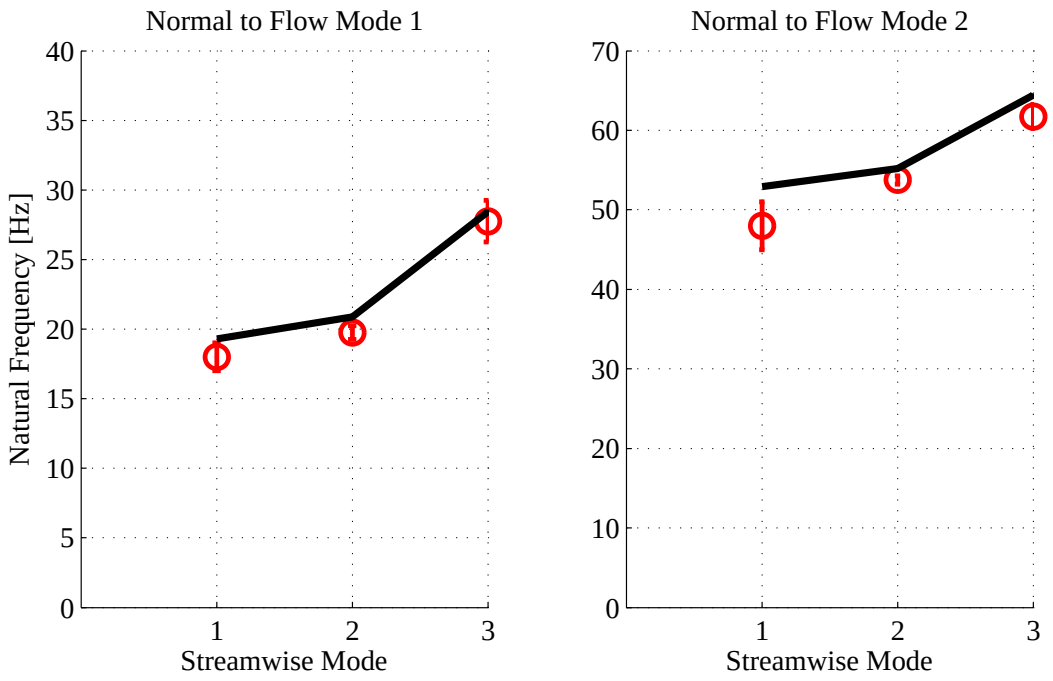

FIGURE 4.12: Natural Frequencies of the FCFC (Configuration 4) Plate: Theory and Experiment

has the trailing edge free and all other edges clamped. Figure 4.13 shows the ground vibration experiment results with no applied tension. Figure 4.14 shows the natural frequencies for the same configuration but with 200 N/m of tension in the cross-flow direction. Two other levels of tension, 56 N/m and 122 N/m, were also tested, and the difference between theory and experiment is within 10%. Overall, the results suggest that the theoretical model captures the fundamental structural dynamics behavior of this plate including tension in the cross-flow direction. In addition, the good agreement between theory and experiment with tension variation suggests that the natural frequencies can be used as a indicator of applied tension. The natural frequencies are easier to measure and can be measured more accurately than the applied strain. Therefore, in the following aeroelastic experiments, the first natural frequency is used to infer the applied tension.

The structural damping is estimated using the half power method (Thomson

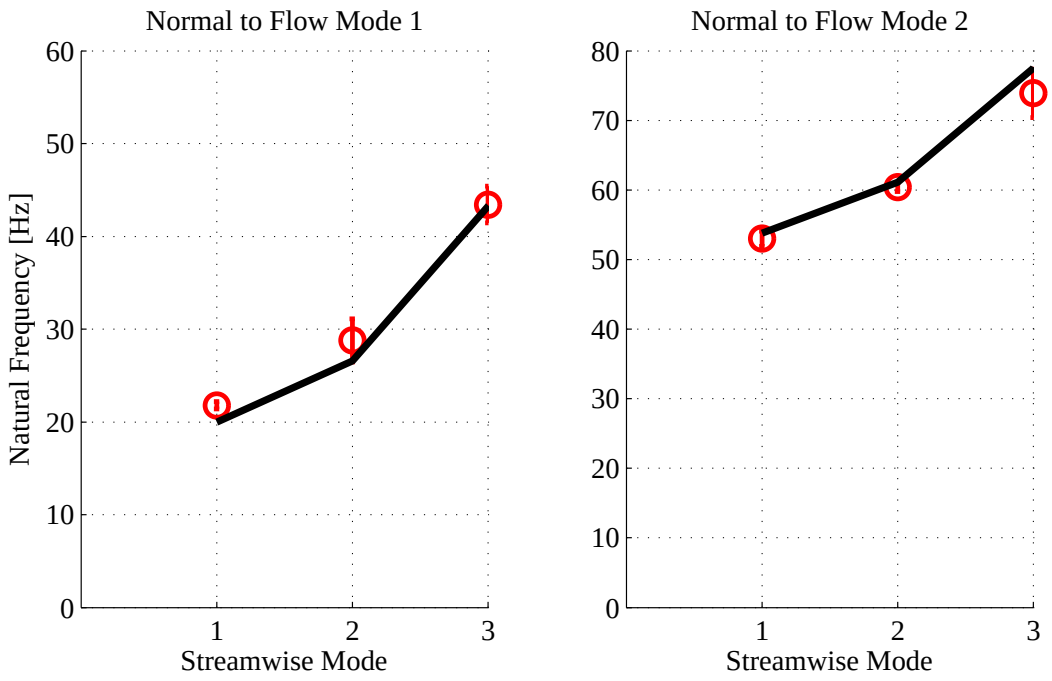

FIGURE 4.13: Natural Frequencies of the CCCF (Configuration 6) Plate: Theory and Experiment, No Tension

(1993), Wang (2011)). The results are only estimates because the half power method does not consider multiple-degree-of-freedom behavior, so each peak is treated as a single-degree-of-freedom response. The damping ratios for the first three modes are 3.6%±1.1%, 5.9%±1.6%, and 5.8%±2.0%. Even though the results are estimates, they do suggest high levels of structural damping that is typically not seen in metallic materials such as aluminum.

4.3.4 Aeroelastic Experiments

The aeroelastic experiments are conducted in the Duke University Wind Tunnel. The baffle is mounted in the wind tunnel and aligned with the flow direction. Figure 4.15 shows the entire baffle set up inside the wind tunnel. Even though the present study does not test the configuration with all edges clamped, this figure demonstrates the approximate sizes of each baffle section.

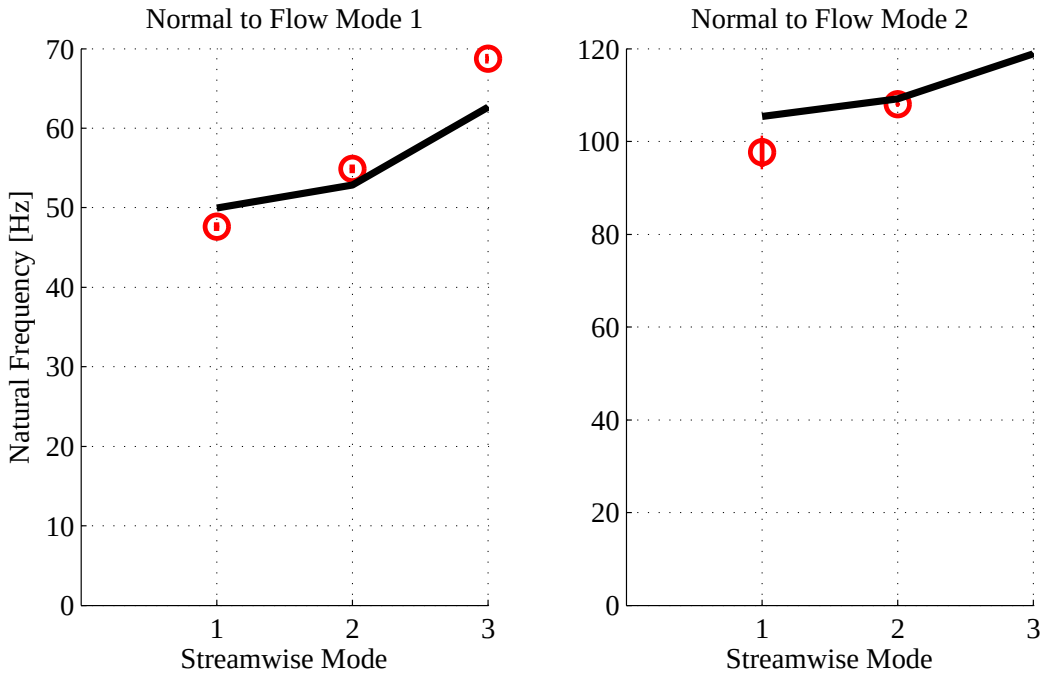

FIGURE 4.14: Natural Frequencies of the CCCF (Configuration 6) Plate: Theory and Experiment for Ty = 200 N/m

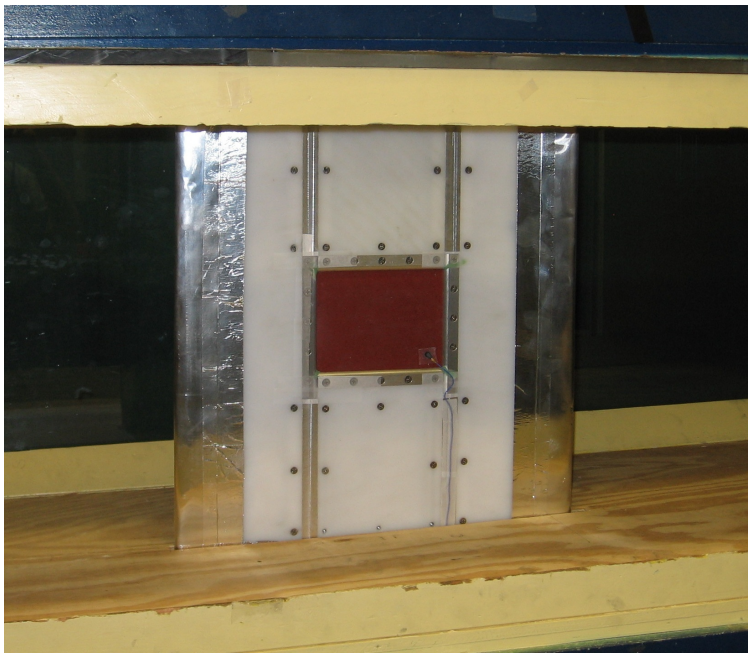

FIGURE 4.15: Photograph of Baffle in Wind Tunnel

Configurations 1 and 2

For Configuration 1, the weight of the plate and the lack of structural rigidity causes initial lateral buckling. This leads to some initial deformation, causing asymmetry in the flow field, as shown in Fig. 4.16. The aeroelastic experiments show that the plate flutters over a significant hysteresis band of air speeds and frequencies. The results are under column Config1a in Table 4.4. Additional experiments were done where the membrane was carefully bent back to be as flat as possible. This significantly reduced the hysteresis band, and moved the flutter boundary results closer to the predicted values. These results are under column Config1b in Table 4.4.

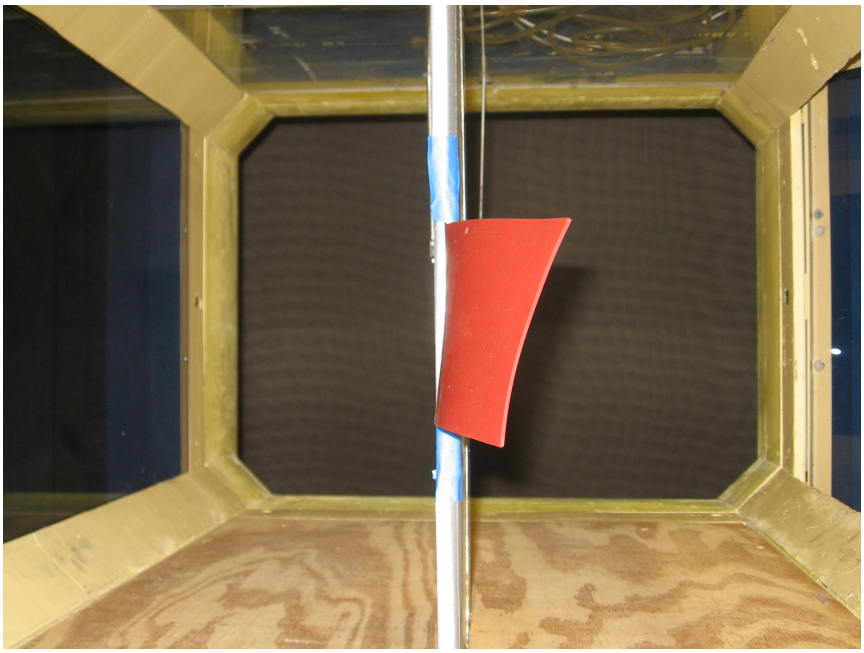

FIGURE 4.16: Photograph of CFFF (Configuration 1) with Lateral Buckling

For Configuration 2, which is the wing configuration with the upper edge clamped, the flutter region lies in a small hysteresis band. The results are in good agreement with theoretical predictions, as shown in Table 4.4. Configurations 1 and 2 are the well-understood panel flutter and wing flutter configurations, respectively. Obtaining good agreement between theory and experiment for these two configurations serves

Table 4.4: Various Boundary Condition Membrane Flutter Experiment Results for Configurations 1 and 2

	Config1a	Config1b	Config2
Upper Flutter Speed (m/s)	17.5	10.5	8.9
Lower Flutter Speed (m/s)	5.9	8.8	7.8
Theory Flutter Speed (m/s)	9.78	9.78	7.71
Upper Flutter Freq (Hz)	8.2	6.5	3.7
Lower Flutter Freq (Hz)	3.8	6.0	4.2
Theory Flutter Freq (Hz)	8.27	8.27	3.92

as validation before exploring other configurations.

Configuration 4

This section presents the experiments for Configuration 4, which has the top and bottom edges clamped and remaining edges free. Figure 4.17 shows the baffle structure without the leading edge and trailing edge sections, because only the top and bottom edges are clamped. The flow goes from left to right in the photograph.

For this configuration, flutter was near the predicted air speeds, and there was significant nonlinear behavior for some cases. Limit cycle oscillation amplitudes were about an order of magnitude higher than the thickness of the specimen. The flutter experiments are also conducted over a range of applied tension in the cross-flow direction, ranging from no tension to 50 N/m. Figure 4.18(a) shows the theoretical and experimental results for flutter speed versus applied tension, and Fig. 4.18(b) shows the flutter frequency versus applied tension.

The flutter speed trend is in good agreement with theoretical predictions. The flutter speed increases when the tension increases, as expected. Some of the measured flutter frequencies are in good agreement with theory, but some trials showed flutter frequencies that are much higher than, though not exactly twice, the expected flutter frequency. For those cases, there is also a smaller but distinct response near the expected flutter frequency denoted by the diamond symbols in Fig. 4.18(b). The

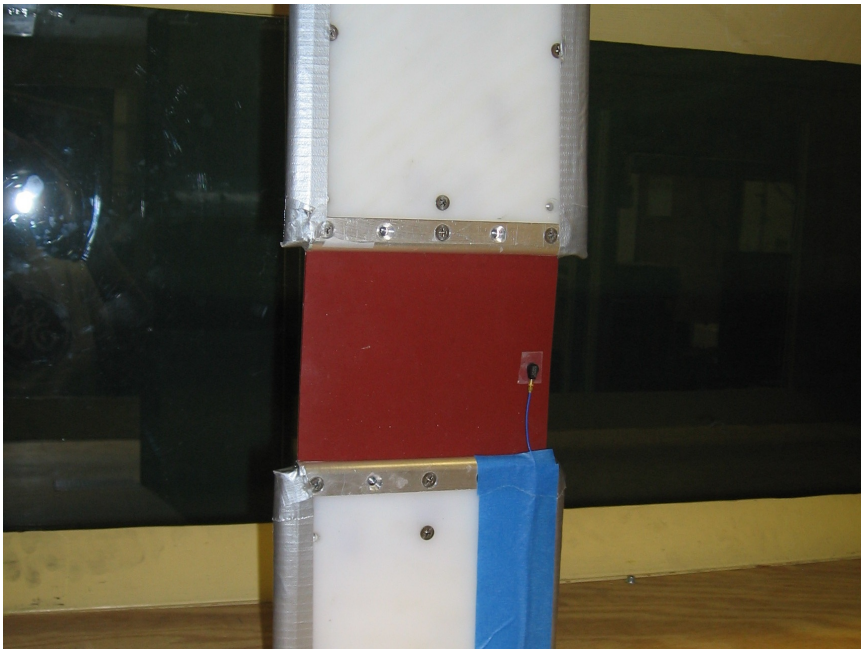

FIGURE 4.17: FCFC (Configuration 4) Experiment Specimen

presence of two frequencies in the limit cycle response indicates nonlinear behavior, which may be due to the out-of-flatness of the specimen. The out-of-flatness is caused by non-parallel edges due to misalignment between the top and bottom baffle sections, because the two sections are harder to align properly without either the leading or trailing edge baffle section as a guide. Figure 4.19 shows an example of the nonlinear response.

The flutter test results have an "upper" and "lower" velocity and frequency because of the experimental hysteresis. Figure 4.20 shows the RMS response (proportional to displacement) of the specimen as the air speed varies. The data point marks the flutter point as the air speed is increased, but the response dies out at a lower air speed when the air speed is reduced from the initial flutter speed. This may be due to nonlinear material properties for this particular test specimen, due to either nonlinear stress-strain relations or possibly viscoelastic effects since the material is rubber-like. However, the hysteresis band is small and the linear theory is able to

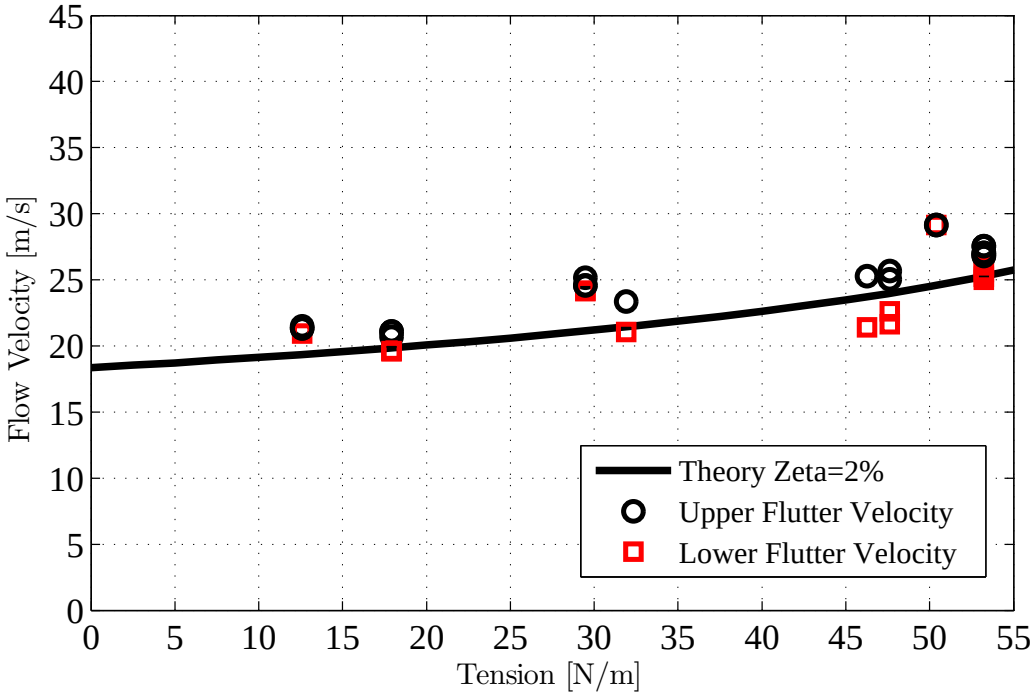

(a) Flutter Speed Results

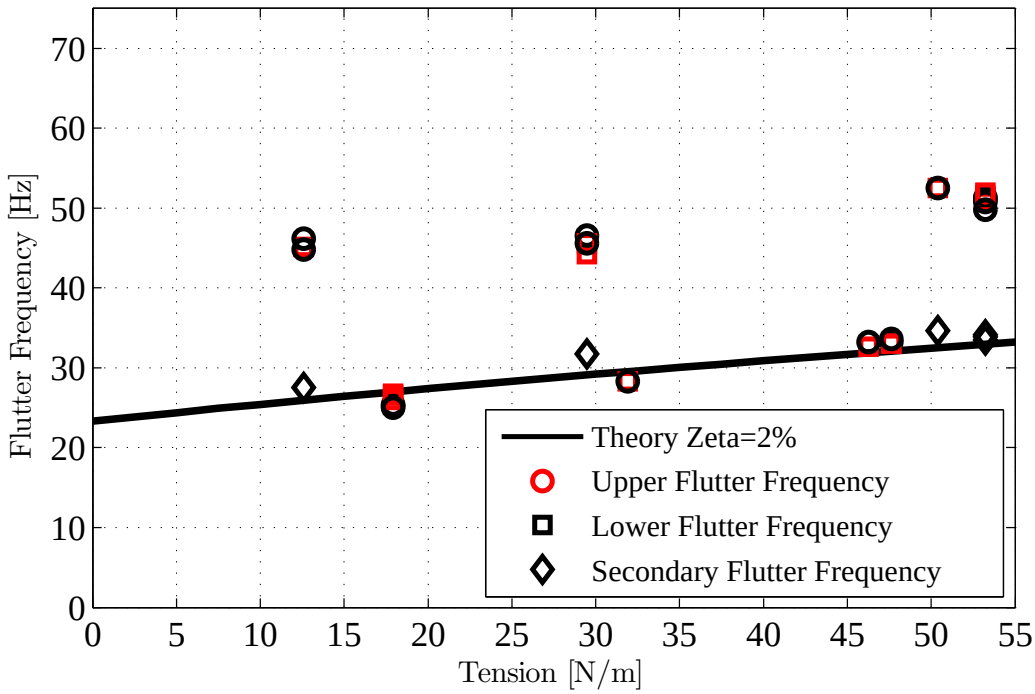

(b) Flutter Frequency Results

FIGURE 4.18: FCFC (Configuration 4) Aeroelastic Results

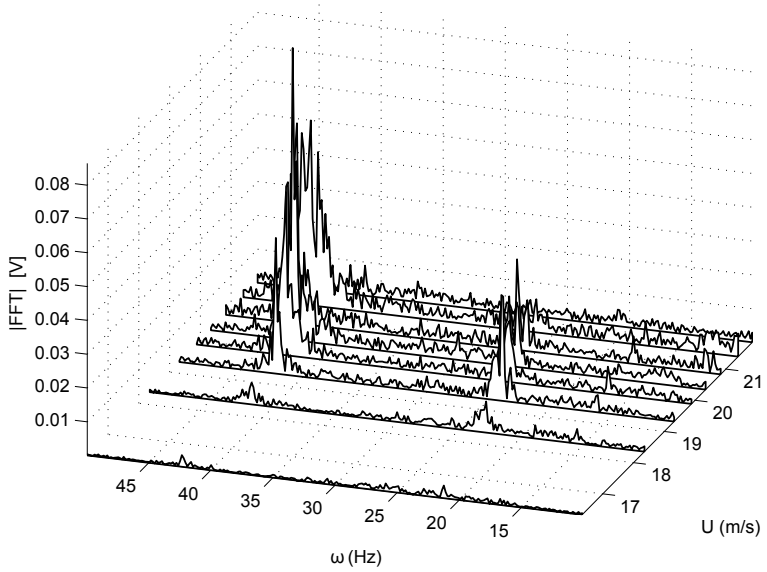

FIGURE 4.19: Waterfall for FCFC (Configuration 4) Showing Nonlinear Response

predict the flutter speed with good accuracy.

Configuration 6

This section contains the experimental results for Configuration 6, which has the trailing edge free and other edges clamped. This configuration is of particular interest due to the similarities to the NASA CML design. Figure 4.21 shows the baffle structure without the trailing edge section, since the trailing edge is free and the other three edges are clamped. The flow moves from left to right in the photograph.

In this case, experimental flutter occurs near the predicted air speeds and frequencies. Oscillation amplitudes were about 5 times the thickness of the specimen. The flutter experiments contain a range of applied tension in the cross-flow direction, ranging from no tension to 200 N/m. Figure 4.22(a) shows the theoretical and experimental results for flutter speed versus applied tension, and Fig. 4.22(b) shows the flutter frequency versus applied tension.

The flutter speed and frequency are generally in good agreement for moderate

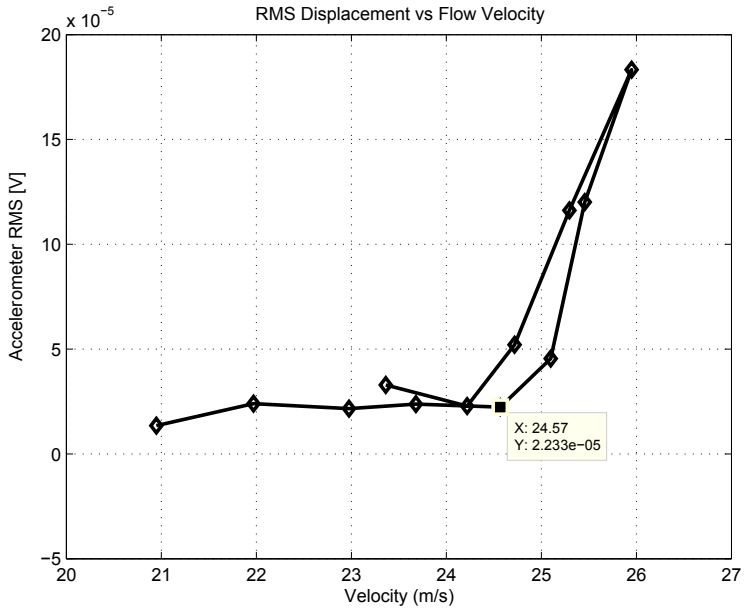

FIGURE 4.20: RMS Response for FCFC (Configuration 4)

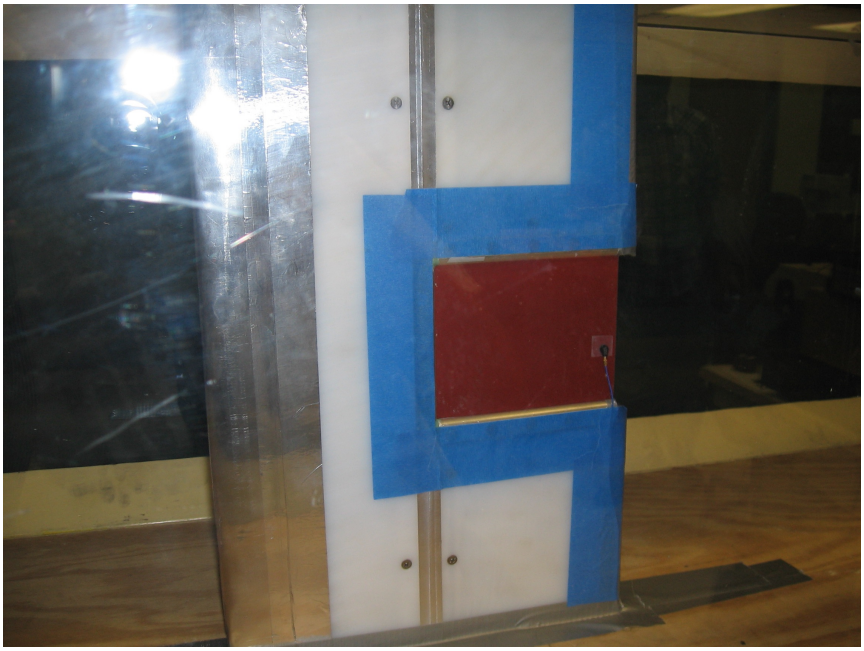

FIGURE 4.21: Experiment Specimen without Trailing Edge Section

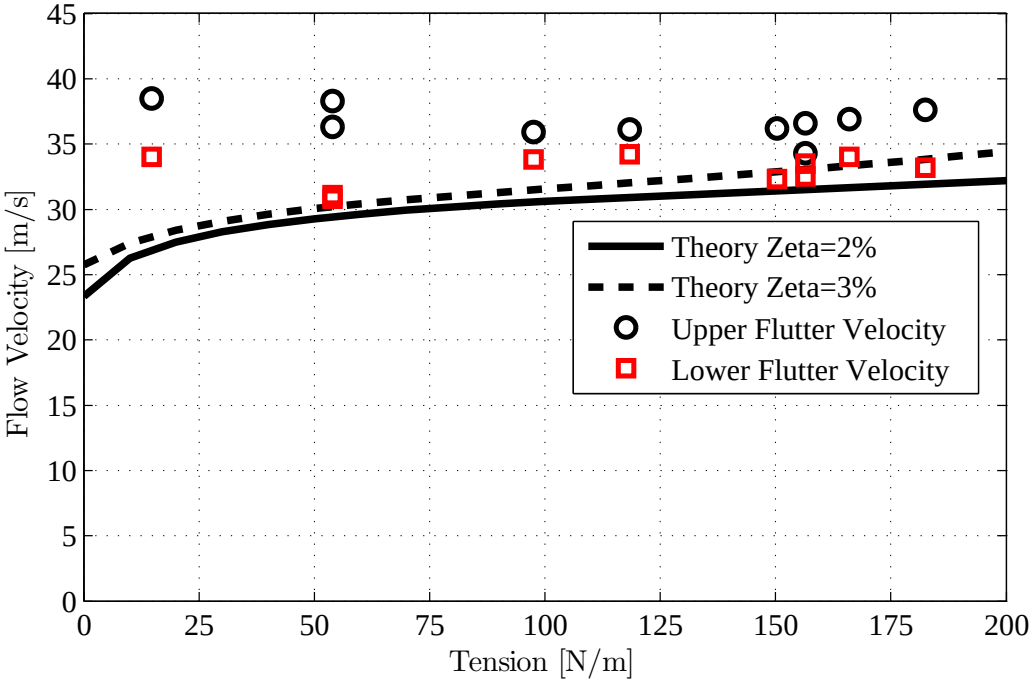

(a) Flutter Speed Results

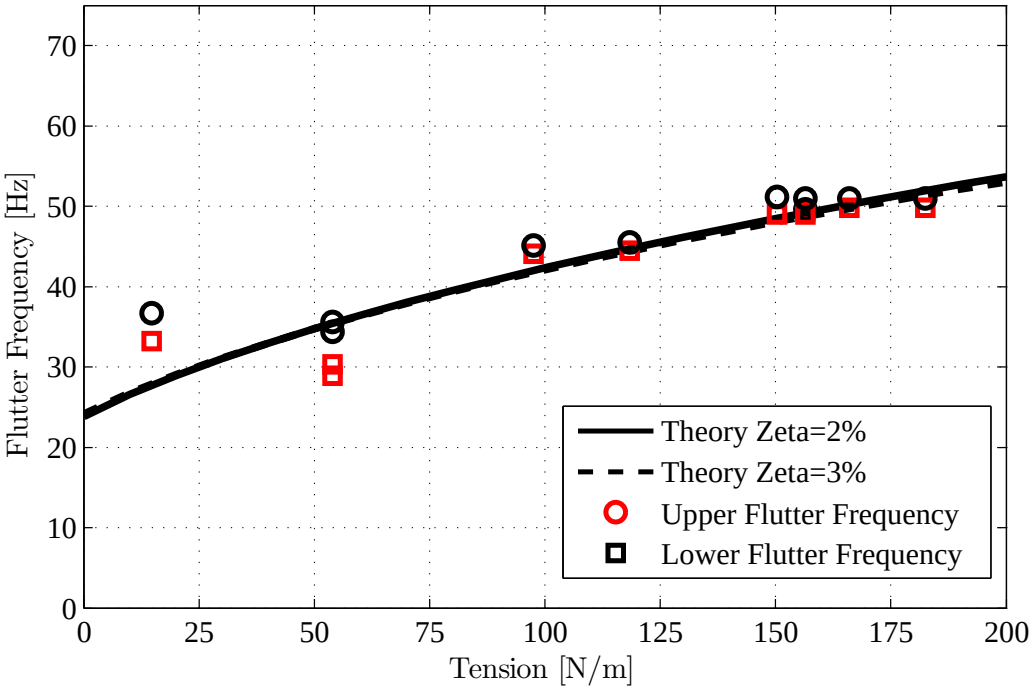

(b) Flutter Frequency Results

FIGURE 4.22: CCCF (Configuration 6) Aeroelastic Results

to high values of tension. Both flutter speed and frequency results are shown as an interval because hysteresis is observed in experiment, again likely a result of nonlinear material properties. At low-tension values, the geometric nonlinearities in the plate specimen lead to worse agreement between theory and experiment. Inherent curvature in the specimen, and static deformation from steady aerodynamic loads on the membrane due to slight misalignment between the baffle and the airflow, are both more pronounced at lower tension values and are on the order of the plate thickness. These sources of geometric nonlinearity are in turn more pronounced for plates that are clamped are more than one edge, because both the limit cycle amplitudes and the deformations are on the order of the plate thickness. The importance of having a flat specimen is well-known for the structural panel configuration with all sides clamped. This collection of experiments shows that the same effect is also important for the configuration with three sides clamped. A area of future work is to explicitly explore the effect of including an angle of attack for the structure from both a theoretical and experimental perspective. A non-zero angle of attack would lead to a lift on the structure causing the static deflections observed in the experiment. The static deflections may in turn increase the effective stiffness of the structure causing the larger flutter velocity observed in the experiment. Another potential source of the error is the uncertainty in the level of structural damping. In our theoretical exploration we showed that the flutter velocity of Configuration 6 was the most sensitive to changes in structural damping.

Interestingly, both the theory and the experiment predict that the flutter velocity will remain largely unchanged as the tension increases and the major contribution of the tension will be to increase the flutter frequency. This observation suggests that simply increasing the tension in the this configuration is not enough to improve the stability characteristics. This implies that simply increasing the tension in the NASA CML membrane which is geometrically similar to this configuration, may not

be the best way to increase the flutter velocity.

Configurations 3 and 5

The theory predicts that divergence occurs for both configurations 3 and 5 at a flow velocity of 18.0 m/s and 20.9 m/s, respectively. Figures 4.23(a) and 4.23(b) show the experimental set ups for the two configurations. The two configurations are tested in the wind tunnel, and no self-sustaining oscillations were observed up to an air speed of 40 m/s, which agrees with the theoretical prediction that flutter does not occur. The air speed was not increased past 40 m/s because it pushes against the limitations of the wind tunnel. However, no clear indication of divergence was observed either. For both configurations, static deformation was observed at high air speeds, but it is not clear whether the deformation comes from divergence or from the steady state aerodynamic loads on the specimen due to small nonzero angles of attack of the specimen in the air flow. The inability to observe a specific divergence onset may be due to the flexible nature of our specimen as the literature contains multiple examples of researchers observing an abrupt divergence for more stiff panels with the leading and trailing edge constrained (Ishii (1965), Gislason (1971)).

Two methods were attempted to measure the displacement of the specimen. One is to numerically integrate the accelerometer or laser velocity meter data to obtain position, but noise in the data caused the integrated displacement to drift far from reasonable values. Another method is to use a strain gauge to measure strain on the specimen. However, the strain gauge does not stick easily to the specimen because of the specimen's smooth and rubber-like surface. For future experiments, an effective method for measuring displacement is to use a laser displacement meter pointing at the location at which the most displacement is expected to occur, which is typically in the center of a free edge of the specimen.

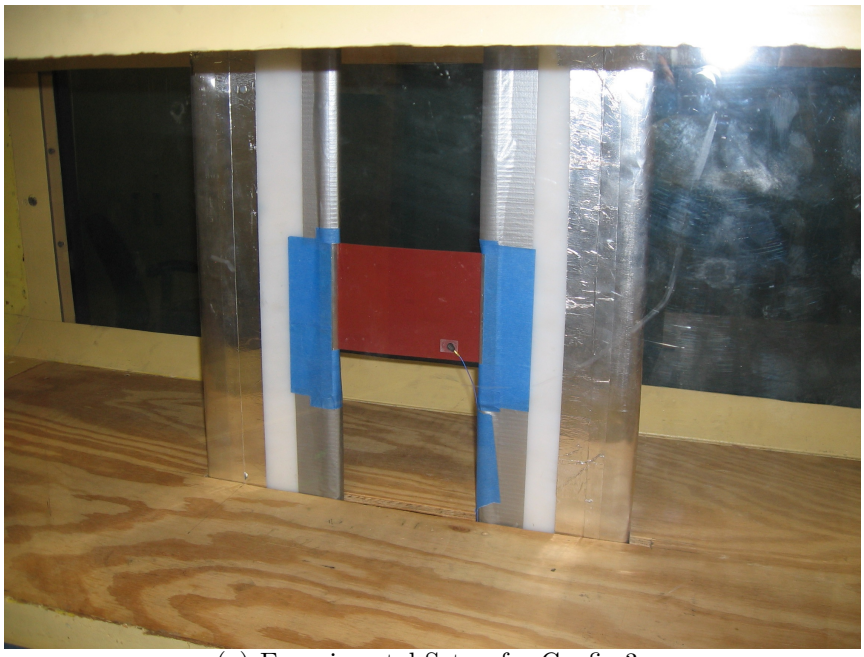

(a) Experimental Setup for Config 3

(b) Experimental Setup for Config 5

FIGURE 4.23: Experimental Setup for Configurations 3 and 5

4.4 Conclusions for the Stability of Membranes with Various Boundary Conditions in Subsonic Flow

This chapter summarizes the theoretical model and experimental set up for studying the aeroelastic behavior of plate-membranes for a variety of boundary conditions. The modular experimental set up offers a convenient method for changing the boundary conditions of the plate. The experimental results show that the structural model is accurate for different boundary conditions and different amounts of tension in the cross-flow direction. The aeroelastic results show that the wing and panel flutter cases behave as predicted. Two additional cases, the case with trailing edge free and the case with both leading and trailing edges free, both exhibit flutter near the predicted flutter speed, but the response is more nonlinear especially for the case with both leading and trailing edges free. Much of the nonlinearity may be attributed to geometry nonlinearity in the specimen, due to inherent curvature as well as steady state aerodynamic loads that deform the specimen if the specimen is not perfectly aligned with the flow. A nonlinear theoretical model is not developed to confirm this hypothesis. Finally the theory predicts divergences for the cases with the leading and trailing edges restrained. Our current experiment setup did not allow us to observe the divergence instability.

Future Work

1. **Different, Stiffer Specimens**: A stiffer material such as aluminum may be tested to minimize the nonlinear effects of static loadings.

2. **Additional Non-geometric Boundary Conditions**: Future work will include an exploration the effect of different support structure orientations on aeroelastic behavior of plates. Due to the low natural frequencies of the membranes, one might expect the dynamics of the structure to which the membrane is attached to, such as an aircraft wing, to affect the dynamics and stability

of the flexible plate. Future work is under way to incorporate the support structure dynamics into the aeroelastic model (Wang et al. (2013)).

3. **Divergence Experiments**: With our current setup we were not able to validate the divergence predictions. A future tasks might include using a laser displacement sensor to better study the deformation of the two configurations that are expected to undergo divergence, and obtaining better aeroelastic experimental results for low tension specimen by carefully adjusting the baffle orientation to minimize static angle of attack.

5

Stability of a Restrained Plate / Membrane in Space

In this chapter we transition from looking at aeroelastic systems to solarelastic systems. While the analysis techniques are similar, the following three chapters look at the research on the stability of structures with applications for solar sails. This research is motivated by the recent interest in solar sail propulsion by space agencies around the world. As mentioned in the introduction, NASA will launch the Sunjammer solar sail towards the sun in 2016. For solar sails such as the Sunjammer, increasing the spacecraft performance has driven designers to implement extremely thin reflective membranes. For these membranes, much of the stiffness is derived from the tension provided by rigid inflatable booms. While the governing structural equations take the same form as the equations explored in the previous section, for the space membrane a different set of terms dominate the structural stiffness.

In this chapter we analyze the stability of a rectangular solar sail membrane by adapting the techniques presented in Spriggs et al. (1969) and Dowell and Ventres (1970). In particular we provide a framework for analyzing the stability of a re-

strained solar sail membrane where either the aspect ratio or the ratio of the tension to the bending stiffness is large. In particular the results are applied to explore the stability of a panel similar to the panels found on the Sunjammer solar sail.

5.1 Model

We will consider the problem of the Sunjammer membrane. The Sunjammer uses four inflatable booms to restrain the reflective membrane structure. The inflatable booms are connected by streamers at approximately one meter spacing. The sail material is then connected to the booms and the streamers. Figure 5.1 contains a picture of a ground vibration test done on a prototype for the Sunjammer. The figure shows the scalloped membrane created by draping the membrane over the streamers. Of particular interest, is the stability of an individual panel of this structure. Figure 5.1 highlights the section of the Sunjammer that we will explore. We will approximate the panel that lies between two streamers and in a single quadrant of the solar sail as a restrained rectangular plate/membrane that is pinned along its long edge, simulating the attachment to the streamers, and clamped and under tension along its short legs simulating the attachment to and the tension provided by the booms. In reality the booms and the streamers are also elastic membranes that are subject to deformations due to the forces on the structure.

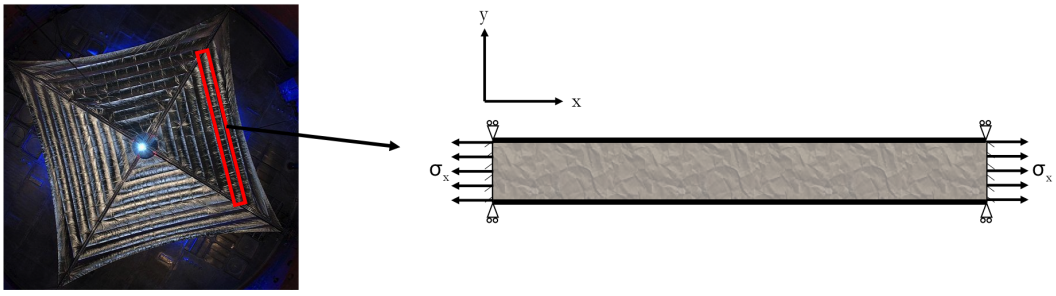

FIGURE 5.1: Structural Schematic of the Sunjammer Panel

For our theoretical model we couple the plate structural model from Eq. 2.24

with the solar radiation pressure model presented in Section 2.2.2. When we combine the models we are able to write out the governing equation as follows:

$$E'h^3\left[\frac{\partial^4 w}{\partial x^4}+2\frac{\partial^4 w}{\partial x^2\partial y^2}+\frac{\partial^4 w}{\partial y^4}\right]-\sigma_x h\frac{\partial^2 w}{\partial x^2}-\sigma_y h\frac{\partial^2 w}{\partial y^2} \\ +P_o\sin 2\gamma(\frac{\partial w}{\partial y}\sin\psi-\frac{\partial w}{\partial x}\cos\psi)+\rho_s h\frac{\partial^2 w}{\partial t^2}=P_o\cos^2\gamma \tag{5.1}$$

It is not practical to solve this equation using the modal expansion technique commonly used in our aeroelastic analysis due to the prohibitively large number of modes required to reach a converged solution. When attempting to directly solve the equations with this technique we observe a non-uniformly converging stability boundary. The problems arise due to multiple length and force scales that are important at different locations on the structure. For the solar sail membranes, the tension terms dominates the stiffness throughout most of the domain. However at small boundary layers the bending dominates the stiffness and plays an important role in determining the stability of the system. As mentioned in the introduction this is a phenomenon that has been observed in the aeroelastic literature for the stability of membranes in supersonic aerodynamic flows (Ellen (1965)). Fortunately, previous researchers have identified methods of determining the stability for these difficult cases. Spriggs et al. (1969) analyze the stability of a two-dimensional plate forced by supersonic flow modeled with piston theory. This system is described by the following equation:

$$E'h^3\frac{\partial^4 w}{\partial x^4}-\sigma_x h\frac{\partial^2 w}{\partial x^2}+\frac{\rho U^2}{M}\frac{\partial w}{\partial x}+\frac{\rho U}{M}\frac{\partial w}{\partial t}+\rho_s h\frac{\partial^2 w}{\partial t^2}=0 \tag{5.2}$$

The equations clearly contain many similarities to Eq. 5.1 that govern the sunjammer membrane. After describing the classic method of dealing with Eq. 5.2 we will outline how the analysis extends to the solar sail analysis. The aeroelastic equations can be

written in nondimensional form:

$$\epsilon^2 \frac{\partial^4 \tilde{w}}{\partial \zeta^4} - \frac{\partial^2 \tilde{w}}{\partial \zeta^2} + \lambda^2 \frac{\partial \tilde{w}}{\partial \zeta} + \beta \frac{\partial \tilde{w}}{\partial \tilde{t}} + \frac{\partial^2 \tilde{w}}{\partial \tilde{t}^2} = 0 \tag{5.3}$$

with

$$\epsilon^2 = \left(\frac{h}{a}\right)^2 \left(\frac{E'}{\sigma_x}\right) \tag{5.4}$$

$$\lambda^2 = \left(\frac{a}{h}\right)^2 \left(\frac{\rho U^2}{M \sigma_x}\right) \tag{5.5}$$

$$\beta^2 = \left(\frac{a}{h}\right)^2 \left(\frac{\rho U^2}{M \sigma_x}\right) \left(\frac{\rho}{\rho_s}\right) \tag{5.6}$$

Where the nondimensional length is $\zeta = x/a$, the nondimensional time is $\tilde{t} = (\sigma_x/\rho_s a^2)^{1/2} t$ and the nondimensional displacement is $\tilde{w}(\zeta, \tilde{t}) = w(x,t)/a$. The authors then introduce the following nondimensional variables motivated by balancing the inertial and aerodynamic forces.

$$\alpha^2 = \epsilon \lambda^2 \quad , \quad \gamma = \epsilon \beta \tag{5.7}$$

The authors assume the following solution:

$$\tilde{w}(\zeta, \tau) = g(\zeta) e^{k\tau} \tag{5.8}$$

where $\tau = \tilde{t}/\epsilon$. Substituting Eq 5.8 into Eq. 5.3 yields the equations analyzed in Spriggs et al. (1969).

$$\epsilon^4 \frac{d^4 g}{d\zeta^4} - \epsilon^2 \frac{d^2 g}{d\zeta^2} + \alpha^2 \epsilon \frac{dg}{d\zeta} + \left(\gamma k + k^2\right) g = 0 \tag{5.9}$$

After introducing these quantities, the authors determine the stability in terms of α, γ, and ϵ. The mathematical technique includes an asymptotic expansion in terms of ϵ for small ϵ and allowing for two length scales, one of order 1 and one of order ϵ near the membrane leading and trailing edge boundaries.

Now returning to the Sunjammer equations. For the Sunjammer we have a three dimensional structure with length a in the x-direction and length b in the y-direction. Nondimensionalizing equations Eq. 5.1 in the same manner as Eq. 5.3 and using $\eta = y/b$ yields:

$$\begin{aligned} E^2\left[\frac{\partial^4\tilde{w}}{\partial\zeta^4} + 2\tilde{h}^2\frac{\partial^4\tilde{w}}{\partial\zeta^2\partial\eta^2} + \tilde{h}^4\frac{\partial^4\tilde{w}}{\partial\eta^4}\right] - \frac{\partial^2\tilde{w}}{\partial\zeta^2} - R_y\tilde{h}^2\frac{\partial^2\tilde{w}}{\partial\eta^2} \\ + L\left[\tilde{h}\frac{\partial\tilde{w}}{\partial\eta}\sin\psi - \frac{\partial\tilde{w}}{\partial\zeta}\cos\psi\right] + \frac{\partial^2\tilde{w}}{\partial\tilde{t}^2} = 0 \end{aligned} \tag{5.10}$$

with $E^2 = (E'/\sigma_x)(h/a)^2$, $R_y = \sigma_y/\sigma_x$, $L = (P_o \sin 2\gamma/\sigma_x)(a/h)$, and $\tilde{h} = a/b$. In the previous equation we have also eliminated the inhomogeneous solar radiation term, because our goal is to determine the stability of the solarelastic system. For the linear system explored in this section the stability is not effected by the inhomogeneous term. We now have a partial differential equation in two spacial variables as well as the time variable. We now assume a single mode expansion of the displacement in the η-direction.

$$\tilde{w}(\zeta, \eta, \tilde{t}) = h(\eta)\hat{w}(\zeta, \tilde{t}) \tag{5.11}$$

where $h(\eta)$ is a beam mode shape that satisfies the boundary conditions in the η direction. Applying Galerkin's method and rearranging the equation to match Eq 5.3 yields:

$$\epsilon^2\frac{\partial^4\hat{w}}{\partial\zeta^4} - \frac{\partial^2\hat{w}}{\partial\zeta^2} + \lambda\frac{\partial}{\partial\zeta} + \epsilon^4 F\hat{w} + \left[\frac{c_o}{c_o - 2(h/a)^2(E'/\sigma_x)\tilde{h}^2 c_2}\right]\frac{\partial^2}{\partial\tilde{t}^2} = 0 \tag{5.12}$$

with

$$c_o = \int_0^1 h^2\, d\eta \quad c_1 = \int_0^1 \frac{dh}{d\eta}h\, d\eta \quad c_2 = \int_0^1 \frac{d^2h}{d\eta^2}h\, d\eta \quad c_4 = \int_0^1 \frac{d^4h}{d\eta^4}h\, d\eta \tag{5.13}$$

$$\epsilon^2 = \left[\frac{c_o}{(a/h)^2(\sigma_x/E')c_o - 2\tilde{h}^2 c_2}\right] \tag{5.14}$$

$$\lambda = -\frac{P_o \sin 2\gamma}{E'}\left(\frac{a}{h}\right)^3 \left[\frac{c_o}{(a/h)^2(\sigma_x/E')c_o - 2\tilde{h}^2 c_2}\right] \cos\psi \tag{5.15}$$

$$F = \tilde{h}^4 \frac{c_4}{c_o} - \frac{\sigma_y}{E'}\left(\frac{a}{h}\right)^2 \tilde{h}^2 \frac{c_2}{c_o} + \frac{P_o \sin 2\gamma}{E'}\left(\frac{a}{h}\right)^3 \frac{c_1}{c_o} \sin\psi \tag{5.16}$$

Comparing the ϵ^2 value from Eq. 5.14 to the value from Eq. 5.4, we see that the value can be driven to small values by either large tensions and small thicknesses, or by small aspect ratios ($1/\tilde{h}$). For the Sunjammer, because the aspect ratio is small we can apply this analysis technique even in the case of no applied tension.

Defining α in the same way as Eq. 5.7, introducing our corresponding time variable $\tau = (E/\epsilon^2)\tilde{t}$, substituting the assumed solution from Eq. 5.8 into Eq. 5.12 and multiplying through by ϵ^2 yields:

$$\epsilon^4 \frac{d^4\hat{w}}{d\zeta^4} - \epsilon^2 \frac{d^2\hat{w}}{d\zeta^2} + \alpha^2 \epsilon \frac{d\hat{w}}{d\zeta} + \left(\epsilon^4 F + k^2\right)\hat{w} = 0 \tag{5.17}$$

Eq. 5.17 is in the same form as Eq. 5.9 and therefore we can apply the results from Spriggs et al. (1969). To solve Eq. 5.17 we assume the following solution motivated by the solution for the pure membrane equation.

$$\hat{w}(\zeta, \tau) = g(\zeta) \exp[Z(\zeta - 1)/\epsilon] e^{k\tau} \tag{5.18}$$

We choose the transformation value Z such that the coefficient of $g'(\zeta)$ is zero. Substituting Eq. 5.18 into Eq. 5.17 yields:

$$\epsilon^4 g''''(\zeta) + 4\epsilon^3 Z g'''(\zeta) + Y g''(\zeta) + (k^2 + W) g(\zeta) = 0 \tag{5.19}$$

$$4Z^3 - 2Z + \alpha = 0$$

$$Y = 6Z^2 - 1 \tag{5.20}$$

$$W = Z^4 - Z^2 + \alpha Z + \epsilon^4 F$$

At this point the proper root for Z is not apparent, however we will be able to determine it when matching the inner solution and the outer solution. To solve Eq. 5.19 we assume that $g(\zeta)$ can be expressed in assymptotic form as $\epsilon \to 0$.

$$g(\zeta) = g_o + \epsilon g_1 + \epsilon^2 g_2 + \ ... \tag{5.21}$$

The goal of this analysis is to capture the behavior at the boundaries as $\zeta \to 0$ and $\zeta \to 1$. We define the following boundary layer variables $\bar{\zeta} = \zeta/\epsilon$ and $\zeta^\star = (\zeta - 1)/\epsilon$. Similar to the expansion for $g(\zeta)$ we will expand the solution near the boundaries as follows:

$$g(\zeta) \approx \epsilon \bar{g}_1(\bar{\zeta}) + \epsilon^2 \bar{g}_2(\bar{\zeta}) + \ ... \tag{5.22}$$

$$g^\star(\zeta) \approx \epsilon g_1^\star(\zeta^\star) + \epsilon^2 g_2^\star(\zeta^\star) + \ ... \tag{5.23}$$

Finally we will also assume an expansion of k,

$$k = k_o + \epsilon k_1 + \epsilon^2 k_2 + \ ... \tag{5.24}$$

Substituting the expansions into Eq. 5.19 yields the following sequence of equations sorted by orders of ϵ

$$[k_0^2 + W]g_0 = 0 \tag{5.25}$$

$$(2k_1k_0)g_0 + [k_0^2 + W]g_1 = 0 \tag{5.26}$$

$$(2k_0k_2 + k_1^2)g_0 + (2k_1k_0)g_1 + [k_0^2 + W]g_2 + Yg_0'' = 0 \tag{5.27}$$

The leading order equations at the boundaries are:

$$\frac{d^4\bar{g}}{d\bar{\zeta}^4} + 4Z\frac{d^3\bar{g}}{d\bar{\zeta}^3} + \frac{d^2\bar{g}}{d\bar{\zeta}^2} + (k^2 + W)\bar{g} = 0 \tag{5.28}$$

$$\frac{d^4g^\star}{d\zeta^{\star 4}} + 4Z\frac{d^3g^\star}{d\zeta^{\star 3}} + \frac{d^2g^\star}{d\zeta^{\star 2}} + (k^2 + W)g^\star = 0 \tag{5.29}$$

The boundary condition functions are required to satisfy the spatial boundary conditions to all orders of ϵ. The solutions also have to match the inner solution. At the

leading edge this requires $\bar{g}(\bar{\zeta}) = g(\zeta)$ as $\bar{\zeta} \to \infty$ and $\zeta \to 0$. Similarly we require that $g^\star(\zeta^\star) = g(\zeta)$ as $\zeta^\star \to -\infty$ and $\zeta \to 1$

Staring with Eq. 5.25, in order to have a nontrivial solution for g_0, it is necessary that

$$k_0^2 = -W \tag{5.30}$$

Since W implicitly depends on Z the transformation variable, once we are able to determine the correct choice for Z we will know the first order frequency. The stability of the system depends on the real part of k so determining k_0 will inform us of the leading order stability boundary. Moving on to Eq. 5.26 we can solve for k_1

$$k_1 = 0 \tag{5.31}$$

Finally we can solve Eq. 5.27 using the results from Eqs. 5.30 and 5.31.

$$Y g_0'' + 2k_0 k_2 g_0 = 0 \tag{5.32}$$

To ensure that this solution can be matched with the boundary solutions we require that g_0 goes to zero at $\zeta = 0$ and $\zeta = 1$. The solution to Eq. 5.32 is $g_0 = A_0 \sin(n\pi\zeta)$ for $n = 1, 2, 3, ...,$. Substituting the solution into Eq. 5.32 yields the equation for k_2.

$$k_2 = \frac{(n\pi)^2 Y}{2k_o} \tag{5.33}$$

In order to determine the transformation variable Z we use the boundary layer equations. Substituting an assumed solution of $\bar{g}_1 = C \exp[\lambda\bar{\zeta}]$ into Eq. 5.28 yields:

$$C(\lambda^4 + 4Z\lambda^3 + \lambda^2) \exp[\lambda\bar{\zeta}] = 0; \tag{5.34}$$

This has a double root at $\lambda = 0$ so the solution after applying the appropriate boundary conditions is $\bar{g}_1 = C_1(-1 - \lambda_1\bar{\zeta} + \exp[\lambda_1\bar{\zeta}])$. Similarly the solution at the other boundary is of analogous form $g_1^\star = C_2(-1 - \lambda_2\zeta^\star + \exp[\lambda_2\zeta^\star])$. λ_1 and λ_2 are

the roots of $\lambda^2+4Z\lambda+Y=0$. In order for the solution to be bounded as $\bar{\zeta}\to\infty$ and $\zeta^\star\to-\infty$, we require $Re[\lambda_1]<0$ and $Re[\lambda_2]>0$. This provides us a condition to select Z. Namely, if Z is real than the $|Z|\leq\sqrt{(1/6)}$. Figure 5.2 shows the possible solutions for Z for different values of α. The red lines are placed at $Re[z]=\sqrt{1/6}$ and $Re[z]=\sqrt{1/6}$ show the feasible values. The red highlights over the black lines show the correct choice for Z. Matching the inner solution with the outer solution

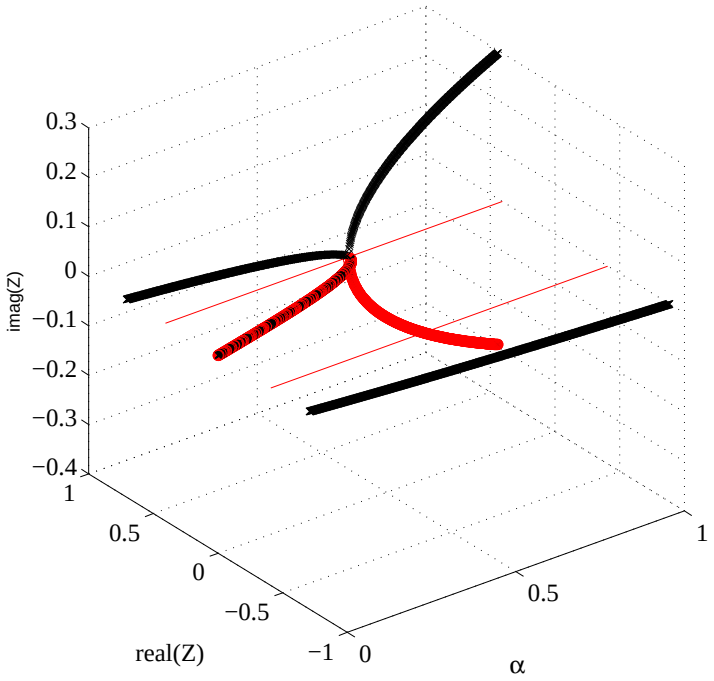

FIGURE 5.2: Z vs α for Membrane Paradox Analysis

determines C_1 and C_2 and allows us to write the specific first order solution for the boundary layer.

$$\begin{aligned}\bar{g}_1 &= \frac{A_o n\pi}{\lambda_1}(-1-\lambda_1\bar{\zeta}+\exp[\lambda_1\bar{\zeta}])\\ g_1^\star &= (-1)^n\frac{A_o n\pi}{\lambda_2}(-1-\lambda_2\zeta^\star+\exp[\lambda_2\zeta^\star])\end{aligned}\tag{5.35}$$

5.2 Stability Analysis

Using the analysis presented in the previous section we can determine the stability of the system. The Solarelastic system becomes unstable when the $Re[k] > 0$. For this section we will use the three term expansion of k and thus the system is unstable when $(Re[k_o] + \epsilon^2 Re[k_2]) > 0$. Figure 5.3 shows the neutral stability boundary for different values of ϵ with $F = 0$. This plot recreates the stability boundary for the two dimensional case that is found in Spriggs et al. (1969). For a given ϵ the system is stable for α's to the left of the curve and unstable for those to the right of the curve. The curve is for the n=1 configuration as it is the most critical of the modes.

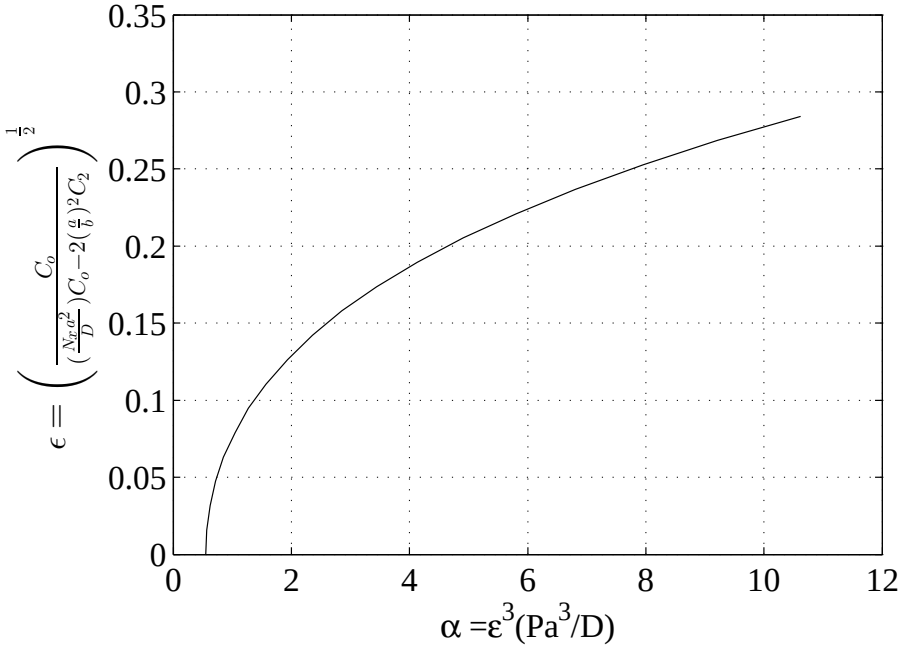

FIGURE 5.3: Perturbation analysis stability boundary for a rectangular membrane without accounting for three dimensional effects (F=0)

Figure 5.4 shows the stability boundary and instability frequency as a function of all three non-dimensional parameters. The result shows that the stability boundary does not depend on the terms in F. This is interesting because it suggests that

constraining the membrane in both directions does not change the stability boundary. However, the lower figure that shows that the F term changes the frequency of the instability.

5.2.1 Damping Impact

Another aspect that we can explore is the impact of including a damping term in the model. In the classic texts, the damping can be provided from the aerodynamics. However, for our case since there is no damping from the solar radiation pressure, the damping must come from the structural model. The inclusion of structural damping is completed by modifying Eq. 5.17 to include a damping term.

$$\epsilon^4 y'''' - \epsilon^2 y'' + \epsilon\alpha y' + F\epsilon^4 y + \gamma\frac{\partial y}{\partial \tau} + \frac{\partial^2 y}{\partial \tau^2} = 0; \tag{5.36}$$

with

$$\gamma = \bar{c}c_o\sqrt{\frac{N_x^2 a^2}{\rho h D}} \tag{5.37}$$

We can then use the results for the frequency directly from Spriggs et al. (1969). The non-dimensional stability boundary is shown for different damping values and F values in Fig. 5.5. The figure shows that including a damping value ($\gamma \neq 0$) causes the instability parameter (α) to be higher for a given ϵ. Second, by including the damping term, we see that the impact of the F term, which comes from the three dimensional boundary conditions (in some part), becomes larger for moderate values of ϵ.

5.2.2 Sunjammer Stability

We can now use our analysis capability to study the stability of the Sunjammer spacecraft membrane section. The Sunjammer is produced by a commercial entity and many of the specifics of the design are not approved for public release. Table

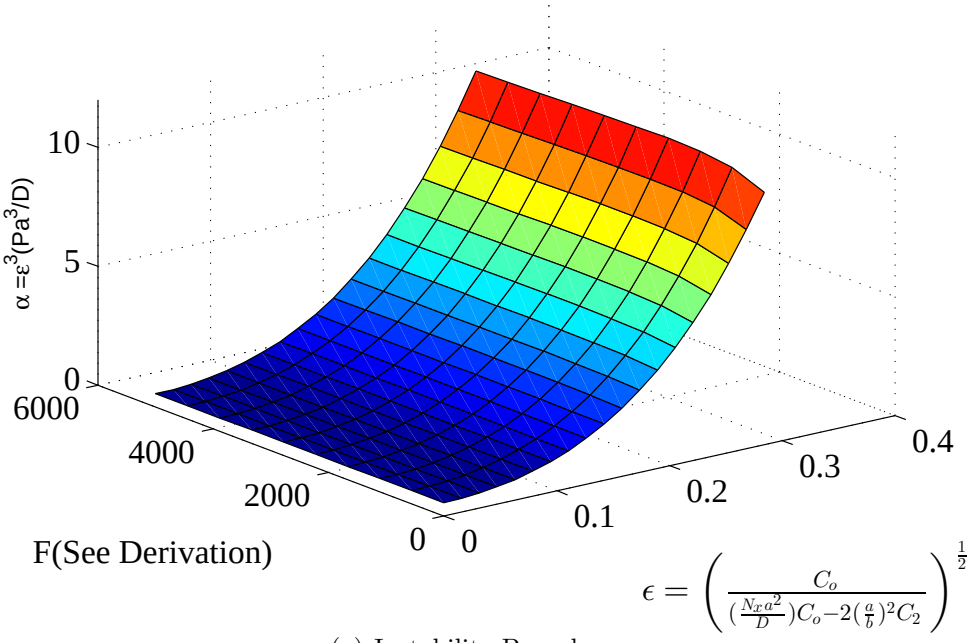

(a) Instability Boundary

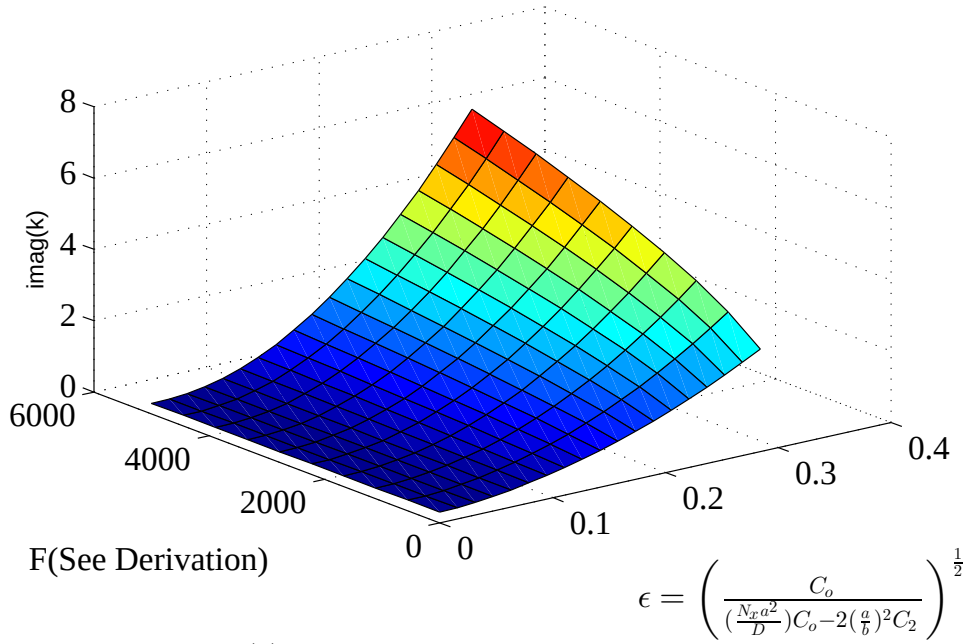

(b) Frequency at Instability Boundary

FIGURE 5.4: Perturbation analysis stability boundary and frequency for a rectangular membrane including three dimensional effects (F≠0)

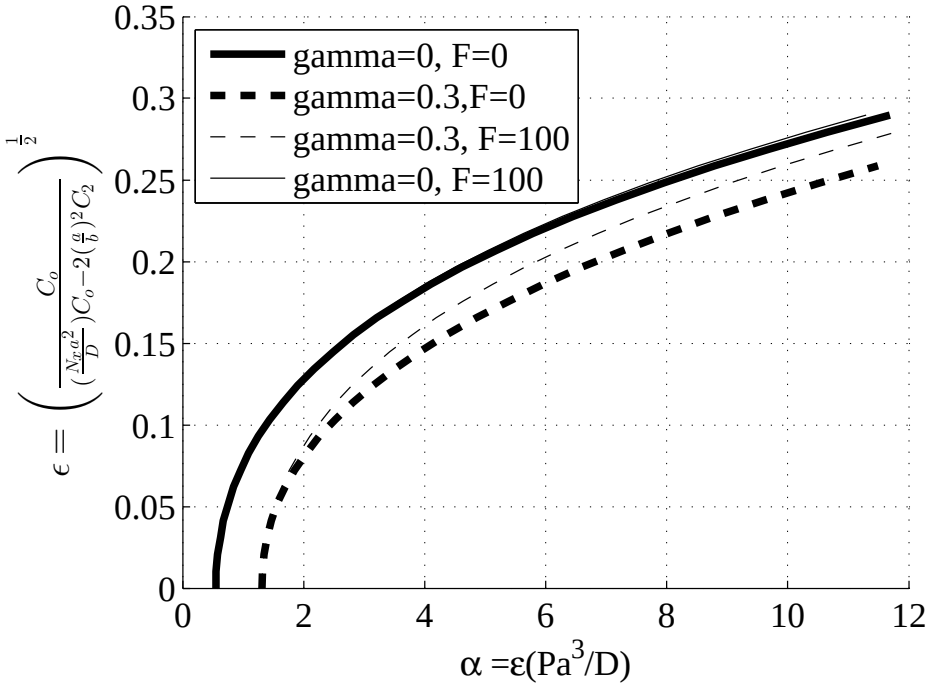

FIGURE 5.5: Structural Damping Impact on Membrane Stability Boundary

5.1 contains our best estimate of the Sunjammer parameters. In particular we will look at a rectangular segment such as the one identified in Fig. 5.1 on the boundary of the sail. Furthermore we will explore the most critical sun loading by choosing $\gamma = \pi/4$ and $\psi = \pi$. This choice is convenient because it eliminates the dependence of F on the P_o.

Figure 5.6 shows the instability radiation pressure as a function of the stress in the x direction. The result shows that for stress levels above 0.2 N/m^2 the Sunjammer will be stable at 1 AU. Furthermore, for less critical cases, such as cases when the sun is not directly overhead the instability radiation pressure increases due to the dependence of the parameter α on $\sin(2\gamma)$ and $\cos(\psi)$. We also see that the instability pressure levels off for low tension values. This is due to the fact that with low tension, ϵ is governed by the large aspect ratio that remains constant as the tension decreases.

Figure 5.7 shows the frequency of the instability. The figure shows that the

Table 5.1: Approximate Sunjammer Parameters

Property	Value	Units
Thickness	5.1e-6	m
Chord	1.0	m
Span	35	m
ρ	1490	kg/m^3
E	9.67e+9	N/m^2
ν	0.33	

instability occurs at an extremely low frequency on the order of 0.1 Hz. This means that each period of oscillation will take 10's of seconds to complete. The long time scales may allow this instability to be controlled with the existing control mechanisms on the spacecraft. Furthermore, based on the literature for supersonic panel and membrane flutter we expect the limit cycle oscillation to be on the order of the

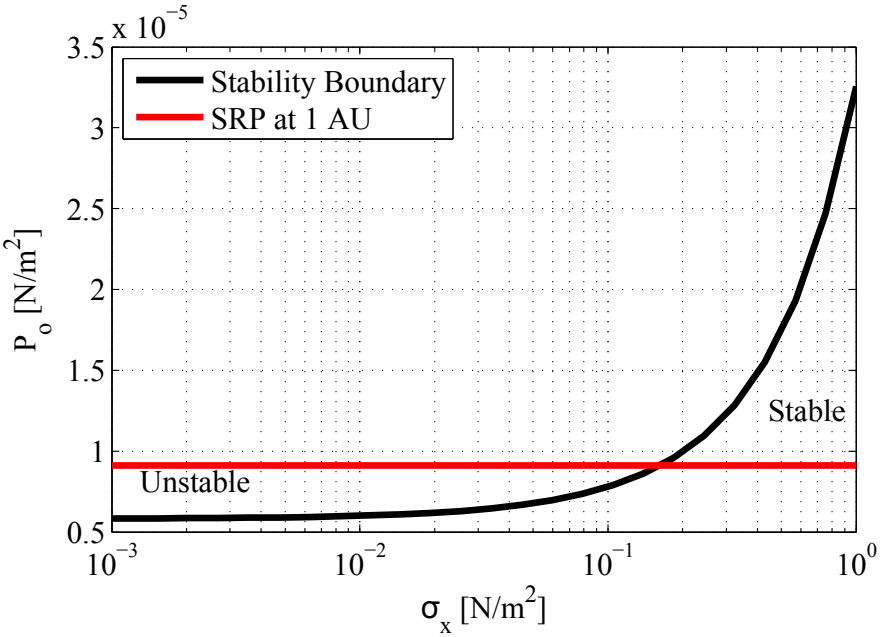

FIGURE 5.6: Sunjammer Stability

thickness of the plate (Dowell and Ventres (1970)). These small oscillations will be difficult to observe and are unlikely to cause structural or control problems for solar sails similar to the Sunjammer.

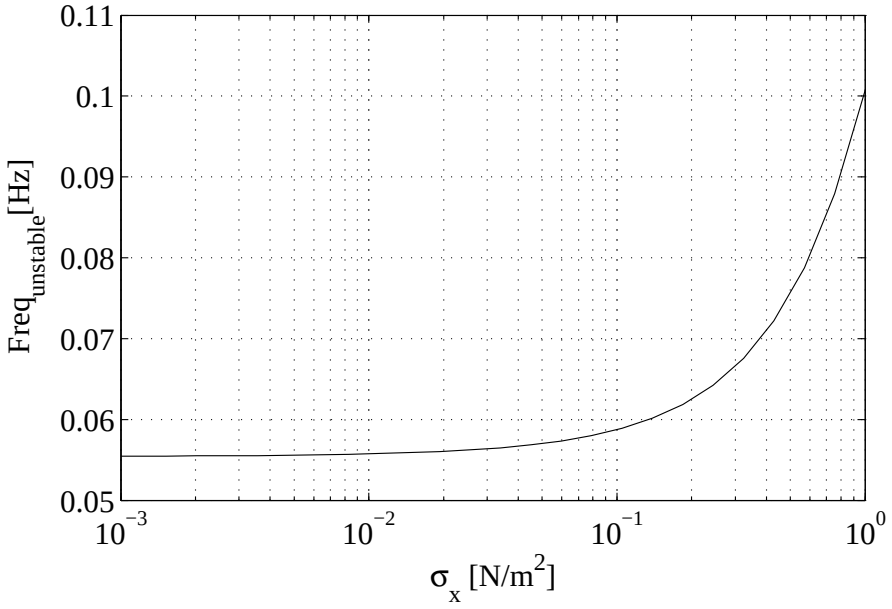

FIGURE 5.7: Frequency of Sunjammer Instability

5.3 Scaling Analysis for Membrane Limit Cycle Oscillation Amplitude

In addition to exploring the stability of the restrained membranes, it is also important to explore the post flutter response to determine how critical the instability will be. While a complete analysis of the post flutter response would require solving a nonlinear equation, in this section we will use a scaling analysis similar to the one developed by Dowell (1969) to get an estimate of the LCO amplitude. For our analysis, we assume that during the limit cycle the inertia, forcing, and linear bending stiffness must all balance with the nonlinear stiffness. For the Sunjammer, the dominant linear stiffness may come from either the bending stiffness or the tension

stiffness. The linear bending stiffness is:

$$Eh^3\frac{w}{a^4} \tag{5.38}$$

The linear tension stiffness is:

$$N_x\frac{w}{a^2} \tag{5.39}$$

Following a scaling analysis from the literature Dowell (1969) we balance the nonlinear bending stiffness in Eq. 5.40 with the larger of the linear bending stiffness from Eq. 5.38 or the linear tension term from Eq. 5.39.

$$Eh\frac{w^3}{a^4} \tag{5.40}$$

The first task for the membrane scaling is determining if the bending stiffness from Eq. 5.38 or the tension stiffness from Eq. 5.39 balances with the nonlinear bending stiffness from Eq. 5.40. To determine this we determine whether if the linear bending stiffness or the linear tension stiffness is larger. If linear bending stiffness is greater, i.e. when $Eh^3/a^2 > N_x$, then balancing the linear bending stiffness with the nonlinear bending stiffness suggests that the LCO amplitude will be on the order of the thickness of the plate, the familiar result.

On the other hand if $Eh^3/a^2 < N_x$ then the linear tension term must balance with the nonlinear bending stiffness term. This leads to the following approximation.

$$w \approx a\sqrt{\frac{N_x}{Eh}} \tag{5.41}$$

An interesting feature of Eq. 5.41 is that increasing the tension, increases the LCO amplitude. Upon further inspection this is consistent with the increasing strength of the tension stiffness and therefore the higher forcing that is required to cause the tensioned membrane to go unstable. It follows that once the membrane does go

unstable, it may enter a large limit cycle oscillation due to the increased force on the structure.

For the Sunjammer panel explored in this sections there are applied tension values where the bending stiffness dominates and others where the tension stiffness dominates. Figure 5.8 shows the two terms of the inequality. When the σ_x is larger than 1e-4 N/m^2 the tension term should balance with the nonlinear bending stiffness.

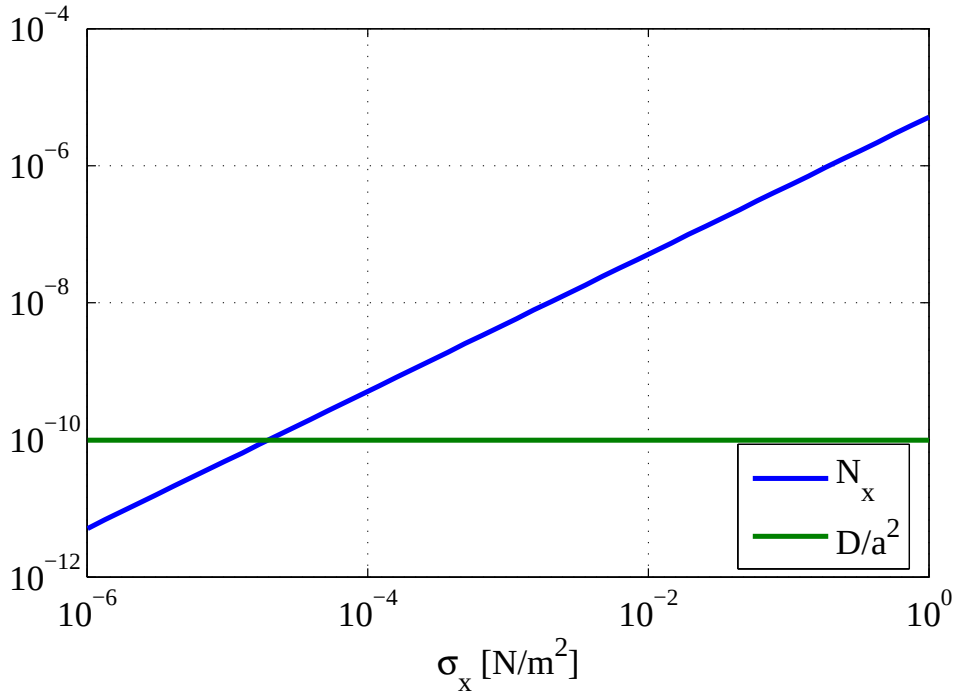

FIGURE 5.8: Eh^3/a^2 vs N_x of Sunjammer Membrane for Different Applied Tension Values

For the case where the tension dominates we can plot the approximate LCO amplitude for different tension values. Figure 5.9 shows the LCO amplitude as the tension increases. The figure shows that at a tensile stress equal to 1 N/m^2 the LCO amplitude is still only 70 times the thickness. This is in comparison to the chord, a, which is 6 million times the thickness. It is clear that the thickness is still the correct scaling length when discussing the LCO amplitude, even when the LCO amplitude

is dominated by the linear tension stiffness balancing with the nonlinear bending stiffness.

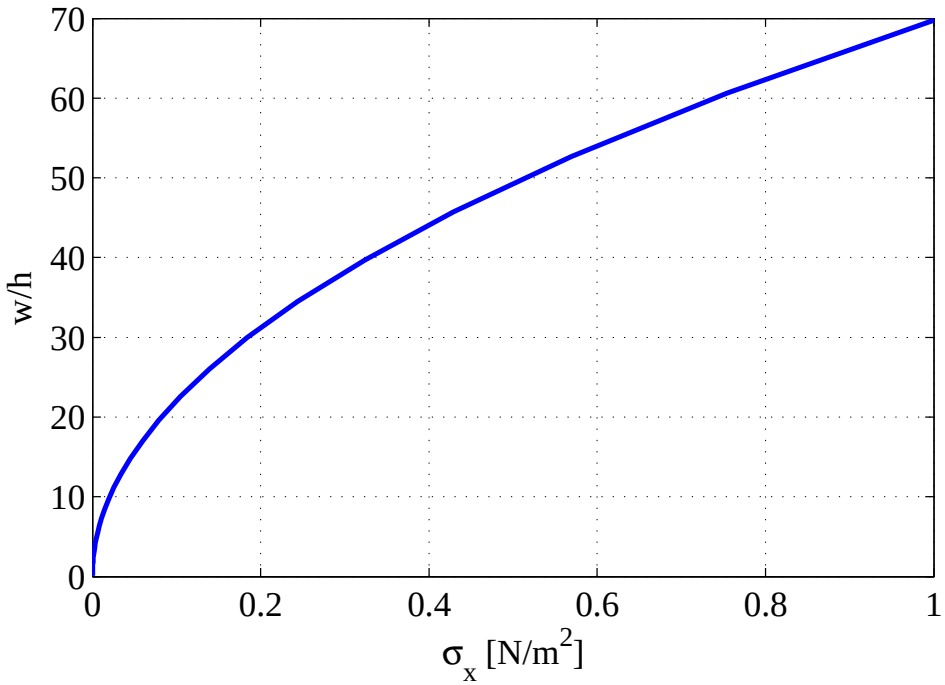

FIGURE 5.9: Sunjammer Membrane LCO Amplitude for Different Applied Tension Values

5.4 Conclusions for the Stability of a Restrained Plate / Membrane in Space

In our research we extended the classic asymptotic analysis of Spriggs et al. (1969) to explore the stability of solar sails. By completing the analogy between the stability of solar sails to the classic aeroelastic model we are able to utilize the previous aeroelastic results to understand the stability behavior of our new system. We use the aeroelastic results to explore the stability of a section of the Sunjammer spacecraft to demonstrate the applicability of the technique. The Sunjammer example for the parameters considered here is shown to be unstable at 1 AU for applied tension values less than 0.2 N/m^2, although the instability is expected to be characterized

by an limit cycle oscillation with an amplitude on the order of the thickness of the membrane.

6

Dynamics and Stability of a Hanging Membrane in a Gravitation Field

In addition to supporting the design effort for solar sails such as the Sunjammer discussed in Chapter 5, our research has also supported the design of additional solar sail architectures. In particular, here we explore the stability of the heliogyro architecture proposed by MacNeal (1971) in the late 1960's. In this architecture, the solar sail spacecraft contains a set of helicopter-like blades. The whole system rotates at a fixed rate causing the blades to be centrifugally stiffened. This architecture has the advantage of not requiring rigid support structures. The lack of rigid support structures reduces the system mass and improves the spacecraft's performance. One of the potential problems faced by heliogyros is that the individual blades, which are thin membranes, remain only lightly tensioned and therefore may be susceptible to dynamic instabilities even with low amounts of external forcing.

Developing solar sail capabilities requires effective means of designing, analyzing and testing solar sail technologies. Because of the cost prohibitive nature of testing the systems and subsystems in space, accurate analysis and response predictions are vital to the future development of the technology. In this chapter a membrane

hanging in a gravitational field is used as an analogy for the heliogyro blades. This chapter implements a solarelastic model that couples a classic beam model to an optical solar radiation model. After describing the solarelastic model, emphasis is placed on the structural model validation using ground vibration experiments in a vacuum chamber and describing a potential design for a solarelastic experiment.

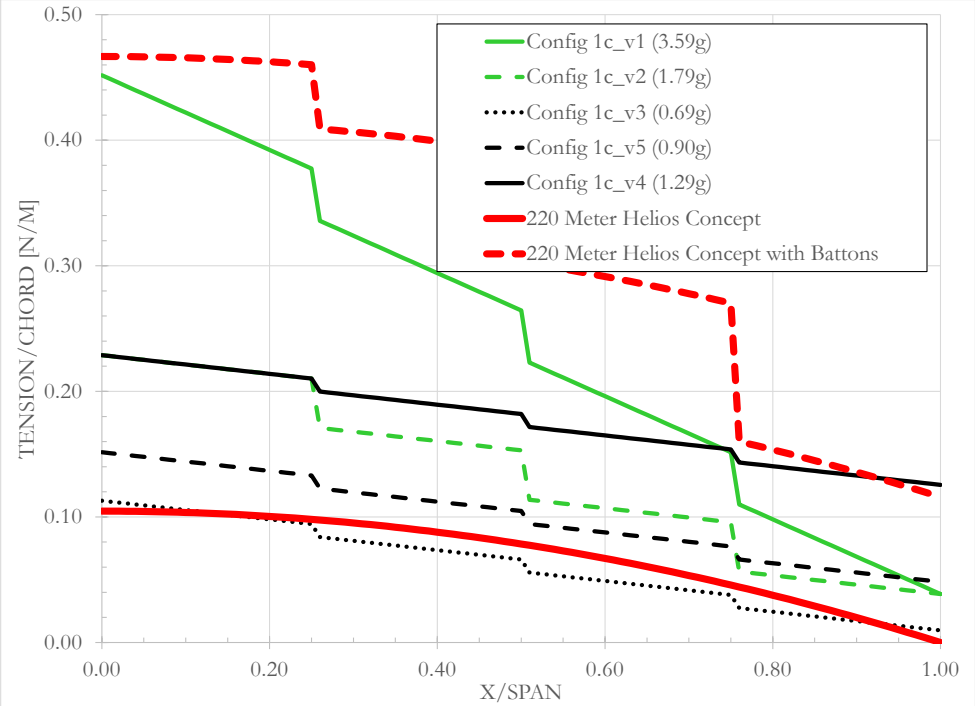

FIGURE 6.1: Comparison of Stress Distributions for Different Blades

The value of analyzing hanging membranes for applications in spinning solar sails is shown in Fig. 6.1. In the figure we see the dimensional stress as a function of the span for two different proposed heliogyro designs as well as for some of the experiment specimens discussed in this section. The figure clearly shows similarities in the stress profiles between the actual design and our ground validation experiments. While the length scales are orders of magnitude different, the dynamics share enough similarities

to make the hanging experiments a valuable exercise.

Publications

1. **Gibbs et al. (2013)** This conference paper explores the coupling between a hanging membrane structure in a gravitational field and solar radiation pressure that is labeled a solarelastic coupling. The gravitationally tensioned membrane is modeled with a classical linear Rayleigh Ritz beam model and the solar radiation pressure is modeled for a perfectly reflective structure. The influence of a gravitational field is included in the structural model to explore the feasibility of designing an experiment to re-create a solarelastic instability on earth. Finally there is a discussion of the ground vibration experiments that have been conducted to validate the structural model.

6.1 Elastic and Solarelastic Model Description

For our analysis we implemented the linear beam in bending and torsion model described in Section 2.1.1. This model is coupled to the optical solar radiation pressure model described in Section 2.2.2. Using the cosine of the angle between the unit normal and the incident radiation described by Eq. 2.58 we are able to write the force cased by the solar radiation as:

$$P_r = P_o \left[\cos^2 \gamma + \sin 2\gamma \left(\frac{\partial w}{\partial y} \sin \Psi - \frac{\partial w}{\partial x} \cos \Psi \right) \right] \tag{6.1}$$

This force is substituted in to the generalized force relationship in bending as:

$$Q_n = \int_0^L \int_{-\frac{S}{2}}^{\frac{S}{2}} P_r(x, y) \phi_i(x) \, dy \, dx \tag{6.2}$$

There is no generalized moment on the structure because the force is uniform in y and acts normal to the blade. The generalized force in bending is dependent on

the motion of the structure through $\partial w/\partial y$ and $\partial w/\partial x$ that appear in the solar radiation force equation. This relationships adds additional stiffness terms to the governing equations and couples the bending equations to the torsion degrees of freedom. Specifically the generalized force can be written as:

$$Q_n = P_o L_y \int_0^{L_x} \left[\cos^2\gamma + \sin 2\gamma \left(\sum_i \Theta_i q_i \sin\psi - \sum_m \phi'_m q_m \cos\psi \right) \right] \phi_n \, dx \quad (6.3)$$

The final form of the equations is the same as the structural equations of motion with a static force and two additional stiffness terms in the bending degrees of freedom. The structural dynamics are evaluated when the radiation pressure is set to zero and the stability is determined by solving the generalized eigenvalue problem that arises when the static force is excluded. The influence of the static force can thought of as a particular solution, which for the linear system does not effect the stability.

6.2 Solarelastic Simulations for the Hanging Beam

Solarelastic simulations are conducted to evaluate the feasibility of a ground solarelastic experiment. The conceptional design of a ground-based solarelastic experiment is to hang a thin membrane in a vacuum chamber and then illuminate the membrane and observe the instability that arises as a function of the illumination strength and incidence angle. Before progressing with the design of such an experiment we want to analyze what strength of illumination that would be required to create an instability and ensure that the level is achievable. The baseline configuration is a piece of 0.1 mil ($2.54\mu m$) thick Mylar that is 84 inches long and 2 inches wide. Table 6.1 includes the material properties of Mylar For this configuration the Ψ and γ angles identified in Figure 6.3 are set to π and $\pi/4$ respectively. For this configuration the model predicts that a static divergence instability. The divergence boundary as the number of bending modes in the simulation is varied is given in Figure 6.2.

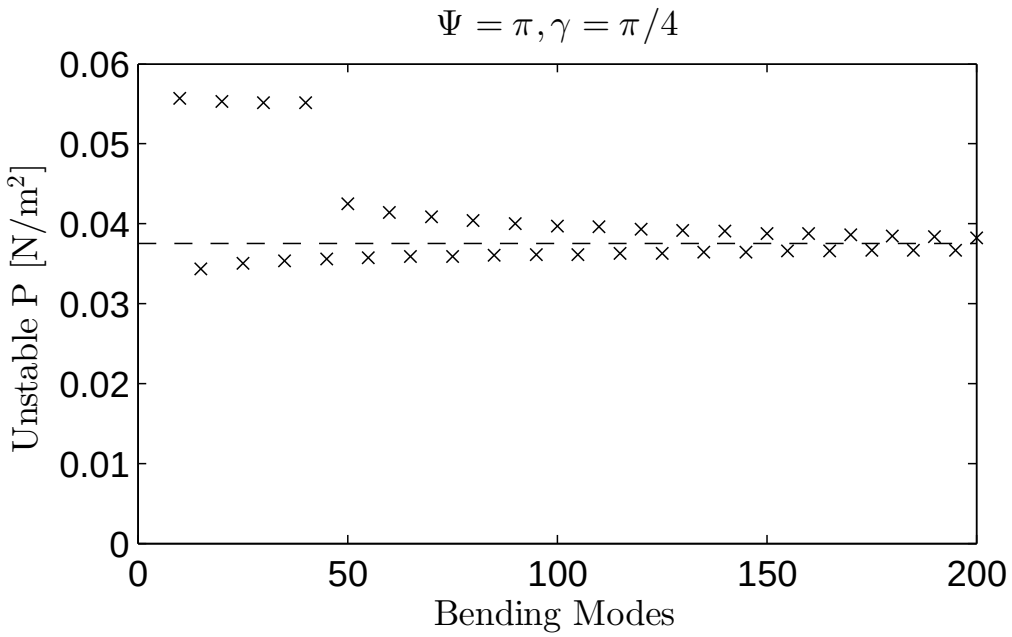

FIGURE 6.2: Modal Convergence of Divergence Boundary for $\Psi = \pi$, $\gamma = \pi/4$ Hanging Membrane Simulation

The initial simulations demonstrated that there is poor modal convergence. Figure 6.4 shows the natural frequency evolution for different number of bending modes. In the figure, the black lines indicate stable frequencies and the red lines indicate unstable frequencies. For the low mode numbers in this figure, the lowest radiation pressure instability oscillates between a first mode divergence and a first and second bending mode flutter. As the number of modes increases the solutions begins to converge to a divergence instability as the primary instability. The dashed line in Figure 6.2 is the divergence boundary of 3.75×10^{-1} N/m^2 which the solutions appears to converge to. For reference, 1 sun at 1 Astronomical Unit (AU), approximately 93 million statute miles, produces a radiation pressure equal to 9.55×10^{-6} N/m^2. This simulation suggests that it may be difficult to recreate a solarelastic instability with a ground based experiment. Additionally, divergence experiments are extremely hard to conduct because divergence is a static phenomenon and is therefore difficult to measure. One method of conducting the experiment without having to achieve the

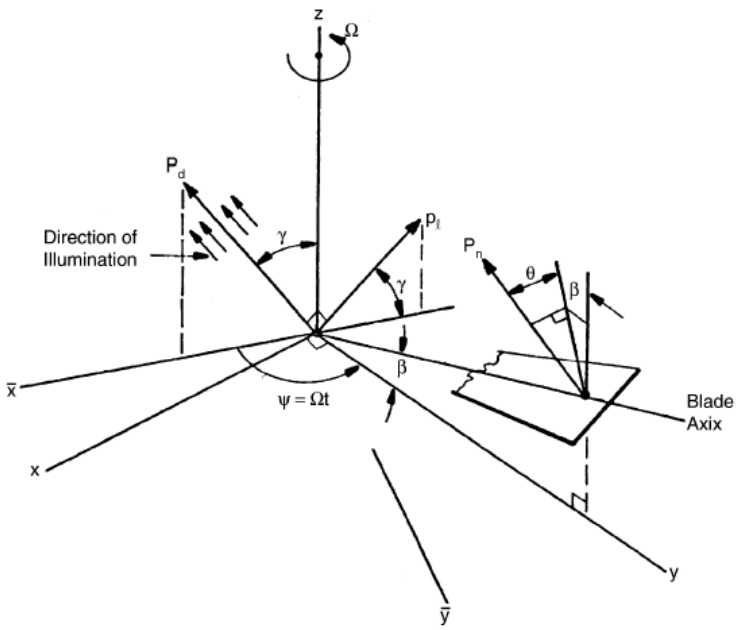

FIGURE 6.3: Schematic showing the coordinate systems and angles for a rotating heliogyro blade. Figure taken from Dowell (2011).

radiation pressure equal to the divergence boundary is to measure the natural frequencies at different radiation pressures and see if the shift in frequency matches the theory for the sub-critical configurations.

The initial simulations also seem to suggest that there is a flutter instability when Ψ=0 which, although it occurs at a higher radiation pressure, may be easier to observe directly. The non-uniform convergence appears to be a function of the membrane nature of this configuration. In the classical aeroelastic literature it is well known that the theoretical methods have trouble predicting instabilities as the bending stiffness goes to zero. To avoid this well known paradox, we could attempt to implement a perturbation method such as the one presented in Chapter 5, to determine the limit for the stability boundary as the bending stiffness goes to zero.

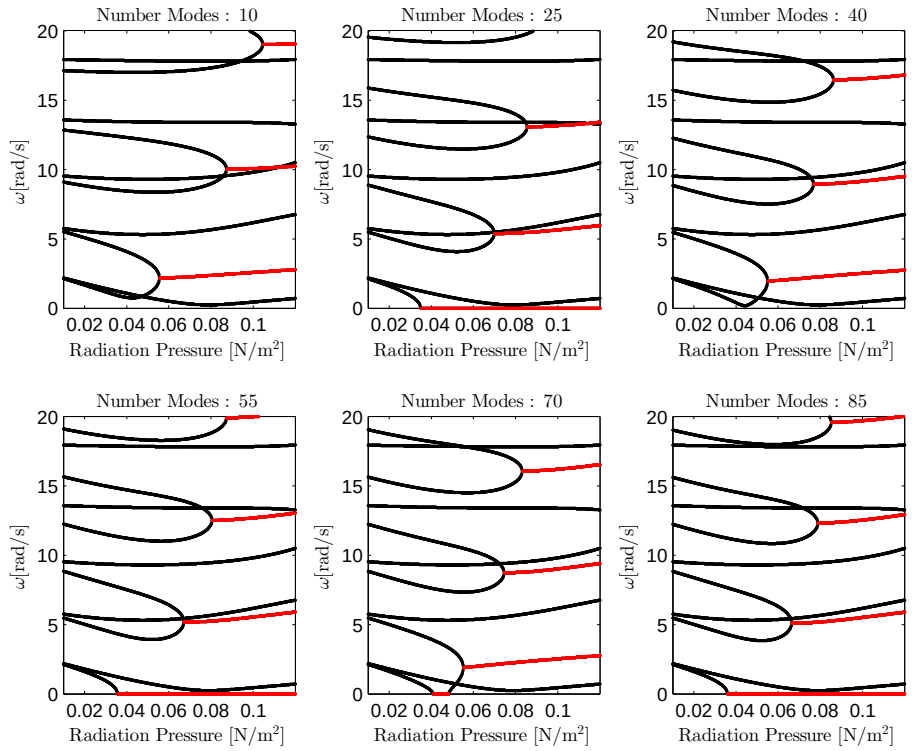

FIGURE 6.4: Eigenvalues for $\Psi = \pi$, $\gamma = \pi/4$ Hanging Membrane Simulation with Increasing Number of Bending Modes

6.3 Structural Model Experimental Validation

Due to the difficulty of modeling solar sail membrane structures, it is useful to validate the structural model with experimental results. Specifically, the natural frequencies and modes shapes of the structure can be deduced from ground vibration experiments. This information can validate that the theoretical model is an accurate representations of the structure. Because of the lightweight nature of the structures, the ground vibration experiments are conducted in a vacuum chamber that produces a vacuum of around 10^{-3} Psi. The insensitivity of the natural frequencies to the air present in the vacuum chamber is confirmed by observing the change in frequencies as the pressure is changed and ensuring that an asymptote is reached by 10^{-3} Psi.

A schematic of the experimental setup is given in Fig. 6.5. Included in this figure is the 2.5 m vacuum chamber, a test specimen, the piezoelectric actuator, a pair of stationary Doppler shift laser vibrometers and the Polytec scanning laser vibrometer (PSLV). To conduct the experiments the test specimen is vertically cantilevered from either a flapping or twisting piezoelectric actuator that inputs energy into the system and excites the desired modes. The actuator is driven by a burst random signal or a frequency chirp signal with random noise. To measure the response a suite of laser vibrometers is targeted at retro reflective dots on the test specimen. In general the stationary vibrometers are used to analyze the system natural frequencies and damping levels and the scanning laser vibrometer is used to analyzed the modes shapes of the structure. Figures 6.6 and 6.7 show the actual experimental setup.

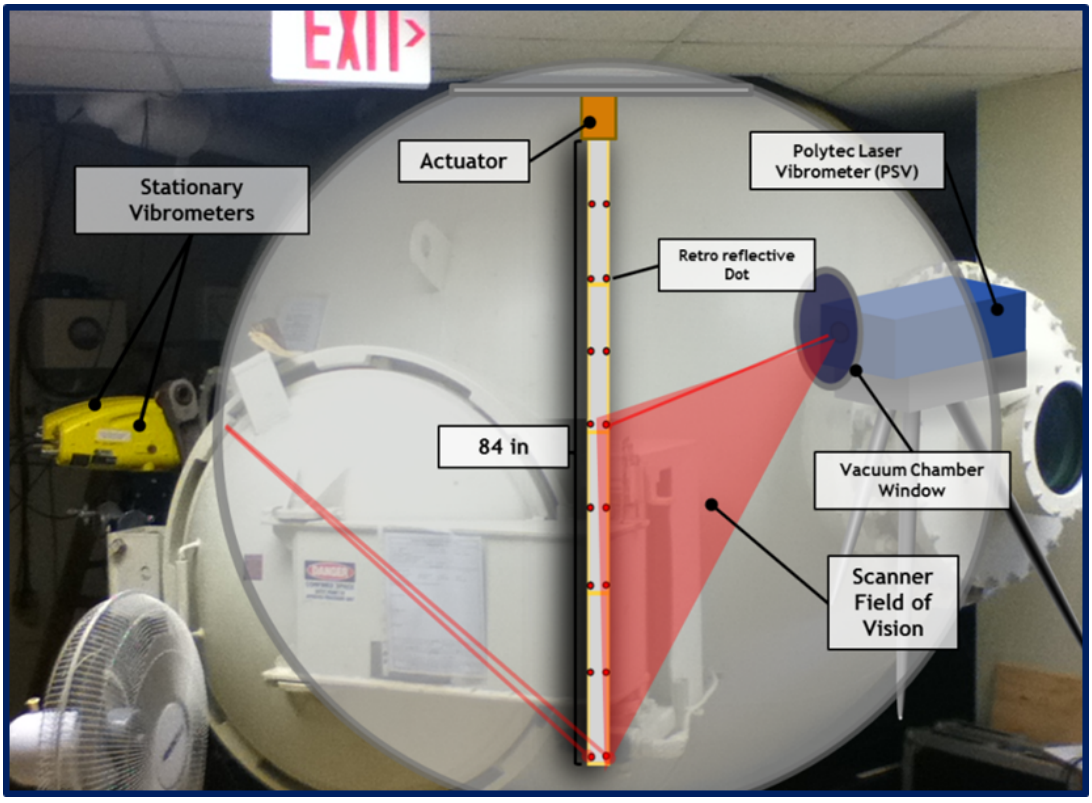

FIGURE 6.5: Schematic of Ground Vibration Experiment Setup in the NASA Langley Research Center 2.5 m Vacuum Chamber

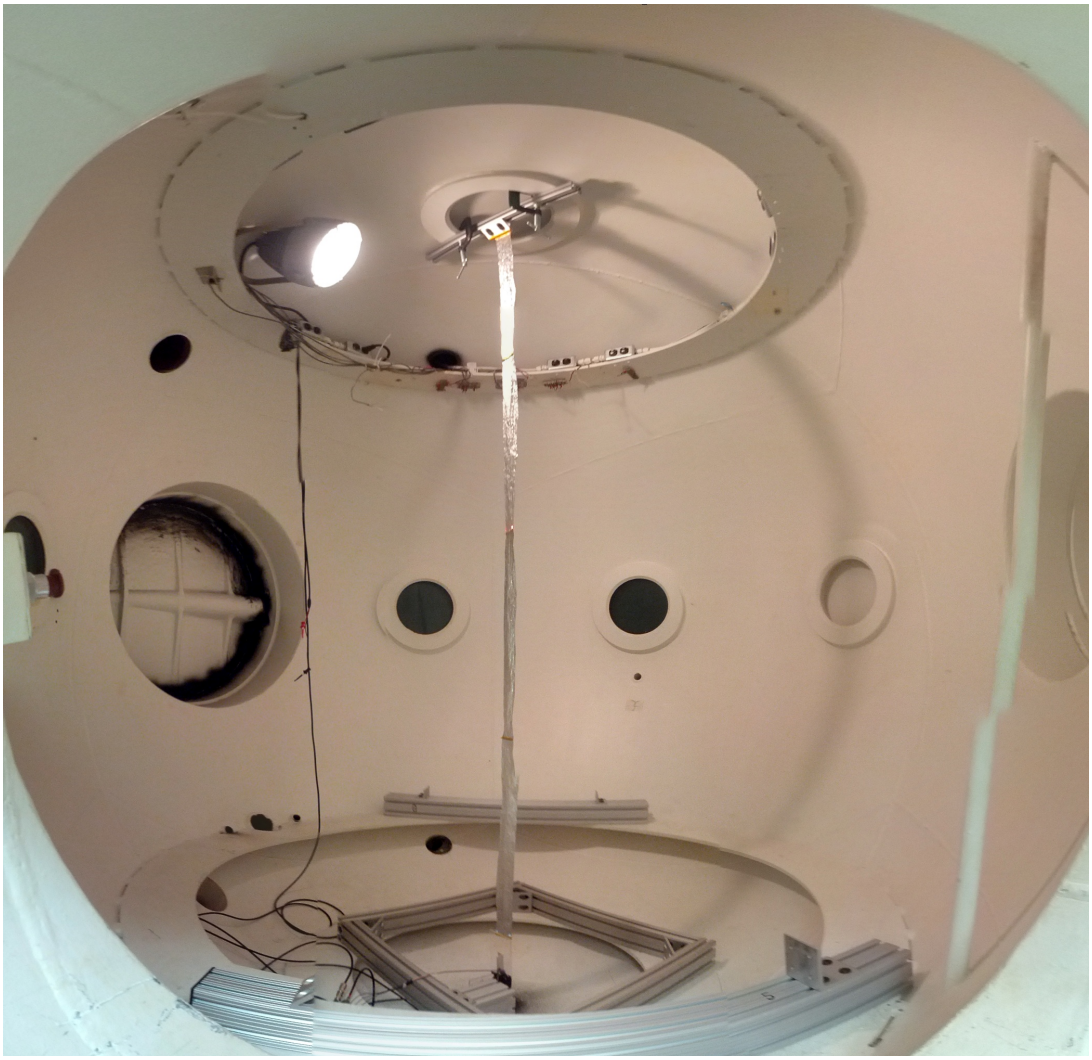

FIGURE 6.6: NASA Langley Research Center 2.5 m Vacuum Chamber Interior

This section contains the results of three different parameter variation studies. The first set explored the dynamics for a set of four blades that have different thicknesses and chords. The current theoretical model predicts that the natural frequencies do not depend on these parameters. The second experiment is an exploration of the damping levels in the structure with different mass distributions. While the natural frequencies for the different configurations will remain constant the experiments show that the damping levels depend on the blade loading. The final set

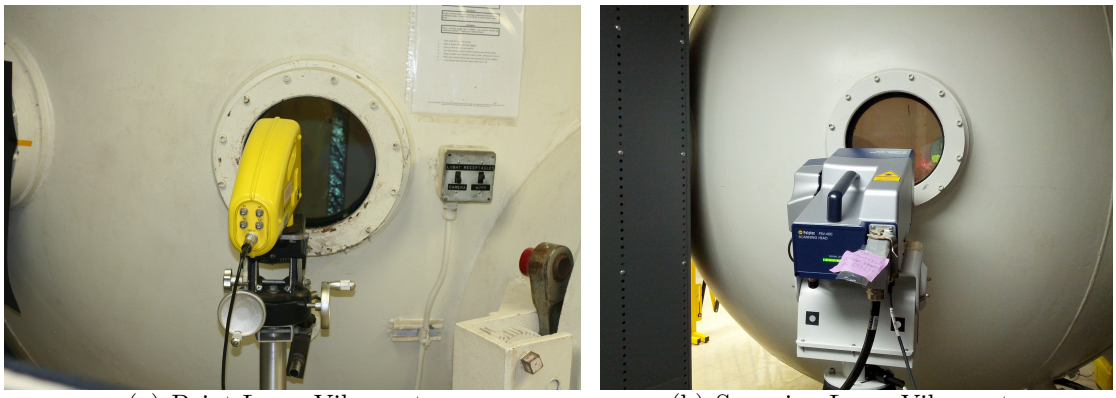

(a) Point Laser Vibrometer (b) Scanning Laser Vibrometer

FIGURE 6.7: Hanging Membrane Experiment Velocity Sensors

of experiments looks at the natural frequency evolution as the span of the blade is changed. In the linear structural model, the span is the only parameter that can be varied to change the natural frequencies of the system.

6.3.1 Experiment 1: Geometry Variation

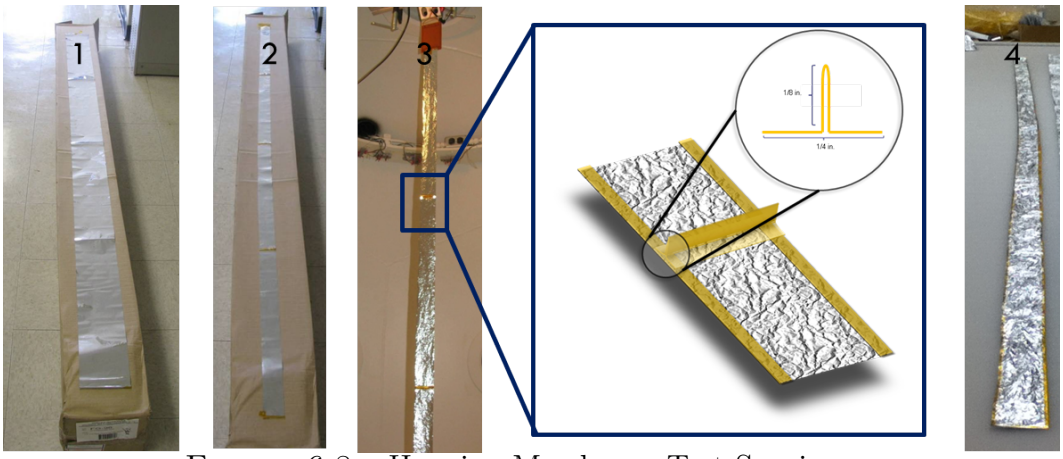

FIGURE 6.8: Hanging Membrane Test Specimens

Four different structures are tested to explore the systems sensitivity to the structure's geometry. Figure 6.8 includes pictures of each on the four experiment specimens. For the third specimen the detail shows a schematic of the tape batons which are used in Configurations 2, 3 and 4. The tape used for the batons and the edge

reinforcements is 2mil thick Kapton tape. More technical details about the four configurations can be found in Table 6.1.

Table 6.1: Hanging Membrane Structural Configurations

Property	Config 1	Config 2	Config 3	Config 4
Material	Kapton	Kapton	Mylar	Mylar
Batons	Straws	Tape	Tape	None
Other			Crumpled	Crumpled Edge Reinforced
Density	1420 kg/m^3	1420 kg/m^3	1400 kg/m^3	1400 kg/m^3
Young's Modulus	2.5 GPa	2.5 GPa	3.7 GPa	3.7 GPa
Poisson's Ratio	0.34	0.34	0.34	0.34
Thickness	25.4 μm	25.4 μm	2.54 μm	2.54 μm
Span	2.13 m	2.13 m	2.13 m	2.13 m
Chord	0.127 m	0.051 m	0.051 m	0.051m

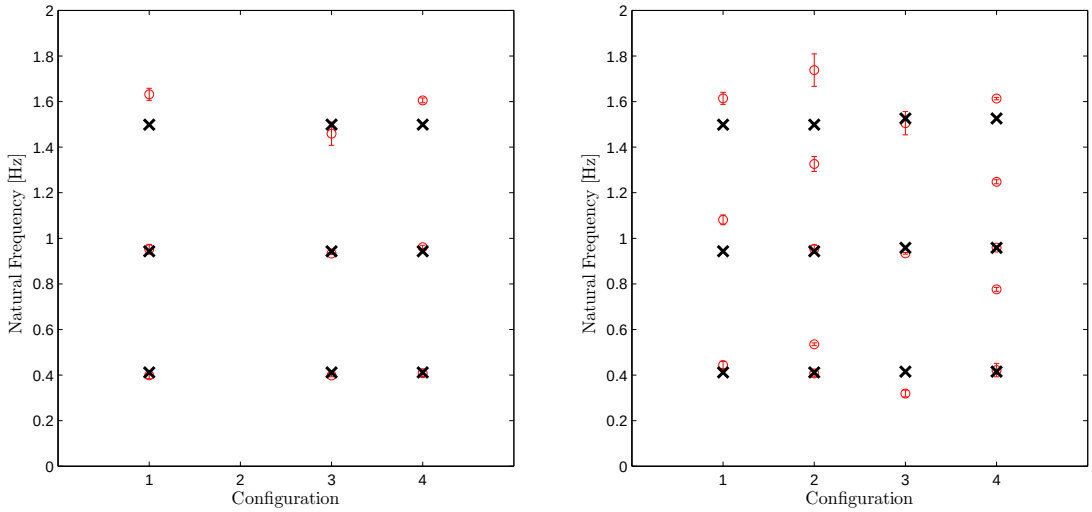

(a) Flap Natural Frequencies

(b) Twist Natural Frequencies

FIGURE 6.9: Summary of the experimentally collected natural frequencies. Theoretical natural frequencies are denoted with a bold x and the experimental results with a red o with error bars.

Frequency response data is collected at the 1/4 span, 1/2 span, 3/4 span and tip, at both chord extremes for each of these configurations. This data is available for Configurations 1, 3 and 4 in Appendix A. The time histories are converted into frequency response functions (FRFs) by using a fast Fourier transform (FFT). The peaks from the FRFs are automatically identified using a Matlab script. These peaks are the natural frequencies of the system. These measured natural frequencies are averaged over all of the points for a given actuator/specimen combination and compared to the theoretical results in Fig. 6.9.

The first observation from the theoretical and experimental results is that the natural frequencies in both twist and flap are not sensitive to the configuration. In fact, because of the dominant nature of the gravitational tension in the dynamics of this system the only parameter that can be effectively varied to change the natural frequency is the span. Second, comparing the two figures it is clear that the natural frequencies in the flap and twist are identical. This makes it difficult to ensure that the natural frequency that is recorded for a given test is either completely flap or twist. The experimental data is instead sorted by the type of actuator that is used, assuming that the actuator places a majority of the energy in the desired mode shapes. This will be validated later in this chapter by looking at the mode shapes for a single configuration.

Next, it is important to look at the agreement between theory and experiment. The agreement for the flap actuated frequencies is good, with all experimental points being well within 10% of the theoretical values. The agreement suggests that the current structural model captures the dynamics for this degree of freedom. In general there is also good agreement for the twist actuated results, although agreement is not as good as for the flap case. Additionally, for Configurations 2 and 4 there are additional response peaks that are observed in the experiment that are not present in the theoretical predicitons. It is unclear at this point what causes these peaks to

arise.

One way of providing insight into the cause of these additional experimental peaks is to explore the associated mode shapes. For this comparison the data collected from the PSLV is used. The frequency response data is analyzed using ME'scope to give modal displacements for each measured frequency peak at the experimental measurement locations. This response is then imported into Matlab to visualize the spatial modes shapes. These mode shapes can be compared to the theoretical mode shapes.

Comparing Mode Shapes using the Modal Assurance Criterion

One method of comparing theoretical mode shapes to experimental mode shapes is through the Modal Assurance Criterion (MAC). This method provides a measure of the similarity and orthogonality of modes and provides a quantitative value of how well the numerical and theoretical mode shapes agree. Mathematically, the MAC is defined as:

$$MAC(V_i, V_j) = \frac{|V_i^T V_j|^2}{(V_i^T V_i)(V_j^T V_j)} \tag{6.4}$$

Before comparing the experimental modes to the theoretical modes, we can look at the MAC values for comparing the theoretical mode shapes sampled at discrete points with themselves. The first step in the structural analysis is to use the beam structural model to calculate a set of spatial eigenvectors which are comprised of modal displacements at discrete and finite locations on the structure. The dot arrangement on the hanging membrane in Fig. 6.5 is an example of the spatial distribution of locations where a mode shape could be defined. However, the current structural model describes the displacements in terms of a linear combination of beam bending and torsion modes shapes that are defined continuously. To deter-

mine the displacements at the desired locations the modal eigenvectors and mode shapes are used to calculate displacements for each of theoretical modes.

This process allows us to write out the structural eigenvectors in the following manner. The n'th spatial modes shape will be denoted as follows

$$V_n^s = \begin{bmatrix} w(x_1) \\ w(x_2) \\ \vdots \\ w(x_M) \end{bmatrix} \tag{6.5}$$

where M is the number of discrete locations where the displacement is defined and the the displacement w at locations x_m can be determined using the eigenvector of the structural model and the assumed mode shapes.

$$w(x_m) = \sum_j V_n(q_j)\phi_j(x_m) \tag{6.6}$$

Before using these mode shapes to compare the theoretical mode shapes to the experimental mode shapes we can explore the dependence of the MAC on the spatial resolution of the measurement locations. By exploring the dependence of the MAC on the distribution of the spatial locations where the mode shape is defined, we can gain some insight into the number and location of instrumentation that should be used in our experiments. To study this impact we looked at the dependence of the MAC for a uniformly distributed sensor location on a 84 inch long, 2 inch wide, aluminized mylar blade.

Because the theoretical mode shapes are well defined, only 2 sensing locations in the chordwise direction are needed to separate between the bending and torsion modes. Adding additional sensing locations in the chordwise direction does not aid the comparison of theory to theory. In the experimental model some additional chordwise motions may appear and thus, additional sensing locations along the chordwise

direction may provide insight. Unfortunately, because the current theoretical model only has bending and torsion degrees of freedom it can not provide insight on the chordwise distribution. The current simulations can provide insight into the number of spanwise measurement locations are needed. For the current analysis we use only the bending degrees of freedom. Because the bending modes are perfectly orthogonal to torsion modes, the torsion modes do not affect the bending MAC in any manner for the rectangular grid.

Table 6.2: Hanging Membrane 5 Spanwise Locations, 2 Chordwise Locations Theoretical MAC

Freq	Mode	B1	B2	B3	B4	B4
0.41	B1	1.000	0.222	0.345	0.612	0.508
0.94	B2	0.222	1.000	0.492	0.657	0.333
1.49	B3	0.345	0.492	1.000	0.436	0.143
2.06	B4	0.612	0.657	0.436	1.000	0.247
2.72	B4	0.508	0.333	0.143	0.247	1.000

Table 6.3: Hanging Membrane 10 Spanwise Locations, 2 Chordwise Locations Theoretical MAC

Freq	Mode	B1	B2	B3	B4	B4
0.41	B1	1.000	0.064	0.083	0.080	0.061
0.94	B2	0.064	1.000	0.167	0.161	0.121
1.49	B3	0.083	0.167	1.000	0.198	0.151
2.06	B4	0.080	0.161	0.198	1.000	0.152
2.72	B4	0.061	0.121	0.151	0.152	1.000

Table 6.4: Hanging Membrane 20 Spanwise Locations, 2 Chordwise Locations Theoretical MAC

Freq	Mode	B1	B2	B3	B4	B4
0.41	B1	1.000	0.017	0.022	0.020	0.013
0.94	B2	0.017	1.000	0.049	0.043	0.029
1.49	B3	0.022	0.049	1.000	0.053	0.035
2.06	B4	0.020	0.043	0.053	1.000	0.031
2.72	B4	0.013	0.029	0.035	0.031	1.000

Tables 6.2, 6.3, and 6.4 contain the MAC matricies for three different spatial sensing locations. The first thing to note is that the diagonal terms are unity. This is expected because we are comparing modes to themselves. Looking at the off diagonal terms in Table 6.2 it is clear that 5 sensing locations in the spanwise direction is not enough, as there are values as high as 0.657 off the diagonal. If only 10 sensing locations were used in the experiments (5 by 2 grid), it would hard to distinguish between the modes. Unfortunately, this is exactly the number of sensing locations that the current experimental data contains. The situation is somewhat improved in the experiment because the 10 points were distributed over half of the span, so the resolution on the bottom half is greater than distributing the 10 uniformly over the entire blade

Tables 6.3 and 6.4 contain a significantly more favorable MAC picture. For the low modes of interest somewhere between 10 and 20 spanwise locations should be used. Noticeably absent in this discussion is any optimization of the measurement location. Currently, we have looked at uniform spacing and have not explored the optimal placement to minimize the number of sensing locations.

Determining Mode Shapes from Experimental Data

To generate the experimental mode shapes we first collect response data at a grid of locations on the experimental specimen. The PSLV collects the response due to a burst random input and returns the frequency response at all of the spatial locations in the grid. The data is then analyzed using the MATLAB SOCIT toolbox. The MATLAB SOCIT toolbox is used to determine the natural frequencies, damping ratio's and mode shapes from the experimental data. The code returns purely real mode shapes. These mode shapes are post processed using the knowledge of the spatial distribution of the sensing locations to create the plots shown in the next section.

Mode Shape analysis for Configuration 3 (Aluminized Mylar, Crumpled, 2 by 84 by 0.1 mil, Tape Batons) with a Twist Piezoelectric Actuator

To demonstrate the capability of the mode shape comparison capability this section looks at the mode shape analysis for Configuration 3 (aluminized mylar, crumpled, 2 by 84 by 0.1 mil, tape batons) actuated by a twist piezoelectric actuator. Figures 6.10 and 6.11 compare the three dimensional representations of the mode shapes between the theory and the experiment. While this comparison produces nice looking pictures, a different and potentially more informative method of examining the theoretical and experimental data is to decompose the deflections into bending and twist components. Figures 6.12 and 6.13 contain the decomposed mode shapes for the experiment and theory respectively.

In Figures 6.12 and 6.13, Mode 1 in the experiment is similar to Mode T1 in the theory, Mode 2 in the experiment is similar to Mode B1 in the theory, Mode 3 in the experiment is similar to Mode B2 in the theory and so on where B and T correspond with theoretical bending and torsion modes respectively. A summary of the experimental mode and their most similar theoretical mode shape is given in Table 6.5. In addition to providing the MAC for the comparison, the table also has the natural frequency for the relevant modes. Even though the actuator was in twist, two bending modes that appeared in the experiment matched very well with the theoretical frequencies. The torsion modes have good correlation on mode shapes between the theory and the experiment. However, the first torsion experimental natural frequency does not agree well with the theoretical predictions.

The two dimensional figures can proved some interesting insight into the nature of the modes. For the experimental modes in Figure 6.12 it appears that experimental modes numbers 1, 4, 5, and 6 are nearly pure twist modes, while modes numbers 2 and 3 are combined bending and twist modes and finally mode number 7 is primarily bending. Because the experiment used a torsion actuator it is not surprising that

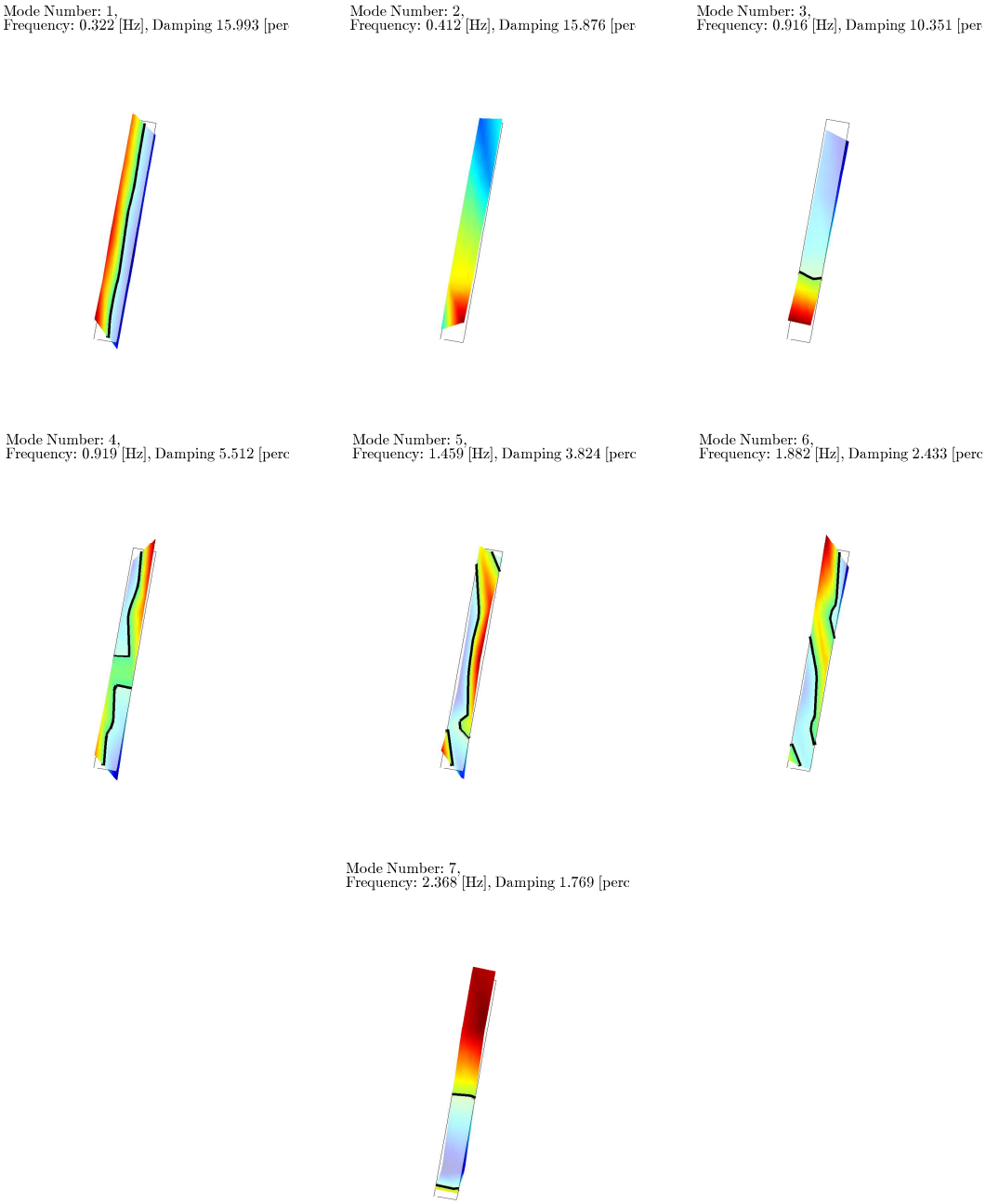

FIGURE 6.10: Experimental Mode Shapes for Configuration 3 (Aluminized Mylar, Crumpled, 2 by 84 by 0.1 mil, Tape Batons) with a Twist Piezoelectric Actuator

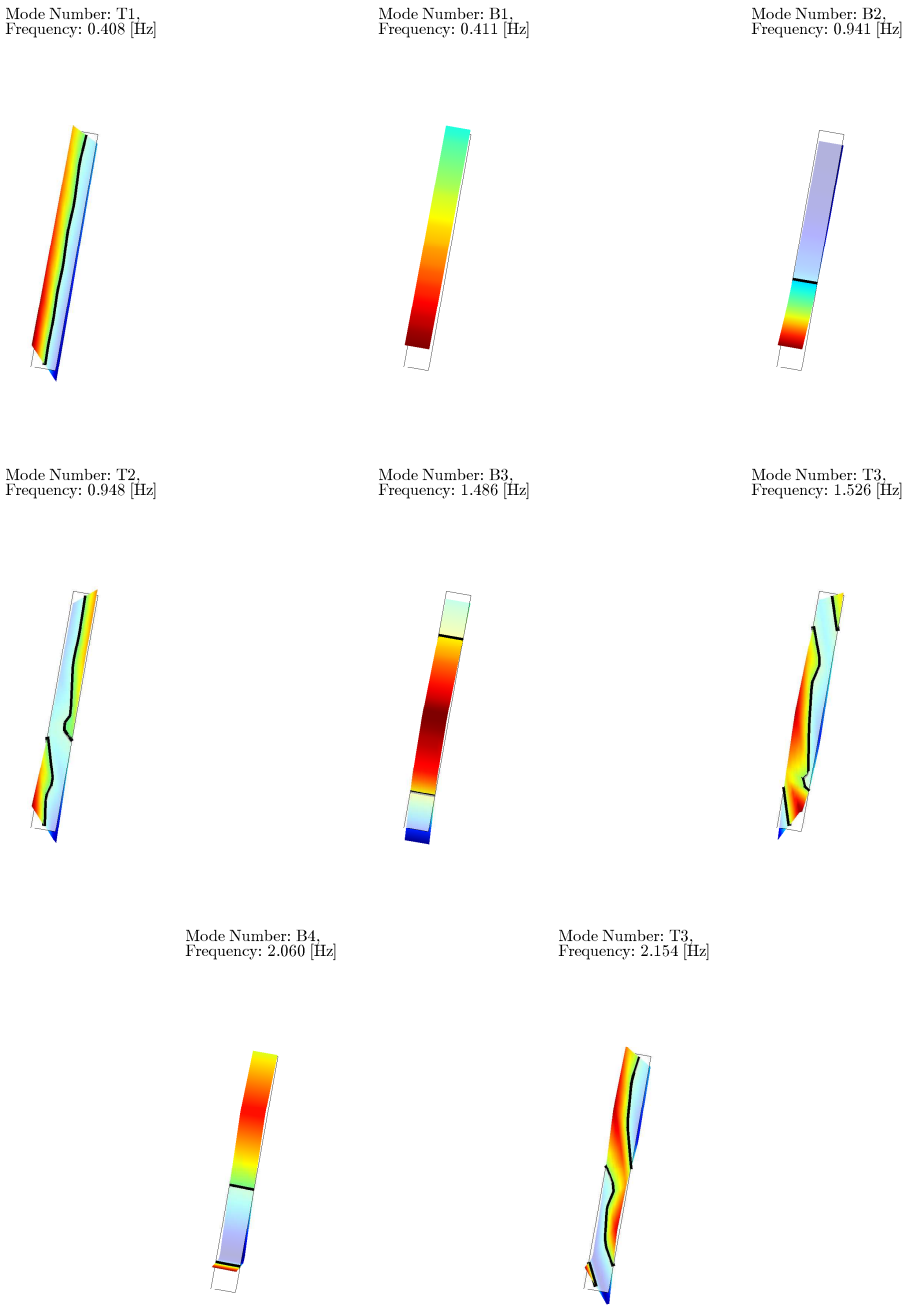

FIGURE 6.11: Theoretical Mode Shapes for Configuration 3 (Aluminized Mylar, Crumpled, 2 by 84 by 0.1 mil, Tape Batons) with a Twist Piezoelectric Actuator

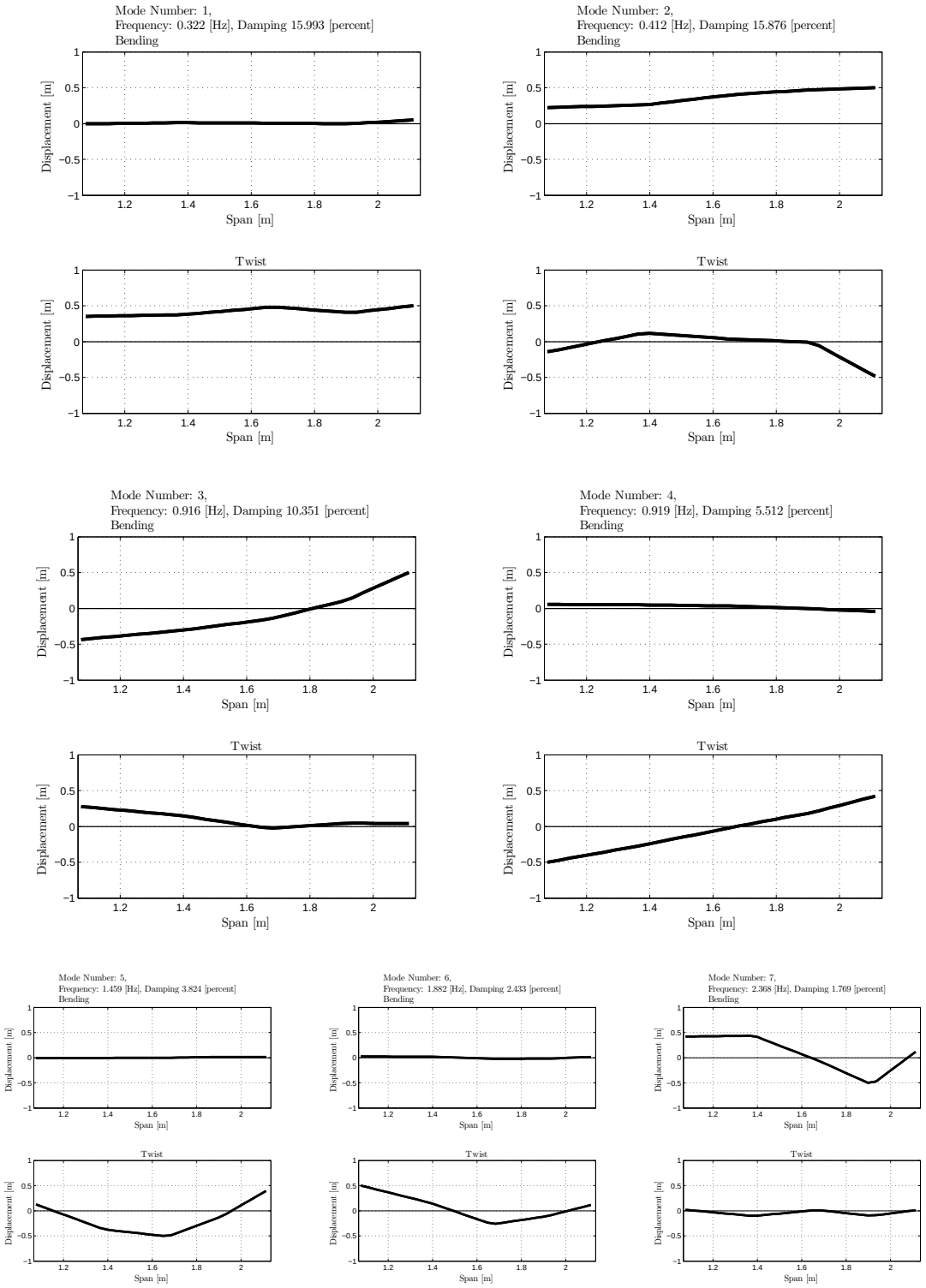

FIGURE 6.12: Experimental Mode Shapes for Configuration 3 (Aluminized Mylar, Crumpled, 2 by 84 by 0.1 mil, Tape Batons) with a Twist Piezoelectric Actuator

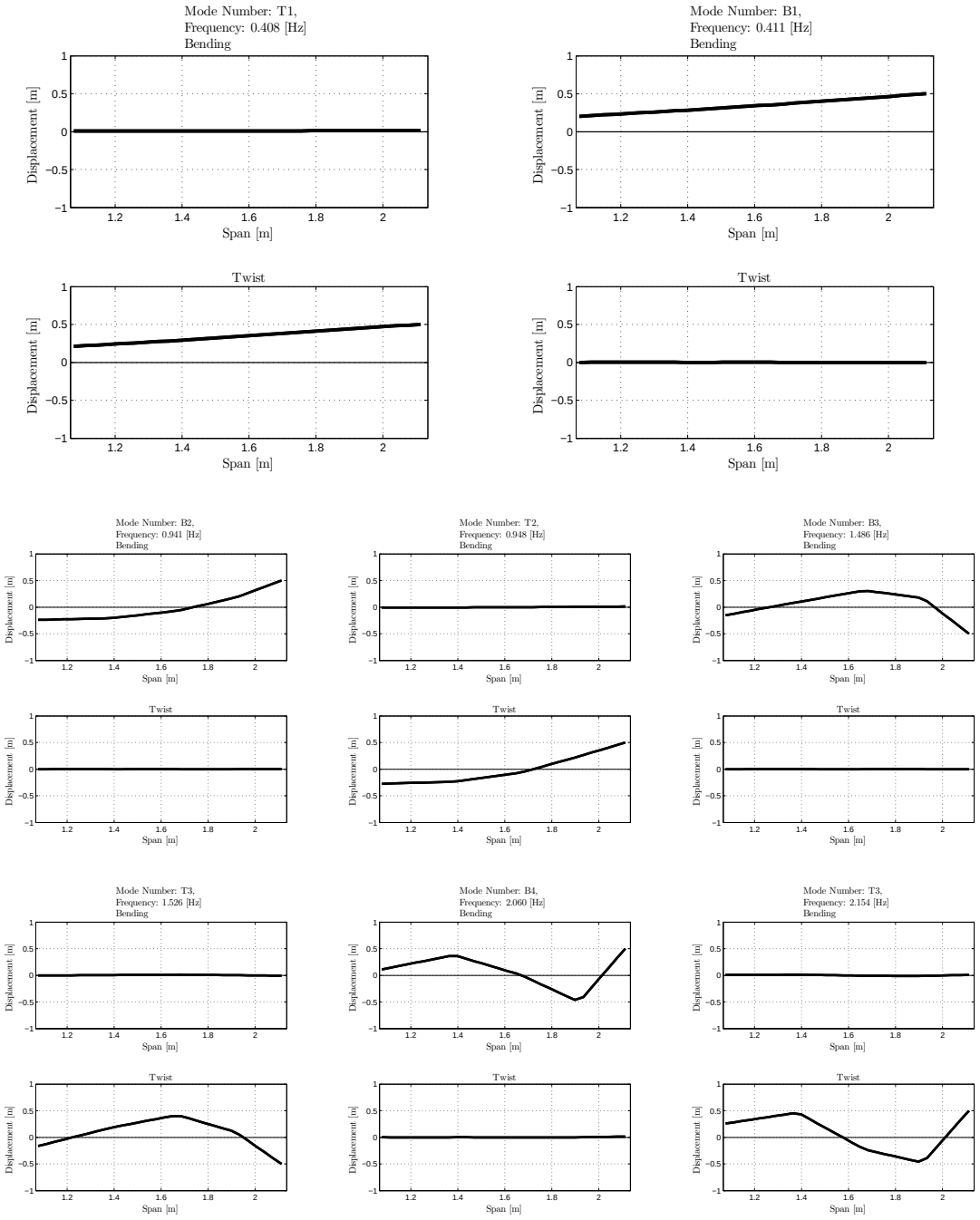

FIGURE 6.13: 2D Theoretical Mode Shapes for Configuration 3 (Aluminized Mylar, Crumpled, 2 by 84 by 0.1 mil, Tape Batons) with a Twist Piezoelectric Actuator

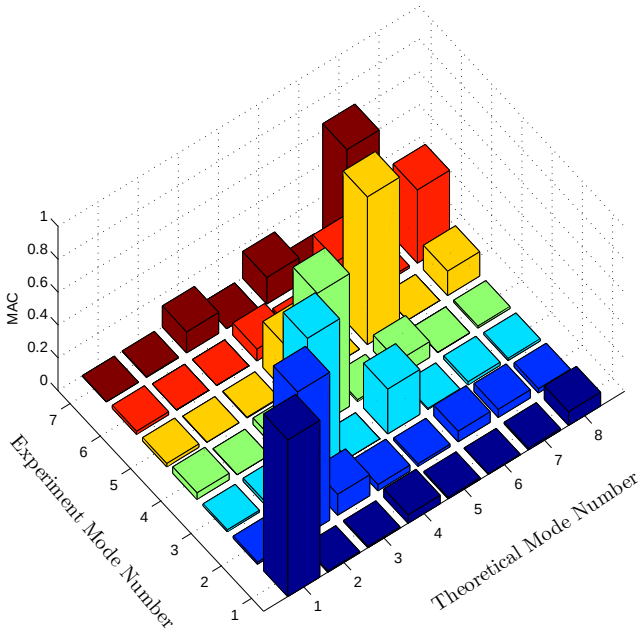

(a)

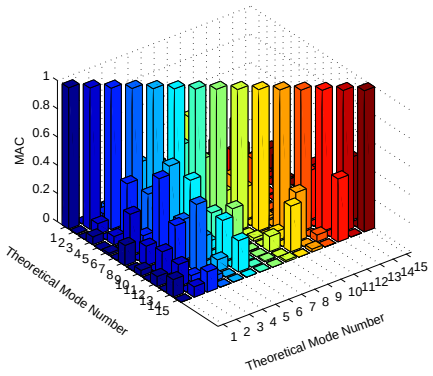

(b)

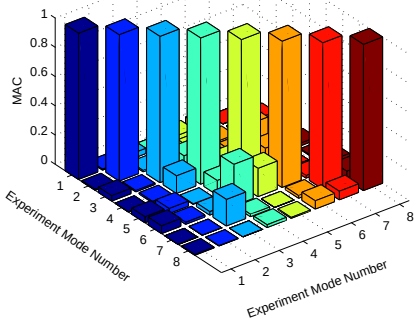

(c)

FIGURE 6.14: MAC for Configuration 3 (Aluminized Mylar, Crumpled, 2 by 84 by 0.1 mil, Tape Batons) with a Twist Piezoelectric Actuator

Table 6.5: Quantitative comparison between the theoretical and experimental mode shapes and frequencies for Configuration 3 (Aluminized Mylar, Crumpled, 2 by 84 by 0.1 mil, Tape Batons) with a Twist Piezoelectric Actuator

Exp Mode Number	Exp Freq [Hz]	Theory Freq [Hz]	Theory Type	MAC
1	0.322	0.408	T1	0.954
2	0.412	0.411	B1	0.900
3	0.916	0.941	B2	0.880
4	0.919	0.948	T2	0.808
5	1.459	1.526	T3	0.898

the observed bending modes have some torsion-like contribution. This is contrasted with the theoretical mode decompositions in Figure 6.13. In this figure it is clear that modes T1, T2, T3 and T4 are pure twist and modes B1, B2, B3 and B4 are pure bending. Theoretically this occurs because no coupling between the bending and torsion degrees of freedom is included in the model, i.e. there are no static imbalance terms.

The experimental 0.322 frequency response is an example of the type of additional peak that was observed in the experiment (because there is also a peak at 0.412 associated with the first bending natural frequency). In this case the appearance of the additional peak is due to the separation of the first bending and first torsion frequencies in the experiment, thus providing two peaks. Even though the system was actuated in torsion, the first torsion mode is the mode which has a frequency that is shifted away from the theoretical prediction. We currently have no hypothesis about why this shift in frequency occurred for this torsion mode. It is possible that the torsion actuator did not twist the system around the elastic axis of the structure which caused some static imbalance in the system which is not modeled and can shift the natural frequencies. However, from the experimental data, only the first mode has the shifted behavior so whatever the effect it is either limited to or most apparent at the lowest frequency torsion mode.

The final table included in this section is Table 6.6. This table contains the full MAC comparison between the theory and the experiment. This data is also represented in graphical form in Figure 6.14 a). This three dimensional bar plot is created directly from the data in Table 6.6. In the table the bolded entries are the entries in a given column that have the largest value. The first observation is that the first torsion mode, although not matching in frequency, has a very strong spatial correlation with the first torsion theoretical mode. In general the experimental torsion mode shapes are well correlated with the theoretical predictions. Figure 6.14 b) shows the MAC of the theoretical modes with themselves when measured at the experiment location. Figure 6.14 c) shows the MAC of the experimental modes with themselves. The data shows that the experimental mode shapes predicted by the analysis are largely orthogonal.

Table 6.6: Quantitative comparison between the theoretical and experimental mode shapes using MAC for Configuration 3 (Aluminized Mylar, Crumpled, 2 by 84 by 0.1 mil, Tape Batons) with a Twist Piezoelectric Actuator

		Experiment						
Mode		1	2	3	4	5	6	7
	Freq	0.32	0.41	0.92	0.92	1.46	1.88	2.37
T1	0.41	**0.954**	0.013	0.012	0.039	0.020	0.019	0.001
B1	0.41	0.006	**0.900**	0.019	0.001	0.001	0.000	0.004
B2	0.94	0.008	0.127	**0.880**	0.039	0.004	0.000	0.128
T2	0.95	0.052	0.037	0.000	**0.808**	0.279	0.073	0.000
B3	1.49	0.009	0.016	0.272	0.010	0.001	0.012	0.162
T3	1.53	0.003	0.065	0.006	0.097	**0.898**	0.311	0.003
B4	2.06	0.011	0.048	0.019	0.000	0.000	0.014	**0.642**
T3	2.15	0.082	0.026	0.013	0.012	0.148	0.446	0.004

6.3.2 Experiment 2: Mass Distribution Variation

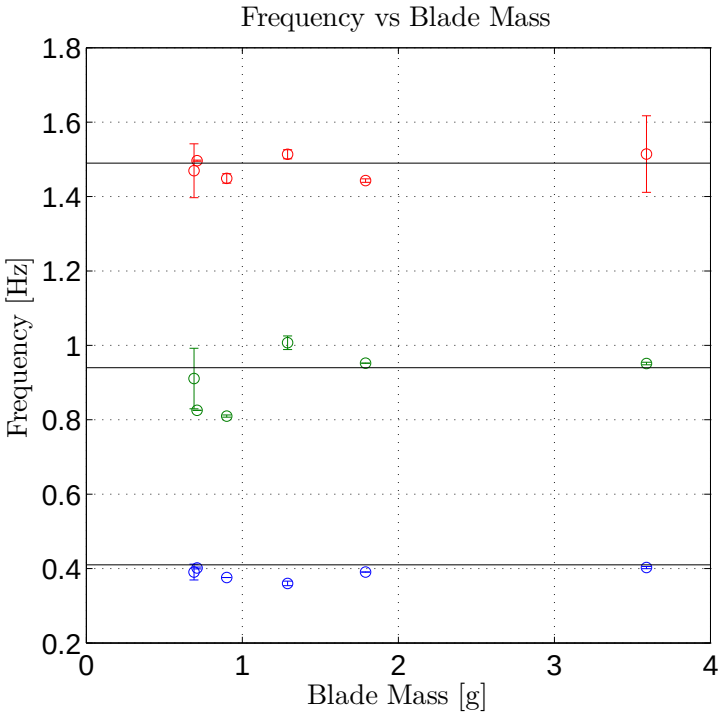

FIGURE 6.15: Hanging Membrane Natural Frequency Dependence on Blade Mass

In addition to studying the dynamics for different chords and thicknesses, we also explored the dynamics of the 84 inch structure with different features. The experiments reported in this section use the flap piezoelectric actuator. The features varied for the structure essentially vary the total weight of the structure. For this experiment the blade geometry, 84 inch span, 2 inch chord, and 0.1 mil thickness, remained constant. The detailed description of each of the configurations is given in Table 6.7.

The current theoretical model predicts that the natural frequency of the blade will not depend on the features that are varied in this experiment. Figure 6.15 shows the experimental frequencies overlaid on the theoretical predictions. While there are some discrepancies between the theory and the experiment, in general the natural

Table 6.7: Hanging Membrane Mass Variation Configurations Tested

Config	Total Mass [g]	Edge Tape	Batons	Tip Weight [g]
1c-v1	3.59	✓	CF	0
1c-v2	1.79		CF	0
1c-v3	0.69		Tape	0
1c-v4	1.29		Tape	0.60
1c-v5	0.90		Tape	0.21
1c-v6	0.71		Tape	0.02

frequencies match the theoretical prediction. Another trend is that the heavier blades tend to agree best with the theory.

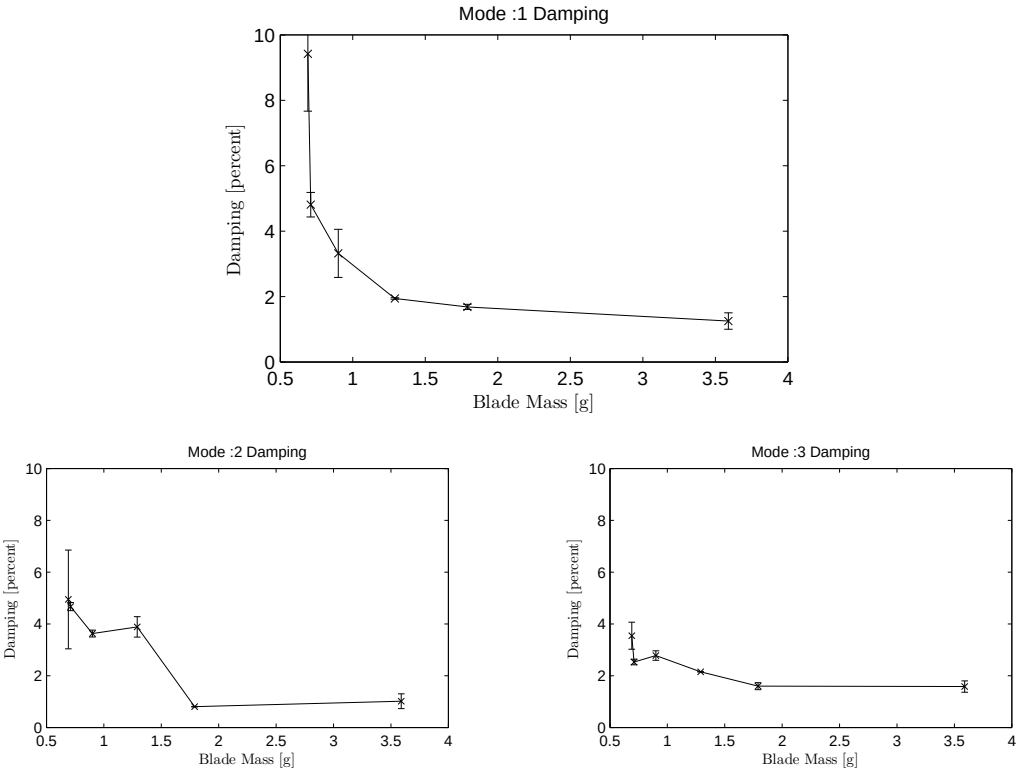

FIGURE 6.16: Hanging Membrane Damping Dependence on Weight

The next observation comes from looking at the damping as a function of blade mass. Figure 6.16 shows the trend for each of the first three structural modes. In general the damping ratio increases with decreasing mass in the structure. This trend is especially pronounced in the fundamental mode where the damping increases from

1.5 percent for the heaviest blade to 10 percent for the lightest blade. Noticeably, as the blade becomes extremely light, the damping levels increase rapidly and the system is extremely sensitive to changes in weight.

There is currently no explanation for this trend, and there is no hypothesis on the underlying physics that would drive this phenomenon. One observation is that the weight of the blade directly correlates to the tension or strain at the root of the blade. If the governing energy loss mechanism occurs at the root of the blade, whether it is due to the interface with the support structure or some other micro-mechanical phenomenon, the changing mass would be felt here the most.

6.3.3 Experiment 3: Span Variation

The final parameter variation experiment explored varying the span. In the simple linear models, varying the span is the only way to change the natural frequency of the system. A trait for all of the blades is that the torsion natural frequencies remain aligned with the bending natural frequencies. The experiment looks at different spans with the flap piezoelectric actuator used to actuate the system and the scanning laser vibrometers used to record the data.

Figure 6.17 shows the first 4 natural frequencies for each of the configurations with the solid lines being the theoretical predictions. In general there is good agreement in trend and magnitude between the theory and the experiment. This experiment demonstrates that the theoretical model can capture the natural frequency trend as the span is varied. This confirms that we have captured the dominating physics in our system.

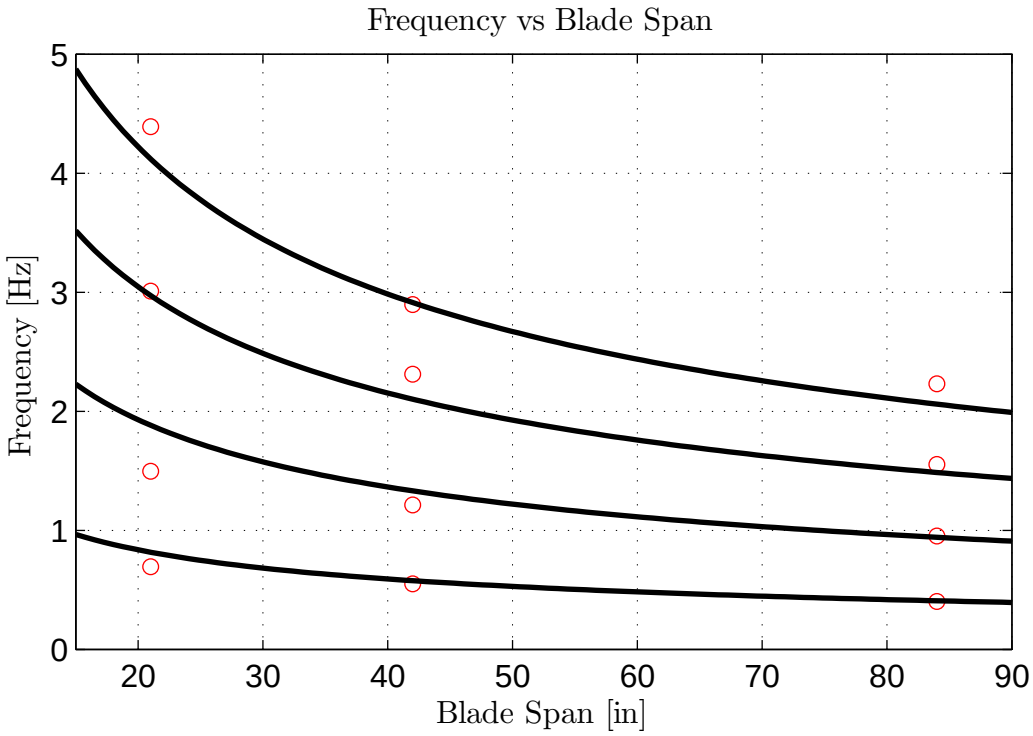

FIGURE 6.17: Hanging Membrane Natural Frequency Dependence on Blade Span

6.4 Conclusion for the Dynamics and Stability of a Hanging Membrane in a Gravitation Field

This section outlines the effort that has been made to build and validate a model that captures a previously unexplored solar radiation-structure interaction. A membrane hanging in a gravitational field is used as an analogy to a heliogyro blade. The document demonstrates how a classical structural model can be coupled with a solar radiation model. Simulations of the coupled solar-structure interaction indicate that an instability can arise due to this interaction. The initial exploration was limited due to the paradoxical nature of forced thin membrane structures. Even when including a large number of degrees of freedom, the stability boundary demonstrated a non-uniform convergence that will be explored in future work.

In an effort to validate the structural model a unique experimental exploration

was undertaken. Specifically a vacuum chamber was used to explore the dynamics of a thin membrane stiffened by gravity. During these experiments the natural frequencies of the structures are identified and shown to compare well with the theoretical predictions. The comparison was validated for different chord, span and thickness experiment specimens. As predicted by the theoretical model, the natural frequencies can only be shifted by changing the span of the structure. These experimental results provide an invaluable method of validating the structural models for these types of thin membranes and begin to build confidence in the models. The experiments also showed that the damping of the hanging membrane is largely dependent on the membrane loading, a trend which can not be explained by the current theoretical model that does not include any energy loss mechanisms. Future work includes designing an experiment to validate the coupled solarelastic model and continuing to explore the reasons for damping in the experiments.

7

Dynamics and Stability of a Spinning Membrane in Space

The focus of this final chapter is theoretical research on the stability of a spinning membrane. This research directly supports the ongoing research on heliogyro solar sails currently underway at NASA. Specifically, this research supports an effort lead by NASA's Langley Research Center (LaRC) to design, build and fly a cubesat sized heliogyro spacecraft. NASA calls the spacecraft the "High-Performance, Enabling, Low-Cost, Innovative, Operational Heliogyro Solar Sail" or HELIOS. As mentioned in the introduction, the nominal design calls for a set of six blades, each with a span of 220 m, chord of 0.75 m and a nominal thickness of 2.54 microns that spin around the hub at a rate of 1 RPM. The analysis presented in this section is based on this configuration, with the goal of developing simple models that can accurately predict the most critical dynamic instabilities and that can be used as preliminary design tools.

The initial solarelastic model uses the linear model of the beam with flap, twist, and in-plane bending. We couple this structural model to a solar radiation force

model. The section then presents the results of a structural analysis using the linear model and compares these results with the published results for a rotating membrane. Next, this section outlines the solarelastic stability boundary for the current HELIOS configuration. The analysis specifically focuses on the convergence behavior of the linear model. The section then compares the initial linear model predictions with the results using the nonlinear model based on the Hodges and Dowell (1974) structural model. We show that the inclusion of the non-linear terms significantly changes the predicted solarelastic behavior of the system. Finally, this section uses the nonlinear model to explore the stability of the proposed HELIOS design. The work presented in this chapter has been published in multiple formats.

Publications

1. **Gibbs and Dowell (2013)** This paper couples linear and nonlinear rotating structural models with an optical solar radiation pressure model for a completely reflective surface. The resulting time varying ordinary differential equations are solved in a quasi-static sense, where an instantaneous stability boundary is determined. The quasi-static analysis with the linear model predicts a divergence type instability and slow and non-uniform modal convergence using parameters for a representative heliogyro spacecraft blade. The nonlinear model predicts a flutter instability at a lower radiation pressure and has improved modal convergence characteristics. The paper uses the nonlinear model to evaluate the stability of a NASA heliogyro concept design and explore the dependence of the stability boundary on the spacecraft rotation rate for the case of the sun directly overhead. Increasing the spin rate of the spacecraft improves the solarelastic stability, but must be traded off with decreased spacecraft maneuverability.

2. **Gibbs et al. (2014d)** In this paper we explore the stability of a particu-

lar propellantless spacecraft, a spinning, helicopter-like solar sail. We show that our model reproduces previously published works and compares well with simulations conducted with a finite element simulation. In addition the paper explores the stability of a proposed spinning solar sail during deployment and identify critical combinations of spin rate and lengths that increase the possibility of an instability arising.

7.1 Theoretical Heliogyro Model

This section will explore the stability of the heliogyro using both a linear and nonlinear model.

7.1.1 Linear Heliogyro Model

The linear theoretical model is similar to the model presented Chapter 6 with the centrifugal tension term from Eq. 2.9 replacing the gravitational tension from Eq. 2.8. In addition to the torsion and out of plane bending degrees of freedom, the spinning solar sail model also includes and in plane bending degrees of freedom. The governing equation for the in plane bending is identical to the out of plane bending equations, however the moment of inertia is modified to take into account the correct cross-sectional dimensions. The structural model also includes the so-called tennis racket effect which stiffens the blade in torsion and softens the blade in the in-plane bending direction. The simplest way to describe the equations is to retain the linear terms in the nonlinear spinning model. The governing equation is repeated here for

convenience.

$$
\begin{aligned}
M_\phi &= \sum_j A_{ij}\Phi_j + B_{ij}\ddot{\Phi}_j \\
L_w &= \sum_j E_{ij}W_j + F_{ij}\ddot{W}_j \\
L_v &= \sum_j K_{ij}V_j + L_{ij}\ddot{V}_j
\end{aligned}
\tag{7.1}
$$

with

$$
\begin{aligned}
A_{ij} &= \int_0^1 \left[\bar{G}Jg_i'g_j' + \frac{1}{2}\bar{m}(1-\xi^2)\bar{k}_a^2 g_i'g_j' + \bar{m}(\bar{k}_{m2}^2 - \bar{k}_{m1}^2)g_i g_j\right] d\xi \\
B_{ij} &= \int_0^1 \bar{m}\bar{k}_m^2 g_i g_j \, d\xi \\
E_{ij} &= \int_0^1 \left[\bar{E}I_1 w_i'' w_j'' + \frac{1}{2}\bar{m}(1-\xi^2)w_i'w_j'\right] d\xi \\
F_{ij} &= \int_0^1 \bar{m}w_i w_j \, d\xi \\
K_{ij} &= \int_0^1 \left[\bar{E}I_1 v_i'' v_j'' + \frac{1}{2}\bar{m}(1-\xi^2)v_i'v_j' - \bar{m}v_i v_j\right] d\xi \\
L_{ij} &= \int_0^1 \bar{m}v_i v_j \, d\xi
\end{aligned}
\tag{7.2}
$$

Using the solar radiation model from Section 2.2.2 we can write out the generalized forces as:

$$
\begin{aligned}
M_\phi &= 0 \\
L_w &= \bar{p}\left[\cos^2\gamma + \sin 2\gamma \sum_j \left(\sin\psi\phi_j - \cos\psi\bar{w}_j'\right)\right] \\
L_v &= -\bar{p}\cos^2\gamma \sum_j \phi_j
\end{aligned}
\tag{7.3}
$$

$\bar{p}$ is the non-dimensional pressure that is equal $\bar{p} = (p_o c)/(m_r\Omega^2 L)$. Substituting Eq. 7.3 into Eq. 7.1, yields the following typical governing linear solarelastic equation

for each degree of freedom.

$$
\begin{aligned}
0 &= \sum_j \left[A_{ij}\Phi_j + B_{ij}\ddot{\Phi}_j \right] \\
\int_0^1 \bar{p}\cos^2\gamma w_i \, d\xi &= \sum_j \left[C_{ij}W_j + D_{ij}\ddot{W}_j + \alpha_{ij}W_j - \beta_{ij}\Phi_j \right] \\
0 &= \sum_j \left[E_{ij}V_j + F_{ij}\ddot{V}_j + \Gamma_{ij}\Phi_j \right]
\end{aligned}
\tag{7.4}
$$

with

$$
\begin{aligned}
\alpha_{ij} &= \bar{p}\sin 2\gamma \cos\psi \int_0^1 w_i w_j' \, d\xi \\
\beta_{ij} &= \bar{p}\sin 2\gamma \sin\psi \int_0^1 w_i g_j \, d\xi \\
\Gamma_{ij} &= \bar{p}\cos^2\gamma \int_0^1 v_i g_j \, d\xi
\end{aligned}
\tag{7.5}
$$

The model incorporates the solar radiation pressure as a static term in the out-of-plane bending equation and additional stiffness terms in the out-of-plane and in-plane bending equations. For this model, the solar radiation pressure couples the in-plane and out-of-plane equations to the torsional degree of freedom, but the solar radiation pressure does not directly affect the torsion equation. Note, the solar radiation terms $A2_{ij}$ and $A3_{ij}$ are time varying when γ is not equal to $n\pi/2$ because the ψ angle varies with time. To account for this we can either use a time marching algorithm or do a snapshot analysis for a fixed ψ.

7.1.2 Nonlinear Heliogyro Model

The nonlinear solarelastic model includes all of the terms described in Section 2.1.4. As with the linear analysis, the influence of the solar radiation pressure is captured by including the generalized force terms described in Eq. 7.3. The final equations are repeated here for convinience, with the main difference between the equations

here and the equations from Section 2.1.4 being the inclusion of the solar radiation pressure it this section. Eq. 7.6 gives the characteristic equation for the i'th twisting degree of freedom.

$$\begin{aligned} 0 = \sum_j \Big[& A_{ij}\Phi_j + B_{ij}\ddot{\Phi}_j \\ & + \sum_k \Big(C_{ijk}V_jW_k + D_{ijk}\dot{V}_j\Phi_k + T1_{ijk}\Phi_j\dot{V}_k \Big) \Big] \end{aligned} \tag{7.6}$$

with

$$\begin{aligned} A_{ij} &= \int_0^1 \Big[\bar{G}Jg_i'g_j' + \frac{1}{2}\bar{m}(1-\xi^2)\bar{k}_a^2 g_i'g_j' \\ &\qquad + \bar{m}(\bar{k}_{m2}^2 - \bar{k}_{m1}^2)g_ig_j \Big]\, d\xi \\ B_{ij} &= \int_0^1 \bar{m}\bar{k}_m^2 g_ig_j\, d\xi \\ C_{ijk} &= \int_0^1 \Delta\bar{E}Ig_iv_j''w_k''\, d\xi \\ D_{ijk} &= \int_0^1 2\bar{m}\bar{k}_a^2 g_i' \frac{v_j'''}{\omega_i^4} g_k'\, d\xi \\ T1_{ijk} &= 2\bar{k}_a^2\bar{m}\int_0^1 g_i'g_j' \left[\int_\xi^1 v_k(\eta)\, d\eta \right] d\xi \end{aligned} \tag{7.7}$$

Similarly Eq. 7.8 provides the characteristic equation for the i'th out-of-plane bending degree of freedom.

$$\begin{aligned} FSF_i = \sum_j \Big[& E_{ij}W_j + F_{ij}\ddot{W}_j + \alpha_{ij}W_j - \beta_{ij}\Phi_j \\ & + \sum_k \Big(G_{ijk}\Phi_jV_k + H_{ijk}\dot{V}_jW_k + T2_{ijk}W_j\dot{V}_k \Big) \Big] \end{aligned} \tag{7.8}$$

with

$$
\begin{aligned}
FSF_i &= \bar{p} \int_0^1 \cos^2 \gamma w_i \, d\xi \\
\alpha_{ij} &= \bar{p} \sin 2\gamma \cos \Psi \int_0^1 w_i w_j' \, d\xi \\
\beta_{ij} &= \bar{p} \sin 2\gamma \sin \Psi \int_0^1 w_i g_j \, d\xi \\
E_{ij} &= \int_0^1 \left[\bar{E} I_1 w_i'' w_j'' + \frac{1}{2} \bar{m} (1 - \xi^2) w_i' w_j' \right] d\xi \\
F_{ij} &= \int_0^1 \bar{m} w_i w_j \, d\xi \\
G_{ijk} &= \int_0^1 \Delta \bar{E} I w_i'' g_j v_k'' \, d\xi \\
H_{ijk} &= \int_0^1 2\bar{m} w_i' \frac{v_j''''}{\omega_i^4} w_k' \, d\xi \\
T2_{ijk} &= 2\bar{m} \int_0^1 w_i' w_j' \left[\int_\xi^1 v_k(\eta) \, d\eta \right] d\xi
\end{aligned}
\tag{7.9}
$$

Finally Eq. 7.10 provides the characteristic equation for the i'th in-plane bending degree of freedom.

$$
\begin{aligned}
0 = \sum_j \Big[& K_{ij} V_j + L_{ij} \ddot{V}_j + \Gamma_{ij} \Phi_j \\
& + \sum_k \Big(M_{ijk} \Phi_j W_k + N_{ijk} \dot{V}_j V_k + T3_{ijk} V_j \dot{V}_k \\
& \qquad - U1_{ijk} W_j \dot{W}_k - U2_{ijk} V_j \dot{V}_k \Big) \Big]
\end{aligned}
\tag{7.10}
$$

with

$$
\begin{aligned}
\Gamma_{ij} &= \bar{p}\cos^2\gamma \int_0^1 v_i g_j \, d\xi \\
K_{ij} &= \int_0^1 \left[\bar{E}\bar{I}_1 v_i'' v_j'' + \frac{1}{2}\bar{m}(1-\xi^2) v_i' v_j' - \bar{m} v_i v_j \right] d\xi \\
L_{ij} &= \int_0^1 \bar{m} v_i v_j \, d\xi \\
M_{ijk} &= \int_0^1 \Delta\bar{E}\bar{I} v_i'' g_j w_k'' \, d\xi \\
N_{ijk} &= \int_0^1 2\bar{m} v_i' \frac{v_j'''}{\omega_i^4} v_k' \, d\xi \\
T3_{ijk} &= 2\bar{m} \int_0^1 v_i' v_j' \left[\int_\xi^1 v_k(\eta)\, d\eta \right] d\xi \\
U1_{ijk} &= 2\bar{m} \int_0^1 v_i \int_0^\xi w_j'(\eta) w_k'(\eta)\, d\eta \, d\xi \\
U2_{ijk} &= 2\bar{m} \int_0^1 v_i \int_0^\xi v_j'(\eta) v_k'(\eta)\, d\eta \, d\xi
\end{aligned}
\tag{7.11}
$$

Combining Eqs. 7.6, 7.8 and 7.10 produces a set of nonlinear ODE's governing the generalized coordinates in twist, flap and in-plane bending. For the special case where the sun is directly overhead, $\gamma = 0$, the equations are time invariant. For this case we can conduct a a linear perturbation analysis around the static equilibrium. For this analysis we expand the generalized coordinates into a static equilibrium coordinate plus a dynamic perturbation.

$$
\begin{aligned}
W_i(\tilde{t}) = W_{oi} + \tilde{w}(\tilde{t}), \quad V_i(\tilde{t}) = V_{oi} + \tilde{v}(\tilde{t}) \\
\Phi_i(\tilde{t}) = \Phi_{oi} + \tilde{\phi}(\tilde{t})
\end{aligned}
\tag{7.12}
$$

Substituting Eq. 7.12 into Eqs. 7.6, 7.8 and 7.10, we first solve for the the static equilibrium solution by solving the leading order nonlinear algebraic equation for Φ_{oi}, W_{oi}, and V_{oi}. Substituting the static equilibrium back into Eqs. 7.6, 7.8 and

7.10 yields a linear equation for the perturbation coordinates. The equation is in the form of a generalized eigenvalue problem that we solve using available eigenvalue solution packages. The eigenvalues of the perturbation coordinates determine the stability of the solarelastic system.

7.2 Simulations Using the Linear Solarelastic Model

7.2.1 Structural Simulations Using the Linear Solarelastic Model

Table 7.1: Baseline Non-Dimensional Parameters for HELIOS

Property	Value
$\bar{EI}_1$	1.58×10^{-13}
$\bar{EI}_2$	1.18×10^{-2}
$\bar{GJ}$	2.38×10^{-13}
$\bar{k}_{m1}$	3.60×10^{-9}
$\bar{k}_{m2}$	9.84×10^{-4}

This section begins by exploring the structural dynamics, in the absence of solar radiation pressure. The structural analysis uses the parameters for the HELIOS concept listed in Table 7.1. By looking at the table, we can see that the terms associated with the bending stiffness terms are much smaller than unity. Because the bending terms are associated with the highest order spatial derivative in the bending equations, our assumed modes, which are chosen to satisfy all of the boundary conditions, are no longer a good approximation of the leading order equation. This manifests itself in requiring a large number of modes to produce a converged solution.

Figure 7.1 shows the natural frequencies as a function of the number of modes that are included in the modal expansion for each degree of freedom. Because the degrees of freedom are uncoupled in the linear structural model, we can examine each of the degrees of freedom independently. The figure also contains the closed form

natural frequencies for the pure membrane case (MacNeal (1971)), where the bending stiffness is identically equal to zero, for the torsion and out-of-plane bending modes. As we increase the number of modes, the natural frequencies predicted by the current model converge to the membrane solution due to the small bending stiffness. The number of modes required to converge the natural frequencies is large because the assumed modes satisfy a fourth-order boundary value problem for the beam, while the dynamics of our spinning system are dominated by the second-order, tension-like term. While, it is possible to use modes that satisfy the second-order membrane equations, they would no longer satisfy all of the boundary conditions required by the beam equation. An alternate approach is to conduct a boundary layer perturbation analysis that finds an outer solution that satisfies the beam equation in a small boundary layer at the root and the tip of the blade, and then an inner solution that satisfies the membrane equation over the remainder of the domain.

7.2.2 Solarelastic Simulations Using the Linear Solarelastic Model

For our initial analysis we choose the HELIOS parameters with the sun inclined at 45 degrees from directly overhead. As mentioned in the derivation for cases when the sun is not directly overhead the coefficients of solar radiation pressure are time varying as the heliogyro blade rotates through different angles of Ψ. For this analysis, we conduct a quasi-steady analysis with the goal of solving for the linear stability boundary for a fixed rotation angle Ψ. The linear stability of the system can be determined as a function of the rotation angle. To determine completely the dynamic stability of the system a numerical time marching algorithm could be used.

The first analysis looks at the stability boundary as the parameter $\bar{p}$ is varied for different number of modes. This helps establish modal convergence and identifies the type of instability that may arise for the HELIOS system. For the initial analysis Ψ is set to 0. Figure 7.2 shows the results of the simulation. The figure shows

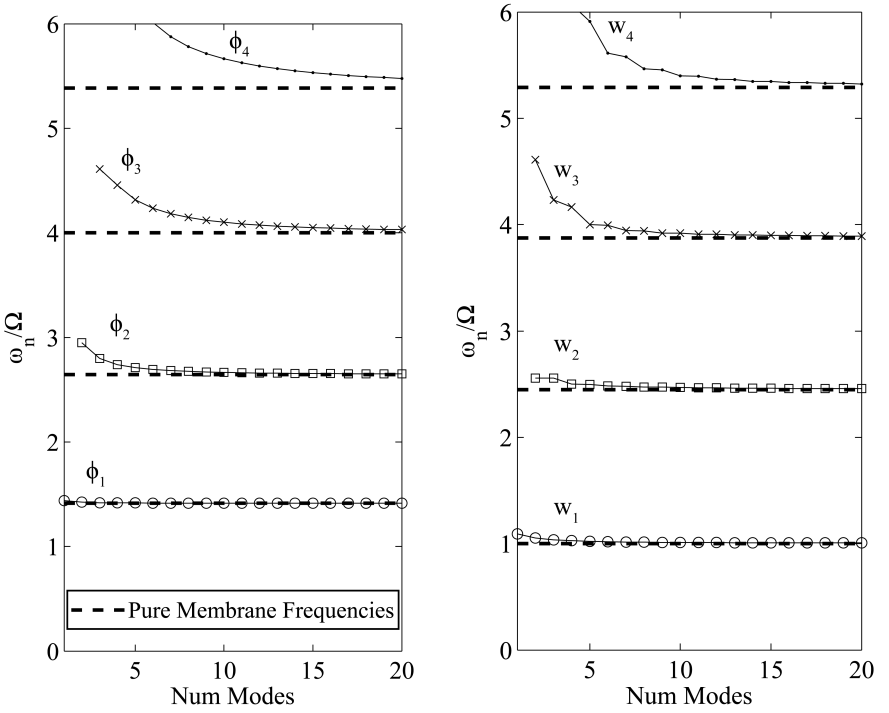

(a) Twist Frequencies (b) Out-of-Plane Bending Frequencies

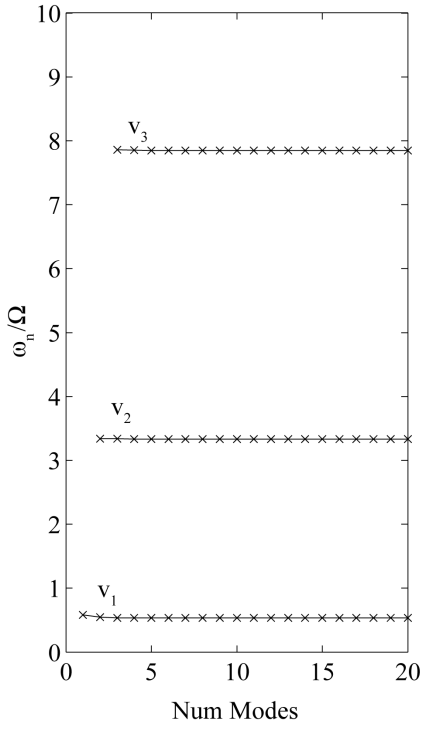

(c) In-Plane Bending Frequencies

FIGURE 7.1: Comparison of HELIOS Frequencies to Analytical Frequencies for a Pure Membrane (MacNeal, 1971)

the frequencies as a function of the non-dimensional solar radiation pressure. The figure identifies locations where the real part of the eigenvalue goes unstable with different color lines. For the current parameters the system transitions between a first bending mode divergence and a first and second bending coalescence flutter instability at a non-dimensional radiation pressure near one depending on if there are an even or odd number of modes in the modal expansion. For these parameters, the stability boundary does not appear to converge to a fixed value or instability type even as you increase the number of assumed modes over 100. We believe that this is a phenomenon similar to the membrane paradox found in the supersonic aeroelastic panel flutter literature (Spriggs et al. (1969)). Because the bending stiffness is such a small term for the current parameters, a more careful perturbation treatment of the system is required to determine the correct stability boundary.

Due to the poor convergence behavior of the linear model, we focused our analysis on the nonlinear model presented in the next section.

7.3 Simulations Using the Nonlinear Solarelastic Model

This section will explore solarelastic simulations for the current design parameters for the HELIOS demonstrator mission. The dimensional structural parameters are included in Table 7.2. These parameters correspond with the non-dimensional parameters listed in Table 7.1. In this section we will explore the following topics.

1. Analysis types for the nonlinear solarelastic model
2. Nonlinear solarelastic model validation and convergence behavior
3. HELIOS nominal spin rate analysis
4. HELIOS deployment analysis

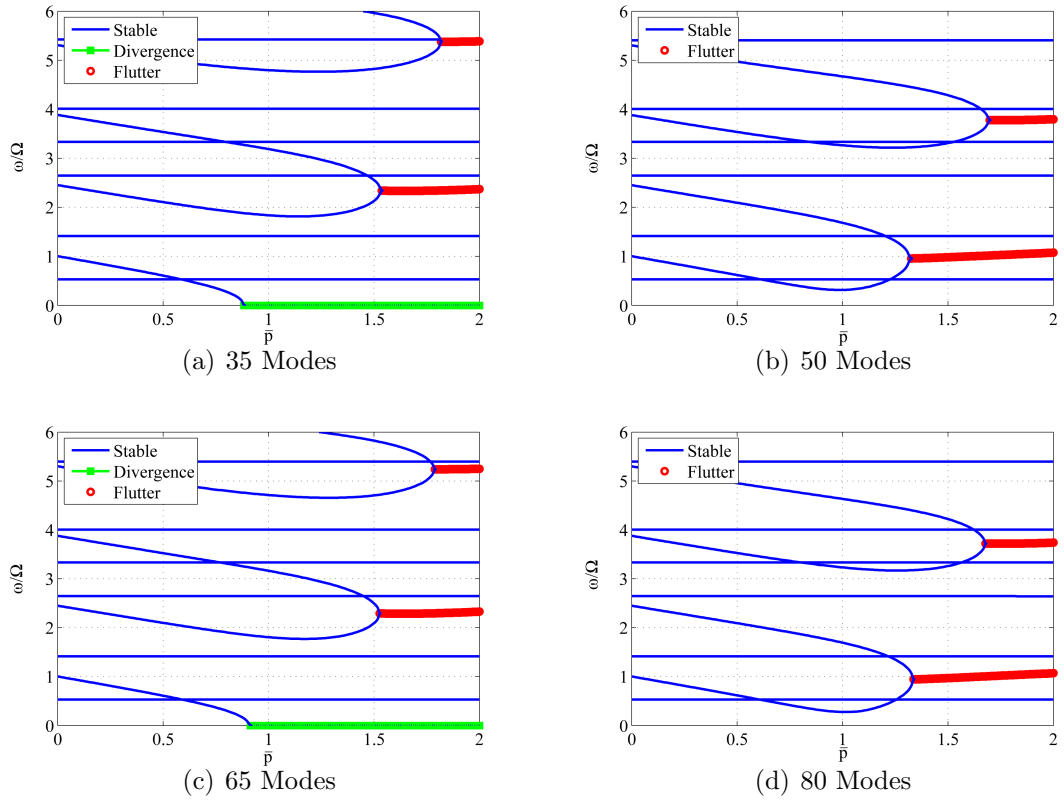

(a) 35 Modes (b) 50 Modes

(c) 65 Modes (d) 80 Modes

FIGURE 7.2: Imaginary Part of the Eigenvalues for HELIOS Configuration with $\gamma = 45\,\text{deg}$ as Number of Modes Varies

7.3.1 Typical Analysis for Nonlinear Solarelastic Model

Before applying our solarelastic model to analyze the HELIOS design, we will discuss the types of simulations that are used to create the results presented throughout the rest of the section. For the perturbation analysis with the sun directly overhead to create the eigenvalue problem we assume that the perturbation coordinates can be represented by $\bar{c}e^{\omega t}$. To run the analysis we determine the eigenvalue, ω, over a range of applied solar radiation pressure, p_o levels. In general the eigenvalues are complex values. The imaginary part of the eigenvalue is the frequency of the oscillation and the real part of the eigenvalue is the growth rate. The blade is stable at radiation pressures where the real part of all eigenvalues is less than zero and unstable if there

Table 7.2: Baseline Dimensional Properties for HELIOS

Property	Value	Units
Thickness (h)	2.74e-6	m
Chord (c)	0.75	m
Span (L)	220	m
ρ	1490	kg/m^3
E	9.67e+9	N/m^2
G	3.64e+9	N/m^2
Ω	1.0	RPM

is one eigenvalue that has a positive real part.

Figure 7.3 shows the eigenvalues for a spinning blade with the parameters listed in Table 7.2. For the simulation, the Rayleigh Ritz expansion includes 40 modes in each of the twist, flap and in-plane degrees of freedom, giving the system a total of 120 generalized coordinates. Figure 7.3 (a) shows the real part of the eigenvalues versus the nondimensional solar radiation pressure. The figure shows that the system will become unstable at a nondimensional solar radiation pressure between 3e-3 and 4e-3. Figure 7.3 (b) shows the evolution of the imaginary portion of the eigenvalue versus the nondimensional solar radiation pressure. The figure shows that the instability is caused by the coalescence of two low frequency modes.

In addition to simulating a range of solar radiation pressures, when parameter variation studies are conducted we are able to improve the speed of our simulations by conducting an intelligent search for the first radiation pressure that has an unstable eigenvalue. The search algorithm starts with a course range of radiation pressure values. Once the first unstable eigenvalue is discovered we have bracketed the instability radiation pressure and can hone in on the instability radiation pressure to the level of precision desired.

When the sun is not directly overhead, we conduct time domain analysis on

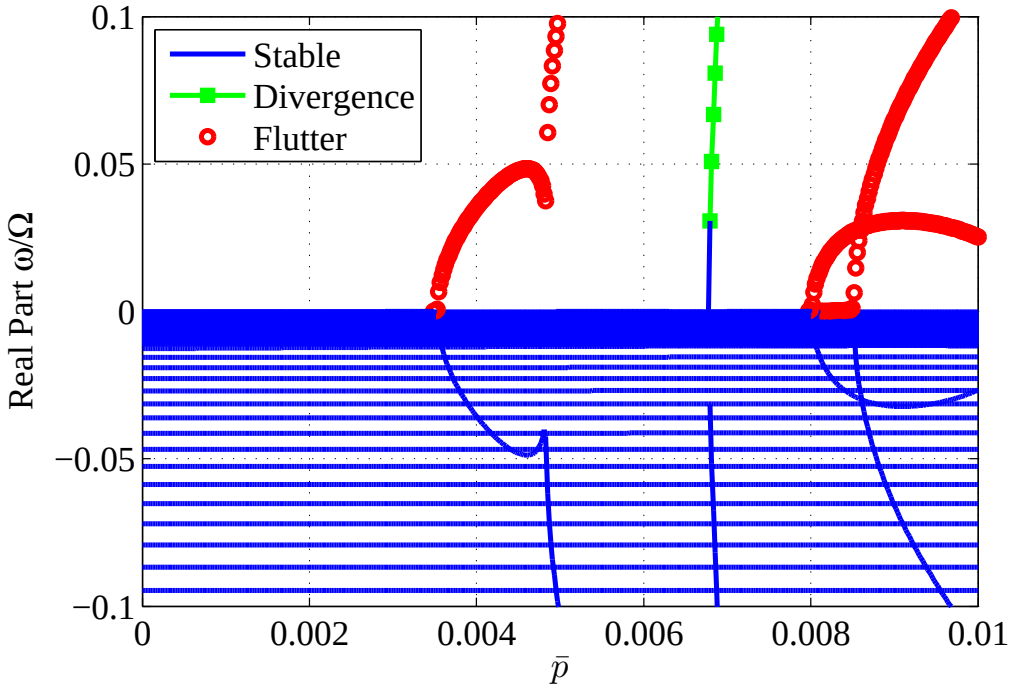

(a) Real Part of the Eigenvalue vs Solar Radiation Pressure

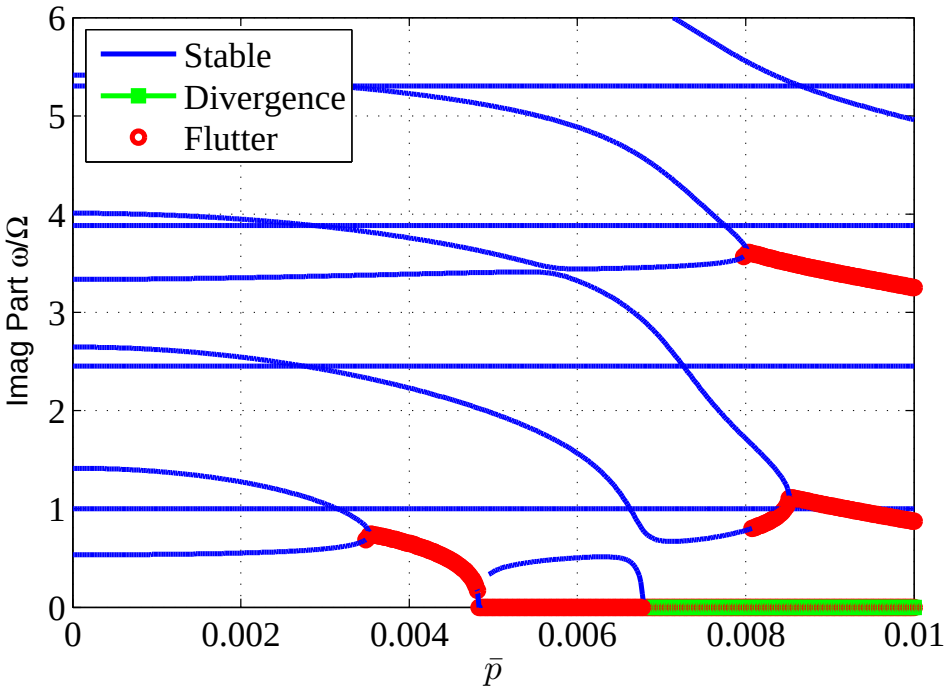

(b) Imaginary Part of the Eigenvalue vs Solar Radiation Pressure

FIGURE 7.3: Eigenvalues for HELIOS Configuration

the governing equations. From the time histories we can determine the damping levels and frequencies by conducting an FFT of the response. Figure 7.4 is a typical time history for the parameters from Table 7.2 and a sun skew angle $\gamma = 0.1$ rad and 5 modes in each of the twist, flap and in-plane degrees of freedom, giving the system a total of 15 generalized coordinates. The smaller degrees of freedom is dictated by the nonlinear nature of the problem that makes time domain simulations computationally expensive. The time history is segmented into three components. The blade is first spun for 2 revolutions with no applied solar radiation pressure. The non-dimensional solar radiation pressure is the linearly increased to its full value, in this case 4.76e-3, over 10 revolutions. The slow ramp is included to ensure that the system does encounter a numerical instability and that we reach the steady-state solution as quickly as possible. After the ramp-up, the simulation is continued for an addition 50 revolutions.

For the simulation presented in Figure 7.4, after arriving at the final pressure we see that the systems enters a limit cycle oscillation but remains stable. In this case, although the radiation pressure is larger than the instability radiation pressure for the sun overhead case, the $\gamma = 0.1$ sun skew angle increases the stability boundary to a larger value. The sun overhead representing the most critical condition from a solarelastic stability perspective is a trend that we have observed in many of our simultaions, however this trend has not been rigorously proven in this document.

7.3.2 Model Validation and Modal Convergence Behavior for Nonlinear Solarelastic Model

To validate our model we can compare our current analysis results to published values from Natori et al. (1989). Table 7.3 contains the nondimensional parameters for the comparison case. Figure 7.5 shows the radiation pressure at which the solarelastic model predicts a divergence instability as a function of the modes in the Rayleigh

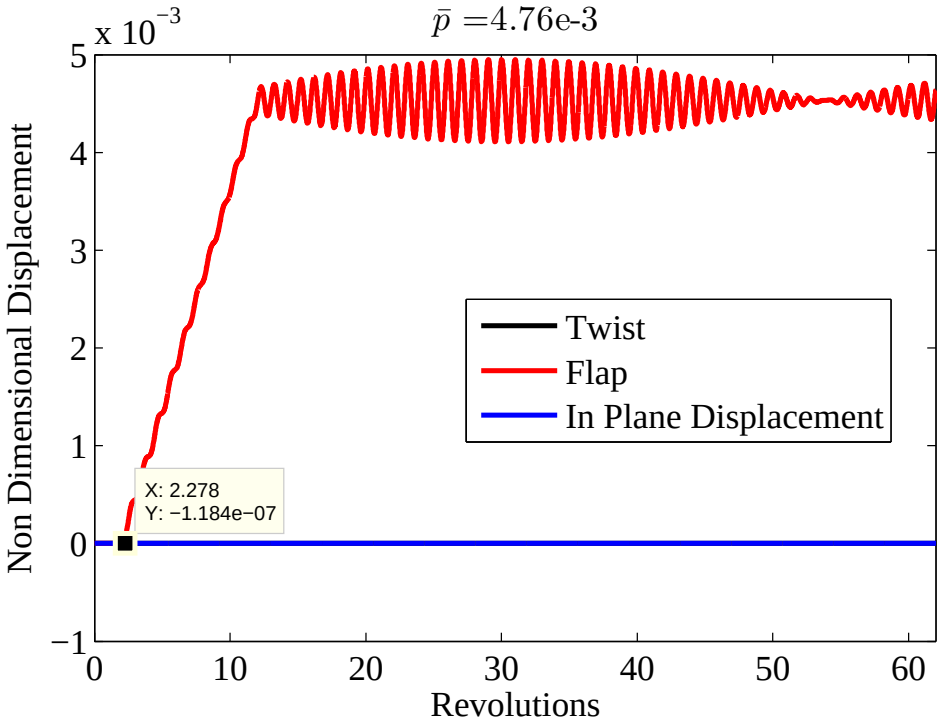

FIGURE 7.4: Time History for HELIOS Configuration with $\gamma = 0.1$ rad

Ritz expansion for the sun overhead case. Figure 7.5 (a) is taken directly from Natori et al. (1989) while Figure 7.5 (b) is created using the current model. Comparing (a) and (b) we can see that the models predict exactly the same behavior, which is expected due to the similarity between the models.

In addition to validating our numerical model against previous results, it is impor-

Table 7.3: Natori et al. (1989) Comparison Non-Dimensional Parameters

Property	Value
$\bar{EI}_1$	2×10^{-16}
$\bar{EI}_2$	4.1748×10^{-5}
$\bar{GJ}$	3×10^{-16}
$\bar{k}_A$	2.8868×10^{-4}
$\bar{k}_{m1}$	6.01×10^{-10}
$\bar{k}_{m2}$	2.8868×10^{-4}

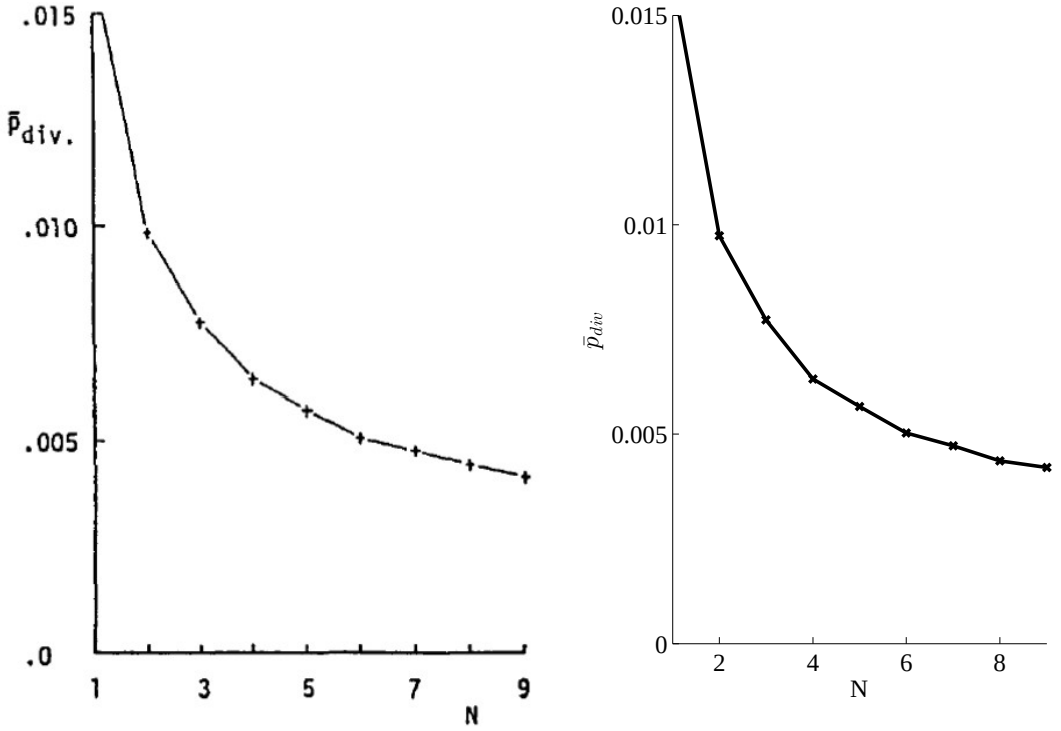

(a) Natori's Results (b) Current Model Results

FIGURE 7.5: Comparison of Modal Convergence of Divergence Boundary for Natori et al. Natori et al. (1989) Rotating Beam with Sun Directly Overhead

tant to validate that the model is numerically converged. Our concern is that for the thin HELIOS blades, we may encounter convergence issues similar to the "Membrane Paradox" discovered when exploring the stability of thin plates and membranes in supersonic flow from the classic aeroelastic literature (Ellen (1965)). Recently Gibbs and Dowell (2014) identified similar behavior in a fully restrained rectangular solar sail membrane, suggesting it may be a problem for the present analysis.

For the heliogyro system the problem arises due to an orders of magnitude mismatch between the tension and bending terms in Eq. 2.37. The modal expansion we implement to solve the partial differential equations uses cantilevered beam modes as a basis function to ensure that we satisfy the full set of boundary conditions required to define a fourth order differential equation. However further inspection of the gov-

erning equations with the nondimensional parameters for the HELIOS, suggests that the first order equation is dominated by the tension terms due to the spinning accelerations that are associated with the second order terms in the differential equation. The small parameter being associated with the highest order derivative makes the system a singular perturbation problem where the majority of the problem is dominated by a second order differential equation, with the fourth order bending stiffness only contributing at a small boundary layer near the root and the tip of the blade.

To establish a baseline we begin by exploring the modal convergence behavior for a 1 m thick version of the HELIOS blade at different spin rates. A thicker blade allows both the out of plane bending stiffness $\bar{EI}_1$ and the in plane bending stiffness $\bar{EI}_2$ to vary from larger than one, where the leading order dynamics are dominated by the bending stiffness, to much below one. Figure 7.6 shows the modal convergence or the the unstable radiation pressure, normalized by the instability pressure of the 40 mode expansion in the out of plane bending, torsion and in plane bending degrees of freedom for three different spin rates. For these spin rates, $\bar{EI}_1$ starts at 2.11 for $\Omega = 0.01$ and decreases to 2.11e-4 for $\Omega = 1.0$. Similarly, $\bar{EI}_2$ starts at 118.4 for $\Omega = 0.01$ and decreases to 1.18e-2 for $\Omega = 1.0$. The simulation predicts a divergence instability for each of the three rotation rates.

The simulation with the slowest spin rate, and correspondingly the largest contribution of bending stiffness has the fastest and most uniform convergence to the solar radiation pressure predicted by the simulation with 40 modes. As the spin rate increases to 1 RPM the stability boundary does not converge to the high mode solution until more than 10 modes are included in the simulation. Additionally, for simulations with less than 10 modes the stability boundary has a jagged response as the modes increase, a feature that we will observe in later simulations.

With a baseline established we can now explore the modal convergence of a membrane with the nominal HELIOS parameters at three different spin rates. Figure

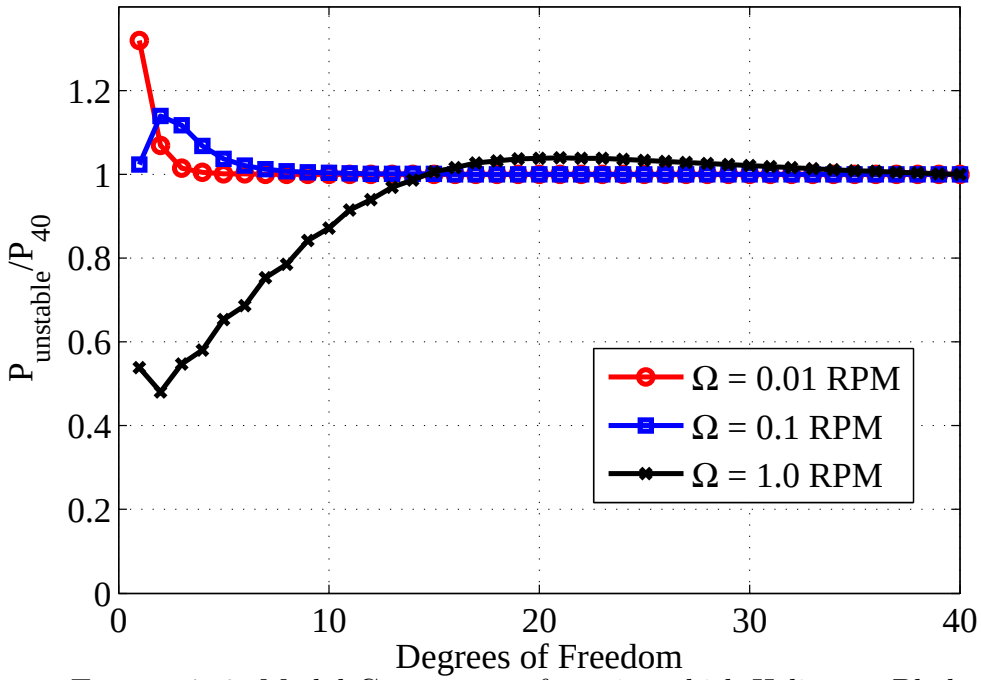

FIGURE 7.6: Modal Convergence for a 1 m thick Heliogyro Blade

7.7 shows the modal convergence of the instability pressure, frequency as well as the change in instability pressure between odd and even mode expansions for $\Omega = 0.5$, $\Omega = 1.0$, and $\Omega = 2.0$. The figure shows that the model predicts divergence for the 40 modes expansion when the spin rate is 0.1 RPM and 2.0 RPM and flutter for 40 modes expansion when the spin rate of 1.0 RPM. All of the simulations contain the nonuniform convergence behavior seen for the $\Omega = 1.0$ RPM simulation in Fig. 7.6. This non-uniform convergence is characterized by a large difference between the odd and even modal expansion instability radiation pressure prediction. If the model is converging to a true solution, one would expect the difference between the odd and even modal expansion to become smaller. Figure 7.7 (c) shows the difference in stability boundary predictions between adjacent number odd and even simulations. For the $\Omega = 0.1$ RPM and 1.0 RPM simulations we can see that the difference between adjacent simulations is trending towards zero for larger expansions. Additionally the

instability radiation pressure in Fig. 7.7 is trending towards a constant value. This provides some confidence that we are approaching a converged solution and there will be no unexpected behavior as we increase the number of modes in our expansion. On the other hand, while the $\Omega = 2.0$ RPM instability pressure is trending to a constant value as we increase the number of modes, the difference between adjacent odd and even simulations is growing suggesting that the model has not converged.

By comparing the trend for $\Omega = 1.0$ RPM when the number of modes is less than 10 to the the $\Omega = 2.0$ RPM, there is a substantial similarity to the trend in the instability pressure and change in pressure between adjacent odd and even simulations. For the $\Omega = 1.0$ RPM simulation we see that increasing the radiation pressure above 15 modes causes the instability to transition from a divergence instability to a flutter instability and an abrupt drop in instability radiation pressure. The similarity of the $\Omega = 2.0$ RPM simulation suggests that not only is the radiation pressure not converged for the simulations, but if the number of modes in the expansion is increased above 40 the instability will transform to flutter instability at a lower radiation pressure, similar to the behavior predicted for the $\Omega = 1.0$ RPM simulation between 15 and 16 modes. This result confirms that we must be aware of the convergence behavior of all simulations presented in this document. The flutter instability predicted for the $\Omega = 1.0$ RPM model is due to a coupling between the in plane bending and torsion degrees of freedom. Therefore, for cases where the in plane stiffness $\bar{E}I_2$ becomes increasingly small, there is a distinct possibility that our model will not converge to the appropriate stability boundary with a finite modal expansion. Practically, this corresponds to the inability to produce a full chart in Figure 7.10. However, for the spin rates and lengths for the HELIOS, we are able to use our model.

Looking closer at the parameters explored in Natori et al. (1989) in light of the modal convergence trends presented in this section we can see that the small $\bar{E}I_2$

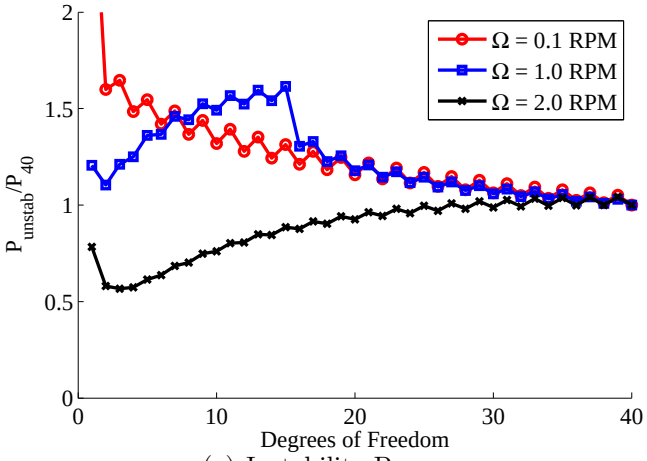

(a) Instability Pressure

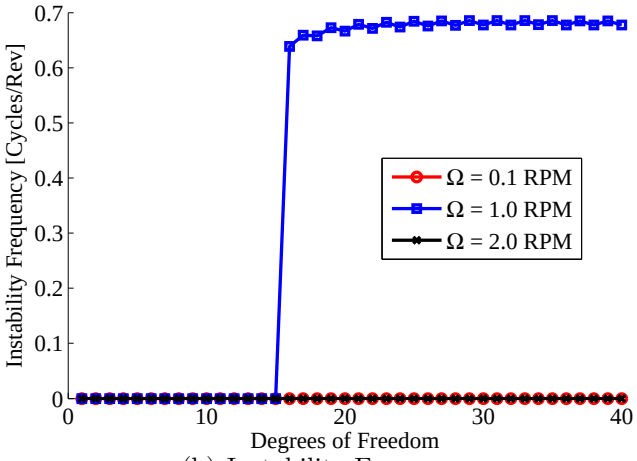

(b) Instability Frequency

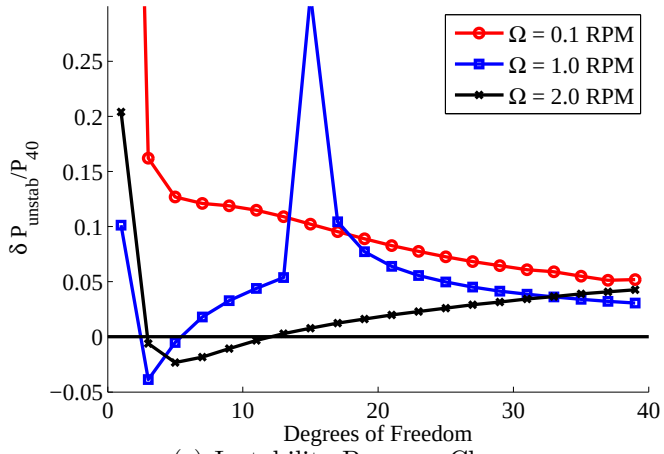

(c) Instability Pressure Change

FIGURE 7.7: Modal Convergence for a Nominal Heliogyro Blade

suggests that a 9 mode expansion may not be large enough to produce a converged solution. Figure 7.8 shows the divergence pressure as well as the change between adjacent modal expansions divergence pressures up to a 40 mode expansion. The figure shows two conditions that suggest the solution may not be converged. First, we see that above 20 modes, the divergence pressure begins to rise again. This is not consistent with a converged solution. Additional, Figure 7.8 (b) shows that the above 20 modes, the absolute value of the difference between the instability radiation pressure of adjacent odd and even mode expansions is growing. From the previous section, this is a likely indicator that the solution is not converged.

Due to the small nature of the $\bar{E}I_2$ we were unable to include enough modes in the simulation to progress towards a converged solution. However, this comparison provided valuable insight into the difficulties of analyzing the solarelastic stability of thin structures. Future work will likely include leveraging many of the lessons learned for the aeroelastic analysis of thin membranes in supersonic flows such as the multiple length scale analysis from Spriggs et al. (1969).

7.3.3 Nominal Spin Rate for Nonlinear Solarelastic Model

Due to the potential of operating the HELIOS in a configuration when a solarelastic instability is possible, the first analysis step is to evaluate what design variables can be changed to increase the stability boundary of the spacecraft. The first design variable we choose to look at is the impact that the spin rate of the heliogyro has on the stability of the structure. The analysis is conducted with the sun directly overhead so the forcing coefficients are time invariant and therefore we were able to use an eigenvalue technique. For this analysis we used the nominal HELIOS parameters and 20 modes in the modal expansion. Figure 7.9 shows the stability boundary in terms of both the solar pressure and instability frequency as the spin rate varies. The figure shows that the solar pressure required to create an instability

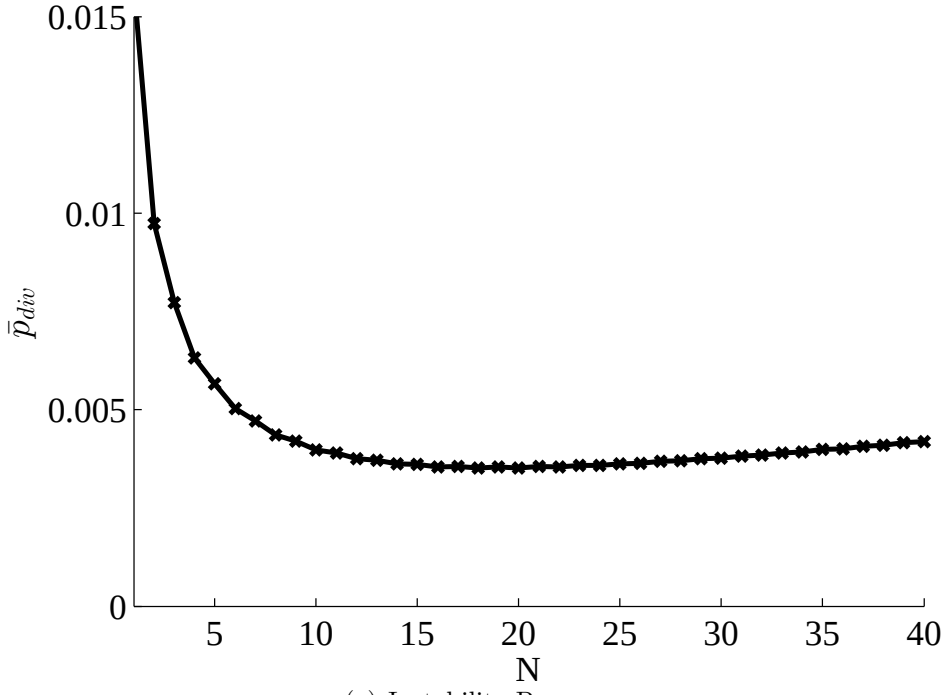

(a) Instability Pressure

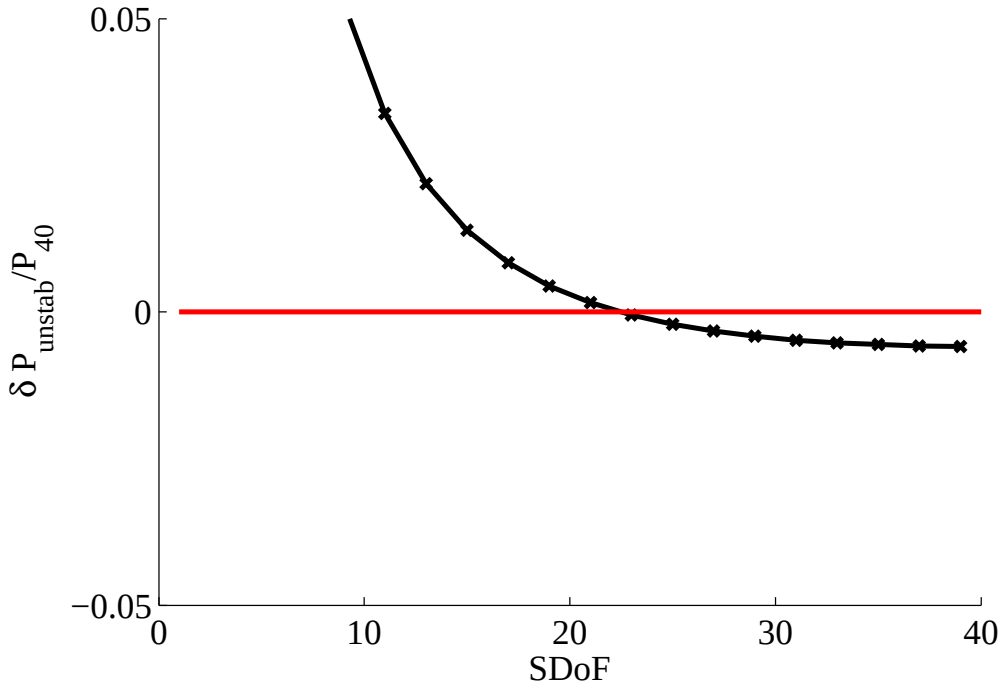

(b) Instability Pressure Change

FIGURE 7.8: Modal Convergence for the Heliogyro Blade from Natori et al. Natori et al. (1989)

increases with the rotation rate. Interestingly at a rotation rate of 1/3 RPM, the instability changes from a divergence instability to a flutter instability. In general, the solarelastic stability of the heliogyro can be improved by increasing the spin rate, however there are trade-offs with the maneuverability and control system bandwidth that must be balanced when choosing the final rotation rate.

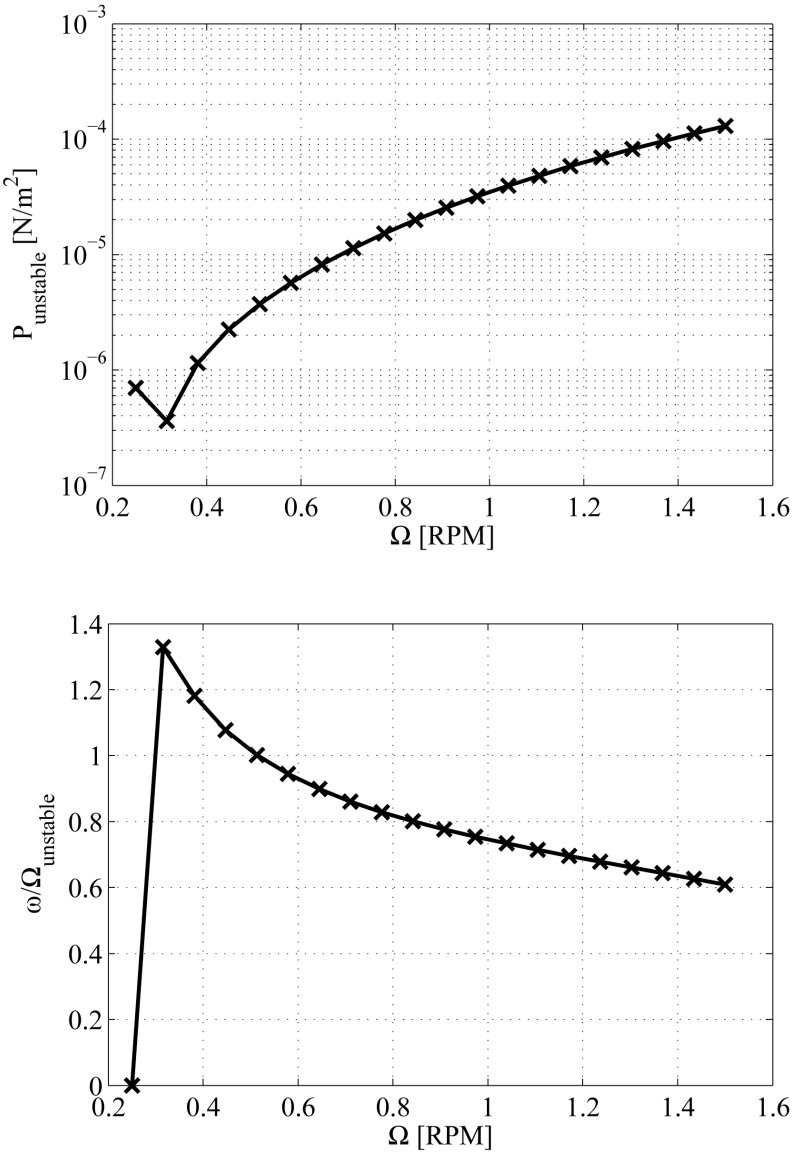

FIGURE 7.9: Stability Boundary for HELIOS Configuration with Sun Overhead for Varying Spin Rates $\mathbf{\Omega}$

As a result of this analysis the HELIOS team decided to change the nominal spin rate of the HELIOS from the preliminary design spin rate or 1/3 RPM to the current design spin rate of 1 RPM.

7.3.4 Deployment Analysis for Nonlinear Solarelastic Model

During the HELIOS deployment the solar sail blades go from short blades that are spinning fast to longer blades that spin at a slower rate. Throughout the deployment the blades are given a collective pitch to generate a moment and increase the angular momentum of the blades. An important area for analysis involves determining the points in the deployment where the combination of spin rate and blade length are most critical for assessing dynamic stability. To explore this phenomenon, this section will look at a parameter study of the nominal HELIOS blade parameters with the span varying between 20 m and the fully deployed 220 m and the spin rate going from 10 RPM down to below the final spin rate of 1 RPM. The simulations use 30 modes in twist, flap and in-plane bending and explores the case with the sun directly overhead.

Figure 7.10 shows the stability boundary during the deployment. The deployment starts in the bottom right hand portion of the figures with a small span and a high rotational speed and traverses to the top left final configuration of 220 m span and and Ω of 1 RPM. For the radiation pressure plot, the axis scale is set so that any white area has a radiation pressure boundary significantly larger than the 0.9e-5 N/m^2 found at 1 AU. For this configuration there are two distinct portions of the stability boundary, a divergence band that runs through the bottom portion of the figure with an instability frequency equal to zero and a flutter band with a non-zero instability frequency. The top right quadrant of the figure does not have stability information because the solutions in the top right quadrant have not converged due to the relative magnitude of the tensile strength to the bending strength.

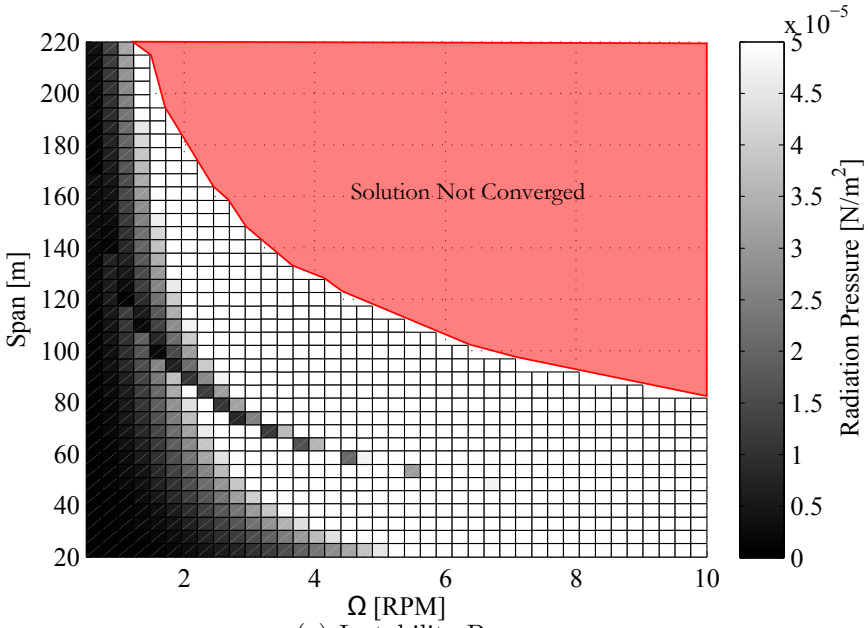

(a) Instability Pressure

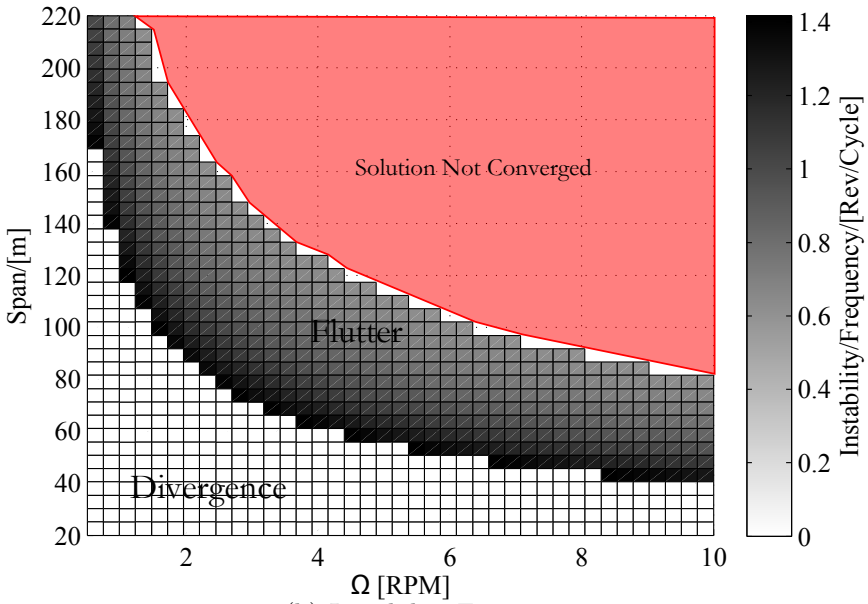

(b) Instability Frequency

FIGURE 7.10: Instantaneous Stability of the HELIOS During Deployment

From a stability perspective an interesting behavior occurs in the transition from the divergence to the flutter band. Especially at slower spin rates, the transition corresponds to a drop in the stability boundary to a value that is below the radiation pressure at 1 AU indicating that an instability is possible. This result suggests that engineers must conduct detailed solarelastic analysis of the complete deployment path to ensure that when moving through unstable bands there is not a catastrophic failure. Because of the slow time scales of the instabilities, a controller may be used to control the unstable dynamics. Alternatively, it appears that the sun-overhead may be the most severe case so the instability may be avoided by positioning the sun at a skew angle from overhead.

7.4 Conclusion for the Dynamics and Stability of a Spinning Membrane in Space

This chapter presents the current stability analysis for the heliogyro. In particular we explore the stability of the HELIOS heliogyro spacecraft. Our analysis using a nonlinear solarelastic model shows that at a spin rate of 1 RPM the system will be stable at the solar radiation pressure at 1AU. Additionally, the analysis of the deployment identifies the critical regions of the deployment where there is a transition from a flutter to a divergence instability. Finally convergence analysis confirms the sensitivity of the current model to the modal expansion.

There continues to be significant avenues for future work related to the stability of the solar sail. Much of the analysis conducted for this chapter focuses on the sun overhead configuration. Future work includes using the model presented in this chapter to conduct a more detailed analysis of sun-skew configurations. Additionally the assumptions made for the nonlinear model including no-precone angle and no root twist can be relaxed to model configurations similar to the actually operating conditions of the HELIOS.

In addition to using the current model, our research also identified avenues for theoretical model improvement. For example, it may be possible to use the multiple length scale analysis presented in Chapter 5 to determine an analytical stability boundary for the spinning configuration. This will be more difficult than the membrane case because multiple degrees of freedom are coupled together. Finally, improving the fidelity of the model could include developing a nonlinear finite element model directly coupled to a solar radiation pressure model. While the techniques presented in this section represent a valuable toolbox for preliminary analysis, final analysis and validation should be conducted using a structural model that can account for the specific features on proposed solar sail.

8

Conclusions and Future Work

This dissertation presents dynamics and stability analysis for a variety of rectangular structures interacting with subsonic fluid flows or solar radiation. In this final chapter we will summarize the key conclusions and findings from our analysis and experiments as well as identify useful avenues for future research.

8.1 Conclusions and Future Work for Aeroelastic Research

In this dissertation we explored the aeroelastic stability and post flutter response of rectangular structures. These rectangular structures form the building blocks of many aerospace structures. Advancing our understanding of their dynamics and stability is valuable in designing the next generation of lightweight and high performance structures. In particular, we explored the stability a cantilevered beam various flow alignments and the stability of a rectangular plate with various boundary condition combinations.

8.1.1 Stability and Nonlinear Response of Cantilevers in Subsonic Flow

In Chapter 3 we explored the stability of a rectangular structure with a single edge clamped. The chapter included analysis and experiments of a cantilevered beam with a clamped edge at multiple yaw angles. Additionally the chapter discusses a pair of experimental studies that characterize the post flutter response of the cantilever in the flapping flag configuration. The key findings for the analysis of the cantilevered beam are:

1. **Instability Type of Cantilever in Yawed Flow Depends on Natural Frequency Spacing**: Depending on the flow orientation a cantilevered beam may loose stability in a multi-mode bending flutter referred to as flapping flag flutter or a coupled bending-torsion instability referred to as wing flutter. Our research demonstrates that the transition between the flapping flag and wing flutter as the flow angle is yawed between the classic configuration depends on the natural frequency spacing of the elastic structure. For the specimens we tested, if the second bending frequency is lower than the first torsion frequency, the systems will go unstable in a flag-like manner until nearly reaching the wing configuration. If the natural frequencies are reversed, the opposite trend is observed.

2. **The Flow Field around the Flapping Flag Remains Attached During LCO**: Through a set of flow visualization experiments using Particle Image Velocimetry (PIV) techniques we have shown that the flow around the flapping flag during its Limit Cycle Oscillation (LCO) remains aligned with the structural motion. This suggests the flow can be modeled with potential flow models and that viscous effects may not dominate the post flutter response of the flapping flag

3. **Quantifying the Post Flutter Tip Displacements of the Flapping Flag Supports Nonlinear Modeling**: Optimal design of systems that utilize a flapping flag instability for energy harvesting or propulsion requires accurate nonlinear modeling of the post-flutter response of the cantilevered beam. Tip LCO amplitude data, such as the data presented in this dissertation, is vital to validating new nonlinear models.

In addition to the key findings, our research has also identified avenues for future research. While specific next steps relating to the research topics are included in Chapter 3, here we include broader areas of study identified by our research. First, we observed a hysteresis band in the experiment at small yaw angles from the flag configuration, regardless of the natural frequency spacing. A valuable area for future research is further characterizing this hysteresis loop as a function of the yaw angle and building an aeroelastic model that is capable of predicting this behavior. The experimental method used to capture the LCO amplitude for the flapping flag could be implemented at various yaw angles to quantify the amplitude and hysteresis behavior. Nonlinear models such as the new nonlinear structural model with nonlinear inertia terms could be coupled to the yawed vortex lattice model to model the post flutter behavior. In addition, careful preparation of the experimental specimens will ensure that the hysteresis behavior is not caused by experimental defects.

Second, while our yawed flow study explored the aeroelastic response at flow angles between classic aeroelastic configurations, there are additional flow yaw angles that could be explored. In particular, one could model the transition from the wing-like configuration to a configuration with the clamped edge normal to the flow and applied at the trailing edge of the structure. This transition is particularly interesting because as noted in Bisplinghoff et al. (1996) sweeping a wing forward causes a critical divergence instability. Therefore the study of yaw angles from the wing-like to the

trailing edge clamp will likely include a transition from a fluttering instability to a static divergence instability.

A third area of future work informed by the flow visualization work, is to improve the fluid models used in our aeroelastic models of the flapping flag. The flow visualization suggest that a nonlinear potential flow model could capture the attached compliant flow seen during the post flutter oscillations of the flapping flag. An example of such a model, as described in Chapter 3, is the nonlinear vortex lattice model found in Attar (2003). One could combine this model with the new nonlinear model with nonlinear inertia terms to create an aeroelastic model that will improve the theoretically predictions of the post-flutter response of the flapping flag.

8.1.2 Stability of Membranes with Various Boundary Conditions in Subsonic Flow

In Chapter 4 we explored the linear stability of plates with six different combinations of boundary conditions. Understanding the stability of simple structures is the foundation for the design and analysis of more complex aerospace structures. The key findings for our theoretical and experimental study of the plates are summarized in the following list.

1. **Critical Instabilities for Plates Identified**: Our analysis predict flutter and divergence instabilities for six different boundary condition combinations. For the four cases with a critical flutter instability, aeroelastic experiments confirmed the instability type, flutter velocity and flutter frequency. For the two cases with a divergence instabilities, experiments showed an absence of flutter but we were unable to confirm the divergence speed.

2. **2D Boundary Conditions Determine Instability Type**: In our study we observed that the structural boundary condition on the leading and trailing edge predict the instability type for the three dimensional plate. If the leading

edge is clamped and the trailing edge is free, then we predict a flutter instability, similar to the flutter instability for the 2D analog, the flapping flag. If the leading and trailing edges are restrained then the critical instability is a divergence instability similar to the divergence predicted for a two dimensional structure with the leading and trailing edge restrained.

3. **Tension in the Normal to the Flow Direction Does Not Significantly Improve Aeroelastic Stability**: In our more detailed analysis of the three sides clamped and trailing edge free configuration, we discovered that increasing the tension in the normal to the flow direction does not significantly increase the flutter velocity. Because this configuration is an approximation of NASA's CML design, it suggests that the stability of the CML will not be significantly improved simply by increasing the applied tension to the membrane.

The future work related to this study contains two aspects. First, the experimental data set could be completed by conducting aeroelastic experiments on the divergence configurations. As mentioned in Chapter 4, our current experimental setup did not allow us to observe divergence in our experiment. While we did note the absence of flutter in the configurations that the theory predicted divergence, it is important to quantify the divergence velocity to further validate the theoretical model.

Second, one could use our model to help design and analyze novel aerospace structures. The applications of lightweight structures vary from noise reduction on transport aircraft to biologically inspired micro-air vehicles. The analysis framework outlined in Chapter 4 provides a valuable preliminary design tool that can be used to identify critical instabilities that may arise. In particular, small changes to the theoretical model, such as including a mean angle of attack, could further advance the applicability of the aeroelastic model. Furthermore, while we demonstrated that

normal to the flow tension does not significantly increase the flutter velocity of the CML-like membrane, one could use the model to explore features or properties that can be changed to improved the dynamic stability.

8.2 Conclusions and Future Work for Solarelastic Research

Solar sails are an important next generation space propulsion technology that may enable vital space missions that include solar weather monitoring and the removal of orbital debris. The analysis in this dissertation focuses on exploring the dynamics and stabilities of the reflective membrane structures that are essential to all solar sail designs. We explored membranes similar to the ones that will appear in both the traditional "square-rig" solar sails as well as the spinning heliogyro class solar sails. In this section we will outline the key findings and future work related to the solarelastic research.

8.2.1 Stability of a Restrained Membrane In Space

Chapter 5 outlines a multiple length scale analysis technique for analyzing the stability of a membrane similar to the membranes that will appear on the proposed "square-rig" Sunjammer solar sail. The key findings from this research are listed below.

1. **Solarelastic Analysis can Leverage Aeroelastic Techniques**: Due to the mathematical similarity between solar radiation and supersonic piston theory aerodynamics we can leverage the techniques previously developed for aeroelastic analysis to predict the stability boundary for solar sails. This is a key finding that has implications on how we analyze the stability of all solar sails and confirms that we can use classic aeroelastic techniques and results.

2. **Restrained Membrane will Flutter**: Using the multiple length scale tech-

nique from the aeroelastic literature we show that a Sunjammer-like membrane will encounter a flutter instability. A scaling analysis suggests that the LCO will be small, on the order of the thickness of the membrane, so therefore the instability is unlikely to cause a catastrophic spacecraft failure.

This research represented of of the first research efforts to determine the solarelastic stability of a proposed solar sail design. As with many early research studies there remains significant avenues for future research related to the solarelastic stability of the membranes required for "square-rig" solar sails. We conducted a scaling analysis to determine the order of magnitude for the LCO of the solar sail. To more accurately predict the post flutter response of the membrane one could conduct a nonlinear analysis. The nonlinear simulation requires coupling a nonlinear structural model with a nonlinear version of the optical solar radiation model. For the membranes used for solar sails, there is not an extensive amount of literature on the proper or appropriate nonlinear structural model to implement. Therefore, the nonlinear modeling will require both theoretical improvements as well as experimental validation if possible.

In addition to nonlinear modeling, the technique used to analyze the stability of the Sunjammer could be expanded to explore different aspect ratios and boundary condition combinations that may be of interest to solar sail designers. The goal of this solarelastic analysis will be ensuring that solar sail designs will not fail when launched due to a solarelastic instability. The analysis will ensure that an instability will not arise, or that if an instability does arise, it will not threaten the solar sail spacecraft.

8.2.2 Dynamics and Stability of a Hanging Membrane in a Gravitational Field

When designing a spacecraft that rely heavily on thin, lightly tensioned membranes to succeed, it is vital to build and validate theoretical models before launching the

spacecraft. In Chapter 6 we discuss theoretical modeling and experimental observations of a lightly loaded thin, reflective membrane in gravity. This research effort is a vital step in building confidence in the theoretical models that are required to design solar sails. The key findings of this research effort are:

1. **Simple Linear Models can Capture the Structural Dynamics**: For the cantilevered thin structure in gravity a simple classic beam / string model is capable of predicting the natural frequencies and mode shapes that are observed in experiments. Furthermore, for structural analysis a reasonable number of modes in the modal expansion is able to produce converged solutions, a trend that is not true for the solarelastic analysis.

2. **Structural Damping Mechanisms are Not Well Understood**: In our experimental observations of the hanging membrane we were unable to clearly identify the key drivers of the measured damping. Potential sources of damping in our experiment include the interface between the actuator and the structure, aerodynamic damping and structural damping. Different experiments identified that all three of these factors contributed to the measured damping, but it is not clear the magnitude of each and therefore we are unable to predict the damping levels that will be present in solar sails that leverage similar membranes.

3. **Flutter Instability Possible in Gravity**: Our analysis shows that a solarelastic instability is possible for a hanging membrane. While it may be difficult to create an experiment to validate this observation, it should be possible to create a situation on earth where a solarelastic instability is observed.

4. **Hanging Membranes are a Valuable Model Validation Tool**: The stress levels and distribution in a hanging membrane are similar to the stress levels

for heliogyro solar sails. Hanging membranes remain a viable and important method of validating theoretical models being used to design heliogyro spacecraft. Due to the lightweigh nature of the membranes, care must be take for the environment, in particular the amount of air present, when conducting the experiments.

While significant progress has been made in modeling the dynamics of a hanging membrane there remain significant areas for future work. The first area of future research is developing a better understanding of the damping mechanisms in the lightly loaded membranes. While we have conducted some preliminary analysis to model the impact of the surrounding fluid, very little effort has gone into analyzing the mechanisms within the structure that can cause damping. For the lightly loaded structure, determining the damping levels could require analyzing the micro level interactions as the energy dissipation may be localized to certain locations. Our observation that increasing the mass of a crumpled membrane decreases the observed damping suggests that exploring and quantifying the impact of crumpling the structure could be a useful exploration.

In addition to increasing our understanding of the structural dynamics, there are significant areas for future work in understanding the solarelastic stability of a hanging membrane. One limitation of the analysis conducted in this dissertation was the number of modes required to arrive at a converged solution. Future work could include applying the multiple length scale analysis method described in Chapter 5 to the hanging membrane. This effort will require analyzing an equation that is similar to, but with a different form of the applied tension, than the membrane explored in Chapter 5. Applying this analysis technique will provide an analytical solution and confirm that the modal solution has converged to the appropriate solution.

The final area of future research is conducting a ground solarelastic experiment. This research task will include designing and instrumenting an experiment that can validate solarelastic models. In order to conduct an experiment on the ground, the current analysis suggests an extreamly large amount of solar radiation will be required. To minimize the required solar radiation pressure one could explore conducting the experiment in a low-g setting such as the international space station or a reduced gravity aircraft such as the one used by NASA's reduced gravity research program. Conducting a solarelastic experiment would be a significant milestone in demonstrating the existence of this type of instability and building confidence in our model.

8.2.3 Dynamics and Stability of a Spinning Membrane in Space

In Chapter 7 we presented stability analysis of a spinning membrane similar to one that would be found on a heliogryo solar sail. In particular we looked at the stability of a proposed heliogyro spacecraft, HELIOS. Using linear and nonlinear modeling we determined that the HELIOS would be stable at 1AU and identified the critical regions during the deployment. The key findings due to our theoretical analysis on spinning solar sails are listed below.

1. **Solarelastic Instabilities Possible for Spinning Solar Sails**: Both linear and nonlinear models of the spinning membrane show that divergence and flutter instabilities are possible. Furthermore, these instabilities for the HELIOS design occur at radiation pressure levels near the levels the ones that the space craft will encounter. As with the hanging models, Rayleigh-Ritz solutions to the solarelastic equations are susceptible to poor modal convergence.

2. **Nonlinear Structural Model Needed for Conservative Prediction of Stability Boundary**: For analysis cases when the sun is directly overhead

of the spinning membrane the critical instability predicted by the nonlinear model arises due to a coalescence between in plane bending and torsion modes. For the linear analysis the in-plane bending and torsion degrees of freedom are not coupled and therefore no instability is predicted. Therefore an accurate prediction of the instability boundary requires one to include the nonlinear terms which couple the degrees of freedom.

3. **Low Radiation Pressure Instability when Transitioning from Divergence To Flutter Instability**: In our analysis of the deployment of the HELIOS we identified divergence and flutter regions during the deployment. The analysis shows that the most critical point occurs at the transition between divergence and flutter. In general the transition is caused by the increasing dominance of the centripetal tension stiffness over the beam-like bending stiffness. When designing heliogyro spacecraft identifying and navigating this transition will be important and require detailed finite element analysis.

4. **"Membrane Paradox" Encountered for Solarelastic Analysis of Spinning Membranes**: Our analysis shows that for cases where the spin rate of the membrane is large or the thickness is small the solarelastic model has poor modal convergence. The behavior is similar to the membrane paradox identified when conducting aeroelastic analysis of membranes in supersonic flows. Convergence analysis is required to ensure a stability prediction is accurate

Although significant progress was made in determining the stability of spinning membranes, there remain many avenues for future research. The first, and most pressing area relates to the modal convergence issues faced when modeling the heliogyro membranes. As more advanced and high performance solar sails are demanded, the analysis methods outlined in this paper will no longer produce converged solutions with a reasonable number of modes. As with the analysis of the hanging solar

sail, one could conduct a multiple length scale analysis to get an asymptotic solution that predicts the instability type and radiation pressure. As with the hanging membrane, the contribution of multiple degrees of freedom and the increased complexity of the spatially varying tension term will make implementing the asymptotic approach more difficult.

A second area of future research includes using the nonlinear structural model to identify the stability of heliogyro membranes in additional operating conditions. In this dissertation we focus on developing the model and conducting analysis with the sun overhead, allowing us to use a perturbation analysis of the nonlinear equations. Our hypothesis based on preliminary explorations is that the sun overhead case is the most critical, however future work could include proving that the most critical stability case is when the sun is overhead and there is no blade pitch. Furthermore future work could integrate the control scheme for a heliogyro mission and ensure that the system is stable throughout the entire mission. This would require analyzing the solarelastic stability for cases when the sun is not overhead and a root blade pitch is defined.

Third, the nonlinear model discussed in this dissertation can be used to conduct a detailed study of the post-flutter response. In our analysis of the restrained membrane a scaling analysis suggests that the LCO is on the order of the thickness. For the cantilever configuration used for heliogyro spacecraft it is likely that the post instability response will be significantly larger and may threaten the spacecraft operation. In addition to using the nonlinear model discussed in this dissertation, future work could include additional validation against other membrane structural models such as finite element simulations and lumped mass simulations.

Finally, improvements to the solar radiation pressure model can be made. In our analysis, even with the nonlinear structural model, we assume a linear solar radiation model. Future work could include improving this model to be consistent

with the nonlinear nature of the structure model. Furthermore, the analysis in this dissertation was conducted for a perfectly reflective surface. Future research can account for the non perfect nature of a real solar sail by accounting for the absorbed solar radiation. The improvements to the solar radiation model can also be incorporated into the other solarelastic models.

8.3 Publications

The research conducted for this dissertation has been published in the archival literature as shown in the following list of publications.

Journal Publications

1. **Gibbs, S.C.**, Wang, I., Dowell, E.H. "Theory and experiment for flutter of a rectangular plate with a fixed leading edge in three-dimensional axial flow", *Journal of Fluids and Structures*, Volume 34, October 2012

2. Wang, I., **Gibbs, S.C.**, Dowell, E.H., "Aeroelastic model of multisegmented folding wings: theory and experiment", *AIAA Journal of Aircraft*, 2012, Volume 49, Number 3

3. **Gibbs, S.C.**, Fichera, S., Zanotti, A., Ricci, S., Dowell, E.H., "Flow field around the flapping flag", accepted to *Journal of Fluids and Structures*, 2014.

4. **Gibbs, S.C.**, Wang, I., Dowell, E.H., "Stability of rectangular plates in subsonic flow with various boundary conditions", accepted to *AIAA Journal of Aircraft*, 2014.

5. **Gibbs, S.C.**, Dowell, E.H., "Membrane paradox for solar sails", accepted to *AIAA Journal*, 2014.

6. **Gibbs, S.C.**, Sethna, A., Wang, I., Tang, D., Dowell, E.H., "Aeroelastic stability of a cantilevered plate in yawed subsonic flow," submitted to *Journal of Fluids and Structures*, 2014.

7. Wang, I., **Gibbs, S.C.**, Dowell, E.H., "Aeroelastic behavior of multi-segmented folding wings: a study of varying fidelity models", submitted to *AIAA Journal of Aircraft*, 2014.

8. Tang, D., **Gibbs, S.C.**, Dowell, E.H., "Theoretical and experimental aeroelastic response with inextensible plate theory", submitted to *Journal of Fluids and Structures*, 2014.

9. Tang, D., **Gibbs, S.C.**, Dowell, E.H., "Nonlinear aeroelasticy analysis with inextensible plate theory including correlation with experiment", submitted to *AIAA Journal of Aircraft*, 2014.

Conference Papers and Presentations

1. **Gibbs, S.C.**, Warren, J.E., Wilkie, W.K., Dowell, E.H., "Stability of rotorcraft for interplanetary space flight", *AHS 70th Annual Forum*, Montreal, Canada, May 20-22 2014.

2. **Gibbs, S.C.**, Dowell, E.H. "Solarelastic stability of the heliogyro", *3rd International Symposium on Solar Sailing*, Glasgow, UK, June 11-13 2013.

3. Wilkie, W.K., Warren, J.E., Juang, J., Horta, L.G., Lyle, K.H., Littell, J.D., Bryant, R.G., Thomson, M.W., Walkemeyer, P.E., Guerrant, D.V., Lawrence, D.A., **Gibbs, S.C.**, Dowell, E.H., Heaton, A.F., "Heliogyro solar sail research at NASA", *3rd International Symposium on Solar Sailing*, Glasgow, UK, June 11-13 2013

4. **Gibbs, S.C.**, Guerrant, D.V., Wilkie, W.K., Dowell, E.H. "Rectangular solar sail flutter", 54th AIAA Structure, Structural Dynamics and Materials Conference, Boston, MA, April 2012.

5. Wang, I., **Gibbs, S.C.**, Dowell, E.H. "Aeroelastic analysis of a folding wing: comparison of simple and higher fidelity models for a wide range of fold angles", *54th AIAA Structure, Structural Dynamics and Materials Conference*, Boston, MA, April 2012.

6. **Gibbs, S.C.**, Wang, I., Giovanetti, E., Dowell, E.H. "Aeroelastic stability for a cantilevered beam in three-dimensional axially misaligned flow", *Fluid and Elasticity 2012*, La Jolla, CA, November 2012.

7. Wang, I., **Gibbs, S.C.**, Dowell, E.H. "Flutter of rectangular plates in three dimensional incompressible flow with various boundary conditions: theory and experiment," *ASME International Design Engineering Technical Conferences*, Chicago, IL, August 2012

8. **Gibbs, S.C.**, Wang, I., Bloomhardt, L., Dowell, E.H. "Aeroelastic behavior of noise-reducing membranes for aircraft lifting surfaces part I: theory", *53rd AIAA Structure, Structural Dynamics and Materials Conference*, Honolulu, HI, April 2012.

9. Wang, I., **Gibbs, S.C.**, Bloomhardt, L., Dowell, E.H. "Aeroelastic behavior of noise-reducing membranes for aircraft lifting surfaces part II: experiment", *53rd AIAA Structure, Structural Dynamics and Materials Conference*, Honolulu, Hi, April 2012.

Appendix A

Hanging Membrane Experimental Results

This appendix contains the transfer function data for the ground vibration experiments conducted at NASA Langley Research Center on the hanging membrane in a vacuum chamber. The experimental data is compared to theoretical predictions using the linear beam model with rigid body modes. Before discussing the experimental results this section discusses how we generate the theoretical transfer functions from the theoretical model. Specifically this section will demonstrate how we can use the beam structural model to generate the transfer function from a root twist or root translation to the response at different locations on the membrane. The first step is to add structural damping to the model. This damping is required because we expect some level in the experiment and furthermore, the system will have infinite responses at the natural frequencies if no energy loss mechanism is included in the system. For this application, the model includes modal damping that is proportional to the natural frequency and the velocity of the plate. Equation A.1 shows the form of the damping term.

Table A.1: Hanging Membrane Experimental Configuration

Property	Symbol	Config 1	Config 3	Config 4
Material		Kapton	Mylar	Mylar
Batons		Straws	Tape	None
Other			Crumpled	Crumpled Edge Reinforced
Density	ρ_s	1420 kg/m^3	1400 kg/m^3	1400 kg/m^3
Young's Modulus	E	2.5 GPa	3.7 GPa	3.7 GPa
Poisson's Ratio	ν	0.34	0.34	0.34
Thickness	h	25.4 μm	2.54 μm	2.54 μm
Span	L_x	2.13 m	2.13 m	2.13 m
Chord	L_y	0.127 m	0.051 m	0.051m

$$\text{Damping} = 2\zeta \begin{bmatrix} \ddots & & \\ & \omega_n & \\ & & \ddots \end{bmatrix} \dot{\tilde{\boldsymbol{q}}} = \tilde{C}\dot{\tilde{\boldsymbol{q}}} \tag{A.1}$$

Substituting Equation A.1 into the beam equation yields the following governing equation

$$\tilde{M}\ddot{\tilde{\boldsymbol{q}}} + \tilde{C}\dot{\tilde{\boldsymbol{q}}} + \tilde{K}\tilde{\boldsymbol{q}} = \bar{V}'\boldsymbol{Q} \tag{A.2}$$

Next harmonic motion for the response and the forcing are assumed.

$$\begin{aligned} \tilde{\boldsymbol{q}} &= \bar{\tilde{\boldsymbol{q}}} e^{i\omega t} \\ \boldsymbol{Q} &= \bar{\boldsymbol{Q}} e^{i\omega t} \end{aligned} \tag{A.3}$$

In general a unit strength $\bar{\boldsymbol{Q}}$ associated with either the rigid body translation or rigid body rotation generalized coordinates, depending on the actuator is used. Substituting this assumption into Equation A.2 and dividing through by $\exp[i\omega t]$ yields:

$$\left(-\omega^2\tilde{M} + i\omega\tilde{C} + \tilde{K}\right)\bar{\tilde{\boldsymbol{q}}} = V'\bar{\boldsymbol{Q}} \tag{A.4}$$

Equation A.4 is then solved at various frequencies to determine the response of the system ($\bar{\tilde{\boldsymbol{q}}}$) due to a unit input. The final step in create a transfer function is to use the $\bar{\tilde{\boldsymbol{q}}}$ to evaluate the displacements at the root and at the location of interest. Dividing the displacements at the location of interest by the displacements at the root produces a frequency dependent transfer function.

A.1 Configuration 1: 84" by 5" x 1 mil Aluminized Kapton with Straw Batons

The first set of experimental results is for the 5-inch wide Aluminized Kapton membrane with the twist piezoelectric actuator installed at the top. The theoretical simulations include structural damping of 0.015. Figure A.1 contain the transfer function between the root and 4 locations on the beam: the 1/4 span, mid span, 3/4 span and tip of the blade. The code defines twist motion as the difference between the left and right velocity vibrations. Therefore the experimental transfer function while unit-less is comprised of mm/s (at location)/ mm/s at root, while the theoretical transfer function, because of the way that the mode shapes are defined has units of radians / radians.

Examining the 1/4 span results in Figure A.1(a), there is good agreement in both phase and magnitude between the theory and experiment. This is the case for the poles, or natural frequency locations, as well as the zeros of the transfer function. The close overlay suggests that for these low frequencies the model is accurately capturing the dynamics of the system. After the third natural frequency, there are discrepancies between the theoretical and experimental responses. First, the fourth experimental frequency is shifted higher in the theory and second the height of the peak of the forth experimental frequency does not closely match the theoretical model. The ability to match the first few modes, but then see a divergence between the theoretical and experimental model is a trend that will continue

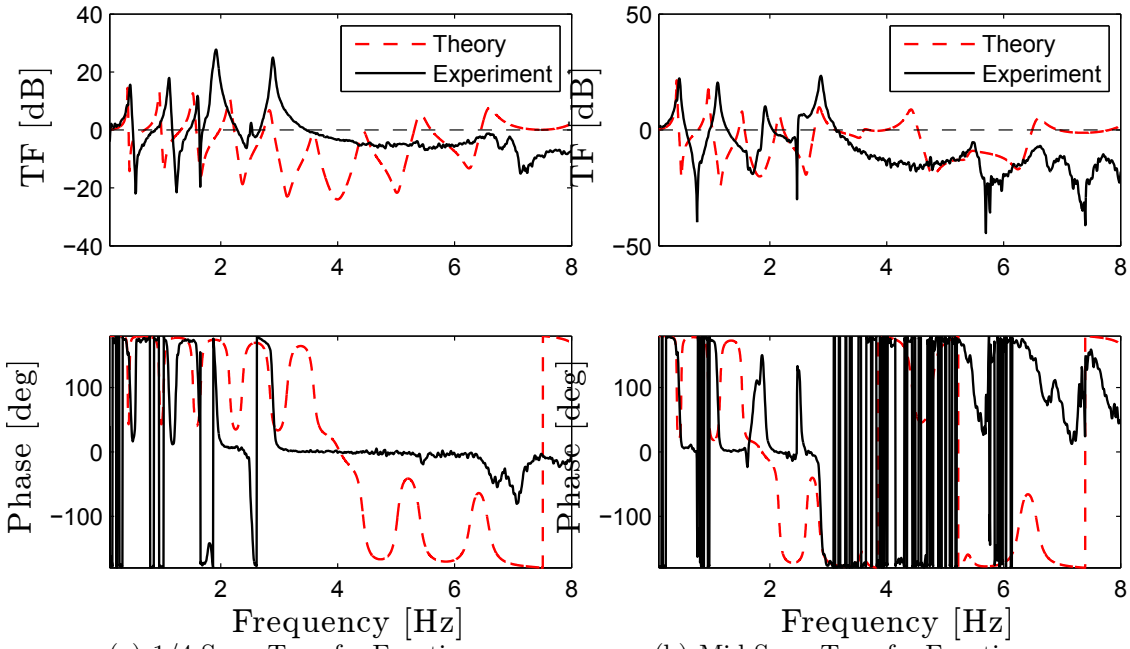

(a) 1/4 Span Transfer Function

(b) Mid Span Transfer Function

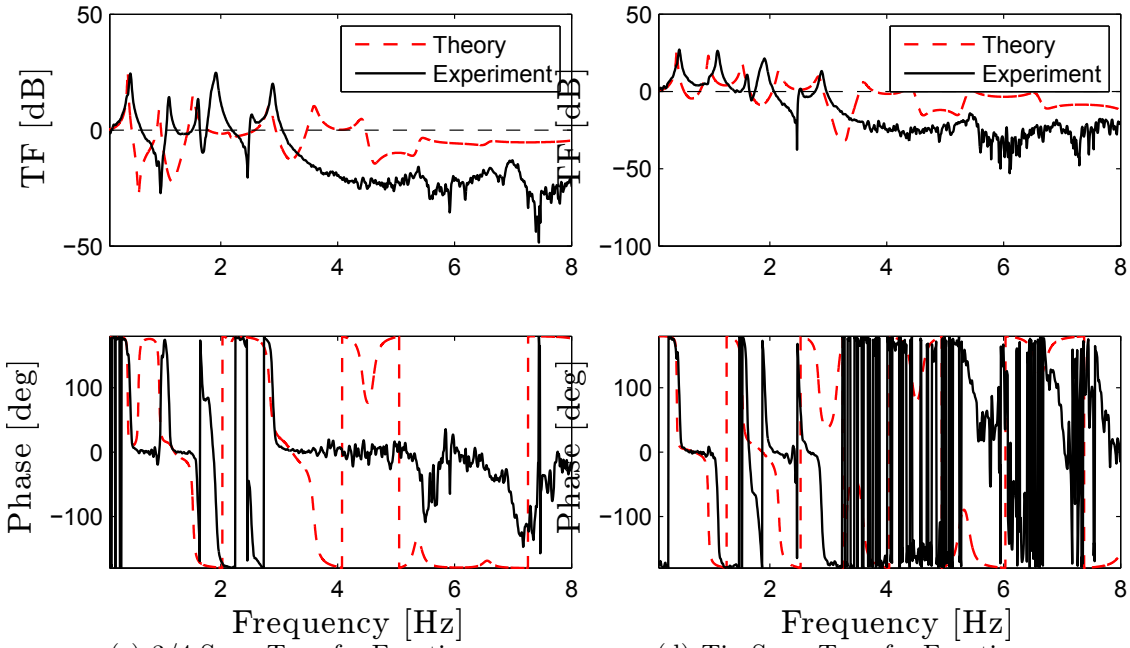

(c) 3/4 Span Transfer Function

(d) Tip Span Transfer Function

FIGURE A.1: Transfer Function for Configuration 1 with Twist Actuator at Four Different Span Locations

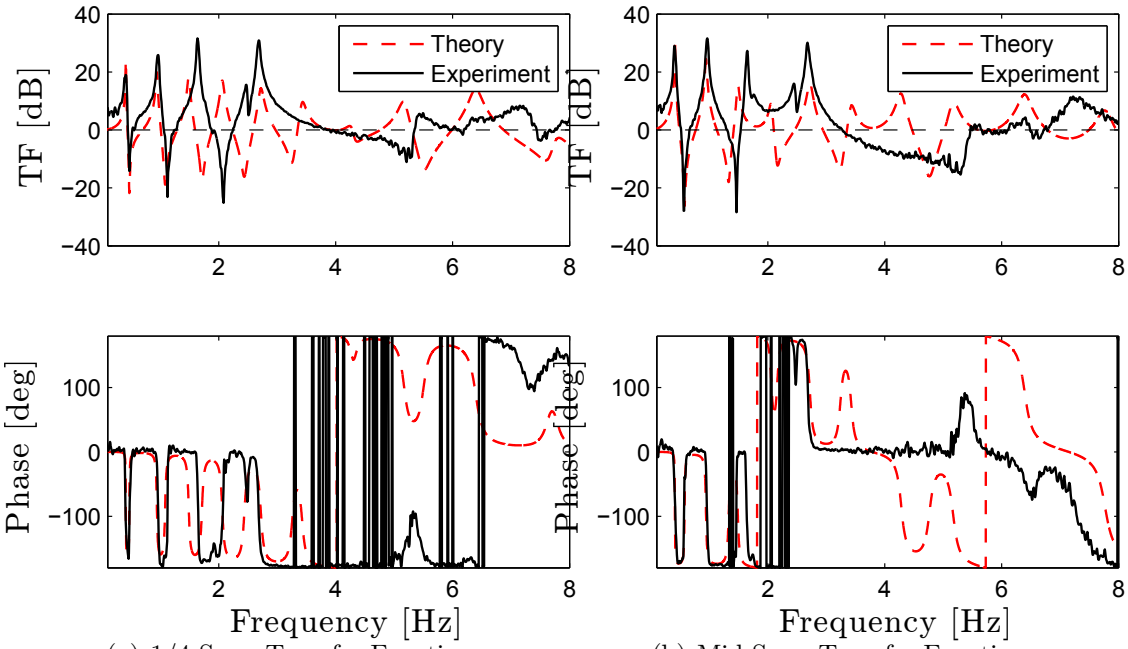

(a) 1/4 Span Transfer Function

(b) Mid Span Transfer Function

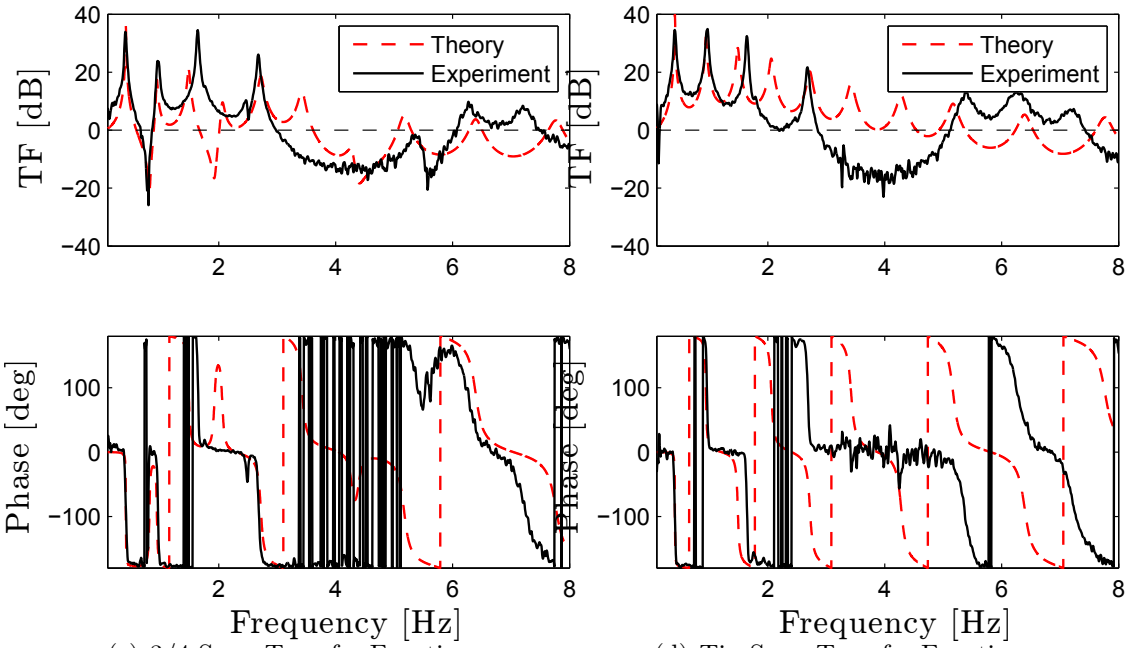

(c) 3/4 Span Transfer Function

(d) Tip Span Transfer Function

FIGURE A.2: Transfer Function for Configuration 1 with Flap Actuator at Four Different Span Locations

throughout this section. Specifically for the twist modes, there are often additional experimental modes that the theoretical model does not predict. While we do not yet have a convincing explanation for these missing frequencies the reason that the higher frequency, higher modes do not match is we may not have spent enough time looking at these frequencies. For the experiment, injecting low frequency noise into the system was the primary interest.

From a fluid structure interaction perspective, because the coupling between the structural model and the fluid model almost exclusively occurs in the low frequency modes, usually the first or second structural modes, the ability of the current theoretical model to predict these modes is very promising.

A trend revealed by the comparison of the response at the 3/4 span with that at the tip of the blade is that the farther away from the actuator the sensing takes place, the harder it is to match the theoretical and experimental transfer functions. Because the structure is highly damped and not very rigid, predicting the motion at the extremes of the blade is difficult. Although the transfer functions no longer lie directly on top of each other, the match between the theoretical and experimental peaks remain encouraging and provide confidence in the ability of the structural model to capture the fundamental dynamics of the system.

In addition to the twist actuator, the experiment used a flap piezoelectric actuator to observe the bending dynamics of the hanging membrane. To calculate the bending displacement, the code takes the average of the left and right measured velocities. Because the bending modes, at least theoretically, are symmetric it should have also been possible to use either the right or left data. The average hopefully removes any twisting behavior and provides a good estimate of the bending behavior of the structure. Figure A.2 contains the theoretical and experimental transfer functions. In general, there is good agreement up to at least the third transfer function peak in all of the four sub figures.

For the mid span data, there is particularly good agreement between the theory and the experiment for both shape and magnitude of the transfer function. For this configuration, there is also divergence of the second zero between the theory and the experiment. At the 3/4 span and tip the shapes of the transfer functions and the first peaks line up well. Overall for this blade, the theoretical model captures the low frequency mode transfer function well which is a requirement for moving forward with this model for the solar radiation pressure-structure interaction problem.

A.2 Configuration 2: 84" x 5" x 0.1 mil Aluminized Mylar Crumpled with Tape Batons

The thinner blade response is inevitably more difficult predict. First, the thinner blade requires a structural damping value of 0.05. The difference between the current specimen and the previous specimen is the thickness, but also the crumpling of this second specimen. The goal of crumpling the membrane was to eliminate any residual stresses in the specimen and hopefully create a somewhat uniform stress distribution in the blade. The crumpling may also have increased the measured damping of the blade. This is a topic that will be explored more in the future research.

Figure A.3 shows the twist actuator results for the thin blade. It is clear that the theoretical model does not match the experimental results quite as well, across the board. While the frequency of the peaks and the zeros line up in the figures, the magnitude of the peaks and the zeros does not. Figure A.3 demonstrates this, as the first two theoretical peaks are much higher than the experimental value while the third peak lines up well. The first explanation for this difference is the structural damping model is not accurate and the first structural modes have higher structural damping than included in the model. However if the structural damping is increased across the board then the agreement for the higher modes is worse. Even with the differences, qualitatively the agreement for the low modes remains good enough to

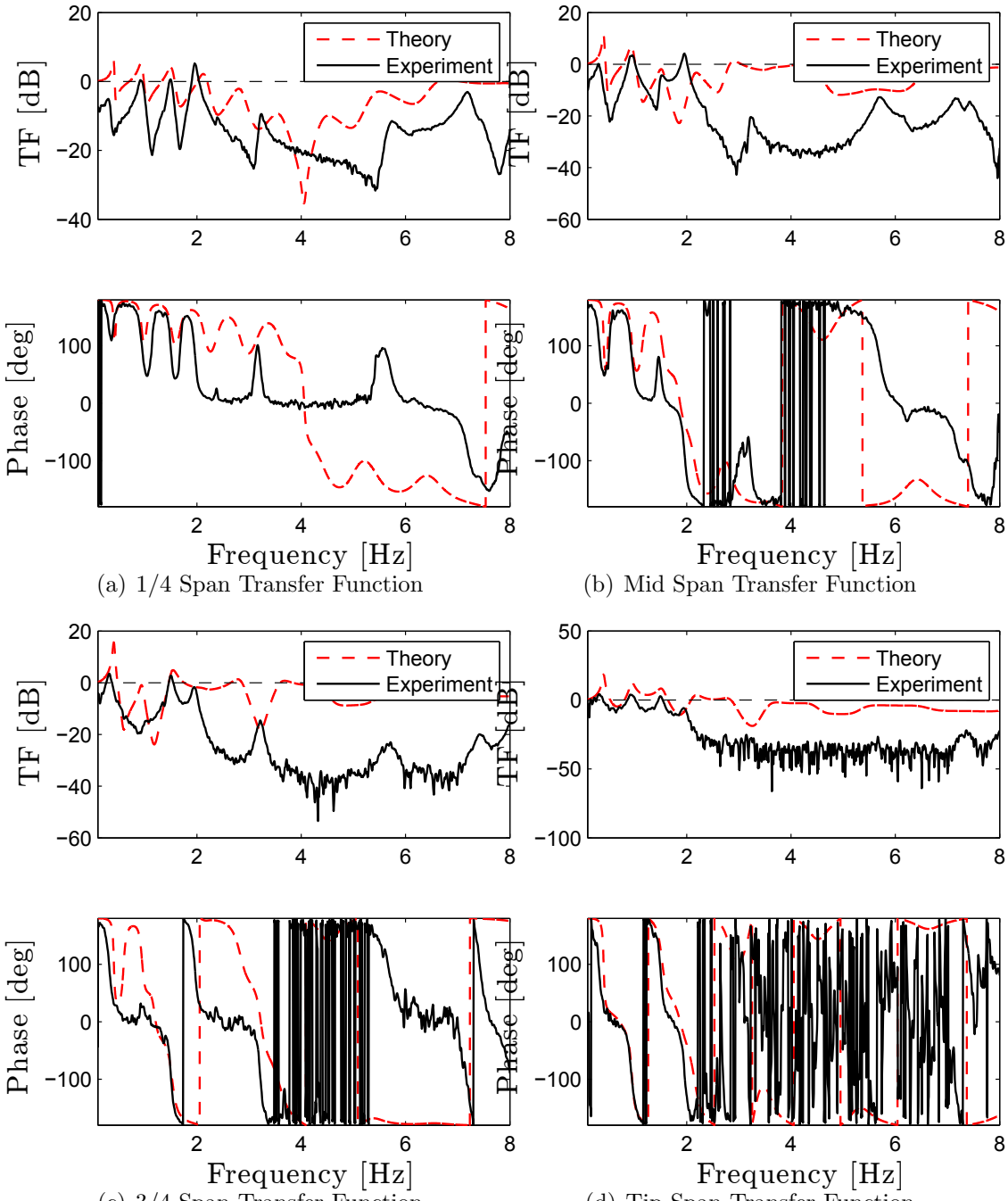

(a) 1/4 Span Transfer Function

(b) Mid Span Transfer Function

(c) 3/4 Span Transfer Function

(d) Tip Span Transfer Function

FIGURE A.3: Transfer Function for Configuration 3 with Twist Actuator at Four Different Span Locations

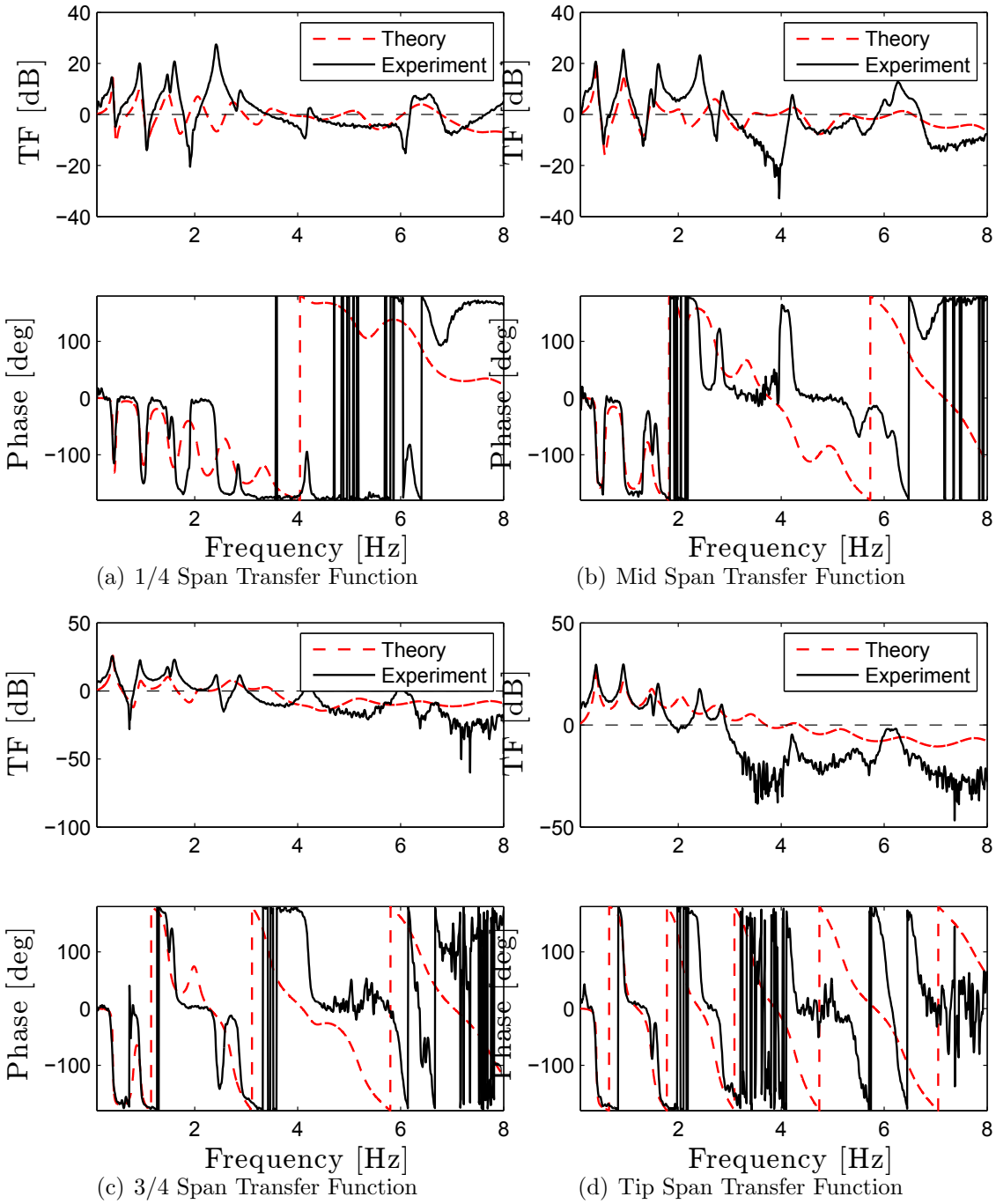

(a) 1/4 Span Transfer Function

(b) Mid Span Transfer Function

(c) 3/4 Span Transfer Function

(d) Tip Span Transfer Function

FIGURE A.4: Transfer Function for Configuration 3 with Flap Actuator at Four Different Span Locations

suggest that the current model may be adequate for solarelastic predictions.

The agreement between the theory and the experiment for the flap actuator further highlights the difference between the theoretical and experimental twist results. In Figure A.4, the theory is consistently matching the experiment in transfer function magnitude and phase. The results suggest that the model captures the bending dynamics even with a thin crumpled membrane. While the test specimen remains the same for both the flap and twist actuators, the actuator must be physically swapped between experiments. This changes the attachment between the test article and the actuator. The uncaptured dynamics of this interface may explain why one experiment produces such good results relative to the same specimen with a different actuator.

A.3 Configuration 3: 84" x 5" x 0.1 mil Aluminized Mylar Crumpled with Edge Reinforcements

In addition to the previous structure, we also conducted experiments on a thin membrane that contained edge reinforcements. The story for this configuration is very similar to the previous configuration, although, in general the model was better able to capture the flap dynamics of the structure. Figures A.5 and A.6 contain the comparison between the theoretical and experimental transfer functions for this configuration. The comparisons for the flap actuator at the 3/4 and Tip of the blade are particularly encouraging for this configuration. The edge reinforcements, like the batons in the previous section, keep the the blade from curling in the chord-wise direction.

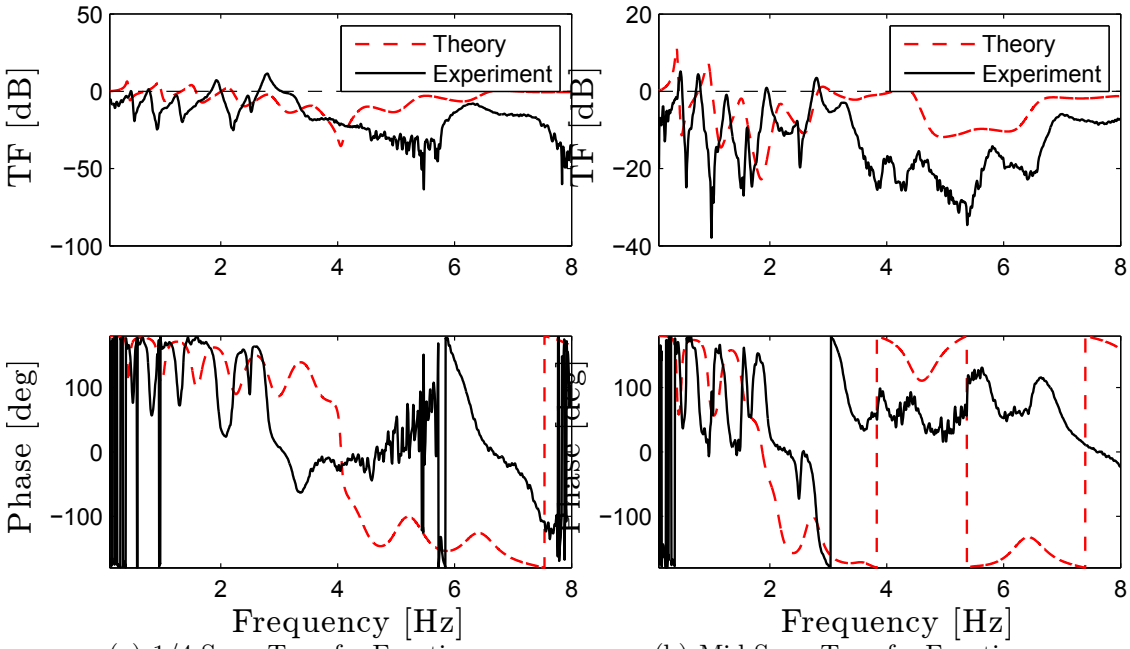

(a) 1/4 Span Transfer Function

(b) Mid Span Transfer Function

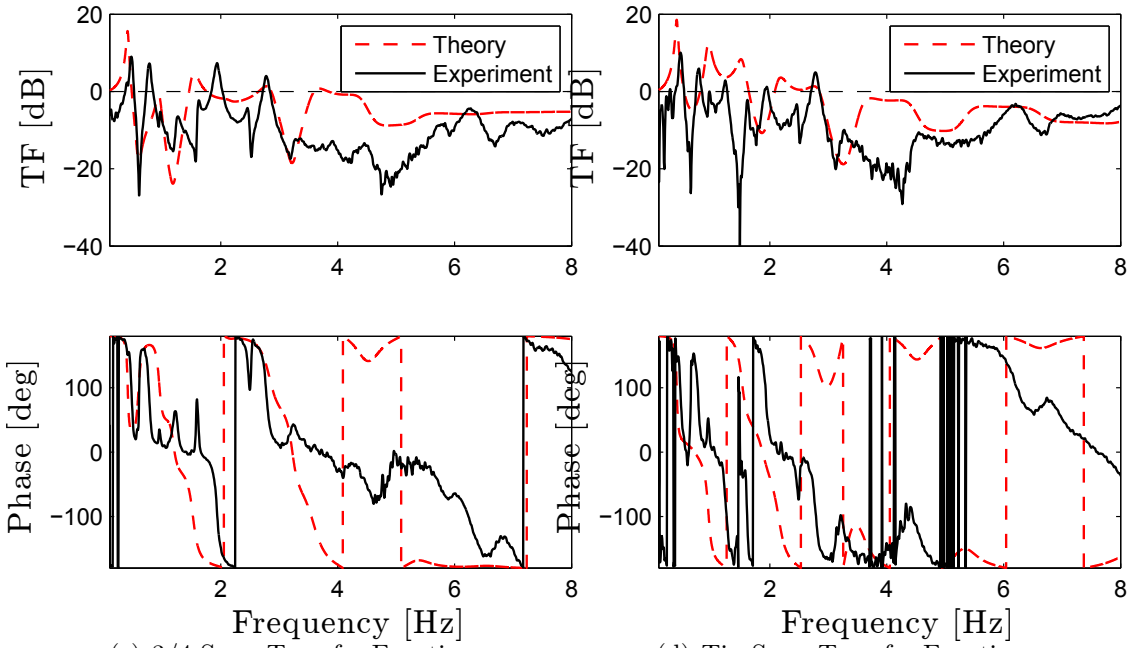

(c) 3/4 Span Transfer Function

(d) Tip Span Transfer Function

FIGURE A.5: Transfer Function for Configuration 4 with Twist Actuator at Four Different Span Locations

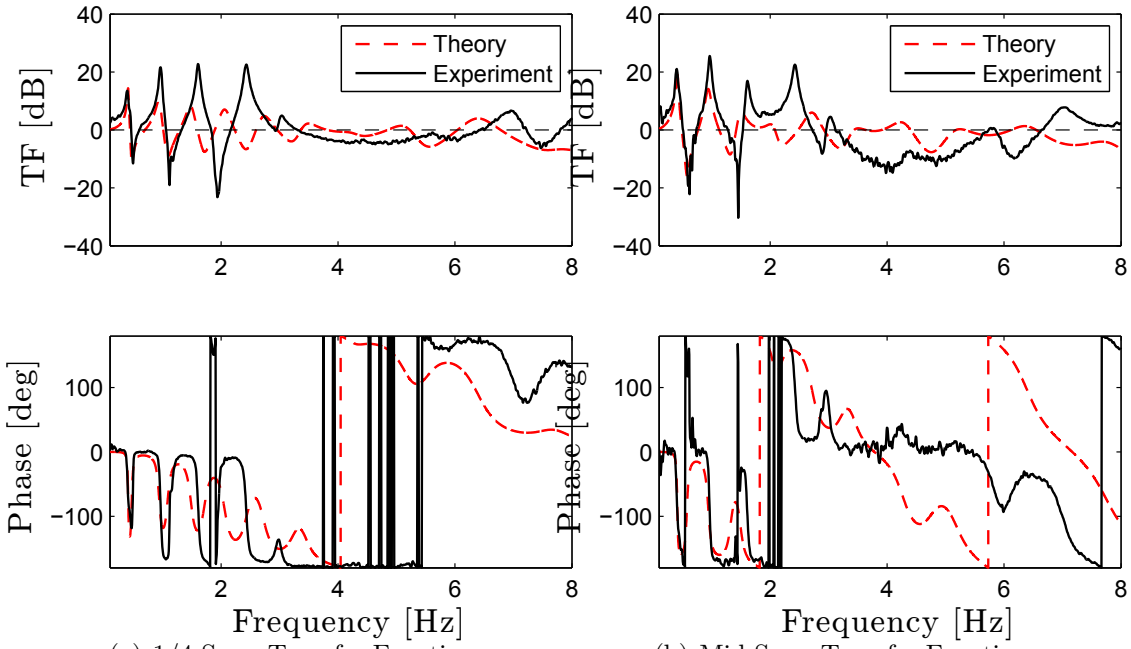

(a) 1/4 Span Transfer Function

(b) Mid Span Transfer Function

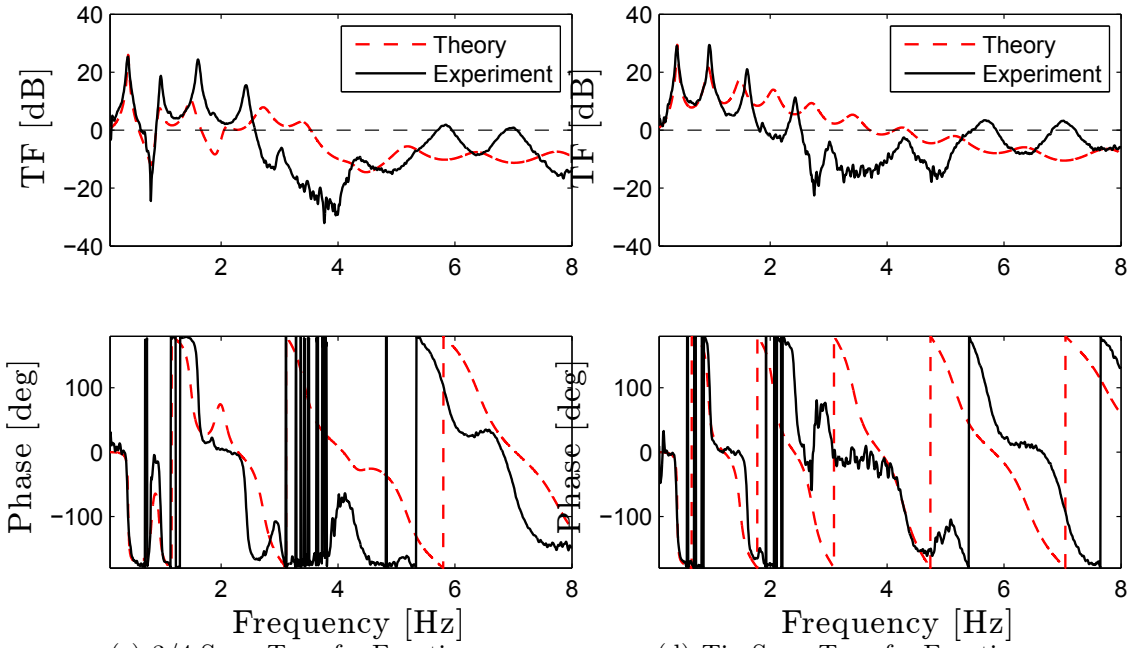

(c) 3/4 Span Transfer Function

(d) Tip Span Transfer Function

FIGURE A.6: Transfer Function for Configuration 4 with Flap Actuator at Four Different Span Locations

Bibliography

Abdulrahim, M., Garcia, H., Ivey, G. F., and Lind, R. (2004), "Flight testing a micro air vehicle using morphing for aeroservoelastic control," in *45th AIAA/ASME/ASCE/AHS/ASC Structural, Structural Dynamics and Materials Conference*, Palm Springs, California.

Attar, P. (2003), "Experimental and theoretical studies in nonlinear aeroelasticity," Ph.D. thesis, Duke University.

Balint, T. and Lucey, A. (2005), "Instability of a cantilevered flexible plate in viscous channel flow," *Journal of Fluids and Structures*, 20, 893–912.

Barmby, J. G., Cunningham, H. J., and Garrick, I. E. (1951), *Study of Effects of Sweep on the Flutter of Cantilever Wings*, National Advisory Committee for Aeronautics, Report 1014.

Berens, M. (2008), "Potential of multi-winglet systems to improve aircraft performance," Ph.D. thesis, der Technischen Universitat Berlin.

Berton, J. J., Envia, E., and Burley, C. L. (2009), "An analytical assessment of NASA's N+1 subsonic fixed wing project noise goal," in *15th AIAA/CEAS Aeroacoustics Conference*, Miami, Florida.

Bisplinghoff, R. L., Ashley, H., and Halfman, R. L. (1996), *Aeroelasticity*, Courier Dover Publications.

Bloomhardt, E. M. and Dowell, E. H. (2011), "A study of the aeroelastic behavior of flat plates and membranes with mixed boundary conditions in axial subsonic flow," in *52nd AIAA/ASME/ASCE/AHS/ASC Structural, Structural Dynamics and Materials Conference*, Denver, Colorado, AIAA-2011-1995.

Choudhari, M. M., Lockard, D. P., Macaraeg, M. G., Singer, B. A., Streett, C. L., Neubert, G. R., Stoker, R. W., Underbrink, J. R., Berkman, M. E., Khorrami, M. R., and Sadowski, S. (2002), *Aeroacoustic Experiments in the Langley Low-Turbulence Pressure Tunnel*, National Aeronautics and Space Administration, NASA/TM-2002-211432, Hampton, Virginia, NASA/TM-2002-211432.

Clarke, A. C. (1973), *The Best of Arthur C Clarke; 1956-1972*, Sidgwick and Jackson.

Doaré, O. and Michelin, S. (2011), "Piezoelectric coupling in energy-harvesting fluttering flexible plates: linear stability analysis and conversion efficiency," *Journal of Fluids and Structures*, 27, 1357–1375.

Doaré, O., Sauzade, M., and Eloy, C. (2011), "Flutter of an elastic plate in a channel flow: Confinement and finite-size effects," *Journal of Fluids and Structures*, 27, 76–88.

Dowell, E. H. (1969), "Nonlinear flutter of curved plates," *AIAA Journal*, 7, 424–431.

Dowell, E. H. (1975), *Aeroelasticity of Plates and Shells*, Noordhoff International Publishing, Leyden, The Netherlands.

Dowell, E. H. (2011), "Can solar sails flutter?" *AIAA Journal*, 49, 1305–1307.

Dowell, E. H. and Ventres, C. S. (1970), "Flutter of low aspect ratio plates," *AIAA Journal*, 8, 1162–1164.

Dowell, E. H., Clark, R., Cox, D., Curtiss Jr., H. C., Edwards, J. W., Hall, K. C., Peters, D. A., Scanlan, R., Simiu, E., Sisto, F., and Strganac, T. W. (2004), *A Modern Course in Aeroelasticity*, Kluwer Academic Publishers, 4th edn.

Dunnmon, J. A., Stanton, S. C., Mann, B. P., and Dowell, E. H. (2011), "Power extraction from aeroelastic limit cycle oscillations," *Journal of Fluids and Structures*, 27, 1182–1198.

Ellen, C. H. (1965), "Approximate solutions of the membrane flutter problem," *AIAA Journal*, 3, 1186–1187.

Eloy, C. and Schouveiler, L. (2011), "Optimization of two-dimensional undulatory swimming at high Reynolds number," *International Journal of Non-Linear Mechanics*, 46, 568–576.

Eloy, C., Souilliez, C., and Schouveiler, L. (2007), "Flutter of a rectangular plate," *Journal of Fluids and Structures*, 23, 904–919.

Eloy, C., Lagrange, R., Souilliez, C., Schouveiler, L., et al. (2008), "Aeroelastic instability of cantilevered flexible plates in uniform flow," *Journal of Fluid Mechanics*, 611, 97–106.

Eloy, C., Kofman, N., and Schouveiler, L. (2012), "The origin of hysteresis in the flag instability," *Journal of Fluid Mechanics*, 691, 583–593.

Garrick, I. E. and Reed III, W. H. (1981), "Historical development of aircraft flutter," *Journal of Aircraft*, 18, 897–912.

Giacomello, A. and Porfiri, M. (2011), "Energy harvesting from flutter instabilities of heavy flags in water through ionic polymer metal composites," in *Proceedings of SPIE 7976*, San Diego, California.

Gibbs, S. C. (2012), "Linear Aeroelastic Stability of Beams and Plates in Three Dimensional Flows," Master's thesis, Duke University.

Gibbs, S. C. and Dowell, E. H. (2013), "Solarelastic stability of the heliogyro," in *3rd International Symposium on Solar Sailing*, Glasgow, UK.

Gibbs, S. C. and Dowell, E. H. (2014), "Membrane paradox for solar sails," *accepted to AIAA Journal*.

Gibbs, S. C., Wang, I., Bloomhardt, E., and Dowell, E. H. (2012a), "Aeroelastic behavior of noise-reducing membranes for aircraft lifting surfaces part I: theory," in *53rd AIAA/ASME/ASCE/AHS/ASC Structural, Structural Dynamics and Materials Conference*, Honolulu, Hawaii.

Gibbs, S. C., Wang, I., and Dowell, E. H. (2012b), "Theory and experiment for flutter of a rectangular plate with a fixed leading edge in three-dimensional axial flow," *Journal of Fluids and Structures*, 34, 68–83.

Gibbs, S. C., Guerrant, D., Wilkie, W. K., and Dowell, E. H. (2013), "Rectangular solar sail flutter," in *54th AIAA/ASME/ASCE/AHS/ASC Structural, Structural Dynamics and Materials Conference*, Boston, Massachusetts.

Gibbs, S. C., Sethna, A., Wang, I., Tang, D., and Dowell, E. H. (2014a), "Aeroelastic stability of a cantilevered plate in yawed subsonic flow," *Submitted to Journal of Fluids and Structures*.

Gibbs, S. C., Fichera, S., Zanotti, A., Ricci, S., and Dowell, E. H. (2014b), "Flow field around the flapping flag," *Accepted to Journal of Fluids and Structures*.

Gibbs, S. C., Wang, I., and Dowell, E. H. (2014c), "Stability of rectangular plates in subsonic flow with various boundary conditions," *Accepted to AIAA Journal of Aircraft*.

Gibbs, S. C., Warren, J. E., Wilkie, W. K., and Dowell, E. H. (2014d), "Stability of rotorcraft for interplanetary space flight," in *American Helicopter Society 70th Annual Forum*, Montreal, Canada.

Gislason, T. (1971), "Experimental investigation of panel divergence at subsonic speeds," *AIAA Journal*, 9, 2252–2258.

Goland, M. (1945), "The flutter of a uniform cantilever wing," *Journal of Applied Mechanics*, 12, A197–A208.

Gordnier, R. E. and Visbal, M. R. (2002), "Development of a three-dimensional viscous aeroelastic solver for nonlinear panel flutter," *Journal of Fluids and Structures*, 16, 497–527.

Hall, K. C. (1994), "Eigenanalysis of unsteady flows about airfoils, cascades, and wings," *AIAA Journal*, 32, 2426–2432.

Han, J.-H., Lee, J.-S., and Kim, D.-K. (2009), "Bio-inspired flapping UAV design: A university perspective," in *The 16th International Symposium on: Smart Structures and Materials & Nondestructive Evaluation and Health Monitoring*, pp. 72951I–72951I.

Hellum, A., Mukherjee, R., and Hull, A. (2011), "Flutter instability of a fluid-conveying fluid-immersed pipe affixed to a rigid body," *Journal of Fluids and Structures*, 27, 1086–1096.

Hodges, D. and Dowell, E. (1974), *Nonlinear Equations of Motion for the Elastic Bending and Torsion of Twisted Nonuniform Rotor Blades*, National Aeronautics and Space Administration.

Howell, R., Lucey, A., Carpenter, P., and Pitman, M. (2009), "Interaction between a cantilevered-free flexible plate and ideal flow," *Journal of Fluids and Structures*, 25, 544–566.

Huang, L. (1995), "Flutter of cantilevered plates in axial flow," *Journal of Fluids and Structures*, 9, 127–147.

Ishii, T. (1965), "Aeroelastic instabilities of simply supported panels in subsonic flow," in *AIAA/RAeS/JSASS Aircraft Design and Technology Meeting*, Los Angeles, California.

Kehoe, M. W. (1995), *A Historical Overview of Flight Flutter Testing*, National Aeronautics and Space Administration, NASA Technical Memorandum 4720.

Kornecki, A. (1974), "Static and dynamic instability of panels and cylindrical shells in subsonic potential flow," *Journal of Sound and Vibration*, 32, 251–263.

Kornecki, A., Dowell, E., and O'Brien, J. (1976), "On the aeroelastic instability of two-dimensional panels in uniform incompressible flow," *Journal of Sound and Vibration*, 47, 163–178.

MacNeal, R. (1971), *Structural dynamics of the heliogyro*, NASA CR-1745.

MacNeal, R. H. and Hedgepeth, J. M. (1978), "Helicopters for interplanetary space flight," in *34th National Forum of the American Helicopter Society*, Washington, DC.

Marques, S., Timme, S., Badcock, K., Khodaparast, H., Prandina, M., and Mottershead, J. (2013), "The Enabling Certification by Analysis (ECERTA) Project," *CFD4aircraft.com*.

Michelin, S., Llewellyn Smith, S., and Glover, B. (2008), "Vortex shedding model of a flapping flag," *Journal of Fluid Mechanics*, 617, 1–10.

NASA (2000), *National Aeronautics and Space Administration: Strategic Plan 2000*, NASA, Washinton, D.C.: NASA Headquarters.

Natori, M., Nemat-Nasser, S., and Mitsugi, J. (1989), "Instability of a rotating blade subjected to solar radiation pressure," in *30th Structures, Structural Dynamics and Materials Conference*, Mobile, Alabama.

PIVTEC (2013), "PIVview 2C version 3.2, User Manual," .

Raffel, M., Willert, C. E., and Kompenhans, J. (1998), *Particle Image Velocimetry: A Practical Guide; with 24 Tables*, Springer.

Song, A., Tian, X., Israeli, E., Galvao, R., Bishop, K., Swartz, S., and Breuer, K. (2008), "Aeromechanics of membrane wings with implications for animal flight," *AIAA journal*, 46, 2096–2106.

Spriggs, J. H., Messiter, A. F., and Anderson, W. J. (1969), "Membrane flutter paradox- an explanation by singular-perturbation methods." *AIAA Journal*, 7, 1704–1709.

Streett, C., Lockard, D., Singer, B., Khorrami, M., and Choudhari, M. (2003), "In Search of the Physics: The Interplay of Experimental and Computation in Airframe Noise Research: Flap-Edge Noise," in *Proc. 41st AIAA Aerospace Sciences Meeting and Exhibit*, Reno, Nevada, AIAA-2003-977.

Streett, C. L., Casper, J. H., Lockard, D. P., Khorrami, M. R., Stoker, R., Elkoby, R., and Wenneman, W. F., U. J. R. (2006), "Aerodynamic Noise Reduction on High-Lift Devices on a Swept Wing Model," in *Proc. 44th AIAA Aerospace Sciences Meeting and Exhibit*, Reno, Nevada, AIAA-2006-212.

Taneda, S. (1968), "Waving motions of flags," *Journal of the Physical Society of Japan*, 24, 392–401.

Tang, D., Gibbs, S. C., and Dowell, E. H. (2014a), "Nonlinear aeroelastic analysis with inextensible plate theory including correlation with experiment," *Submitted to AIAA Journal of Aircraft*.

Tang, D., Gibbs, S. C., and Dowell, E. H. (2014b), "Theoretical and experimental aeroelastic flapping flag response: correlation with inextensible beam theory," *Submitted to Journal of Fluids and Structures*.

Tang, D. M., Yamamoto, H., and Dowell, E. H. (2003), "Flutter and limit cycle oscillations of two-dimensional panels in three-dimensional axial flow," *Journal of Fluids and Structures*, 17, 225–242.

Tang, L. and Païdoussis, M. (2007), "On the instability and the post-critical behaviour of two-dimensional cantilevered flexible plates in axial flow," *Journal of Sound and Vibration*, 305, 97–115.

Tang, L. and Païdoussis, M. (2008), "The influence of the wake on the stability of cantilevered flexible plates in axial flow," *Journal of Sound and Vibration*, 310, 512–526.

Templin, R. J. (2000), "The spectrum of animal flight: insects to pterosaurs," *Progress in Aerospace Sciences*, 36, 393–436.

Thomson, W. (1993), *Theory of Vibrations with Applications*, Prentice Hall, Englewood Cliffs, New Jersey.

Tsuda, Y., Mori, O., Funase, R., Sawada, H., Yamamoto, T., Saiki, T., Endo, T., and Kawaguchi, J. (2011), "Flight status of IKAROS deep space solar sail demonstrator," *ACTA Astronautica*, 69, 833–840.

Wang, I. (2011), "An Analysis of Higher Order Effects in the Half Power Method for Calculating Damping," *Journal of Applied Mechanics*, 78, 014501, doi:10.1115/1.4002208.

Wang, I., Gibbs, S. C., Bloomhardt, E. M., and Dowell, E. H. (2012a), "Aeroelastic Behavior of Noise-Reducing Membranes for Aircraft Lifting Surfaces Part II: Experiment," in *53rd AIAA/ASME/ASCE/AHS/ASC Structures, Structural Dynamics, and Materials Conference*, Honolulu, Hawaii.

Wang, I., Gibbs, S. C., and Dowell, E. H. (2012b), "Aeroelastic model of multisegmented folding wings: theory and experiment," *Journal of Aircraft*, 49, 911–921.

Wang, I., Gibbs, S. C., and Dowell, E. H. (2012c), "Flutter of rectangular plates in three dimensional incompressible flow with various boundary conditions: Theory and experiment," in *ASME 2012 International Design Engineering Technical Conferences and Computers and Information in Engineering Conference*, pp. 51–63, American Society of Mechanical Engineers.

Wang, I., Gibbs, S. C., and Dowell, E. H. (2013), "Aeroelastic analysis of a folding wing: comparison of simple and higher fidelity models for a wide range of fold angles," in *54th AIAA/ASME/ASCE/AHS/ASC Structures, Structural Dynamics, and Materials Conference*, Boston, Massachusetts.

Watanabe, Y., Suzuki, S., Sugihara, M., and Sueoka, Y. (2002a), "An experimental study of paper flutter," *Journal of Fluids and Structures*, 16, 529–542.

Watanabe, Y., Isogai, K., Suzuki, S., and Sugihara, M. (2002b), "A theoretical study of paper flutter," *Journal of Fluids and Structures*, 16, 543–560.

Wilkie, W. K., Warren, J. E., Juang, J., Horta, L. G.and Lyle, K. H., Littell, J. D., Bryant, R. G., Thomson, M. W., Walkemeyer, P. E., Guerrant, D. V., Lawrence, D. A., Gibbs, S. C., Dowell, E. H., and Heaton, A. F. (2013), "Heliogyro Solar Sail Research at NASA," in *Third International Symposium of Solar Sailing*, Glasgow, U.K.

Zhang, J., Childress, S., Libchaber, A., and Shelley, M. (2000), "Flexible filaments in a flowing soap film as a model for one-dimensional flags in a two-dimensional wind," *Nature*, 408, 835–839.

Zhao, L., Huang, Q., Deng, X., and Sane, S. P. (2010), "Aerodynamic effects of flexibility in flapping wings," *Journal of the Royal Society Interface*, 7, 485–497.

Biography

Samuel Chadwick Gibbs IV (Chad) was born and raised in Portola Valley, California, a small town near Stanford University. Chad moved to North Carolina in 2006 to attend Duke University where he received his Bachelors of Science in Mechanical Engineering and Material Science in May 2010. After graduating he chose to advance his technical expertise by pursing a Doctorate at Duke University. As a graduate student, Chad researched aeroelasticity and solarelasticity under Dr. Earl Dowell. He received his Masters of Science in Mechanical Engineering in May 2012 and his Doctorate in May 2014. Chads research was supported by NASA Office of the Chief Technologist Space Technology research fellowship.

Outside of school, Chad has been an active member of the Duke community. He led the development of a website for the Duke Aeroelasticity Research Group to increase the groups visibility, strengthen its reputation and showcase the groups research achievements. In designing the website, Chad helped to create the groups self-contained identity that its members, the Mechanical Engineering department, and Duke University can leverage for recruiting and fundraising. His efforts led to an expansive web presence at aeroelasticity.pratt.duke.edu. Chad also enjoys basketball, rugby, golf and running. Chad enjoys traveling and has played golf in 6 countries (US, Mexico, Ireland, Iceland, UK, and France).

Honors and Awards

- NASA Office of the Chief Technologist Space Technology Research Fellowship

- Sigma Xi, Sally Hughes-Schrader Travel Grant
- Duke MEMS Retreat: Best Presentation (2013), Best Presentation of a Poster (2012), Best-Poster runner-up (2011)
- Duke Pi Tau Sigma Scholarship